

University of Alberta

Composite Connections Using High Performance Concrete

by

Sadegh Kazemi

A thesis submitted to the Faculty of Graduate Studies and Research in partial fulfillment of the requirements for the degree of

**Doctor of Philosophy
in
Structural Engineering**

Department of Civil and Environmental Engineering

©Sadegh Kazemi
Fall 2013
Edmonton, Alberta

Permission is hereby granted to the University of Alberta Libraries to reproduce single copies of this thesis and to lend or sell such copies for private, scholarly or scientific research purposes only. Where the thesis is converted to, or otherwise made available in digital form, the University of Alberta will advise potential users of the thesis of these terms.

The author reserves all other publication and other rights in association with the copyright in the thesis and, except as herein before provided, neither the thesis nor any substantial portion thereof may be printed or otherwise reproduced in any material form whatsoever without the author's prior written permission.

*Dedicated with love to my family,
for inspiring me to keep following my dreams .*

Abstract

With the ever increasing concerns about the structural adequacy of buildings and infrastructures, particularly in harsh environments with limited funding for ongoing maintenance, a significant need exists to develop highly durable and rapidly constructed structural systems. To this aim, recent advances in the development of high-performance material allow for the introduction of innovative girder configuration systems using the ultra-high performance fiber-reinforced concrete (UHPFRC) material as flange and direct embedded steel plate as web. The proposed composite member will result in a durable building or bridge superstructure construction with reduced life-cycle cost, longer life span, and enhanced environmental sustainability (Hegger 2006, Graybeal and Tanesi 2007, and Rauscher 2011). To cope with the higher cost of the high-performance material, innovative designs should be implemented in detailing of composite members to make sure that the material is best used where it is most required. To date, however, there has been very limited research on the structural behaviour of this member configuration.

The objectives of the current study are twofold. The first phase focuses on development of a UHPFRC material incorporating 0-5% randomly distributed short steel fibers using the conventional moist curing technique without added heat or pressure to be representative of potential applications requiring in-situ casting. The addition of steel fibers to the UHPFRC matrix was found to significantly enhance the mechanical properties of the UHPFRC material in compression, flexure, tension and shear. In addition, the peak compressive, flexural, equivalent tensile strength, and shear strengths of the material were found to decrease with an increase in the specimen size, indicating that a size effect exists for members constructed with UHPFRC material.

The second phase of the research focuses on the development of a composite connection system, which ensures an efficient composite action between embedded steel web and concrete flanges. A commercially available finite element package, ABAQUS® 6.11 was used to simulate the response of the composite connection system subjected to the pull-out load and to minimize the need for full-scale

structural testing. A total of 42 specimens were designed, constructed, and tested to capture the experimental response of the composite connections subjected to the pull-out loading. The influence on the pull-out capacity of the composite connection from shape and size of holes (which is cut through the embedded web), embedded length of steel plate, plate thickness, fiber content, double headed stud (which is passed through hole), and concrete member depth are investigated. In addition, comparisons of the connection specimen performance to those constructed with conventional fiber-reinforced concrete (FRC) material were completed. It was found that compared to connection systems constructed with FRC material, the use of UHPFRC can substantially enhance the load carrying capacity and ductility of the connection systems subjected to the pull-out and push-out loading.

Acknowledgements

I would like to express my sincere gratitude to everyone who, by their encouragement, support, and help has contributed to the completion of this research project. Financial support for this study provided by the Natural Sciences and Engineering Research Council (NSERC) is gratefully acknowledged. Personal financial assistance in the form of scholarships/awards from the Faculty of Graduate Studies and Research, Shell Canada, University of Alberta Graduate Student Research Assistant Award, Government of Alberta Graduate Citizenship Award, MCAA, Canadian Precast Concrete institute, Canadian Society for Civil Engineering, and Department of Civil and Environmental Engineering are greatly appreciated. The author thanks Lehigh Inland Heidelberg Cement (Canada), Bekaert, BASF, Decon Stud, and Waiward Steel fabrication Ltd. for supplying the material used in this study.

I would like to express my sincere gratitude to Dr. Roger Cheng who supervised, supported, and mentored me throughout the course of this research. I also extend my gratitude to the other members of my committee: Dr. Rober Driver (Committee Chair), Dr. Khaled Gala (External Examiner), Dr. Yaman Boluk, and Dr. Zihui Xia for providing valuable comments toward this research. Intellectual helps from Dr. Adam S. Lubell is also acknowledged.

The acknowledgement is also extended to the several graduate students and staff in the Department of Civil and Environmental Engineering at the University of Alberta for their valuable contributions to the success of this project. Technical contributions to this work deserve acknowledgement. Many thanks to Greg Miller for instrumentation, Cameron West, and Robert Anusic for physical test setup assistance.

Last, but not the least, I would like to take this opportunity to express my special thanks to my family, in particular, my lovely wife, Meimanat, for unending love, encouragement, and support she has shown me over the years. She has made every moment of my life joyful and hopeful to progress. Thank you for everything....

Table of Contents

1	Introduction	1
1.1	Motivation	1
1.2	High Performance Material	2
1.3	Composite Connection	3
1.4	Research Significance	5
1.5	Project Objectives and Scope.....	5
1.6	Organization of the Thesis.....	7
2	Review of the Literature.....	9
2.1	Introduction.....	9
2.2	Mechanical Properties of UHPFRC Material.....	9
2.2.1	Compressive Response.....	10
2.2.2	Flexural Response	17
2.2.3	Tensile Response	26
2.2.4	Direct Shear Response.....	31
2.2.5	Rheological properties.....	34
2.3	Mechanical Properties of FRC	36
2.3.1	Compressive Response.....	36
2.3.2	Flexural-Tensile Response.....	37
2.3.3	Equivalent Tensile Response	38
2.3.4	Direct Shear Response.....	40
2.4	Composite Connection	41
2.4.1	Response under Shear Loading	42
2.4.2	Response under Tensile and Compressive Loading.....	55
3	Mechanical Properties of UHPFRC material: Experimental Program	65

3.1	Introduction.....	65
3.2	Mix Preparation and Development.....	66
3.2.1	Portland Cement	66
3.2.2	Silica Fume.....	68
3.2.3	Sand.....	68
3.2.4	Superplasticizer.....	69
3.2.5	Water	69
3.2.6	Steel Fibers.....	69
3.3	UHPFRC Mix Composition	70
3.4	Mixing, Sampling and Curing.....	71
3.4.1	Mixing.....	71
3.4.2	Placement.....	75
3.4.3	Curing	77
3.5	Specimen Geometry and Test Set-up	77
3.5.1	Compressive Strength.....	77
3.5.2	Flexural Strength	79
3.5.3	Shear Strength.....	89
4	Mechanical Properties of UHPFRC Material: Test Results and Discussion.....	91
4.1	Introduction.....	91
4.2	Compression Response.....	91
4.2.1	Stress-Strain Response.....	92
4.2.2	Influence of Sand to Cement (S/C) ratio	94
4.2.3	Influence of Silica Fume to Binder ratio.....	94
4.2.4	Influence of Fiber Volume-Fraction	95
4.2.5	Influence of Consolidation	97
4.2.6	Influence of Specimen Size and Shape	97

4.2.7	Time Development.....	99
4.3	Flexural Response.....	101
4.3.1	Overview of Flexural Test Results.....	101
4.3.2	Load-Deflection Response.....	102
4.3.3	Stages in Flexural Fracture of UHPFRC.....	104
4.3.4	Cracking and Peak Strength.....	107
4.3.5	Influence of Size Effect.....	110
4.3.6	Influence of Consolidation.....	111
4.3.7	Influence of Time Development.....	111
4.3.8	Flexural Toughness Factor (FTF).....	112
4.4	Direct Shear Response.....	116
4.4.1	Shear-Slip Relationship.....	116
4.4.2	Stages in Shear Fracture of UHPFRC.....	118
4.4.3	Peak Shear Strength.....	121
4.4.4	Shear Toughness Factor (STF).....	124
4.5	Equivalent tensile strength (ETS).....	127
4.5.1	Analytical model for ETS-CMOD.....	129
4.5.2	Iterative Process.....	131
4.5.3	Correlation between Deflection and Crack Width.....	132
4.5.4	Cracking Equivalent Tensile Strength (CETS).....	134
4.5.5	ETS-CMOD Curve.....	135
4.5.6	Peak Equivalent Tensile Strength (PETS).....	136
5	Composite Connections: Experimental Program.....	140
5.1	Introduction.....	140
5.2	Description of Pull-Out Specimen.....	140
5.3	Specimen Nomenclature.....	141

5.4	Specimen Fabrication	143
5.5	Composite Connection Components	144
5.5.1	Concrete Beam	144
5.5.2	Embedded Steel Plate	147
5.5.3	Double Headed Stud	149
5.6	Ancillary Material Tests	150
5.6.1	Concrete	150
5.6.2	Embedded Steel Plate	158
5.7	Pull-out Test Setup	161
5.8	Instrumentation	164
5.8.1	External Instrumentation	164
5.8.2	Strain Gauges	164
5.8.3	Data Acquisition	166
5.8.4	Digital Imaging Correlation System	166
5.9	Test Procedure	168
6	Composite Connections: Test Results and Discussion	169
6.1	Introduction	169
6.2	General Observation	172
6.3	Overview of Failure Mechanisms	175
6.3.1	Pull-Out Failure	176
6.3.2	Steel Yielding Failure	177
6.3.3	Splitting Failure	178
6.3.4	Breakout Failure	179
6.3.5	Concrete Side Failure	180
6.4	Pullout Response of Composite Connection with Ω -shaped Tension key	181
6.4.1	Influence of Hole Diameter	181

6.4.2	Influence of Plate Thickness.....	191
6.4.3	Influence of plate embedment length.....	200
6.4.4	Influence of Fiber Volume Fraction.....	205
6.4.5	Influence of Concrete Generation	212
6.5	Pullout Response of Connection with Puzzle-Strip Tension key	218
6.5.1	Influences of plate thickness.....	219
6.5.2	Influence of concrete generation.....	224
6.6	Circular-Shaped Tension Key	227
6.6.1	Influence of Tension Key Size	227
6.6.2	Influence of Double-Headed Stud (DHS).....	233
6.6.3	Influence of Plate Thickness.....	236
6.6.4	Influence of Concrete Generation	239
7	Finite Element Analysis of Composite Connections	245
7.1	Introduction.....	245
7.2	Description of Model in ABAQUS	245
7.2.1	Specimen Configuration.....	246
7.3	Analysis Type	248
7.3.1	ABAQUS/Standard	248
7.3.2	ABAQUS/Explicit.....	248
7.4	Material Property	251
7.4.1	Steel Material.....	251
7.4.2	Concrete Constitutive Model.....	252
7.4.3	Mechanical Properties of UHPFRC and FRC Material	257
7.5	Loading	261
7.6	Element.....	262
7.6.1	Mesh Sensitivity	263

7.7	Contact Interaction	265
7.8	Boundary Conditions	266
7.9	Verification of Results	267
7.9.1	General Observation	267
7.9.2	Comparison of Numerical and Experimental Results.....	271
7.10	Parametric Analysis.....	278
7.10.1	Composite Connection under Pull-out Loading	279
7.10.2	Composite Connection under Push-out Loading	292
8	Summary, Conclusion, and Recommendation.....	297
8.1	Summary	297
8.2	Conclusion	299
8.2.1	Mechanical Properties of UHPFRC material	299
8.2.2	Composite Connection.....	303
8.3	Ongoing and Future Research.....	306
	List of References.....	308

List of Tables

Table 3-1: Chemical analysis of type HE cement (ASTM C 25-06)	66
Table 3-2: Physical properties of type HE cement.....	67
Table 3-3: Mineralogical properties analysis of type HE cement	67
Table 3-4: Physical properties of silica fume (CAN/CSA-A23.5-M86).....	68
Table 3-5: UHPFRC composition normalized by mass of cement.....	70
Table 3-6: As-built prism specimen properties for flexural test.....	81
Table 3-7: Rate of flexural loading.....	82
Table 3-8: Location parameters of camera	85
Table 3-9: As-built prism specimen properties for direct shear.....	89
Table 4-1: Compressive strength of CU-50 specimens	96
Table 4-2: Compressive strength conversion factors between cylinders and cubes	99
Table 5-1: Details of composite connections with UHPFRC material	142
Table 5-2: Details of composite connections with FRC material	143
Table 5-3: UHPFRC composition normalized by the mass of cement.....	144
Table 5-4: FRC material composition.....	146
Table 5-5: Geometry of double headed stud	150
Table 5-6: Summary of results of companion samples for composite connection made of FRC concrete.....	151
Table 5-7: Summary of results of companion samples for composite connection constructed with UHPFRC material	152
Table 5-8: Geometrical and mechanical properties of coupon tests	161
Table 6-1: Experimental results of composite connections system with Ω -shaped tension key.....	171
Table 6-2: Experimental results of composite connection systems with puzzle-strip tension key.....	171
Table 6-3: Experimental results of composite connection systems with O-shaped tension key.....	172
Table 7-1: The parameters of concrete damage plasticity model	255
Table 7-2: The parameters of concrete smeared cracking (CSC) model.....	256
Table 7-3: The elastic parameters for the UHPFRC and FRC material	257

List of Figures

Figure 2-1: Influence of silica fume content on the compressive strength of UHPFRC material (Le et al. 2007 [after]).	12
Figure 2-2: Influence of fiber volume-fraction on the compressive strength of UHPFRC material (Le et al. 2007 [after]).	14
Figure 2-3: Compressive stress-strain response of UHPFRC material, a) influence of fiber on compressive strength (Skazlic and Bjegovic 2009), b) schematic of the improvement in softening response with increasing fiber volume-fraction.	15
Figure 2-4: Variation of compressive strength of UHPC material against time (Graybeal 2000).	17
Figure 2-5: Flexural response of NSC, FRC, and UHPFRC material.	18
Figure 2-6: Variation of flexural-tensile strength against the specimen height (Reineck and Greiner 2010).	22
Figure 2-7: Variation of cracking flexural-tensile strength of UHPFRC material against the specimen height (after Frettlöhr et al. 2012).	23
Figure 2-8: Peak flexural-tensile strength of UHPFRC material against the specimen height (after Frettlöhr et al., 2012).	24
Figure 2-9: Fiber orientation and distribution in UHPFRC material (Boulekbache et al. 2010).	25
Figure 2-10: Variation of tensile strength against the crack opening.	28
Figure 2-11: Variation of experimental scale factor against the beam depth (CEB-FIP 1999).	30
Figure 2-12: Variation of scale factor against prism height (Chanvillard and Rigaud 2003).	30
Figure 2-13: Overall configuration of JSCE-G 53 direct shear test setup (JSCE-G 53 1999).	32
Figure 2-14: compressive stress-strain response of FRC material with different fiber types (Mirsayah and Banthia, 2002).	37
Figure 2-15: Flexural prism under 4-point loading, a) schematic of FRC prism specimen after the formation of macro crack, b) formation of plastic hinge at flexural crack, c) stress block at the cracked section (Dinh, 2010).	39
Figure 2-16: Variation of equivalent tensile strength (ETS) against the CMOD response of LSC, NSC, and HSC FRC material (Shoab 2012).	40
Figure 2-17: Variation of shear strength of FRC material against fiber volume fraction (Mirsayah and Banthia 2002).	41
Figure 2-18: Geometry of the standard push-out test (EC4 2004).	42
Figure 2-19: push-out test setup (Hegger et al. 2009).	44
Figure 2-20: Single push-out test set-up (Hegger et al. 2009).	45

Figure 2-21: Influence of test set-up on the push-off load carrying capacity of composite connections with different shear key configurations (Rauscher 2011).	45
Figure 2-22: Shear key configurations: a) puzzle-strip shear key, b) saw-tooth-I shear key, c) saw-tooth-II shear key (Hegger et al. 2009).	46
Figure 2-23: Direction of applied shear loading (Hegger et al. 2009).	46
Figure 2-24: Influence of load direction on the pull-off capacity of composite connections (Rauscher 2011).	46
Figure 2-25: Failure modes of embedded steel plate with puzzle-strip hole subjected to shear loading (Hegger et al. 2009).	47
Figure 2-26: Influence of plate thickness on the deformed shape of puzzle-strip shear key (Rauscher 2011).	47
Figure 2-27: Influence of plate thickness on the peak push-off load carrying capacity of the composite connections (Rauscher 2011).	48
Figure 2-28: Influence of randomly distributed fiber volume fraction on the peak push-off load carrying capacity of the composite connections (Rauscher 2011).	49
Figure 2-29: Influence of concrete cover depth on the peak push-off load carrying capacity of the composite connections (Hegger et al. 2009).	50
Figure 2-30: Failure mode of composite connection system constructed with: a) UHPC material, b) HSC material (Rauscher 2011).	51
Figure 2-31: Influence of concrete generations on the peak push-off load carrying capacity of the composite connections (Rauscher 2011).	51
Figure 2-32: Influence of transverse reinforcements passed though hole on the peak push-off load carrying capacity of the composite connections (Wurzer 1997).	52
Figure 2-33: Multiaxial stress in the contact area between the concrete shear key and steel plate (Wurzer 1997).	52
Figure 2-34: Overall configuration of embedded corrugated steel plate with Ω -shaped shear key (Rohem, 2009).	53
Figure 2-35: Twisting in the shear key (Röhm, 2009).	54
Figure 2-36: Push-off test with puzzle-strip shear key and spiral springs (Abramski et al. 2010).	55
Figure 2-37: Geometry of composite girders with circular and rectangular hole (Abramski et al. 2010).	56
Figure 2-38: Secondary bending moment resulting from the shear force acting at opening (Abramski 2010).	56
Figure 2-39: Composite girders with opening in web (Kohlmeyer 2007).	57
Figure 2-40: location of the strain gauges (Kohlmeyer 2007).	58
Figure 2-41: Variation of tensile loading in each headed studs against the total applied load (Kohlmeyer 2007).	58

Figure 2-42: Composite beam with multiple opening in steel web (after Abramski et al. 2010).....	59
Figure 2-43: Break-out failure in the composite connections constructed with embedded steel plate in the normal strength concrete flange (Abramski et al. 2010).....	60
Figure 2-44: geometry of pull-out connection (Abramski et al. 2010).	60
Figure 2-45: Variation of pull-out load against the relative slip for the composite connections constructed with embedded steel plate in normal strength concrete (Hegger et al. 2013).	61
Figure 2-46: Schematic of the break-out failure in the pull-out test (Burger 2009). 62	
Figure 2-47: Plate yielding failure in the pull-out test (Burger 2009).	62
Figure 2-48: Overall configuration of composite connection: a) under pull-out loading, b) Under push-out loading, c) side view of composite connection (Hegger et al. 2009).	63
Figure 2-49: The composite connection under pull-out test after failure (Hegger et al. 2009).....	64
Figure 2-50: Composite connection under push-out test after failure (Hegger et al. 2009).....	64
Figure 3-1: Short steel fibers, $l_f=13$ mm and $d_f=0.2$ mm.....	70
Figure 3-2: High performance mixer with inclined pan.	71
Figure 3-3: Material addition and corresponding power consumption during the UHPFRC mixing.....	72
Figure 3-4: a) Addition of steel fibers to mix, b) Finished UHPFRC mix.....	73
Figure 3-5: Relation between normalized peak power consumption of mixer and fiber volume fractions.....	74
Figure 3-6: Pat diameter of UHPFRC matrix and slump test in accordance with ASTM C 230/ C 230M-03.	75
Figure 3-7: Top view of casting method.....	76
Figure 3-8: Fiber dispersion at the top surface of ground CY-50 cylinder specimen including a) $V_f = 0\%$, b) $V_f = 2\%$, and c) $V_f = 4\%$	77
Figure 3-9: (a) Compression cylinder specimens including (right to left) CU-100, CU-75, and CU-50, (b) ASTM C39 compression test setup using a yoke with 3 LVDTs at 120° to measure axial stress-strain response.....	79
Figure 3-10: Test set-up of flexural test.	80
Figure 3-11: Flexural prism specimen samples including (top to bottom) PF-50, PF-100, PF-150, and PF-200.	80
Figure 3-12: Schematic of flexural test setup.....	83
Figure 3-13: Experimental setup of digital image correlation (DIC) system.....	84
Figure 3-14: a) Painted specimen, b) Black speckling on the front surface of prism.....	85

Figure 3-15: Vertical measurement points and virtual extensometer location in the VIC-3D software.	87
Figure 3-16: Side view of ASTM C1609 flexural test setup with two LVDTs mounted on back side of prism specimens.....	88
Figure 3-17: a) Direct shear test set-up in MTS 1000 machine, b) Schematic of test set up.....	90
Figure 4-1: Typical stress-strain curves from compression tests of different cylinder sizes.	93
Figure 4-2: Typical failure mode for (a) CY-75 before loading, (b) CY-75 with $V_f = 0\%$, (c) CY-75 with $V_f = 2\%$, (d) CY-100 before loading, (e) CY-100 with $V_f = 0\%$, (f) CY-100 with $V_f = 2\%$	93
Figure 4-3: Influence of cement/sand and SF/B ratio on normalized compressive strength of the UHPFRC material.	94
Figure 4-4: Influence of SF/B on the compressive strength of the UHPFRC material.	95
Figure 4-5: Compression failure in CY-200 specimens, left to right: $V_f = 0, 2,$ and 4.96	
Figure 4-6: Influence of consolidation on the compressive strength of the CU-50 specimens.....	97
Figure 4-7: Influence of V_f on the average 28 days compressive strength of the CU-50 and CU-100 specimens.....	98
Figure 4-8: Influence of V_f on the average 28 days compressive strength of the CY-50, CY-75, and CY-100 specimens.....	99
Figure 4-9: Time development of the CU-50 compressive strengths.....	100
Figure 4-10: Time development of CU-50 compressive strengths during the first 72 hours.	101
Figure 4-11: Normalized load-deflection response of the PF-200 specimen: comparison of LVDT and DIC measurement.	102
Figure 4-12: Comparison of the flexural load-deflection response of the PF-50 specimens with different V_f	103
Figure 4-13: Comparison of the flexural load-deflection response of the PF-50, PF-100, PF-150, and PF-200 specimens with $V_f = 2\%$ and 4%	104
Figure 4-14: Different stages in the flexural fracture of the UHPFRC material: Linear Stage (Curve I-II); Hardening Stage (Curve II-III); Softening Stage (Curve II-III).	106
Figure 4-15: Mid-span deflection at cracking load for different prism specimen sizes.	107
Figure 4-16: Influence of fiber content, SF/B ratio and size effect on the: (a) first crack strength (FCS); and (b) peak load equivalent strength (PLES).	108
Figure 4-17: Influence of three different fiber content and specimen size on FCS of UHPFRC.....	109

Figure 4-18: Influence of consolidation on the peak load equivalent strength (PLES) of PF-50.....	109
Figure 4-19: Influence of fiber content and specimen size on the PLES of UHPFRC material.....	111
Figure 4-20: Time development of First Crack Strength (FCS) of PF-50 specimens.	112
Figure 4-21: Time development of peak load equivalent strength (PLES) of PF-50 specimens.....	112
Figure 4-22: Influence of fiber volume fraction (V_f) and consolidation on the FTF of PF-50 prism specimens ($L/150$).	114
Figure 4-23: Crack development in PF-100 including (top to bottom) mix with $V_f=0\%$, $V_f=2\%$, $V_f=4\%$	114
Figure 4-24: Influence of fiber volume fraction on FTF of specimens of different sizes including PF-50, PF-100, PF-150, PF-200 with $V_f=2\%$	116
Figure 4-25: Influence of fiber volume fraction on FTF of specimens of different sizes including PF-50, PF-100, PF-150, PF-200 with $V_f=4\%$	116
Figure 4-26: Typical shear load slip curves for PS-50 specimens.	117
Figure 4-27: Failure of PS-50: (a) without fiber, (b) with fiber.....	118
Figure 4-28: Typical shear load-slip curves for the UHPFRC material.....	119
Figure 4-29: Variation of peak shear strength factor, k_v , with SF/B for PS-50 specimens.....	122
Figure 4-30: Variation of k_v against V_f for vibrated and non-vibrated PS-50 and vibrated PS-100.....	123
Figure 4-31: Relationship between SSF_{peak} and V_f for PS-50 with $V_f = 0-5\%$	123
Figure 4-32: Variation of SSF_{peak} against V_f for PS-50 and PS-100.....	124
Figure 4-33: (a) Influence of V_f , consolidation, and specimen size on STF of PS-50 ($h_n/30$); and (b) variation of STF with different h_n/m for PS-50 and PS-100 specimens.....	125
Figure 4-34: a) disturbed zone in crack UHPFRC beam, and b) Variation of curvature along the beam (after Casanova and Rossi 1996).	127
Figure 4-35: Full response of UHPFRC prism specimen under flexure and compression: (a) Geometry and situation; (b) Stiffness (c) Stress profile and definition of maximum stress softening.....	128
Figure 4-36: Situation of CMOD and equivalent tensile strength at two different steps.	132
Figure 4-37: Variation of CMOD against mid-span deflection for prism specimens.	133
Figure 4-38: Values of υ upsilon for prism specimens with $V_f = 2\%$, $V_f = 4\%$, and average υ value.	134

Figure 4-39: Equivalent tensile strength-CMOD response of PF-50 prism specimens with different fiber volume fraction.	135
Figure 4-40: Effect of fiber volume fraction on PETS of UHPFRC.....	137
Figure 4-41: Influence of specimen size on PETS of UHPFRC with $V_f = 0, 2\%$, and 4%	138
Figure 4-42: Relationship between the decrease in PETS and UHPFRC prism specimens with $V_f = 0\%, 2\%$, and 4%	138
Figure 4-43: Relationship between the CMOD and prism specimen size for two different fiber volume fractions.....	139
Figure 5-1: Overall geometry and configuration of the pull-out specimen, a) Front view, b) Side view.	141
Figure 5-2: Top view of reinforcement cage, double headed stud (DHS) and formwork.	146
Figure 5-3: Composite connection after casting and screeding.	147
Figure 5-4: configuration of the embedded steel plate with different tension key configurations.	148
Figure 5-5: Geometry and configuration of the embedded steel plate: a) Ω -shaped tension key; b) O-shaped tension key; c) P-S tension key.	149
Figure 5-6: Geometry of double headed stud (DHS).	150
Figure 5-7: Compressive stress-strain behaviour of the FRC material.	153
Figure 5-8: Flexural test set-up on notched PF-100 prism specimens.....	154
Figure 5-9: Flexural load-deflection responses of companion UHPFRC PF-50 and FRC PF-100.....	154
Figure 5-10: Variation of PETS of UHPFRC and FRC material against the change in fiber volume fraction (V_f).....	155
Figure 5-11: ASTM C1609-10 Flexural Prism Layout and Deformation Model (Adapted from Armelin and Banthia, 1997).	156
Figure 5-12: a) Cross section of prism, b) Stress distribution, c) Force Diagram in the cross section.....	157
Figure 5-13: ASTM C1609-10 Flexural prism layout and deformation model (Adapted from Armelin and Banthia, 1997).	158
Figure 5-14: Dimensions of the tension coupon test taken from plate material.....	159
Figure 5-15: Coupon test with painted surface and extensometer.....	160
Figure 5-16: Typical Stress-strain curves of coupons test samples.....	160
Figure 5-17: Geometry of Pull-out specimen under tensile loading in MTS-1000 machine.....	163
Figure 5-18: Clevis and filler plates to grip the embedded steel plate to top cross-head of MTS-1000 machine.....	163

Figure 5-19: Front view of instrumentation including vertical LVDTs mounted on both side of steel plate and a pair of strain gauges mounted next to tension key.	165
Figure 5-20: Top view of instrumentation including four horizontal LVDTs mounted on top back-side of steel plate and a pair of Vertical LVDTs attached to embedded steel plate.	165
Figure 5-21: General view of the horizontal LVDTs mounted on back side of concrete beam and vertical LVDTs attached to embedded steel plate.....	166
Figure 5-22: Front view of the painted concrete beam and the data extraction point for DIC.....	168
Figure 6-1: Typical pull-out load-slip response of composite connection system..	173
Figure 6-2: Pull-out failure, a) schematic side view of the connection specimen, b) front view of the connection specimen at the end of the test.....	177
Figure 6-3: Schematic of splitting failure in the composite connection.....	178
Figure 6-4: Breakout failure modes in the composite connections with different tension key configurations, a) O-shaped tension key in UHPFRC beam, b) Ω -shaped tension key in UHPFRC beam, c) puzzle-strip tension key in UHPFRC beam, d) Ω -shaped tension key in FRC beam.....	180
Figure 6-5: Concrete side failure in composite connection system.....	181
Figure 6-6: Overall failure of Ω S-U-50-10-2 specimen (Ω -shaped tension key, hh = 50 mm, UHPFRC material with $V_f = 2\%$, plate thickness = 10 mm).....	183
Figure 6-7: Pull-out load-slip response of Ω S-U-50-10-2 connection specimens....	184
Figure 6-8: Failure cracks growth throughout testing of Ω S-U-50-10-2 specimen (First Specimen).....	184
Figure 6-9: Variation of average compressive strain against slip for the Ω S-U-50-10-2 specimen (First Specimen).....	185
Figure 6-10: Overall failure of Ω S-U-70-10-2 specimen (Ω -shaped tension key, hh= 70 mm, UHPFRC material with $V_f = 2\%$, plate thickness = 10 mm).	186
Figure 6-11: Load-slip response of Ω S-U-70-10-2 specimens.	187
Figure 6-12: Failure cracks growth throughout testing of Ω S-U-70-10-2 specimen (First Specimen).....	187
Figure 6-13: Overall failure of Ω S-U-90-10-2 specimen (Ω -shaped tension key, hh = 90 mm, UHPFRC with $V_f = 2\%$, t _{pl} = 10 mm), a) First Specimen, b) Second Specimen.	189
Figure 6-14: Load-slip response of Ω S-U-90-10-2 specimens.	189
Figure 6-15: Failure cracks growth throughout testing of Ω S-U-90-10-2 specimen (first specimen).	190
Figure 6-16: Influence of tension key diameter on load bearing capacity of composite connection with $V_f = 2\%$ and different tension key size.....	191

Figure 6-17: Overall failure of Ω S-U-70-8-2 specimen (Ω -shaped tension key, hh = 70 mm, UHPFRC with Vf = 2%, tpl = 8 mm).....	192
Figure 6-18: Load-slip response of Ω S-U-70-8-2 specimens.....	193
Figure 6-19: Failure cracks growth throughout testing of Ω S-U-70-8-2 specimen (First specimen).....	193
Figure 6-20: Load-steel strain response at mid-span for specimens of Ω S-U-70-8-2 specimen (first specimen).....	194
Figure 6-21: Overall failure of Ω S-U-70-12-2 specimen (Ω -shaped tension key, hh = 70 mm, UHPFRC with Vf = 2%, tpl = 12 mm).....	195
Figure 6-22: Load-slip response of Ω S-U-70-12-2 specimens.....	195
Figure 6-23: Failure cracks growth throughout testing of Ω S-U-70-12-2 specimen (first specimen).....	196
Figure 6-24: Overall failure of Ω S-U-70-16-2 specimens (Ω -shaped tension key, hh = 70 mm, UHPFRC with Vf = 2%, tpl = 16 mm), a) First Specimen, b) Second Specimen.....	197
Figure 6-25: Load-slip response of Ω S-U-70-16-2 specimens.....	197
Figure 6-26: Failure cracks growth throughout testing of Ω S-U-70-16-2 specimen (first specimen).....	198
Figure 6-27: Overall failure of Ω S-U-70-20-2 specimen (Ω -shaped tension key, hh = 70 mm, UHPFRC with Vf = 2%, tpl = 20 mm), a) First specimen, b) Second specimen.....	199
Figure 6-28: Load-slip response of Ω S-U-70-20-2 specimens.....	199
Figure 6-29: Failure cracks growth throughout testing of Ω S-U-70-20-2 specimen (First specimen).....	199
Figure 6-30: Influence of plate thickness on load bearing capacity of composite connection with Vf = 2%.....	200
Figure 6-31: Crack pattern after failure for composite connection with UHPFRC: a) Ω S-U-70-16-2 specimen with embedded length of 100 mm, b) Ω S-U-70-16-2 specimen with embedded length of 150 mm.....	201
Figure 6-32: Overall failure of Ω S-U-70-16-2 specimen (Ω -shaped tension key, hh = 70 mm, UHPFRC with Vf = 2%, tpl = 16 mm, embedded length of 150 mm).....	203
Figure 6-33: Load-slip response of Ω S-U-70-16-2 specimens.....	203
Figure 6-34: Failure cracks growth throughout testing of Ω S-U-70-16-2 Specimen.....	204
Figure 6-35: Influence of plate embedment length on load bearing capacity of composite connection with Vf = 2% and circular tension key.....	205
Figure 6-36: Overall failure of Ω S-U-70-10-0 specimen (Ω -shaped tension key, hh = 70 mm, UHPFRC with Vf = 0%, tpl = 10 mm).....	207
Figure 6-37: Load-slip response of Ω S-U-70-10-0 specimens.....	207

Figure 6-38: Failure cracks growth throughout testing of Ω S-U-70-10-0 specimen (first specimen).	208
Figure 6-39: Overall failure of Ω S-U-70-10-4 specimen (Ω -shaped tension key, hh = 70 mm, UHPFRC with $V_f = 4\%$, tpl = 10 mm).	210
Figure 6-40: Load-slip response of Ω S-U-70-10-4 specimens.	210
Figure 6-41: Failure cracks growth throughout testing of Ω S-U-70-10-4 specimen (first specimen).	211
Figure 6-42: Influence of the fiber volume fraction ($V_f = 0\%$, 2% , and 4%) on the PPL of Ω S-U-70-10 specimens.	212
Figure 6-43: Overall failure of Ω S-F-70-10-1 specimen (Ω -shaped tension key, hh = 70 mm, FRC with $V_f = 1\%$, tpl = 10 mm).	214
Figure 6-44: Load-slip response of Ω S-F-70-10-1 specimens.	214
Figure 6-45: Failure cracks growth throughout testing of Ω S-F-70-10-1 specimen (first specimen).	215
Figure 6-46: Overall failure of Ω S-F-70-16-1 specimen (Ω -shaped tension key, hh = 70 mm, FRC with $V_f = 1\%$, tpl = 16 mm).	216
Figure 6-47: Load-slip response of Ω S-F-70-16-1 specimens.	217
Figure 6-48: Failure cracks growth throughout testing of Ω S-F-70-16-1 specimen (first specimen).	217
Figure 6-49: Influence of concrete generation on load bearing capacity of composite connection with Ω -Shaped tension key.	218
Figure 6-50: Overall failure of PS-U-70-10-2 specimen (Puzzle strip tension key, hh = 70 mm, UHPFRC with $V_f = 2\%$, tpl = 10 mm), a) First specimen at the PPL level, b) First specimen at the end of test, c) Second Specimen.	220
Figure 6-51: Load-slip response of PS-U-70-10-2 specimens.	221
Figure 6-52: Failure cracks growth throughout testing of PS-U-70-10-2 specimen (first specimen).	221
Figure 6-53: Overall failure of PS-U-70-16-2 specimen (Puzzle strip tension key, hh = 70 mm, UHPFRC with $V_f = 2\%$, tpl = 16 mm).	222
Figure 6-54: Load-slip response of PS-U-70-16-2 specimens.	223
Figure 6-55: Failure cracks growth throughout testing of PS-U-70-16-2 specimen (first specimen).	223
Figure 6-56: Influence of plate thickness on load bearing capacity of composite connection with puzzle-strip tension key.	224
Figure 6-57: Overall failure of PS-F-70-10-1 specimen (Puzzle strip tension key, hh = 70 mm, FRC with $V_f = 1\%$, tpl = 10 mm).	225
Figure 6-58: Load-slip response of PS-F-70-10-1 specimens.	226
Figure 6-59: Failure cracks growth throughout testing of PS-F-70-10-1 specimen (first specimen).	226

Figure 6-60: Influence of concrete generation on load bearing capacity of composite connection with $V_f = 2\%$ and puzzle-strip tension key.	227
Figure 6-61: Overall failure of OS-U-50-10-2 specimen (O-shaped tension key, $h_h = 50$ mm, UHPFRC with $V_f = 2\%$, $t_{pl} = 10$ mm).....	229
Figure 6-62: Load-slip response of OS-U-50-10-2 specimen.	229
Figure 6-63: Failure cracks growth throughout testing of OS-U-50-10-2 specimen (first specimen).	230
Figure 6-64: Overall failure of OS-U-70-10-2 specimen (Circular tension key, $h_h = 70$ mm, UHPFRC with $V_f = 2\%$, $t_{pl} = 10$ mm), a) First specimen, b) Second specimen.	231
Figure 6-65: Load-slip response of OS-U-70-10-2 specimens.	231
Figure 6-66: Failure cracks growth throughout testing of OS-U-70-10-2 specimen (first specimen).	232
Figure 6-67: Influence of tension key size on load bearing capacity of composite connection with $V_f = 2\%$ and circular tension key.	233
Figure 6-68: Overall failure of OS-U-70-10-2 specimen (Circular tension key, $h_h = 70$ mm, UHPFRC with $V_f = 2\%$, $t_{pl} = 10$ mm, No Double Headed Stud).	234
Figure 6-69: Load-slip response of OS-U-70-10-2 Specimen with no double headed stud (DHS).....	235
Figure 6-70: Failure cracks growth throughout testing of OS-U-70-10-2 specimen (first specimen).	235
Figure 6-71: Influence of concrete generation on load bearing capacity of composite connection with $V_f=2\%$ and circular tension key.	236
Figure 6-72: Overall failure of OS-U-70-16-2 specimen (Circular tension key, $h_h = 70$ mm, UHPFRC with $V_f = 2\%$, $t_{pl} = 16$ mm).	237
Figure 6-73: Load-slip response of OS-U-70-16-2 specimens.	238
Figure 6-74: Failure cracks growth throughout testing of OS-U-70-16-2 specimen (first specimen).	238
Figure 6-75: Influence of embedded plate thickness on load bearing capacity of composite connection with $V_f = 2\%$ and circular tension key.	239
Figure 6-76: Overall failure of OS-F-70-10-1 specimen (circular tension key, $d_h = 70$ mm, FRC with $V_f = 1\%$, $t_{pl} = 10$ mm).....	240
Figure 6-77: Load-slip response of OS-F-70-10-1 specimens.....	241
Figure 6-78: Failure cracks growth throughout testing of OS-F-70-10-1specimen (first specimen).	241
Figure 6-79: Overall failure of OS-F-70-16-1 specimen (Ω -shaped tension key, $d_h = 70$ mm, FRC, with $V_f = 1\%$, $t_{pl} = 16$ mm).....	242
Figure 6-80: Load-slip response of OS-F-70-16-1 specimen.....	243
Figure 6-81: Failure cracks growth throughout testing of OS-F-70-16-1 specimen (first specimen).	243

Figure 6-82: Influence of concrete generation on load bearing capacity of composite connection with $V_f = 2\%$ and circular tension key.	244
Figure 7-1: Geometry of the composite connection system, a) embedded steel plate in concrete beam, b) Components of connection.	246
Figure 7-2: Geometry of a quarter of the composite connection.	247
Figure 7-3: Planes of symmetry and loading in pullout test.	247
Figure 7-4: Influence of time increment on the load-slip behaviour of composite connection.	250
Figure 7-5: Stress-strain relationship for steel material.	252
Figure 7-6: Stress-strain relationship of concrete in uniaxial compression.	254
Figure 7-7: Stress-strain relationship of concrete in uniaxial tension.	254
Figure 7-8: Concrete failure in plane stress (DS Simulia 2010).	257
Figure 7-9: Material behaviour of UHPFRC material in compression and tension.	259
Figure 7-10: Material behaviour of FRC material, a) compressive behaviour, b) tensile behaviour.	259
Figure 7-11: Variation of peak pull-out load against the dilation angle of the UHPFRC material (Ψ factor).	261
Figure 7-12: Smooth step amplitude definition in ABAQUS.	262
Figure 7-13: Geometry of 8-node element.	263
Figure 7-14: Meshing pattern for the FEM composite connection model.	264
Figure 7-15: Influence of friction factor on the PPL of composite connections with Ω -shaped tension key and UHPFRC material ($V_f = 2\%$).	266
Figure 7-16: Rigid support block.	267
Figure 7-17: comparison of FEM and experimental test result for the composite connection made of UHPFRC material and Ω -shaped tension key.	268
Figure 7-18: Break-out failure mode in the connection system constructed with Ω -shaped plate and UHPFRC material ($V_f = 2\%$).	269
Figure 7-19: Stress distribution in the embedded steel plate and concrete pin.	270
Figure 7-20: Influence of CDP and CSC on the PPL of Ω S-U-70-10-2 composite connection (Ω -shaped tension key, $h_h = 70$ mm, UHPFRC with $V_f = 2\%$, $t_{pl} = 10$ mm).	272
Figure 7-21: Influence of Ω -shaped tension key diameter on the PPL of composite connection with $V_f = 2\%$	273
Figure 7-22: Variation of peak pull-out load (PPL) against the embedded plate thickness for composite connection with $V_f = 2\%$	274
Figure 7-23: Influence of plate embedment length on the PPL of composite connection with $V_f = 2\%$	274
Figure 7-24: Influence of plate thickness on load bearing capacity of composite connection with $V_f = 2\%$	275

Figure 7-25: Influence of fiber volume-fraction on the PPL of composite connection with embedded length of 100 mm, plate thickness of 10 mm.	276
Figure 7-26: Influence of concrete generation on the PPL of composite connection with Ω -shaped tension key, plate thickness = 10 mm.	277
Figure 7-27: Influence of concrete generation on the PPL of composite connection with Ω -Shaped tension key and plate thickness of 16 mm.	277
Figure 7-28: Influence of DHS on the PPL of composite connection with O-shaped tension key.....	278
Figure 7-29: Normal and shear stresses on inclined sides of the Ω -shaped holes..	279
Figure 7-30: Geometry and configuration of Ω -shaped tension key.	280
Figure 7-31: Influence of different Ω -Shaped tension key configuration on the PPL of composite connection with embedment length of 150 mm.	280
Figure 7-32: Influence of plate thickness on the PPL of composite connection with O-Shaped tension key and UHPFRC material with $V_f = 2\%$	281
Figure 7-33: Influence of plate thickness on the PPL of composite connections with embedded length of 150 mm and UHPFRC material incorporating $V_f = 2\%$	282
Figure 7-34: Influence of plate embedment length on the PPL of the composite connections with Ω -shaped hole and UHPFRC material incorporating $V_f = 2\%$	283
Figure 7-35: Influence of O-shaped tension key size on the PPL of composite connection with UHPFRC material incorporating $V_f = 2\%$	284
Figure 7-36: Influence of UHPFRC peak equivalent tensile strength on the PPL of composite connections with embedded length of 150 mm, plate thickness of 16 mm, and UHPFRC material incorporating $V_f = 2\%$	285
Figure 7-37: Influence of DHS on the PPL of composite connection with O-Shaped tension key.....	286
Figure 7-38: Influence of DHS on the PPL of the composite connection with puzzle-strip tension key.....	286
Figure 7-39: Influence of concrete generation on load bearing capacity of composite connection with Ω -shaped tension key.....	287
Figure 7-40: Overall geometry of connection with multiple tension keys.....	288
Figure 7-41: Geometry of a quarter of the composite connection with multiple tension key.....	289
Figure 7-42: Overall configuration of the embedded steel plate, concrete pin, and double headed stud (DHS).	289
Figure 7-43: Influence of multiple tension keys on the PPL of connection system with of Ω -shaped tension key.	290
Figure 7-44: Geometry of the FEM model with embedded steel plate oriented perpendicular to the beam axis.	291
Figure 7-45: Influence of the plate direction on the PPL.	291

Figure 7-46: Geometry of the push-out test from Hegger et al. (2009).	292
Figure 7-47: Variation of push-out test against the slip between the steel plate and concrete beam, a) Experimental results (Hegger et al. 2009), b) FEM results..	293
Figure 7-48: Variation of peak push-out load against the concrete cover thicknesses.	293
Figure 7-49: Typical layout of the FEM push-out model.....	294
Figure 7-50: Influence of DHS and concrete generation on the peak push-out load of composite connection with Ω -shaped tension key.....	294
Figure 7-51: Influence of concrete cover depth on the peak push-out load of the composite connections with UHPFRC and FRC material.	295
Figure 7-52: Influence of fiber volume-fraction on the PPOL of composite connection with embedded length of 100 mm.....	296

List of Abbreviations

The following abbreviations are used in this document.

Symbols Definitions

ASTM	American Society for Testing Material
ACI	American Concrete Institute
BF	break-out failure
CCM	concrete constitutive model
CDP	concrete damaged plasticity
CETS	cracking equivalent tensile strength
CPL	cracking pull-out load (kN)
CMC	cracking model for concrete
CMOD	crack mouth opening displacement (mm)
COV	coefficient of variation
CSC	concrete smeared cracking
CSF	concrete side-failure
CU-50	50 mm cube specimens
CU-100	100 mm cube specimens
CY-50	50 mm cylinder specimens
CY-75	75 mm cylinder specimens
CY-100	100 mm cylinder specimens
DIC	digital image correlation
DTT	direct tensile testing
DTS	direct tensile strength
ECZ	elastic compression zone
ETS	equivalent tensile strength
ETZ	elastic tensile zone
FEA	finite element analysis
FEM	finite element method
FCS	flexural first cracking strength
FRC	fiber reinforced concrete
FTF	flexural toughness factor
FTT	flexural tensile testing
HE	high early strength cement
HPC	high performance concrete

HRWRA	higher range water reducer admixture
HSC	high strength concrete
JSCE	Japan Society of Civil Engineering
LES	linear elastic stage in pull-out test
LEZ	linear elastic zone in prism under flexural load
LOP	limit of proportionality
LVDT	linear variable displacement transducer
MPL	maximum post-cracking load
MST	mass scaling technique
NSC	normal strength concrete
PCS	Post cracking stage in pull-out test
PETS	peak equivalent tensile strength
PLES	flexural peak load equivalent strength
PF	Pull-out failure
PF-50	50 x 50 x 150 mm prism specimens for flexural test
PF-100	100 x 100 x 300 mm prism specimens for flexural test
PF-150	150 x 150 x 450 mm prism specimens for flexural test
PF-200	200 x 200 x 600 mm prism specimens for flexural test
POT	pull-out test
PPL	peak pull-out load (kN)
PPT	peak pull-out test
PS-50	50 x 50 x 150 mm prism specimens for shear test
PS-100	50 x 50 x 150 mm prism specimens for shear test
RBM	rigid body motion
SF	silica fume; splitting failure
SFRC	steel fiber reinforced concrete
SP	superplasticizers
SLS	serviceability limit state
SPF	steel pull-out failure
SSF	shear slip factor
STF	shear toughness factor
STT	split tensile testing
SYF	steel yielding failure
TFZ	tension free zone
THZ	tension hardening zone
TSZ	tension softening zone

TI	time increment (ABAQUS/Explicit)
UHPC	ultra-high performance concrete
UHPFRC	ultra-high performance fiber-reinforced concrete
3-D	three dimensional

Nomenclature

The following symbols are used in this document.

Symbols	Definition
A_{eff}	effective area in shear (mm ²)
A_m	Area under shear load-deflection curve (N.mm)
A_{sc}	cross-sectional area of stud (mm ²)
A_{sp}	net tensile cross-sectional area of embedded steel plate (mm ²)
b	overall width of prism specimens (mm)
b_{eff}	effective width of prism specimens in direct shear test (mm)
c	compressive zone depth (mm)
C_r	compressive strength of uncracked FRC material (MPa)
d_f	fiber diameter (mm)
d_{notch}	depth from top of notch to extreme compression fiber (mm)
E_c	elastic modulus of concrete (MPa)
$(FTF)_h$	flexural toughness factor (MPa)
f'_c	cylinder compressive strength at the age of 28 days (MPa)
f'_{cu}	compressive strength of 50 mm cube at the age of 28 days (MPa)
$f'_{c,t}$	compressive strength (MPa) at time t (days)
$f'_{cu,60}$	compressive strength (MPa) at the age 60 days
f_f	flexural strength (MPa)
f_t	flexural-tensile strength (MPa)
f_v	shear strength (MPa)
F_u	ultimate tensile strength of stud (MPa)
$F_{y,st}$	static yield strength of steel (MPa)
$F_{y,dy}$	dynamic yield strength of steel (MPa)
F_y	yield strength of steel (MPa)
h_n	effective prism height after accounting for notch (mm)
h	overall height of prism specimens (mm)
h_h	height or diameter of hole cut though the embedded steel plate (mm)
h_1	reduced prism height in shear test (mm)
h_{eff}	effective prism height (mm)
h_{ep}	Length of embedded steel plate (mm)
l_f	fiber length (mm)
k_v	shear factor

k_f	flexural tensile strength factor
L	span of prism in flexure, center to center of supports (mm)
L_{cz}	perturbed length of beam around the flexural main crack (mm)
m	arbitrary number
M_{int}	internal flexural moment (N.mm)
M_{ext}	flexural moments caused by applied loading (N.mm)
M_{uc}	internal flexural moments in un-cracked zone (N.mm)
M_{cr}	internal flexural moments in cracked zone (N.mm)
N_{ext}	external axial load (kN)
N_{uc}	external axial load in the un-cracked zone of flexural prism (kN)
N_{ext}	external axial load in the cracked zone of flexural prism (kN)
N_y	yielding pull-out load in the composite connection system (kN)
P	flexural load (kN)
P_{MPL}	flexural peak load (kN)
P_{LOP}	flexural cracking load (kN)
Q_n	nominal strength of one stud shear connector (kN)
SF/B	silica fume to binder ratio
STF	shear toughness factor (MPa)
t_w	web thickness (mm)
t	time
t_p	thickness of embedded steel plate (mm)
T_r	tensile strength of cracked FRC material (MPa)
V_{cr}	first-cracking shear load (kN)
V_f	fiber volume fraction
V_{peak}	peak shear load (kN)
w	crack width (mm)
$\Psi_{L/m}^h$	flexural toughness (area under the curve) up to deflection L/m (N.mm)
α	flexural crack height to specimen height ratio
α_{fl}	factor representing the concrete brittleness
α_1	parameter to define equivalent concrete stress block at ultimate condition
β_1	parameter to define equivalent concrete stress block at the ultimate condition
Γ	shear toughness (area under the curve) up to deflection of h_n/m (N.mm)
$\Delta_{cr,e}$	slip between embedded steel plate and concrete beam corresponding to equivalent cracking load (mm)
Δ_{peak}	slip between embedded steel plate and concrete beam corresponding to peak pull-out load (mm)

Δ_{peak}	slip between embedded steel plate and concrete beam corresponding to pull-out load at the failure (mm)
δ	flexural deflection (mm)
δ_{cr}	shear slip (mm)
δ_{sl}, δ_{sr}	Support vertical deflection under flexural load (mm)
δ_{ms}	mid-span vertical deflection under flexural load (mm)
ε_{shear}	shear strain
ξ_{SF}	scale factor
ξ_f	fiber factor
ν	Poisson's ratio
ϑ	ratio of flexural crack width to mid-span deflection
μ	shape factor
χ_{el}	curvature in elastic zone
χ_{cz}	curvature in cracked zone
$\sigma_w(w)$	tensile stress of UHPFRC material after cracking (MPa)
σ_{true}	true tensile strength of steel plate (MPa)
σ_{nom}	nominal (engineering) tensile strength of steel plate (MPa)
ε_{nom}	nominal (engineering) tensile strain of steel plate
γ	shear strain
φ	angular opening of the main flexural cracks
Λ	connection ductility factor

Chapter 1

1 Introduction

1.1 Motivation

The traditional composite girder systems constructed with concrete flanges and steel webs have been built for several decades and extensive research program have been completed around the world to develop a detailed understanding of the load transfer mechanism in different components of such girders (Viest 1956, Sayed-Ahmed 2001, Metwally and Loov 2003). Most of these girders are exposed to aggressive environmental conditions, which accelerate the material degradation and increase concerns about the structural adequacy. As an alternative to the earlier girder configurations with conventional material, a hybrid composite member using UHPFRC flanges and embedded steel webs was proposed in this study.

The proposed girders features: 1) higher strength-to-weight ratio, which minimizes the substructures costs and is beneficial in several applications including the short to medium span bridge superstructure construction, and the long-span roof system for the industrial buildings (Simon et al. 2002, Hegger et al. 2006, Abramski et al. 2010), 2) lower self-weight (smaller and lighter members), which facilitates the pre-fabrication process and transportation in modular form to remote areas, expedite the construction process, and minimize the traffic flow disruptions in highly congested areas (Siokola 1999, Hegger 2000, Hartmann 2005, Resplendino, and Bouteille 2006, Graybeal 2007). According to Tanaka et al. (2006), the use of UHPFRC material resulted in a 40% reduction in the total dead load of a girder system compared to that with conventional concrete material. 3) more slender and attractive structural members with shallower construction depths, which offers a higher headroom clearance (Rauscher 2011).

The UHPFRC material features an extremely low permeability (exchange of substances between concrete material and environment) resulting from the dense

matrix that can ultimately contribute to structures with longer life spans and reduced maintenance cost (Charron et al. 2004, Schmidt and Fehling 2003, McDonald 2005, and Grabeal 2006). However the use of this material increases the volumetric cost of the material as compared to conventional concrete material. To cope with the higher cost of the HPC material, innovative design in detailing of composite members should be implemented to allow the best use of material where it is required.

The connection between the embedded steel web and the concrete flange in the proposed girder is expected to be heavily stressed under the applied load. Thus a proper connection system is essential to prevent potential premature failure that adversely affects the overall performance of the girder superstructures. As such, the main objective of this research program was to evaluate the structural response of a novel composite connection system that features an enhanced load carrying capacity and ductility, improved long-term response, and accelerated construction process as compared to earlier configurations with conventional material.

While some past experimental studies separately investigated the mechanical properties of ultra-high performance fiber-reinforced concrete (UHPFRC) in the material scale (De Larrard 1994, Richard and Cheyrezy 1995, Rossi et al. 2005, Habel et al. 2006) and the response of composite connections (Hegger et al. 2009 and Abramski 2010), minimal studies have been completed on the response of the composite connections constructed with UHPFRC material under the pull-out or push-out loading.

1.2 High Performance Material

UHPFRC is a new class of advanced cementitious material that has been developed in recent decades. The UHPFRC mix composition is formulated of constituent materials, which substantially differ from the normal fiber reinforced concrete (FRC) material and is distinguished mainly with a high volume fraction of cement, silica fume and fiber volume content (De Larrard 1994, Richard and Cheyrezy 1995, Rossi et al. 2005, Habel et al. 2006). No coarse aggregates are used for this type of concrete, which prevents the formation of early-age microcracking (Rossi 2005). A high rheological property with very low water-to-cementitious ratio ($w/c < 0.2$) can

be obtained for the UHPFRC material through the use of a high range water reducer. When compared with other types of concrete, UHPFRC material exhibits exceptional mechanical properties including a compressive strength of 150-250 MPa, tensile strength of 8-17 MPa, significant strain hardening capacity, and remarkable fracture energy of 20–30 kJ/m² (Richard and Cheyrezy 1997, Rossi et al. 2005). These significant improvements in the mechanical properties were achieved by 1) careful particle-size gradation of the fine aggregates and cementitious material used in the matrix and 2) the use of randomly distributed short steel fibers, which bridge across the microcracks, thus retarding the crack propagation and enhance the UHPFRC load carrying capacity (Richard and Cheyrezy 1994 and 1995, Rossi 2005).

In addition, the use of UHPFRC material in the proposed composite girder will result in a durable girder system, which promotes reduced life-cycle cost, longer life spans, and enhanced environmental sustainability (Racky 2004, Tavakoli and Bouteille 2013) through: 1) a significant enhancement in the permeability of UHPFRC material by using a dense homogeneous matrix with discontinuous pore structure, which notably protect against the freeze and thaw cycle and the ingress of detrimental substances. These phenomena would lead to corrosion of rebars and results in delamination, deterioration and spalling of concrete (Roux et al. 1996, Bonneau et al. 2000, Vernet 2003, Charron et al. 2004, Schmidt and Fehling 2005, Bierwagen 2005, McDonald 2005, and Grabeal and tanesi 2007, Spasojevic 2008,)) and 2) controlling the crack width at serviceability (w) to prevent the formation of macrocracks, i.e., crack width at peak tensile strength (w_{PTS}) along the members (Aldea et al. 1995, Rosi 2005).

1.3 Composite Connection

In a composite girder system, the flanges are designed to transfer the normal forces from bending while the steel web withstands shearing stresses generally demanded of a girder. The transfer mechanism of forces at the interface between concrete and steel is conventionally realized by several types of shear connectors including headed studs (An and Cederwall 1996, Bursi and Gramola 1999, Hegger 2001, Qian and Li 2006). The headed stud shear connector is generally used for modular construction, but needs a significant welding, which introduces concerns with

respect to fatigue and cost (Oehlers and Foley 1985, Schmitt et. al. 2005, Feldmann et al. 2008, Hegger et. al. 2006). In addition, no promising response for headed studs in composite connection systems with high-performance concrete material is reported, as the headed stud system has a limited load carrying capacity and ductility (Hegger et al. 2001, Hegger and Rauscher 2006). Thus, to offset these concerns, several past researchers demonstrated the feasibility of direct embedment of the steel web into the concrete flanges constructed with the conventional concrete material (Moo et al. 2003, and Metwally and Loov 2003). This connection system had been previously used in several bridge constructions in Asia and Europe including a three-span bridge with a maximum span of 97 m in Japan (Kurita and Ohyama 2002). However all these past research focused on the conventional concrete material with compressive strength below 70 MPa and brittle response in tension. Most of these connection systems were found to poorly represent the system strength, which is mainly associated to the brittle nature of the conventional concrete (Nie et al. 2004). In contrast, the composite connections with UHPFRC material incorporating moderate volume fraction of steel fibers were reported to gradually damage by ductile yielding of the UHPFRC materials. This phenomenon resulted in a higher load-carrying capacity, stiffness, and large displacement ductility capacity and ensures the shift of failure mode from brittle concrete fracture to ductile yielding of UHPFRC materials in composite sections (Hegger et al. 2008).

While the majority of the research into these composite connections have been completed on shear response of those with the conventional concrete material (Hegger et al. 2009 and Abramski 2010), minimal attention has been given to connection system that take advantages of the high performance material. Therefore, a research program was proposed herein to develop a good understanding of the pull-out and push-out behaviour of composite connections constructed with direct embedment of steel plates in ultra-high performance fiber-reinforced concrete (UHPFRC) and fiber-reinforced concrete (FRC) material.

1.4 Research Significance

A detailed understanding of the mechanical properties of the UHPFRC material is required to efficiently use its available capacity and satisfy the performance requirements of the structural members. While numerous studies have investigated the compressive and flexural-tensile strength of this type of concrete, the role of the fiber volume-fraction and specimen size on these properties has not been widely considered. Further, there is no available research, which addresses the behaviour of UHPFRC material under direct shearing action. This study has been completed to provide insight into the lack of knowledge for the compressive response of the UHPFRC material using cylinder and cube specimens over a size range of 3 and 2. Flexural tests of un-notched prisms as well as the shear tests of notched prisms were also completed over a size range of 4 and 2. An inverse-analysis technique was used to derive the equivalent tensile mechanical properties relative to the crack mouth opening displacement (CMOD) using the flexural load-deflection responses.

The use of UHPFRC material in the composite connections constructed with direct embedment of steel plate in concrete beams can lead to potential savings in the lifecycle costs of composite sections. In addition, the use of this material was predicted to produce a structural composite connection with significantly higher load carrying capacity along with enhanced ductility compared to those constructed with conventional normal strength concrete flange and stud connection. The influence on the behaviour of the composite connections from several parameters was investigated through an experimental and numerical program, which are discussed in future chapters.

1.5 Project Objectives and Scope

This project included two main phases: 1) Investigate the influences of the specimen size and fiber content on the mechanical properties of the ultra-high performance fiber reinforced concrete (UHPFRC) at the material scale and 2) Experimental and numerical investigation of the pull-out behaviour of the composite connections constructed with embedded steel plate in FRC and UHPFRC beam.

In the first part of the research, a unique UHPFRC material suitable for in-situ casting and incorporating 0 to 5% volume-fraction of short steel fibers was developed using a locally available materials. The compressive response of UHPFRC material using cylinder and cube specimens over a size range of 2 and 3 was established. Flexural tests of un-notched prisms under 4-point bending were completed over a size range of 4. A back-analysis technique, originally proposed by AFGEC (2002) was used to derive the equivalent tensile mechanical properties relative to the crack mouth opening displacement. In addition, the direct shear tests were performed on prism specimens over a size range of 2 to establish the influence of specimen size on the mechanical properties of UHPFRC material in shear. The measured test results from flexural and shear tests were further analyzed to evaluate the influence of fiber content and specimen size on the flexural and shear toughness. In all cases, three companion vibrated 50 mm cube specimens (CU-50) tested in compression at either 28 days or the same days of test were cast from each mix. The average strength of these cubes served as a reference strength parameter to allow correlation between the other response parameters evaluated. In addition to the mechanical properties outlined above, the influence of UHPFRC mix composition and energy imparted by the mixer on its rheological properties was also studied.

In the second part of the study, the pull-out response of 42 composite connections constructed with embedded steel plate in concrete beam was studied. Two different generations of concrete, i.e., UHPFRC material with $V_f = 0\%$, 2% , and 4% and fiber reinforced concrete (FRC) material with $V_f = 1\%$, was used for the beam. In order to minimize the need for experimental testing, preliminary finite element models was adopted to rationally select the parameters affecting the performance of composite connection response subjected to pull-out loading. Based on the FEM analysis results, a series of specimens were cast and tested at the University of Alberta. This unique investigation allowed the verification of the connection components including the geometry and size of hole cut through the embedded plate, embedded plate thickness, embedded length of steel plate, concrete type, and fiber volume fraction on the pull-out response of composite connection. In addition the influence from the connections' components on the pull-out load-slip response, failure mode, and crack growth pattern and width in concrete beam for each group of pull-out

specimens are investigated. Numerical simulation models have been developed and validated against the experimental results. After validation of the FEM models, a series of parametric analysis were completed on the response of the composite connections subjected to pull-out and push-out loading.

1.6 Organization of the Thesis

This document is organized into eight chapters and this section provides an overview of the thesis content. Chapter 1 consists of the introduction to the project and objective and scope of the experiment.

An overview of background information relevant to the mechanical properties of two different generation of concrete, i.e., UHPFRC and FRC material, in compression, flexure, flexural-tensile, and direct shear is provided in first part of Chapter 2. The second part of chapter 2 presents a review of the past experimental and numerical research on two different connection systems: 1) traditional shear studs attached to a small steel flange, which is welded to the steel web, and 2) direct embedment of the steel web (with holes cut through it) into concrete flange. The influence of different parameters on the force carrying capacity, interface slip, crack localization, and overall connection deformation is also discussed in Chapter 2.

Chapter 3 reports on the mix design development and the experimental methods to characterize the mechanical properties of UHPFRC material. The relevant standardized test protocols for compression (ASTM C39), flexure (ASTM C1609 and JSCE-G552) and direct shear (JSCE-G 553) are explained. The results of the mechanical properties of the UHPFRC and FRC materials in compression, flexure, flexural-tensile, and direct shear are analyzed and discussed in Chapter 4.

Details of specimen configurations, fabrication, curing, instrumentations and test procedure for the composite connections are provided in Chapter 5. The testing procedure for small scale specimens (coupon test) are also described in detail. Chapter 6 includes the results and discussion of pull-out test, which includes the visual observations, Digital Image Correlation (DIC) measurement results, plots of pull-out load against slip between embedded steel plate and concrete beam, strain gauge results, crack initiation and propagation in concrete beam, and the ductility of

the connection specimen. The influence on the load slip response of the composite connection from the embedded plate thickness, embedment length, holes size and shape (Ω -shaped, puzzle-strip, and circular shaped holes) were also investigated.

Chapter 7 outlines the details of finite element models and analyses developed for composite connections under pull-out and push-out loading. The chapter is started with a brief introduction and review of the concept of the finite element method, followed by a detailed discussion of the specific features implemented in the proposed composite connections. The results of FEM analyses are compared against the experimental measurements. After validation of the finite element model with the experimental results, a parametric study is conducted to investigate the influence of connection's components on the pull-out and push-out loading.

Chapter 8 summarizes the conclusions drawn from the current experimental and numerical studies. Based on the findings in this research program, a series of recommendations for future work are given.

Chapter 2

2 Review of the Literature

2.1 Introduction

This chapter of the thesis presents a summary of the existing research and literature that are applicable to the current study on: 1) the mechanical properties of two different types of concrete, i.e., ultra-high performance fiber-reinforced concrete (UHPFRC) and fiber reinforced concrete (FRC) in compression, flexure, tension, and shear; 2) the response of composite connections constructed with embedded steel plate in concrete beam under pull-out and push-out loading.

2.2 Mechanical Properties of UHPFRC Material

The use of ultra-high performance fiber reinforced concrete (UHPFRC) has received considerable attention from the research and industrial communities over the past decade. Although no unique and widely accepted definition for UHPFRC material exists, it was classified as a cement-based composite matrix with the 28 days compressive strength exceeding 150 MPa, exhibiting a pseudo-strain hardening response in tension after cracking, and presenting a very low permeability. The UHPFRC's strain hardening response is accompanied by the formation of dense multiple micro-cracks, which is an essential characteristic to achieve high tensile strength and ductility (Richard and Cheyrezy 1997, Racky 2004, Rossi 2005, Tavakoli and Bouteille 2013). Several researchers in the past studied the mechanical properties of UHPFRC in compression, flexure, flexural-tensile, and shear. A summary of each is presented below.

2.2.1 Compressive Response

The use of high strength concrete started during the 1970s with the development of a 230 MPa concrete with a water-to-cement (w/c) ratio of 0.2-0.3 and a very fine cement of Blaine value up to 8000 cm²/g (Odler 1972a, 1972b; Yudenfreund 1972a, 1972b; Brunauer 193a , 1973b). This significant improvement in the compressive strength was achieved through the development in the packing density and decrease in the porosity of the matrix by reducing the amount of entrapped air and the water (Yudenfreund 1972a). Roy et al. (1972) developed a 510 MPa concrete by employing a hot pressing technique: temperature of 150°C and a pressure of 170-340 MPa.

A macro-defect-free (MDF) cements with a compressive strength of 200 MPa were developed in early 1980s after the development of superplasticizers and pozzolanic admixtures such as silica fume (Birchall et al. 1981a and 1981b, 1983). However, the creep properties of the MDF cement was not promising. (Kendall et al. 1983, Alford and Birchall 1985). The densified small particles (DSP) with a very low porosity were developed in 1981 by Bache (1987). Microsilica and high-range water reducer (HRWR) was used in this concrete to reduce the porosity and enhance the particle packing density. A compressive strength between 120-250 MPa was reported for the DSP material.

Minimal, if any, high strength concrete was available commercially until ultra high performance concrete (UHPC) material was first introduced by De Larrard and Sedran (1994). UHPC was in fact a further development of the DSP material (De Larrard and Sedran 1994). This material was characterized by a low water to binder ratio of 0.14 and a high volume of cementitious material compared to the older similar types. The UHPC material was reported to have highly improved material properties including the mechanical strengths, durability, and workability. (De Larrard 1994, Sedran 1994, De Larrard 1994 and 1995, Angot 1994). Despite its promising mechanical properties, the UHPC material was found to be extremely brittle in both compression and tension, in which the peak compressive load was followed by a rapid and uncontrolled decrease in load-carrying capacity.

Reactive Powder Concrete (RPC), with a maximum grain size of 0.6 mm and $V_f = 1.5$ to 3% ($l_f/d_f = 13/0.15 \text{ mm}$) offering a 230 MPa compressive strength, was developed in France to mainly offset the brittleness response of this type of material (Richard and Cheyrezy 1995). The RPC was later commercialized under the trade name DUCTAL, produced by Bouygues-Lafarge-Rhodia in France, with compressive strength of 160 to 240 MPa. Richard and Cheyrezy (1995) developed a 650 MPa concrete with a 10% volume fraction of steel fibers. The curing process completed with a temperature of 400°C and a pressure of 50 MPa. A compressive strength of up to 800 MPa was gained for this product with a steel aggregate (Richard and Cheyrezy 1995).

The UHPFRC material has gained a significant attention during the last decades. Some UHPFRC was developed in past decade in Europe (e.g. Richard 1995, Rossi 1997, Rossi 2002) and in North America (e.g. Graybeal 2006, Habel et al. 2008, Naaman 2010, Wille et al. 2010). The typical response of UHPFRC material in compression is characterized by a linear elastic behaviour up to the first cracking strength of the material, a strain-hardening phase up to the maximum load, and a strain softening phase after the maximum load is reached. The *Association Française de Génie Civil (AFGC) Interim Recommendations for Ultra High Performance Fibre-Reinforced Concretes* indicates that UHPFRC tends to have the following properties: compressive strength that is greater than 150 MPa, short discontinues steel fiber to ensure ductile response, and high binder content with a dense particle packing. Furthermore, UHPFRC tends to have very low water content and can achieve sufficient rheological properties through a combination of optimized granular packing and the addition of high-range water-reducing admixtures (AFGC 2002).

2.2.1.1 Influence of Silica Fume

Silica fume (SF) with spherical particles less than 100-150 μm in diameter, is a highly reactive pozzolan material, which used as a micro-filler in the UHPFRC material to optimize the packing density and improve the microstructure of the matrix (Bache 1987, De Larrard 1994, Morin and Tenoudji 2001 and 2002, Rossi et al. 2005). The use of silica fume with lower carbon content was experimentally proved to result in concrete with higher compressive strength (Wille et al. 2011).

The influence of silica fume content on the compressive strength of the UHPFRC material was studied by different researchers (Cohen et al., 1994, Chung, 2002, Goldman and Bentur, 1994, Yan, Sun, and Chen, 1999). It was reported that a high concentration of SF (more than 20% of the cementitious material) can notably increase the compressive strength of UHPFRC material. This is because the addition of SF to matrix decreases the void spaces in the matrix, as its extremely fine particles tend to pack between the larger particles. In addition, higher concentration of SF in the matrix increases the pozzolanic reaction with calcium hydroxide (CH) and produces more calcium silicate hydrates (CSH) in the fresh mix, which is the main source of the strength gain in concrete.

Anh-Tuan et al. (2012) studied the influence of 0%, 10%, 20%, 30%, and 40% silica fume, as a replacement by cement, on the peak compressive strength of a UHPC for both normal and high temperature curing regimes. According to Figure 2-1, the mix with 20% silica fume presented the highest compressive strength at 7 and 28 days for the both curing regimes. A silica fume to binder ratio of 0.2-0.25 was adopted by other recent researchers (Morin et al. 2001, Morin et al. 2002, Habel et al. 2006, Grabeal 2006, Wille et al. 2011).

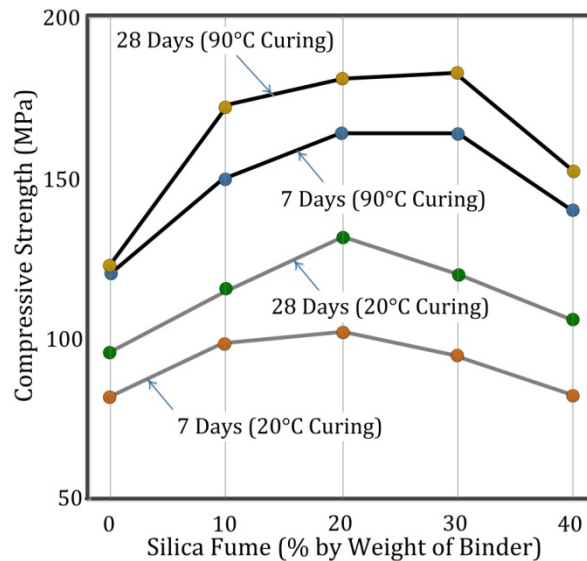


Figure 2-1: Influence of silica fume content on the compressive strength of UHPFRC material (Le et al. 2007 [after]).

2.2.1.2 Influence of Fiber Content

Some limited past researches have attempted to quantify the improvement relative to the fiber volume-fraction in UHPFRC material. Richard and Cheyrezy (1995) incorporated 1.5-3% of short steel fibers with a diameter of 0.15 mm and length of 13 mm in the plain RPC material to improve its brittle behaviour in compression. According to them, the economic optimum fiber volume-fraction was found to be 2%. An average improvements of 26% and 29% in peak compressive strength was found after the addition of $V_f = 2\%$ to plain matrix for two different generations of reactive powder concrete (RPC), i.e., RPC200 and RPC800 respectively. Average compressive strength of 170-230 MPa and 490-680 MPa were reported for RPC200 and RPC800, respectively.

Wille et al. (2011) reported that the addition of randomly distributed short steel fibers with an aspect ratio of 65 ($L_f/D_f = 13/0.2$) to plain matrix at the volume fractions of $V_f = 2.5$ and 6% increased the compressive strength by 5.5 and 13% over the mix without fibers (Wille et al. 2011).

The influence of $V_f = 0\%$, 1%, 2%, 3%, and 6% short steel fiber ($l_f = 13$ mm and d_f of 0.2 mm) on the compressive strength of both 50 mm and 100 mm cubes were studied at both 7 days (7d) and 28 days (28d) (Le et al. 2009). Two different curing regimes were used: Ambient condition (20°C) and high temperature condition (90°C). As shown in Figure 2.2, no significant improvement in compressive strength (at both 7d and 28d) was found for mixes with $V_f = 1\%$ for both curing regimes. However the addition of $V_f = 2\%$, 3%, and 6% to mix with 20°C curing regime was found to increase the 7 days compressive strength by 7.5%, 5%, and 20% respectively. Similar results was found for 28 days compressive strength where 2.4%, 12%, and 31% improvements in compressive strength was found as 2%, 3.5%, and 6% fibers were added to plain mix. According to them, similar trend was observed for mixes with 90°C curing regime where the average compressive strength for each mix was 40% higher than those with ambient curing condition. Lower standard deviation was reported for compressive strength of the mixes at the age of 28 days than those at 7 days. This phenomenon was more pronounced for the mixed with ambient curing.

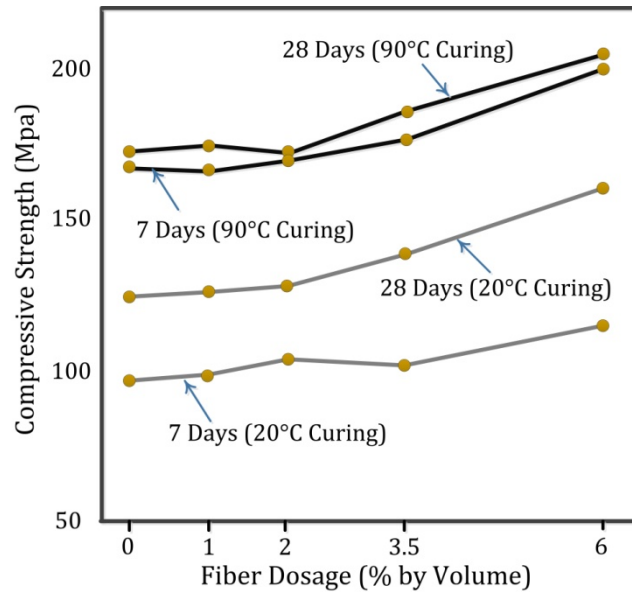
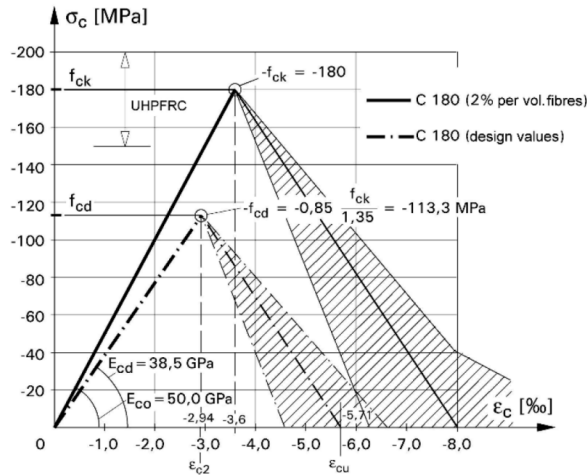


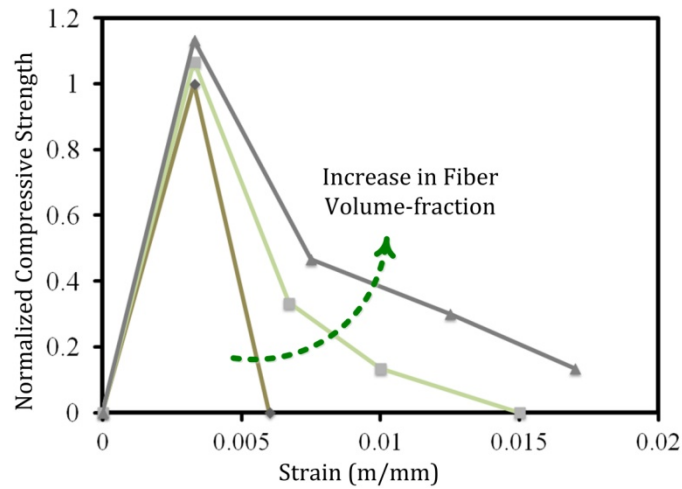
Figure 2-2: Influence of fiber volume-fraction on the compressive strength of UHPFRC material (Le et al. 2007 [after]).

Skazlic and Bjegovic (2009) showed that adding 2, 3, and 5% short steel fiber with $L_f = 13$ mm and $d_f = 0.15$ mm to UHPFRC matrix, with an average compressive strength of 180-220 MPa, resulted in 16% and 22% improvement in the compressive strength over that with no fiber. The influence of the fiber length on the compressive strength was also investigated by the same authors. No significant improvement in the compressive strength of UHPFRC was found as the fiber length was increased (Skazlic and Bjegovic 2009).

According to Figure 2.3, not only the steel fibers contribute to the peak compressive strength of UHPFRC, but it significantly improves its post-peak ductility and energy absorption capacity in compression making it suitable in many applications such as seismic design, blast and high-strain rate loading. This is due to the fiber bridging effect across the cracks in matrix which tends to confine the concrete through the uniformly distributed steel fiber (Olsen and Billington 2011, Wille et al. 2011, Stengel et al. 2012).



a)



b)

Figure 2-3: Compressive stress-strain response of UHPFRC material, a) influence of fiber on compressive strength (Skazlic and Bjegovic 2009), b) schematic of the improvement in softening response with increasing fiber volume-fraction.

2.2.1.3 Influence of Specimen Size

Prior researches have established that the compressive strength of UHPFRC material depends not only on the matrix ingredients and steel fibers but also on the size of the specimens (Ma and Tue 2012, Graybeal et al. 2008, Issa et al. 2000, Skazlic et al. 2008, An et al. 2008, and Wille et al. 2011). Limited past research investigated the relationship between different specimen sizes and the compressive strength of UHPFRC material.

The use of 100 mm diameter cylinders has been previously proposed to evaluate the compressive strength of UHPFRC (AFGC 2002 and JSCE 2008). However, this specimen size imposes requirements for precise end grinding and use of high capacity testing machines, which may not be feasible in all laboratories. As such, many researchers have investigated the possibility of using smaller size specimens.

The results show that the smaller cylinders and cube specimens tend to show a slightly higher compressive strength (Ma and Tue, 2012, Graybeal et al. 2008, Issa et al. 2000, and Skazlic et al. 2008, and An et al. 2008, Wille et al. 2011). Skazlic and Bjegovic (2009) investigated the influence of the specimen size on the mechanical properties of UHPFRC material with an average compressive strength of 150 MPa. A 20% decrease in the compressive strength of UHPFRC mixes was reported as the cube specimen size was increased from 40 mm to 100 mm. This is most likely because the smaller samples have less likelihood of having low strength elements. Higher compressive strength was reported for cube specimen, compared to cylinder specimen with maximum nominal size (Skazlic and Bjegovic 2009).

Graybeal et al. (2009) investigated the influence of the specimen size and shape (i.e., cubes and cylinders) on the compressive strength of DUCTAL material with 2% volume-fraction of short steel fibers. Similar compressive strength was reported for the CY-100, CY-75, and CU-100 specimens. However, the smaller specimen sizes, i.e. CU-50 and CY-50, had higher compressive strengths than those with larger sizes.

While some past research program investigated the influence of specimen size on the compressive strength of UHPFRC material, no clear relationships were established between the peak compressive strength of cylinder and cube samples of different sizes as the fiber volume-fraction changes between 0 to 5%.

2.2.1.4 Time Development

The evolution of the mechanical properties of UHPFRC material in compression with time was studied by several past researchers (Habel and Viviani 2000, Denarie 2000, Bruhwiler 2006, and Grabeal 2007). The initial set time of UHPFRC material is mainly dependent on the components of cementitious material, the chemical properties of the admixture, and the curing conditions. An initial and final set time

of 12-24 hours was reported in the literature (Graybeal 2006). A high rate of strength development, after the completion of initial set, was reported for UHPFRC material particularly during the first week where 60% of the compressive strength at the age of 28 days was reached. After this stage the rate of strength gain decreased until a plateau was reached at the age of 30 days. See Figure 2-4. Graybeal (2006) proposed the following expression to describe the rate of compressive strength development of UHPFRC material over the time.

$$f'_{c,t} = f'_c \left[1 - \exp \left(- \left(\frac{t-0.9}{3} \right)^{0.6} \right) \right] \quad (2-1)$$

It was reported that the peak compressive strength of UHPC material tends to slightly increase after the plateau was reached. However a very low rate was reported for this stage (Graybeal 2006, Habel 2006).

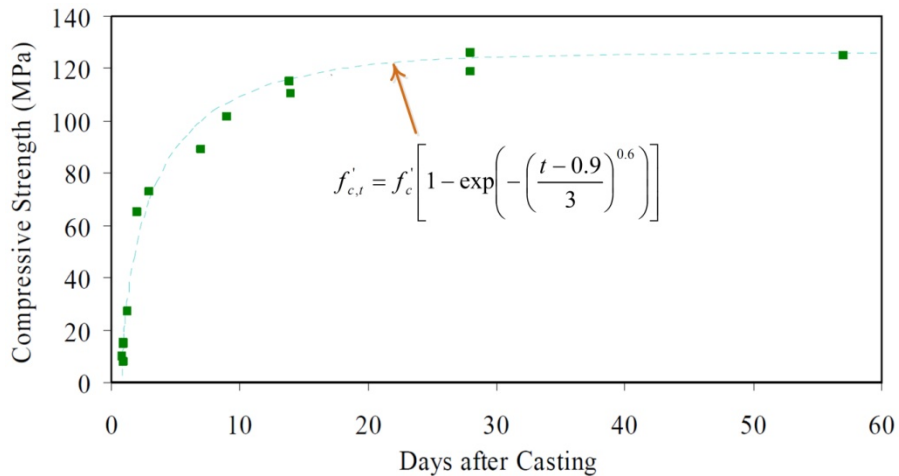


Figure 2-4: Variation of compressive strength of UHPC material against time (Graybeal 2000).

2.2.2 Flexural Response

The flexural load-deflection responses of UHPFRC, FRC, NSC are illustrated in Figure 2-5. Contrary to the conventional FRC material with a softening response after the limit of proportionality (LOP), the typical response of the UHPFRC material subjected to flexure is characterized by a linear elastic behaviour up to the LOP, a strain-hardening phase up to the maximum post-cracking load (MPL), and a strain softening phase after the maximum load is reached (Richard and Cheyrezy 1997,

Habel et al. 2008, and Charron et al. 2008). The performance of the UHPFRC material subjected to flexural load is mainly influenced by the matrix components, steel fibers, and specimen size. Each of these factors is briefly explained below.

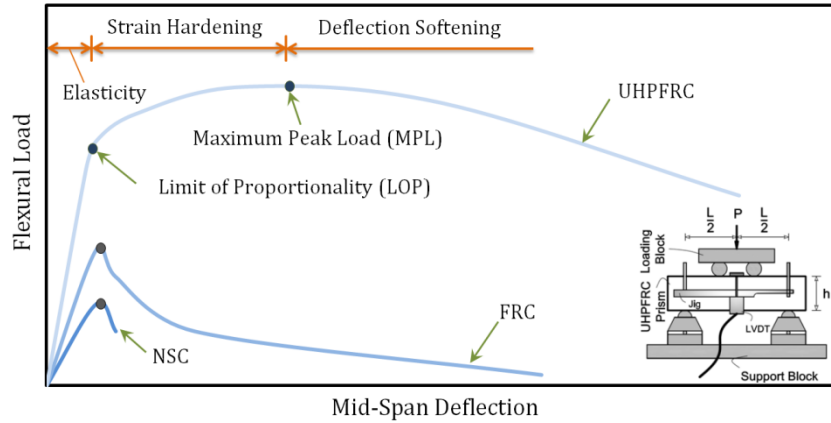


Figure 2-5: Flexural response of NSC, FRC, and UHPFRC material.

2.2.2.1 Flexural Strength

The ASTM C1609 standard test method is the most widely accepted test method for characterizing the flexural response of the small-scale concrete prisms. The schematic of the test setup (beam with third-point loading) is shown in Figure 2-5. The load-deflection response of the prism is captured during the test to determine the flexural first crack strength (FCS) and flexural peak load equivalent strength (PLES) of UHPFRC which correspond to limit of proportionality (P_{LOP}) and maximum post-cracking load (P_{MPL}) respectively. With h representing the the prism specimen height, the FCS and PLES are calculated using Equations (2-2) and (2-3). For UHPFRC with fairly nonlinear behaviour, the PLES has no physical meaning, but it can be used for comparative purpose.

$$FCS = \frac{3P_{LOP}}{h^2} \quad (2-2)$$

$$PLES = \frac{3P_{MPL}}{h^2} \quad (2-3)$$

Schmidt and Frohlich (2010) investigated the influence of two different loading patterns, i.e., three-point test set-up, proposed by RILEM TC 162-TDF, and 4-point test setup, which is based on German Association of Structural Concrete (DAfStb

2003), on the flexural response of the UHPFRC material. It was found that the flexural strength resulting from the 3-point bending test tends to be lower and more scattered than those from the 4-point bending test.

2.2.2.2 Influence of Fiber Content

The addition of randomly distributed discontinuous short steel fibers to plain UHPFRC mix is known to significantly improve its mechanical response in flexure compared to the plain UHPFRC matrix. The resulting product can be efficiently used in different structural members that are subjected to loading conditions which require a deflection hardening, limited crack opening, high post-crack flexural stiffness, and high durability performance. Moreover, the addition of short steel fibers to the UHPFRC matrix can partially replace the flexural steel reinforcement and improve the reinforcement spacing (Chanvillar and Rigaud 2003, Naaman 2002, Reinhardt 2003, Markovic 2005, Reinhardt 2006, Kim et al. 2011).

While the addition of short steel fibers to plain UHPFRC matrix did not result in significant improvements in the first crack strength (FCS), several researches indicated that it substantially enhance the PLES and the post cracking flexural strength of the UHPFRC material. These enhancements in the mechanical properties are associated to the fiber bridging effect across the cracks in matrix, where the load carried by the cracked matrix was transferred to the uniformly distributed steel fiber. According to Markovic 2006, the increase in the interfacial bond strength between steel fibers and matrix as well as the reduction in the fiber diameter can best enhance the fiber bridging effect. Significant improvement in the interfacial bond strength between matrix and steel fibers is reported in UHPFRC material with higher SF content. This is mainly associated to the formation of a strong transition zone in matrix with high SF concentration which significantly improves the pullout behaviour of steel fibers in concrete (Yan et al. 1999).

The influence of fibers length, i.e., $l_f = 9$ and 17 mm and fiber volume fraction, i.e., $V_f = 1\%$ and 2.5% on the flexural strength of UHPFRC material was investigated by Schmidt and Frohlich (2010). The prism specimens with $V_f = 2.5\%$ exhibited an 8% and 44% increase in the maximum peak load (MPL) compared to the control specimens incorporating 1% of shorter and longer steel fiber respectively. Similar

results were reported by Markovic (2005). According to Markovic (2006), the addition of short and long steel fibers to UHPFRC matrix can respectively enhance the peak tensile strength and the strain hardening behaviour of UHPFRC concrete. Thus an efficient combination of different fiber length would result in a substantial improvement in the both strain hardening and peak tensile strength.

The influence of six different fiber volume fraction ($l_f/d_f = 13/0.2$) on the flexural-tensile strength of 100 mm x 100 mm x 400 mm prism specimen subjected to 3 point bending load was recently studied by Kang et al. (2010). It was reported that the addition of 1%, 2%, 3%, 4%, and 5% volume fraction of short steel fiber to plain UHPFRC matrix increased the flexural-tensile strength by a factor of 1.8, 3.7, 5.2, 5.77, and 6.9. The significant improvements at the higher fiber dosage were developed by the fact that more fibers oriented in the direction of tensile stresses (parallel to the long direction of the prism), making a greater proportion of the fibers effective to bridge flexural cracks (Chanvilalrd and Rigurad 2003, Kang et al. 2010).

Although the use of the short steel fibers in the UHPFRC matrix enhances its flexural-tensile response, it was found that high concentration of fibers can increase the likelihood of fiber balling and clumping. This phenomenon reduces the uniform distribution of steel fibers, material homogeneity, and interfacial bond between steel fibers and matrix, which would influence the pull-out response of the steel fibers. To address this issue, several researchers proposed to use a fiber hybridization concept to mitigate problems associated with fiber balling and mix workability while maintaining the desired mechanical performance (Markovic 2006, Will et al. 2012, and Grünewald et al. 2000).

2.2.2.3 Influence of Specimen Size

Several past researchers studied the influence of specimen size and geometry on the mechanical properties of the UHPFRC material in flexure through the testing of geometrically scaled prisms (Frettlöhr et al. 2011). A series of tests was performed by Frettlöhr and Reineck (2009) to investigate the influence of specimen size on the flexural tensile strength of the UHPFRC material with different heights, $h = 25\text{--}150$ mm. The research was completed on two different UHPFRC material, i.e., Ductal

with an average compressive strength of 211 MPa and Duracrete Plus with a $f'_c=170$ MPa. A 2% steel fibers was used in both concrete materials. The results of the experimental tests indicated a very clear size effect for both materials. While similar flexural tensile strength was found for the specimens with 25 and 50 mm height, 21%, 26%, and 38% decrease in flexural tensile strength were found as the specimen height was increased from 50 mm to 75 mm, 100 mm, and 150 mm, respectively (Frettlöhr and Reineck 2009).

The size effect was more pronounced for the specimens with larger width-to-height ratio (Frettlöhr and Reineck 2009). The experimental tests on the 50 mm prism specimens indicated that the increase in b/h ratio from 1 to ratios of 3 and 5 would result in 11% and 20% decrease in the flexural tensile strength of the UHPFRC material. Similar results were also found for the specimen with a h = 75 mm, where 9% and 18% decrease in the flexural tensile strength was found as the b/h ratio was increased from 1 to ratios of 3 and 5. It was reported that the size effect was most likely caused by the fiber orientation in prism specimens which mainly influenced by the specimen geometry and size. (Grenier 2006 and 2007, Reineck and Frettlöhr, 2010, Frettlöhr, Reineck, and Reinhardt, 2012).

Chanvillard and Riguard (2003) studied the influence of specimen size on the mechanical properties of UHPFRC material ($f'_c = 160 - 240$ MPa and $f_t \geq 10$ MPa) in flexure and direct tension. The results of flexural tests show that the cracking and peak flexural-tensile strength as well as the strain hardening behaviour of UHPC material decreases as the prism height increases. According to them, this size effect is mainly associated with the fiber orientation than the size effect.

Reineck and Greiner (2007 and 2010) studied the influence of the specimen height on the flexural tensile strength of the UHPFRC material with compressive strengths of 160 to 180 MPa. The information from a 10 years experimental program for six different specimen height, h = 40, 50, 70, 100, 150, and 200 mm were compiled and given in Figure 2-6. The results show that the flexural tensile strength of the mix with an average compressive strength of 170 MPa decreased by 17%, 30%, 39%, and 46% as the specimen sized increased from 40 mm to 70, 100, 150, and 200 mm.

Similar trend was observed for the mix with compressive strength of 200 MPa where the flexural tensile strength linearly decreased as the specimen height increased (Reineck and Greiner 2007 and 2010). According to the authors the decrease in the strength was associated to the fact that less fiber are aligned in the direction of the tensile stresses, as the specimen size increases.

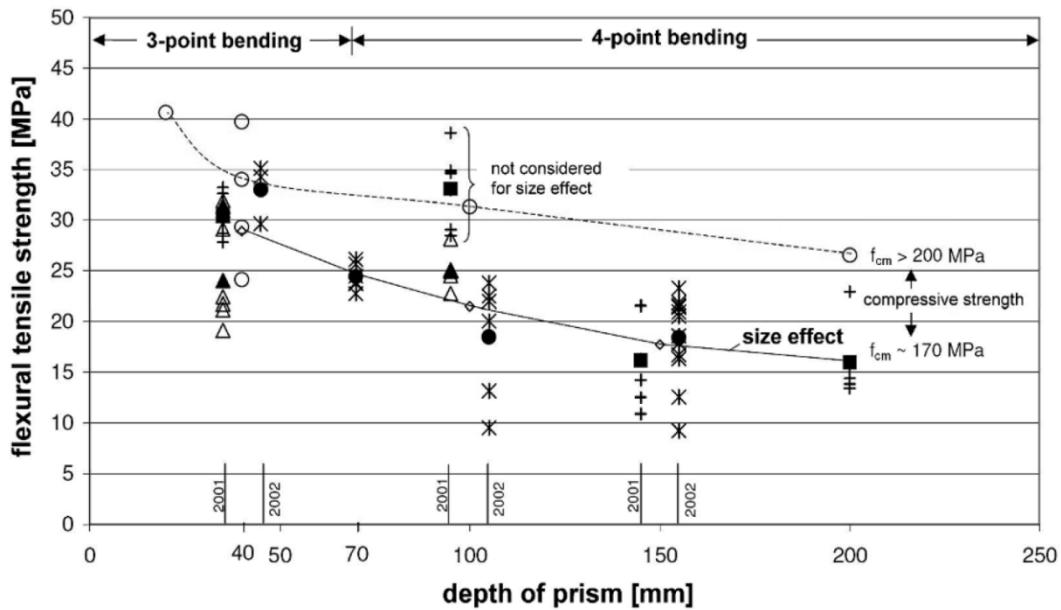


Figure 2-6: Variation of flexural-tensile strength against the specimen height (Reineck and Greiner 2010).

Frettlöhr et al. (2012) completed a series of experimental flexural tests on two different UHPFRC materials: 1) DUCTAL material incorporating short steel fibers with $d_f = 0.175$ mm and $l_f = 13$ mm and having a compressive strength of 211 MPa, and 2) Duracrete Plus with $d_f = 0.2$ mm and $l_f = 13$ mm and having a compressive strength of 169 MPa. The influence on the flexural-tensile strength from the specimen height of $h = 25$ -150 mm, and width-to-height ratios of $b/h = 1, 3,$ and $5,$ were investigated by the authors. A significant decrease in the peak tensile and flexural-tensile strength of the UHPFRC material was found with increasing the specimen height. See Figure 2-7 and Figure 2-8. They reported that the increase in the specimen height from 25 to 150 mm would result in a 58% decrease in the elastic (cracking) flexural-tensile strength of Ductal material. A similar trend was found for the specimens with different width to height ratios, where the flexural strength decreased as the width-to-height ratios increased from 1 to 5. However, it

was reported that the width-to-height ratio has no influence on the FCS of UHPFRC material (Frettlöhr et al. 2012). Similar trend was observed for the peak flexural-tensile strength of the UHPFRC material, as shown in Figure 2-7. The following two expressions were proposed for the prism specimens with $h \leq 150 \text{ mm}$.

$$f_{ct,Ductal} = 48 - \frac{h}{7} \quad (2-4)$$

$$f_{ct,DP} = 41 - \frac{h}{7} \quad h \leq 150 \text{ mm} \quad (2-5)$$

where $f_{ct,Ductal}$ and $f_{ct,DP}$ is the peak flexural-tensile strength of the Ductal and Duracrete Plus material respectively (Frettlöhr et al., 2012).

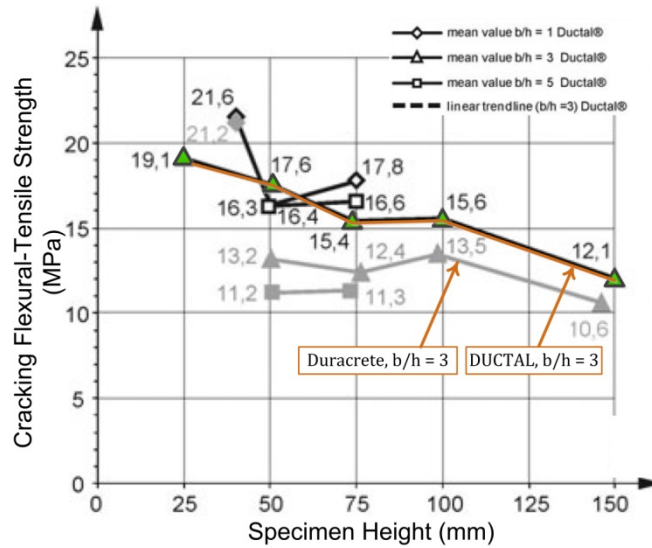


Figure 2-7: Variation of cracking flexural-tensile strength of UHPFRC material against the specimen height (after Frettlöhr et al. 2012).

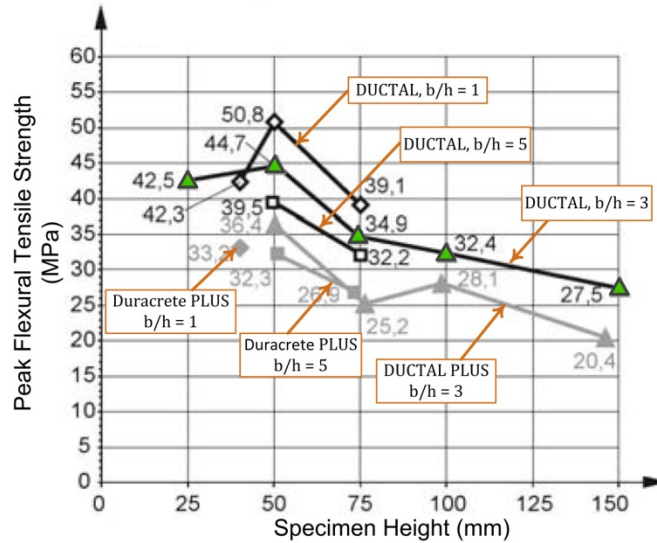


Figure 2-8: Peak flexural-tensile strength of UHPFRC material against the specimen height (after Frettlöhr et al., 2012).

Most of the past researchers concluded that the scale factor phenomenon or size effect is most likely attributed to the fiber orientation in the UHPFRC mix. A series of factors influence the orientation and distribution of steel fibers in a fresh mix which includes the workability of the fresh concrete mix, the overall geometry of the short steel fibers, fiber contents, fiber matrix interaction, casting method, and the condition of flow confinement (wall effect). The later one is influenced by the geometry of the mold and was found to orient most of the fibers parallel to the long direction of the prism, as indicated in Figure 2-9. This would, in turn, allow more proportion of the steel fibers to effectively bridge the flexural cracks (Boulekbache et al. 2010). According to Reineck and Greiner (2007 and 2010), a nearly one-dimensional fibre orientation was found near the surface of the prism specimens, while the core area contain randomly distributed fibers.

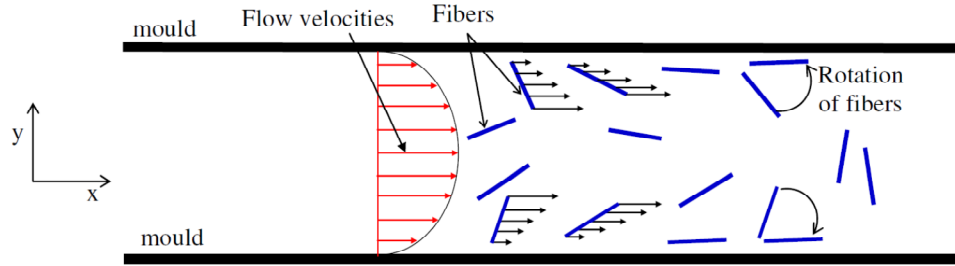


Figure 2-9: Fiber orientation and distribution in UHPFRC material (Boulekbache et al. 2010).

2.2.2.4 Flexural Toughness

The flexural toughness factor (FTF) of the concrete is a key property that characterizes its energy absorption capability to prevent brittle disasters (Shah et al. 1995). The most frequently used technique to characterize the mechanical properties of fiber reinforced concrete in toughness is flexural toughness testing (JCI Standard SF-4, 1984). The conventional notion of FTF is the areas or a proportion of the areas under the flexural load-deflection curves between the deflection of zero to a specific value.

In order to quantify the residual strength in concrete material, a series of toughness factor was proposed by different standard codes in the past. The following flexural toughness factor was proposed by JSCE-G 552-1999 which is similar to the ASTM C1609 procedure except the flexural energy up to a deflection of span/150 is converted to parameter called the flexural toughness factor (FT)

$$FTF = \frac{A_m L}{m b h^2} \quad (2-6)$$

where A_m is the area under the flexural load-deflection curve up to a specific deflection of L/m . A value of $m=150$ was chosen by JSCE to reflect the serviceability limit states of deflection and cracking. Terms L , b , and h are the length and effective height and width of the specimen respectively.

Several past studies have demonstrated the effectiveness of short steel fibers in improving the flexural toughness of the UHPFRC material (Richard and Cheyrezy, 1994, Richard and Cheyrezy 1995, Dugat et al. 1996, Bayard and Plé 2003, Alaei and

Karihaloo 2003, and Shaheen and Shrive, 2006). While a relatively weak toughness factor was reported for the plain UHPFRC matrix ($V_f = 0\%$), many researchers showed that the addition of a moderate volume-fraction of short steel fibers can significantly improve the flexural toughness. Wille et al. (2010) reported an energy absorption capacity of 130 kJ/m^3 for UHPFRC material with 2% fiber volume fraction which is notably higher than that with no fibers.

This significant enhancement in the FTF of UHPFRC material is mainly associated to the fact that the addition of short steel fibers tends to shift the post peak response of from a sudden drop in the load-deformation curve in the matrix with no fibers to a large post-cracking deformation response in those with short steel fibers. This improvement is more pronounced for the UHPFRC matrix with a higher silica fume (SF) content, as the addition of SF to the UHPFRC matrix results in a more brittle matrix (Pfeifer, 2010). However, significantly higher interfacial bond between the steel fibers and matrix was found for those with higher SF content, which improves the pull-out resistance of fibers and enhances the toughness.

The UHPFRC's high toughness property suggest a potential use in many applications where the structure require a significant integrity without collapse under the dynamic loads such as blast explosion, seismic loading, and more.

While the addition of short steel fibers to matrix was found to significantly enhance the UHPFRC's flexural toughness, the influence of the fiber volume fraction on this factor has not been investigated yet. In addition no past researches address the influence of the specimen size on the toughness factor. Thus, in this research the influence of $V_f = 0 - 5\%$ on FTF of UHPFRC prism specimens over a size range of 2 are investigated in section 5.1.6.

2.2.3 Tensile Response

The tensile strength of the UHPFRC material is appreciably higher than that of other types of concrete and this can allow significant tensile forces to be sustained. The mechanical properties of the UHPFRC material in tension is mainly distinguished from that of preceding generation of concrete (e.g. FRC) by its post-cracking strain hardening behaviour after the formation of the first crack (Richard and Cheyrezy

1995, Rossi et al. 2005, Habel et al. 2008, Chanvillard and Rigaud 2003). Several researches were completed in the past to extract the equivalent tensile strength of the UHPFRC material from the flexural test results (Chanvillar and Rigaud 2002, Frettlöhr 2009). It was reported that the flexural-tensile strength of the UHPFRC material depends on several factors including the matrix strength, fiber content (the number of fibers bridging a flexural crack), fiber alignment pattern, and the geometry of the specimen (Markovic 2006). Each of them is discussed below.

2.2.3.1 Equivalent tensile response

Several test methods were proposed in the past to derive the mechanical properties of the concrete in tension which includes the split tensile testing (STT) of cylinders, direct tensile test (DTT), and the flexural-tensile test (FTT) of prism specimens. A relatively good agreement between the peak tensile strength from the STT and DTT was reported by Graybeal (2006). However, a significant discrepancy between the stress-strain response in tension from STT and DTT was reported. This difference in stress-strain response is more pronounced for post cracking response of the UHPFRC materials incorporating steel fibers (Graybeal 2006).

Direct tensile test (DTT) is the most reliable test setup to characterize the tensile strength of UHPFRC. However, this test requires a more sophisticated setup than that used in the flexural test which may not be feasible in most of the laboratories. Thus, in the absence of DTT, the equivalent tensile response can be achieved through a back analysis using simpler flexural test results (Chanvillard 2006, AFGC 2002).

Many researchers investigated the relation between the flexural-tensile strength (FTS) and the direct tensile strength (DTS) of UHPFRC material, as the later one is implemented in the design of structural elements. According to several test results, the flexural tensile strength of UHPFRC extracted from a bending test is higher than those derived from direct tensile test (Chanvillard and Rigaud 2003, Graybeal 2006, Reineck and Frettlöhr 2010).

The equivalent tensile response of the UHPFRC material derived from an inverse analysis is presented in the Figure 2-10. In the early stage of loading, linear elastic

stage, the UHPFRC material tends to have an elastic behaviour in tension. In this stage, several microcracks with a maximum length of 5-10 mm and width of 1-5 μm form in the weak interface zone including the interface between short steel fibers and aggregates (Markovic 2006). A linear stress distribution across the cross section was considered for this stage which is characterized by an elastic modulus.

The next stage, tension hardening zone, is the initiation of several microcracks around the first discontinuity (crack) in the high-moment region. As the flexural load increases, the microcracks tend to grow more rapidly to form a single and longer crack, called macrocrack, which cover the majority of the specimen depth. After the hardening stage, a softening response was observed for the UHPFRC material. This stage refers to the evolution of the failure, which is governed by the fiber bridging. The shape and the slope of the softening curve are significantly impacted by the fibers content in the fractured zone and its alignment along the prism specimen (Markovic 2006).

The cracking equivalent tensile strength (CETS) and peak equivalent tensile strength (PETS) were respectively used to distinguish the boundaries between the elastic and hardening zone as well as the hardening and softening zone, as shown in Figure 2-9 as σ_{cc} and σ_{pc} , respectively. The CETS and PETS are discussed more in below.

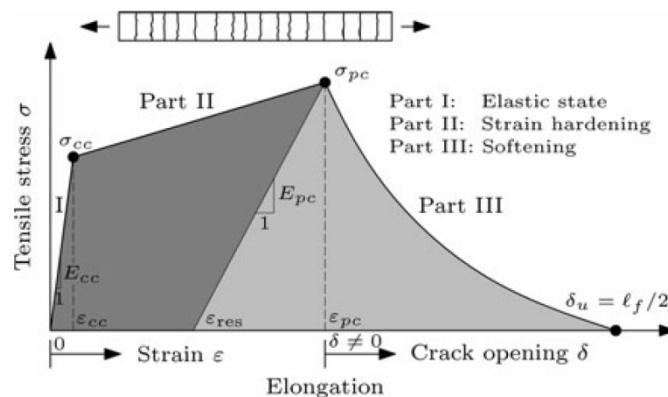


Figure 2-10: Variation of tensile strength against the crack opening.

Cracking equivalent tensile strength (CETS)

The cracking equivalent tensile strength (CETS) is one of the key parameter in the design of structural elements, particularly for those which are susceptible to the formation of cracks, including the sewage pipes, industrial floor systems. Several researches were investigated the relation between the cracking flexural-tensile strength and the cracking tensile strength (from direct tensile test) and it was found that the CETS of UHPFRC material is significantly smaller than the FCS (Carpinteri and Chiaia, 2002, Chanvilalrd 2006). The following empirical expression was initially proposed by the International Federation for Structural Concrete CEB-FIP that relates the direct tensile strength of brittle material to the flexural strength of a prism specimen (CEB-FIP 1997).

$$f_t = \xi_{SF} \cdot f_f \quad (2-7)$$

$$\xi_{SF} = \frac{\alpha_{fl} \left(\frac{h_p}{h_0}\right)^{0.7}}{1 + \alpha_{fl} \left(\frac{h_p}{h_0}\right)^{0.7}} \quad (2-8)$$

where ξ_{SF} is the scale factor and tends to approach a value of 1.0, as the specimen height increases. The variation of the scale factor against the specimen height is given in Figure 2-11 and Figure 2-12. The f_f is the flexural strength of prism specimen under flexural loading, f_t is the mean axial tension strength, h_p is the effective prism height, $h_0 = 100 \text{ mm}$ and α_{fl} is a factor which ranges between 1 and 2 and is dependent on the brittleness of the concrete and increases with increasing brittleness of the concrete. A value of 2 was proposed by the Association Française de Génie Civil (AFGC) Interim Recommendations for the Ultra High Performance Fibre-Reinforced Concretes (AFGC 2002).

The scale effect phenomena, ξ_{SF} , in concrete arises from the formation of micro-cracking ahead of the crack tip, leading to a higher limit of proportionality (first flexural cracking point) compared to the real tensile strength. Models based on the cohesive crack concept best describe this phenomenon. The proposed model in CEB-FIP (2003) is a simplified model describing this scale effect.

Chanvilard and Rigaud (2003) studied the influence of specimen size and steel fibers ($V_f = 2\%$) on the tensile mechanical properties of the DUCTAL material. It was found that the ratio of FCS to cracking tensile strength directly obtained from direct tension test decreases as the specimen height increases which implies that the tensile strength is highly size dependent (Chanvilard and Rigaud, 2003).

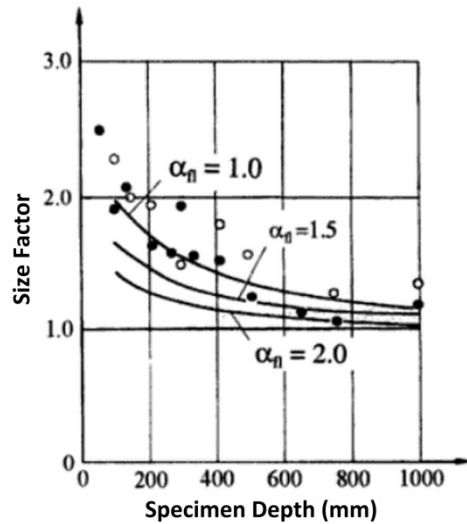


Figure 2-11: Variation of experimental scale factor against the beam depth (CEB-FIP 1999).

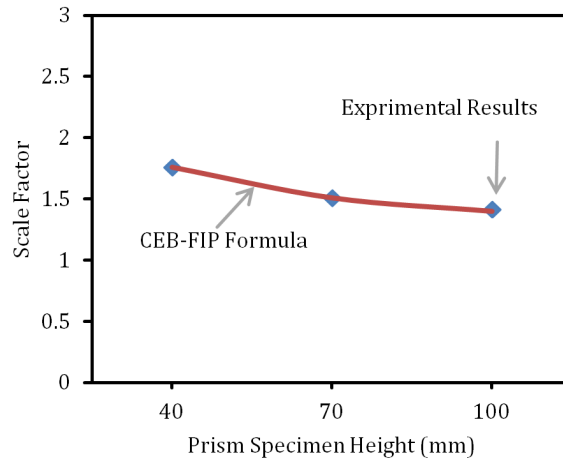


Figure 2-12: Variation of scale factor against prism height (Chanvilard and Rigaud 2003).

Peak equivalent tensile strength (PETS)

Several techniques have been proposed to extract the post-cracking tensile strength of fiber reinforced concrete from the flexural response of prism. The Association Française de Génie Civil (AFGC) proposed an analytical-numerical approach to extract the tensile stress-crack opening relation from flexural test result (AFGC 2000). This technique is described in more detail in chapter 5 of this thesis.

Prior research has shown that UHPFRC has exceptional tensile mechanical properties including PETS, post-cracking strain hardening and a high deformation capacity to the peak tensile strength (Rossi et al. 2005, Habel et al. 2008). A series of experimental tests were completed by Chanvilard and Rigaud (2003) to characterize the post-cracking tensile behaviour of DUCTAL material. They reported a noticeable strain hardening up to 0.15% (strain at the end of strain hardening region) for a commercially available DUCTAL material containing 2% volume-fraction of straight steel fibers. It was found that the strain hardening behaviour and the maximum PETS were mainly affected by the fiber contents and their orientations along the prism specimens. It was also reported that the PETS, obtained from a flexural test, decreases as the prism specimen height increases. They concluded that the cracking and peak equivalent tensile strength as well as the strain hardening behaviour of UHPFRC material are substantially affected by the specimen size and the fiber content (Chanvillard and Rigaud 2003). Similar results were reported by other recent researches (Reineck and Greiner 2007, Reineck and Frettlöhr 2010, Frettlöhr et al. 2012).

2.2.4 Direct Shear Response

Understanding of the mechanical properties of UHPFRC material in shear allows establishing its shear stress-strain response and developing the constitutive model which is essential for the stress analysis of the concrete members, particularly for those that shear stresses dominate the design. Researches related to the direct measurements of the material properties of UHPFRC in shear are limited. However, several shear test setups were proposed during the past years to measure the direct shear strength of concrete and they are summarized in other publication (Xu and Reinhardt 2005). A Z-shape test setup was initially used to measure the shear

strength and shear toughness of normal strength concrete and FRC material (Hsu et al. 1987, Valle and Buyukozturk 1993). However the Z-shaped test method was found to considerably deviate from the state of pure shear failure.

No standard test method is currently established in North America or Europe to evaluate the mechanical properties of concrete in shear. However the Japan Society of Civil Engineers (JSCE-G 553-1999) established a simple test method to measure the direct shear strength of concrete, as shown in Figure 2-13. This test setup was slightly modified by Mirsayah and Banthia (2002), as significant deviation between the expected plain of failure and the shear failure location was observed in several tests. This deviation is most probably caused by a complex state of stress which is not well understood. To generate a pure shear failure, it was proposed to make an all-around-notch with a minimum height of 25% of total specimen height to allow the shear failure occur along the plane of weakness (Mirsayah and Banthia, 2002). Good results were found after a pair of notches was introduced.

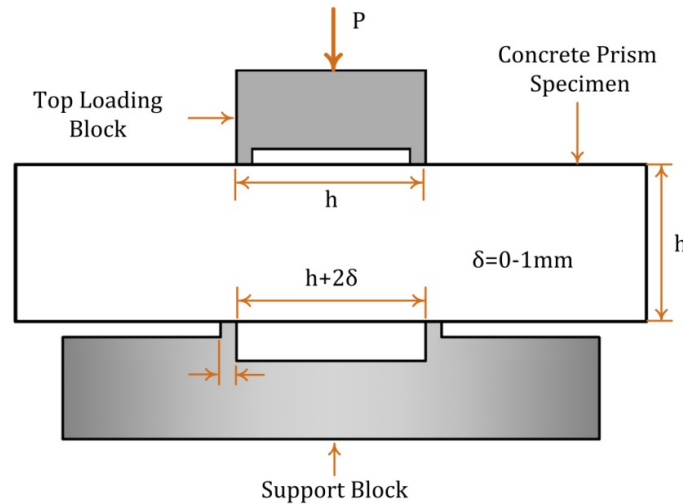


Figure 2-13: Overall configuration of JSCE-G 53 direct shear test setup (JSCE-G 53 1999).

The basic equation in AFGC-07 to predict the shear strength of members made of UHPFRC material is assumed to be as follows:

$$V_u = V_{Rb} + V_a + V_f \quad (2-9)$$

where V_{Rb} , V_a , V_f are the contribution of UHPFRC matrix, longitudinal reinforcement, and short steel fibers to the shear resistance. The contribution of concrete is as follows.

$$V_{Rb} = \frac{1}{\gamma_E} \frac{0.21}{\gamma_b} k \sqrt{f_{cj}} b_0 d \quad (2-10)$$

$$k = \begin{cases} 1 + 3 \frac{\sigma_{cm}}{f_{tj}} \\ 1 - 3 \frac{0.7\sigma_{tm}}{f_{tj}} \end{cases} \quad (2-11)$$

The terms σ_{cm} and σ_{tm} are the mean stress in the compressive and tensile part of the beam. To Account for the uncertainty in the above equation (originally proposed for HPC material), $\gamma_E \gamma_b = 1.5$ was considered in this equation. The fiber contribution to shear strength is as follows.

$$V_{Rb} = \frac{S\sigma_p}{\gamma_b f \tan \beta_u} \quad (2-12)$$

where S is the area of fiber effect and for a rectangular and T-shaped section is ($S = b_0 d$). Factor σ_p is residual tensile strength and is defined as below.

$$\sigma_p = \frac{1}{K} \frac{1}{w_{lim}} \int_0^{w_{lim}} \sigma(w) dw \quad (2-13)$$

where K is the fiber orientation factor, and w_{lim} is the maximum crack width under the combined stresses and defined as follows.

$$w_{lim} = l_c \varepsilon_u \leq 0.3 \text{ mm} \quad (2-14)$$

The shear strength and ductility of the UHPFRC material are significantly influenced by the fiber volume contents and the critical crack opening width. The later factor was found to be substantially influenced by the specimen geometry and size. According to Spasojević (2009), the shear strength tends to decrease, as the specimen height increases.

While limited research was completed on the shear strength of high performance concrete, there is a little information on describing the effect of mix design parameters and fiber volume fractions on the shear response of the UHPFRC

material. In addition, the influence on the mechanical properties of UHPFRC material in shear from the specimen size is an important factor that needs to be well established.

2.2.4.1 Shear Toughness

The shear toughness or shear toughness factor (STF) was initially introduced to quantify the energy dissipation capacity of the fiber reinforced concrete (Barragan et al. 2000). The STF was defined as the area under the shear load-deflection curve up to a certain displacement. The shear toughness parameter was first defined as the area under shear load-displacement curves for a fiber reinforced concrete with hooked end steel fibers (Khaloo and Kim 1997, Barragan et al. 2006). A size-independent STF was developed by modifying the expression for flexural toughness factor proposed in JSCE-G 552-1999 (Higashiyama and Banthia, 2008).

$$STF = \frac{A_m}{\frac{h_e}{m} b_e h_e} \quad (2-15)$$

where A_m is the area under the shear load-deflection up to a certain deflection of h_e/m . Terms h_e and b_e are respectively the effective height and width of the specimen in the direct shear test after accounting for all-around notch.

While many recent research investigated the influence of short steel fibers on the shear toughness of the FRC concrete, there is no research in literature that assess the shear toughness response of the UHPFRC material. In addition the effect of steel fiber and the specimen size on the shear toughness of UHPFRC material has not been studied.

2.2.5 Rheological properties

UHPFRC material is mainly distinguished from the older generation of the concrete material by a relatively low water to cement ratio, i.e., $w/b < 0.2$ and an optimized granular packing. While this would result in a considerable enhancement in the mechanical properties of UHPFRC material, it is well know that a workable (self-compactable) mix cannot be achieved without the use of high range water reducer (HRWR) admixture. The addition of HRWR to concrete mix was found to

significantly enhance the mix workability, which is crucial to gain a uniform dispersion of fibers (Markovic 2006).

Several researches in the past investigated the chemical reaction between different types of superplasticizer (SP) and the cementitious materials in the concrete and it was reported that the use of polycarboxylate superplasticizers significantly enhances the consistency and the rheological properties of the UHPFRC material compared to other commercially available SP. In addition it would enhance the mixing time, liquefaction and initial setting, workability, and strength gain rate of UHPFRC material (Cazacliu and Roquet 2009).

Silica fume, on the other hand, play an important role in the enhancement of the rheological properties of UHPFRC material which contains a high amount of fine sands. This is because the use of high concentration of silica fume would enhance the yield stress of fresh mix by increasing the cohesion of the particles which governs the degree of slump flow (Morin et al. 2001).

The mix compositions and the lack of coarse aggregates in the UHPFRC mix require the use of a high energy mixing equipment and sufficient mixing time to produce a homogenous product. The influence of the mix composition, mixing duration, and energy imparted by the high performance mixer on the rheological properties and the properties of UHPFRC material was studied by Mazanec et al. (2009). It was noted that a long mixing time is required for the mass-production of the UHPFRC material, which reduces the plant production capacity. According to him, the use of more optimized particle size distribution in the matrix, higher silica fume concentrations, and higher energy imparted by the mixer can significantly reduce the total mixing time.

In order to measure the workability and slump flow of the fresh plain UHPFRC material, a mini-slump cone originally developed by Kantro (1980) was used as a fast and convenient method to carrying out sufficient number of slump flow tests in relatively short time. However, this method cannot be used for mixes with steel fiber. Instead, a fiber factor is introduced by Wille et al. (2011) to evaluate the workability of the UHPFRC and is defined as follows:

$$\xi_f = V_f \times \frac{l_f}{d_f} \quad (2-16)$$

where l_f and d_f are respectively length and diameter of the steel fiber. Maximum values of $\xi_f \approx 2$ and 2.5 are proposed by other researchers that are respectively attributed to $V_f = 3$ and 4% for the steel fiber used in this study. According to Markovic (2005), maximum values of $V_f = 1\%$ and 4% should be respectively used for short ($l_f = 13 \text{ mm}$) and long fiber ($l_f = 60 \text{ mm}$).

While some research were carried out in the past to study the equivalent tensile strength of UHPFRC material, there is not enough information to describe the influence of the fiber content and specimen size on the equivalent tensile strength of the UHPFRC. These issues are addressed in this research and the results are summarized in the chapter 5.

2.3 Mechanical Properties of FRC

2.3.1 Compressive Response

Several past researchers reported that the addition of short steel fibers to plain normal strength concrete increases the peak compressive strength. Fanella and Naaman (1985) reported a 15% improvement in the peak compressive strength of FRC material after the addition of 3% steel fibers with a length of $l_f = 19\sim 25 \text{ mm}$ and aspect ratio $l_f/d_f = 47\sim 100$ to plain normal strength concrete. Wafa and Ashour (1992) reported a 5% improvement in the peak compressive strength after the addition of 1.5% steel fibers with $l_f/d_f = 75$ and $l_f = 60 \text{ mm}$ to plain mix.

Compared with normal strength concrete with a sudden brittle behaviour in compression after the peak load, the FRC material tends to show a higher peak response, ductility and energy absorption capacity in compression. This is mainly attributed to significant contribution of fiber to the post-peak response of FRC material (Soroushian and Bayasi 1991, Ezeldin and Balaguru 1992).

According to the past research on the FRC material containing 2% steel fiber with $l_f/d_f = 57\sim 60$ ($l_f = 30\sim 50 \text{ mm}$), more enhanced post-peak response in compression was found for mixes with hooked-end fibers as compared with those incorporating the

crimped or straight fibers. See Figure 2-14. This phenomenon would result in a higher ductility and energy absorption capacity, which makes the FRC material more practical for many applications, particularly those in the high seismic area (Soroushian and Bayasi 1991, Wafa and Ashour 1992, Balaguru and Foden 1996, Shoaib 2012).

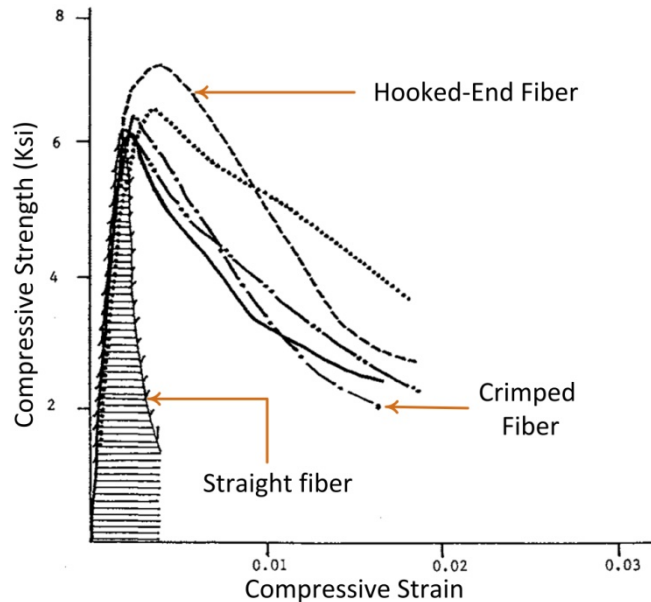


Figure 2-14: compressive stress-strain response of FRC material with different fiber types (Mirsayah and Banthia, 2002).

2.3.2 Flexural-Tensile Response

The flexural capacity of the FRC material is known to be improved by incorporating a moderate volume-fraction of steel fibres. Several researches on the mechanical properties of the FRC material in flexure have been conducted and the results have been published in different sources (Soroushian and Bayasi 1991, Balaguru et al. 1992, Wafa and Ashour 1992, Balaguru and Foden 1996, Shoaib 2012).

Balaguru et al. (1992) showed that the addition of 0.4% and 0.75% of steel fiber to FRC material significantly increased the peak flexural load carrying capacity of the prisms. However no more improvement in the peak flexural load was observed as 1.1% and 1.5% fiber was added to mix. Instead an appreciable enhancement in the post-peak loading response in flexure was observed for mixes with 0.75%, 1.1%, and 1.5% as compared with mix incorporating 0.4% fiber. This significant enhancement in the flexural capacity of the FRC material is related to the contribution of the steel fibers in bridging the tensile

cracking. The influence of two different fiber lengths with similar diameter, i.e. $d_f = 0.5 \text{ mm}$ was investigated in this research. According to Balaguru et al. (1992), no significant enhancement in the FRC peak flexural load and ductility was found after the fiber length was increased from 30 mm to 50 mm (Balaguru et al. 1992).

2.3.3 Equivalent Tensile Response

Several attempts have been done over the last decades to relate the flexural load-deflection of the FRC material to its uniform equivalent tensile strength (UETS). An analytical model was proposed by Armelin and Banthia (1997) and Dinh (2009) to obtain the UETS against the crack mouth opening displacement (CMOD) for FRC material (Armelin and Banthia 1997, Dinh 2009). The response of the FRC prism specimen was modeled as a pair of rigid block at both side of a single flexural crack near the middle of the prism specimen, as shown in Figure 2-15. The axial equilibrium requires that the tensile (T) and compressive (C) forces are equal. The CMOD was extracted from the mid-span deflection, δ , as below.

$$CMOD = \frac{2(h-c)\delta}{l-a} \quad (2-17)$$

where l and a is shown in Figure 2-15. Using the equilibrium in cracked section, the uniform tensile stress can be formed as follows.

$$\sigma_{fu} = \frac{2M_{ext}}{bh(h-c)} \quad (2-18)$$

where c is the neutral axis and is as follows.

$$c = \frac{2M}{0.85bhf'_c} \quad (2-19)$$

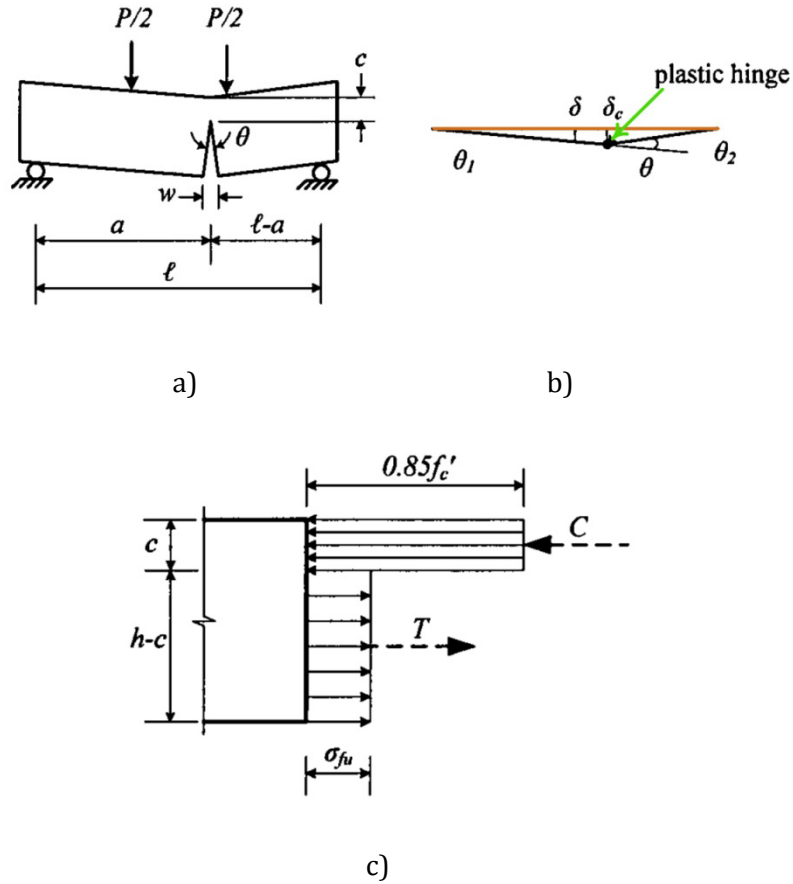


Figure 2-15: Flexural prism under 4-point loading, a) schematic of FRC prism specimen after the formation of macro crack, b) formation of plastic hinge at flexural crack, c) stress block at the cracked section (Dinh, 2010).

Following the above mentioned model, Shoaib (2012) quantified the contribution of double-hooked steel fibers to the tension resistance of three different FRC material types, i.e., low strength concrete (LSC or LWC in the figure), normal strength concrete (NSC), and high strength concrete (HSC), as shown in Figure 2-16. Compared to NSC and LSC materials, higher ETS or σ_{tu} was found for high strength FRC material. This higher strength is caused by a stronger interfacial bond between steel fibers and FRC matrix (Naaman and Najm 1991). An analytical model was proposed for the normalized ETS as follows.

$$\sigma_f = \begin{cases} 2.9 \frac{CMOD}{0.2} \sqrt{V_f f'_c} & CMOD < 0.2 \text{ mm} \\ 2.9(1.03 - \frac{CMOD}{5.8}) \sqrt{V_f f'_c} & CMOD \geq 0.2 \text{ mm} \end{cases} \quad (2-20)$$

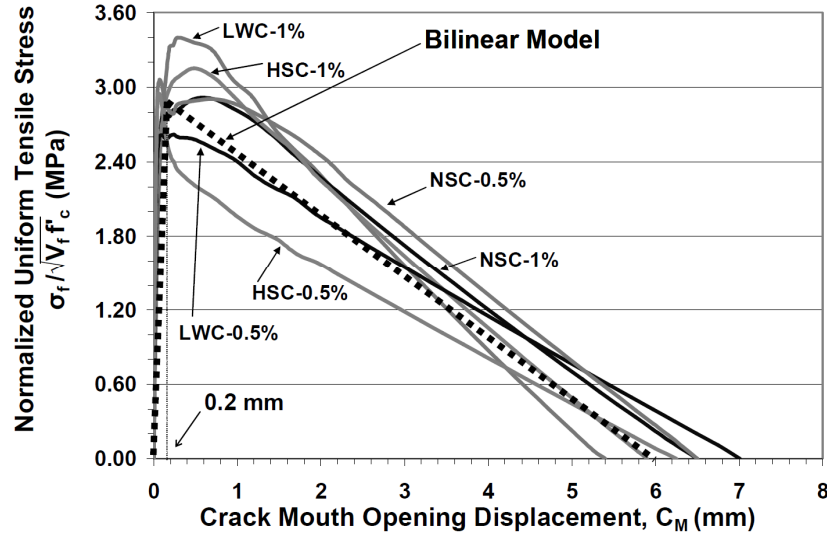


Figure 2-16: Variation of equivalent tensile strength (ETS) against the CMOD response of LSC, NSC, and HSC FRC material (Shoib 2012).

2.3.4 Direct Shear Response

Several researches investigated the response of FRC material subjected to direct shear loading (Mirsayah and Banthia 2002, Shoib 2012). Mirsayah and Banthia (2002) was the first to introduce the modified direct shear test originally proposed by JSCE-G 553-1999 standard. The shear load was applied to the concrete prism by a pair of loading block with two knife edges at both top and bottom sides of the prism specimens. The peak shear stress, f_v , of FRC material was determined as follows:

$$f_v = \frac{V_{max}}{b_{eff}d_{eff}} \quad (2-21)$$

where V_{max} is the peak shear load sustained by the notched specimen, b_{eff} and d_{eff} are respectively the effective width and height of the notched sections.

Unlike plain FRC material ($V_f = 0\%$) with a brittle behaviour or catastrophic load reduction in shear, the FRC material with higher fiber content are able to sustain a significant shear forces even without any ordinary reinforcement. While the lightweight FRC matrix did not significantly benefit from the addition of steel fibers to plain FRC matrix, Shoib (2012) found that the addition of 1% by volume of steel fibers to plain FRC matrix was resulted in 60% increase in shear resistance of high strength concrete ($f_c = 62 \sim 80 \text{ MPa}$) and 36% for NSC ($f_c = 26 \sim 34 \text{ MPa}$). This is most

probably attributed to the improvement in the fiber-matrix interfacial bond in high strength concrete (Naaman and Najm 1991, Valle and Buyukozturk 1993). Similar results was reported by Valle and Buyukozturk (1993)

The influence of the randomly distributed discrete steel fibers on the mechanical properties of FRC material in shear has been examined in the past few decades (Sharma 1986, Banthia 1992, Dinh et al. 2010, Shoaib et al. 2012). A significant increase in the shear strength of FRC material incorporating steel fiber was reported. The variation of shear strength against the fiber volume fraction in FRC material is plotted in Figure 2-17. Mirsayah and Banthia (2002) investigated the influence on mechanical properties of FRC material from four different fiber types: crimped fiber (CF), crescent-shaped cross section (CR), flattened-end fiber (FE), and circular-shaped cross section (CC). According to them, a higher shear strength was found for the FRC mix containing CF and CR fibers than those incorporating FE and CC fibers (Mirsayah and Banthia 2002, Shoaib 2012).

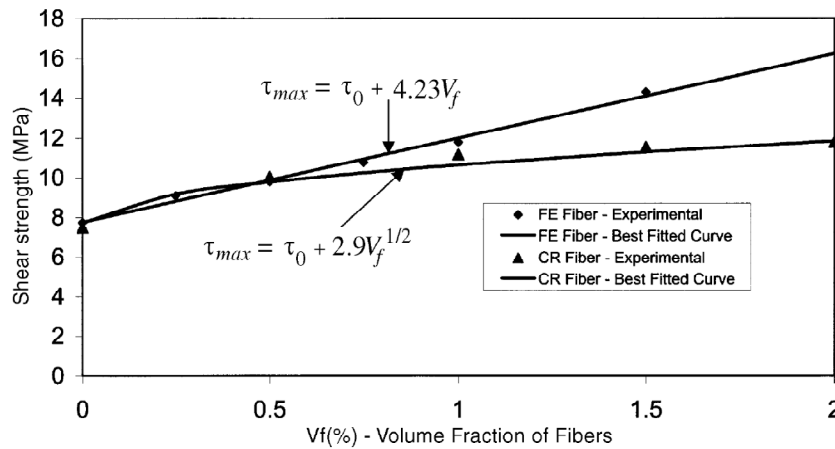


Figure 2-17: Variation of shear strength of FRC material against fiber volume fraction (Mirsayah and Banthia 2002).

2.4 Composite Connection

Composite connections have been long used in several engineering applications including bridges and buildings to take advantage of the increases in its strength, stiffness, and ductility. In order that the composite section act as an integrated structural unit, an efficient connection between concrete and steel is essential to

transfer the shear, tensile and compression stresses. Previous researches have been carried out on the behaviour of composite connection under different loading conditions. Each of these was discussed below.

2.4.1 Response under Shear Loading

In a composite I-shaped beam, the concrete flanges provide flexural resistance and the steel web resists the imposed shear. A connection system for an efficient composite action between the steel web and concrete flange is required to transfer the shear loads. Two different connection systems were proposed in the past: (1) the conventional headed studs (HS) attached to a small steel plate that welded to the web, and (2) direct embedment of the steel web (DESW) into the concrete flange.

2.4.1.1 Headed studs (HS)

The traditional headed stud system is broadly adopted for the conventional composite construction. This system offers increased ability for modular construction with on-site assembly. In order to investigate its load-slip response subjected to the shear loading, standard push-off tests were proposed by different standard codes (ACI 318-05 and Eurocode-4). The geometry of the standard push-out test setup proposed by Eurocode-4 is given in Figure 2-18.

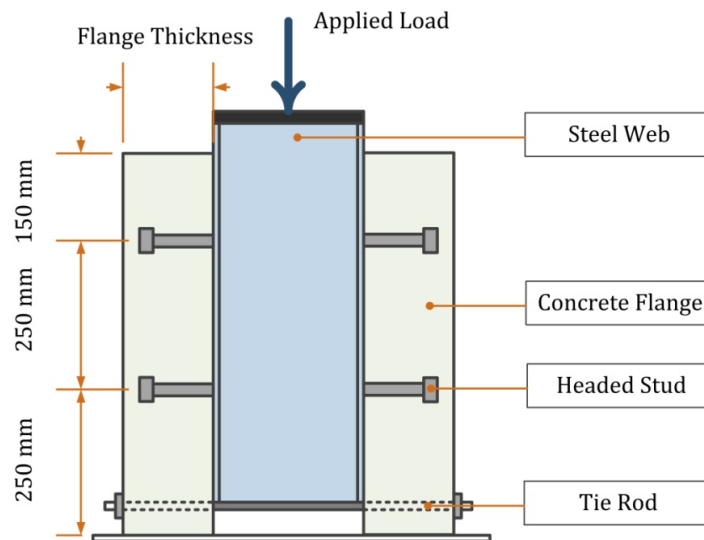


Figure 2-18: Geometry of the standard push-out test (EC4 2004).

The behaviour of headed studs in the composite connections with normal strength concrete (NSC) was extensively studied by several researchers in the past few decades (Nguyen and Kim 2009, Wurzer 1997, Hegger et al. 2001, Schmitt et al. 2005, Hegger et al. 2006). By considering the possibility of crushing of the concrete around the stud or stud shank failure, AISC proposed the following expression for nominal strength of one stud shear connector (Q_n) embedded in a solid slab of concrete without fibers (AISC 2005).

$$Q_n = 0.5A_{SC}\sqrt{f'_c E_c} \leq A_{SC}F_u \quad (2-22)$$

where A_{SC} is the cross-sectional area of stud and F_u is the ultimate tensile strength of stud, and E_c is the elastic modulus of concrete. Similar expression was also adopted in CAN/CSA-S16-09.

While considerable research has been conducted on behaviour of HS subjected to shear loading in composite connection with normal strength concrete (NSC), only limited research has examined the applicability of high performance concrete (HPC) to allow efficient use of this material in composite beam. Hegger et al. (2009) studied the behaviour of HS with a diameter of 22 mm embedded in HPC ($f_{c,cube} = 120$ MPa). According to them, the use of the UHPC material in the composite connection improved the load carrying capacity, fatigue response and the failure pattern as compared to connections made of normal strength concrete. However this connection requires a significant welding, introducing concern with respect to cost and fatigue performance. In addition, the load carrying capacity of the composite connections constructed with the UHPC and HS system is significantly lower than that with DESW (Schmitt et al. 2005, Hegger et al. 2009). Thus some limited recent research focused on the direct embedment of the steel web in the UHPFRC flange (Hegger et al. 2009, Rauscher 2011).

2.4.1.2 Direct Embedment of Steel Web (DESW) System

The response of composite connections made of DESW with different hole configurations, which is cut through the embedded plate, were recently investigated by different researchers (Hegger et al. 2009, Feldman 2011, Heinemeyer et al. 2012). A test set-up similar to the one proposed for standardized push-off test for

the headed stud connection was adopted for this connection, as shown in Figure 2-19. Specimens were evaluated for the test set-up configurations, force transfer capacity, interface slip, crack localization, and overall connection deformations. Each of these are explained in below.

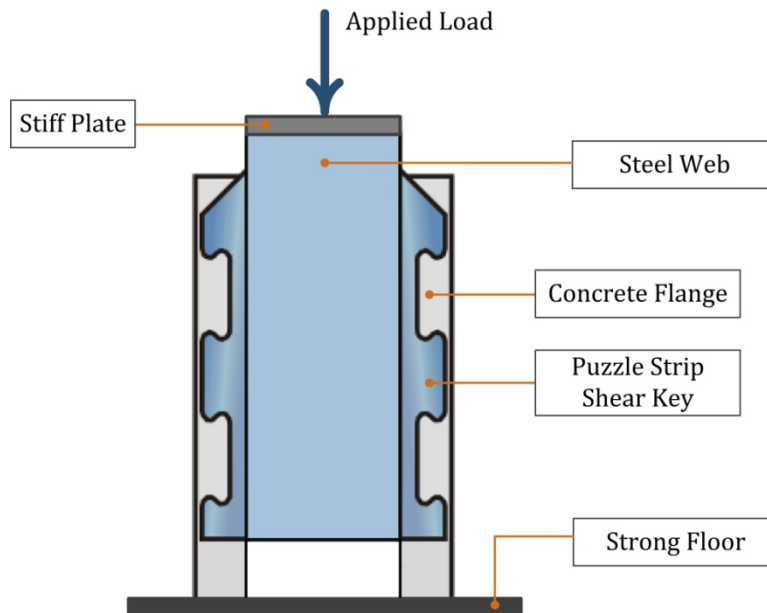


Figure 2-19: push-out test setup (Hegger et al. 2009).

Influence of Test Set-up

German federation of industrial research associations (AiF 2000) proposed a single push-out test (SPOT) as an alternative to the standard push-out test (POT), which is illustrated in Figure 2-20. According to Rauscher (2011), the proposed SPOT test set-up is more convenient, cost effective and flexible than the POT set-up. In order to validate the results of SPOT, a series of tests were completed at the Aachen University and the results were compared against those derived from the POT set-up, as summarized in Figure 2-21. DESW connection system with two different hole configurations, i.e. puzzle strip and saw tooth, were used for the validation purpose. According to them, the SPOT test set-up, despite its simplicity, can generate the load-slip response similar to those extracted from the POT set-up. The crack pattern after failure in concrete shear key was also checked and similar pattern was found for them. While similar initial stiffness, load-slip response were found for both SPOT

and POT, the results of SPOT tends to show a slightly higher (an average 6%) peak push-off load than POT.

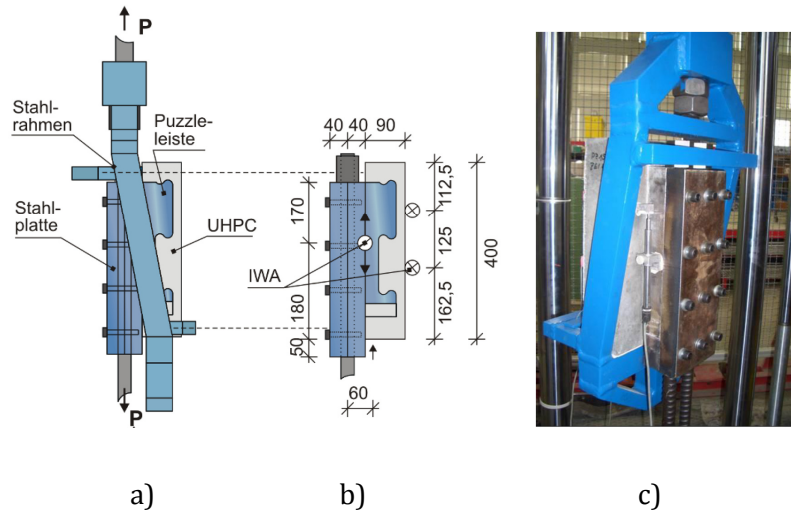


Figure 2-20: Single push-out test set-up (Hegger et al. 2009).

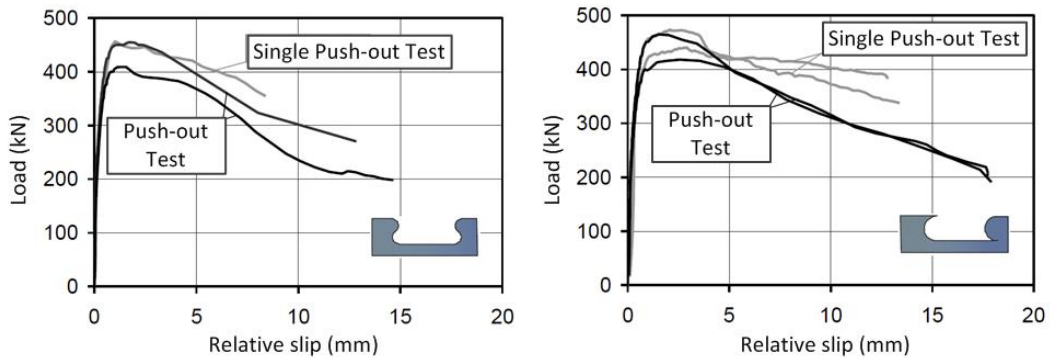


Figure 2-21: Influence of test set-up on the push-off load carrying capacity of composite connections with different shear key configurations (Rauscher 2011).

Influence of Shear Key Configurations

The influence of three different shear key configurations including the puzzle-strip, saw-tooth-I, and saw-tooth-II shear key configurations, as shown in Figure 2-22 and Figure 2-23, on the load-slip response of the composite connection made of UHPC was recently studied by Hegger et al. (2009). Similar load-slip response and peak push-out load were found for the puzzle-strip and saw-tooth-I shear key configuration subjected to the loading direction given in Figure 2-24. This is mainly because the saw-tooth-I shear key has almost similar configuration in front of the

shear key (concave shape). A lower peak push-out shear loading (about 11% lower) along with different post peak load-slip response was observed for the saw-tooth-II shear key. Four different failure modes were observed by Hegger et al. (2009) which include: 1) local concrete failure in front of the shear connector, 2) concrete pry-out failure, 3) shear failure of the concrete, and 4) steel failure, as shown in Figure 2-25.

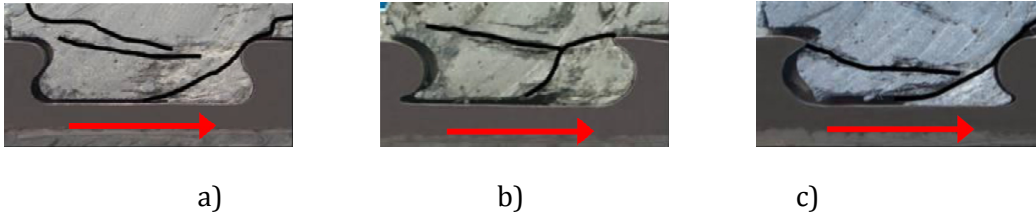


Figure 2-22: Shear key configurations: a) puzzle-strip shear key, b) saw-tooth-I shear key, c) saw-tooth-II shear key (Hegger et al. 2009).

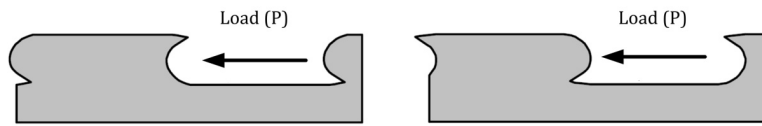


Figure 2-23: Direction of applied shear loading (Hegger et al. 2009).

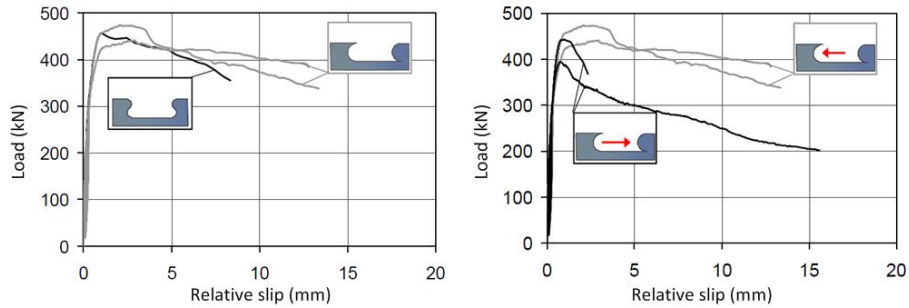


Figure 2-24: Influence of load direction on the pull-off capacity of composite connections (Rauscher 2011).

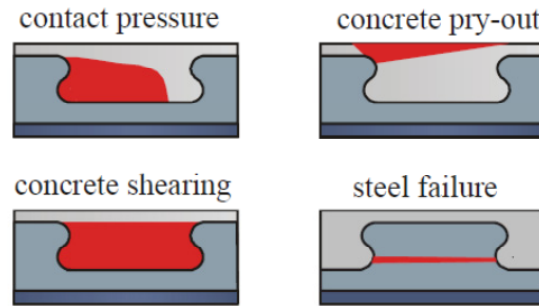


Figure 2-25: Failure modes of embedded steel plate with puzzle-strip hole subjected to shear loading (Hegger et al. 2009).

Influence of Plate Thickness

The influence of three different plate thicknesses (10, 15, and 20 mm) on the PPL of SPOT was investigated, as shown in Figure 2-26. Compared with shear connection with a thickness of 10 mm, 20% and 40% increase in the PPL was found for those with 15 and 20 mm thickness, as shown in Figure 2-27. In addition, the increase in the plate thickness significantly decreases the deformation in the shear key, which is illustrated in Figure 2-26.

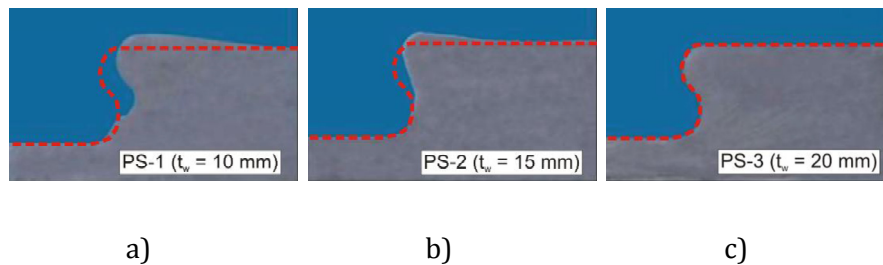


Figure 2-26: Influence of plate thickness on the deformed shape of puzzle-strip shear key (Rauscher 2011).

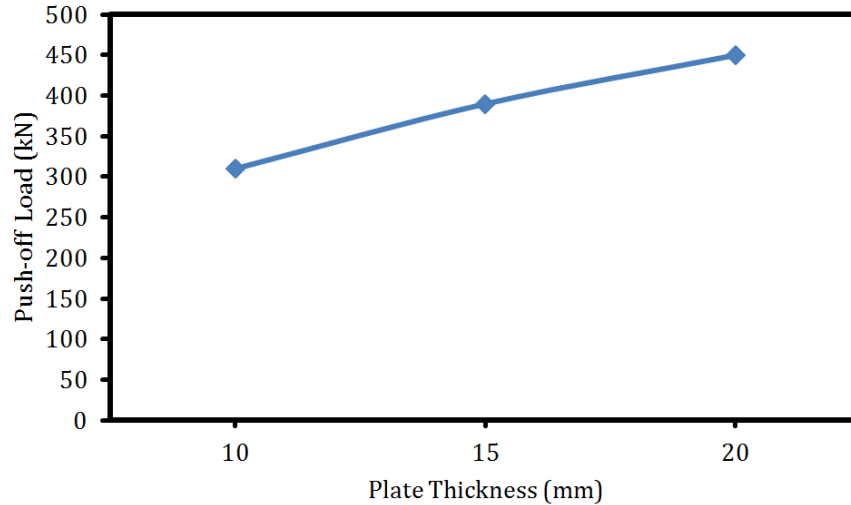


Figure 2-27: Influence of plate thickness on the peak push-off load carrying capacity of the composite connections (Rauscher 2011).

Influence of Fiber Volume-fraction

The influence of the addition of 0.9%-2.5% short steel fibers to UHPC mix (with $f'_c \approx 175 - 190$ MPa) on the PPL of composite connection with puzzle-strip shear key was studied by Rauscher (2011). It was found that the addition of 0.9%, 1.04%, and 2.5% short steel fiber to plain mix was resulted in 40%, 32%, and 54% increase in the PPL, as shown in Figure 2-28. Furthermore, the addition of short steel fibers to UHPC matrix was found to appreciably control the crack formation and propagation in the concrete flange. This would, in turn, prevent the concrete pry-out failure and improve the post peak load-slip response and ductility of connection. This improvement is mainly associated to the fiber bridging effect that retards the crack propagation in regions with high stress concentration (Hegger et al. 2009).

In addition to the appreciable contributions of the fiber content to response of the push-off test subjected to shear loading, the experimental results indicated that the load-slip response and the PPL was influenced by the casting method (Rauscher, 2011). This is mainly because the casting method directly affects the fiber alignment in the concrete flange. Two different method of casting was implemented in an experimental study by Hegger et al. (2009): casting along and across the longitudinal axis of the concrete flange. Higher PPL was found for those specimens constructed with the second method of casting. This improvement is attributed to

fact that more steel fibers aligned across the flange and bridge cracks, thereby reducing crack widths and improving the PPL.

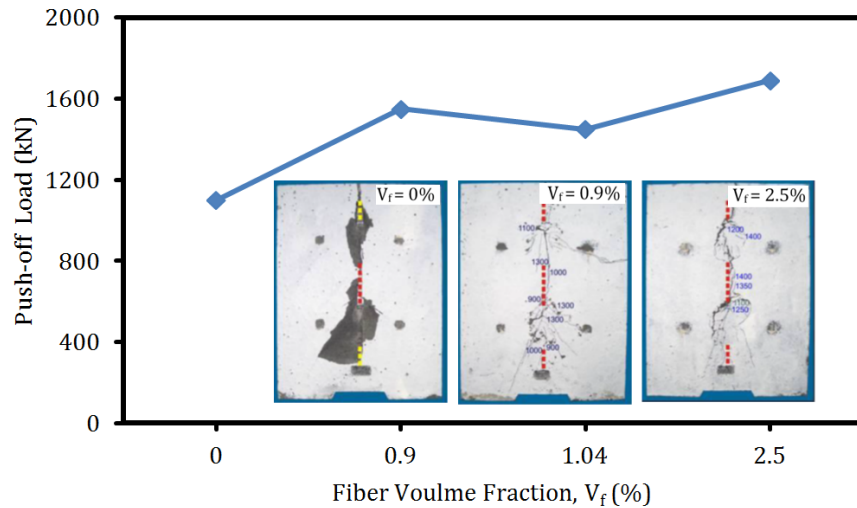


Figure 2-28: Influence of randomly distributed fiber volume fraction on the peak push-off load carrying capacity of the composite connections (Rauscher 2011).

Influence of Concrete Cover

The influence of concrete covers (least distance between the surface of embedded plate and the outer surface of the concrete flange) on the PPL of the composite connection constructed with direct embedment of steel web into concrete flange was studied by Hegger et al. (2009). It was found that the increase in concrete cover thickness from the 10 to 20 mm was resulted in an average increase of 8%, as shown in Figure 2-29. In addition, larger crack width was found at the back side and near the mid-width of the concrete on those specimens with thinner concrete cover. This is more pronounced in the composite connections constructed with concrete incorporating randomly distributed steel fibers, as the steel fibers provide an alternate load transfer path across the cracks; reduce the crack widths and spacing. This phenomenon would in turn result in a significant enhancement in the peak load carrying capacity of connections subjected to shear loading and will generally lead to a more ductile failure mode compared to those specimens made with an equivalent plain concrete material.

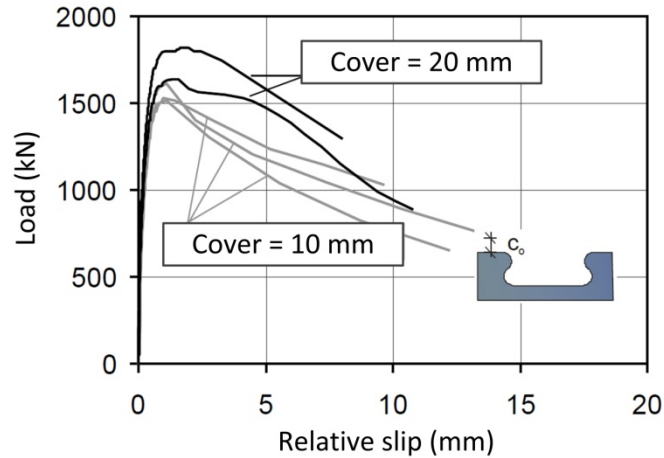


Figure 2-29: Influence of concrete cover depth on the peak push-off load carrying capacity of the composite connections (Hegger et al. 2009).

Influence of Concrete Generation

To investigate the effect of two different concrete types, i.e, UHPC with $f'_c \approx 175 - 190$ MPa and high strength concrete (HSC) with $f'_c \approx 90$ MPa on the load-slip response of the composite connection subjected to shear loading, specimens with puzzle-strip shear key configuration was tested by Hegger et al. (2009). Unlike the composite connection made of UHPC material with a ductile response, a brittle response with a pry-out failure in the concrete flange was observed in the composite connection made of HSC material, as shown in Figure 2-30. The peak push-out load carrying capacity of connection specimens made of HSC and UHPC were compared and 92% increase in the PPL was found for the specimen made of UHPC material Hegger et al. (2009). A substantial improvement in the load-slip response was found for those made of UHPC material which can appreciably enhance the connection ductility, as shown in Figure 2-31. This improvement is mainly attributed to the crack bridging effect in UHPC mix which retards the crack initiation and propagation. In addition, the use of UHPC mix improved the post peak response of the connection.

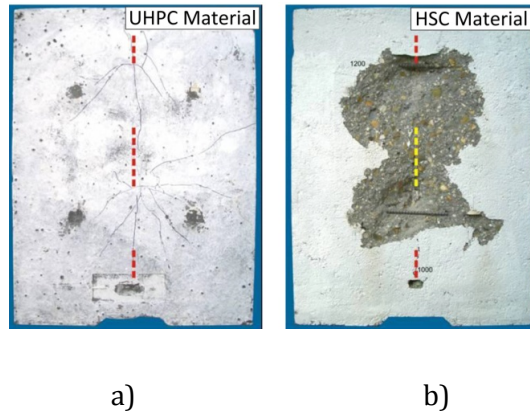


Figure 2-30: Failure mode of composite connection system constructed with: a) UHPC material, b) HSC material (Rauscher 2011).

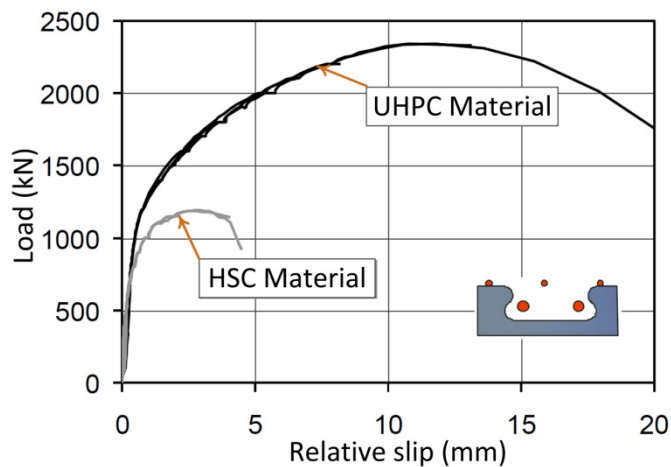


Figure 2-31: Influence of concrete generations on the peak push-off load carrying capacity of the composite connections (Rauscher 2011).

Influence of Transverse Reinforcement

A series of push-off specimens were tested to investigate the influence of the transverse reinforcements, passed through the holes, on the push-off response of the composite connections constructed with the embedded steel plate in the UHPC flange (Wurzer 1997). The results of the experimental program indicated that the addition of two 12M and 20M rebar was respectively resulted in a 41% and 66% increase in the PPL of the composite connection, as shown in Figure 2-32. The state of stress distribution in the concrete shear key (CSK) in front of the steel shear key (SSK) is illustrated in Figure 2-33. An almost hydrostatic stress distribution in front of the SSK was formed for connection subjected to shear loading. However a series

of cracks was observed in the next region where a tensile stresses perpendicular to direction of applied shear loading was observed. Thus using the transverse reinforcement in the CSK was found to enhance the shear capacity of the connection by providing a significant confinement to the concrete shear key and improving the tension capacity of the CSK.

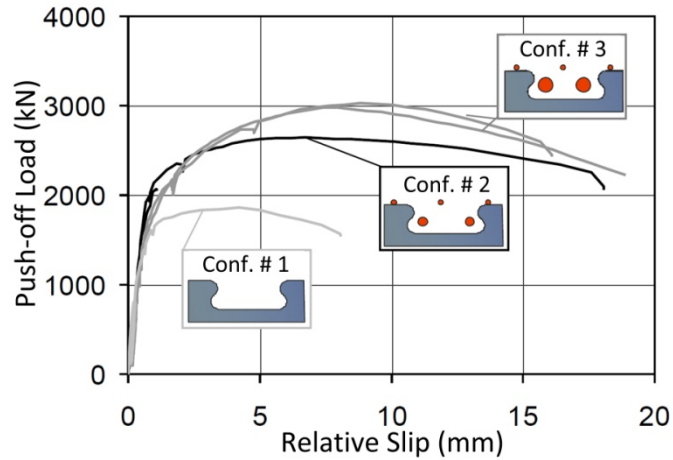


Figure 2-32: Influence of transverse reinforcements passed through hole on the peak push-off load carrying capacity of the composite connections (Wurzer 1997).

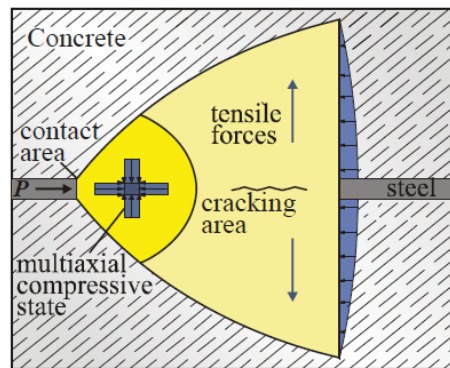


Figure 2-33: Multiaxial stress in the contact area between the concrete shear key and steel plate (Wurzer 1997).

Influence of Corrugation Pattern

The detail of the Embedded corrugated shear connector (ECSC) is given in Figure 2-34, which consists of three main parts: embedded corrugated steel plate, longitudinal reinforcements, and transverse reinforcement. The last two components form block and concrete shear key respectively. There are some limited

studies on the behaviour of ECSC in normal concrete. Sakurada et al. (2002) implemented ECSC in a composite prestressed bridge in Japan. In this connection reinforcing bars are passed through holes, which cut through the embedded steel plate. This type of connection requires no steel flanges to attach the traditional shear connector (stud) to web which can save cost up to 5% of total construction cost as well as time required to weld the steel flange to the corrugated web. In addition, since no welding is required, this type of connection offers a high resistance to fatigue. The similar ultimate capacity was reported for this type of connection compared to those constructed with headed stud (Sakurada 2002).

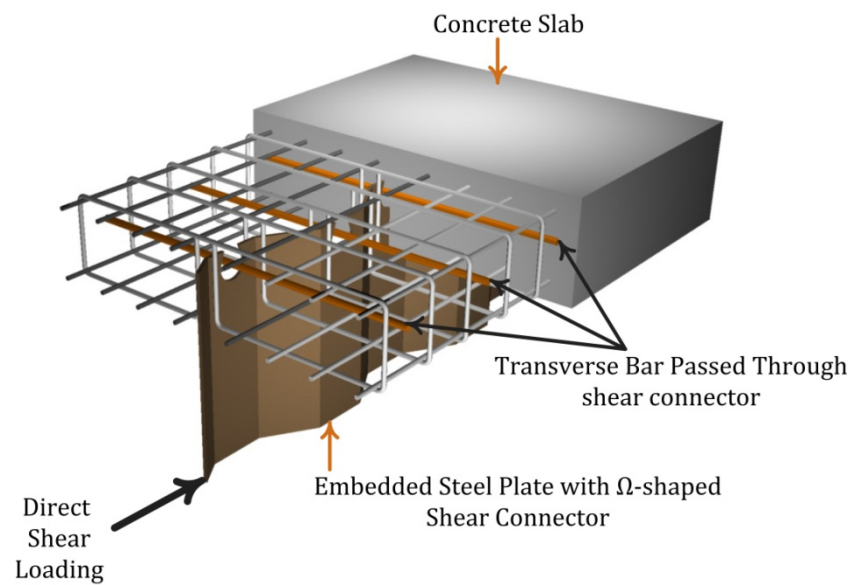


Figure 2-34: Overall configuration of embedded corrugated steel plate with Ω -shaped shear key (Rohem, 2009).

Röhm (2009) investigated the shear transfer mechanism between the corrugated steel web with an Ω -shaped shear connection and concrete flanges in a composite I-shaped beam. A trapezoidal corrugation profile was selected, as this configuration significantly increase the overall load carrying capacity of the composite beam, as compared with those with flat web. This is because the corrugation pattern provides enhanced lateral stability to the girder web without the need for additional stiffeners, thus allowing economical use of thin high strength steel web (Drive et al. 2006).

According to Röhms (2009), the increase in the plate thickness from 8 to 10, 12, 16, and 20 mm was resulted in 13%, 24%, 44%, 64% increase in the peak push-off load. This enhancement is attributed to the higher stiffness provided by the thicker plate which leads to a more solid interaction between the steel and concrete and prevent the excessive distortion in the plate, as shown in Figure 2-35. In addition, larger area is available in connections with thicker plate, which would results in lower bearing stresses and prevents a premature crushing failure in the concrete shear key.

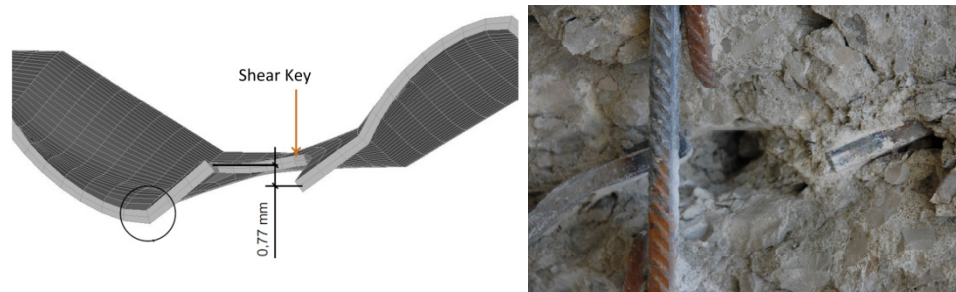


Figure 2-35: Twisting in the shear key (Röhms, 2009).

According to Röhms (2009), the increase in the concrete compressive strength from 25 MPa to 30, 37.5, and 48 MPa respectively resulted in the 8%, 18%, and 40% improvement in the peak push-off load of the specimens with 8 mm embedded plate. Similar trend was observed for those with 16 mm embedded plate. It is also reported that the increase in the embedded length of plate from 100 to 150, 175, and 200 mm resulted in 15%, 30%, and 35% improvement in the peak push-off load. This improvement in the capacity is attributed to higher interfacial bond between embedded plate and concrete.

The influence of the transverse reinforcement on the PPOL of push-out test was studied in the research by Röhms (2009). The results of the experimental tests showed that compared to specimens with 15 mm rebar, a 15% improvement in the PPOL was found for the specimen with 28 mm bar. This is because the use of the larger bar size increases the confinement to the concrete shear key (Röhms 2009).

In order to further improve the mechanical interlock between the concrete shear key and the embedded steel plate, Abramski et al. (2010) proposed to use a series of spiral reinforcements, which are placed in each puzzle-strip holes, as shown in

Figure 2-36. The response of the composite connection subjected to shear loading was studied and it was found that the addition of the spiral springs were resulted in 20% improvement in the peak push-out load carrying capacity of the connection subjected to direct shear loading. In addition, the relative shear slip between the concrete flange and the embedded steel web at the pick load was significantly improved (around 30%) after the spiral springs were introduced to connection.



Figure 2-36: Push-off test with puzzle-strip shear key and spiral springs (Abramski et al. 2010).

2.4.2 Response under Tensile and Compressive Loading

The composite connections should be capable of transferring the in-plane compression or tension load (in the plane of web) between the concrete flange and the steel web. This is more pronounced in the connection systems in the girders with openings in the steel web. The opening is provided to accommodate the typical utility conduits, as shown in Figure 2-37.

Major changes in the behaviour of this composite connection were reported to be along the opening in the web of the beam. This has been results from the secondary moment that illustrated in the Figure 2-38.

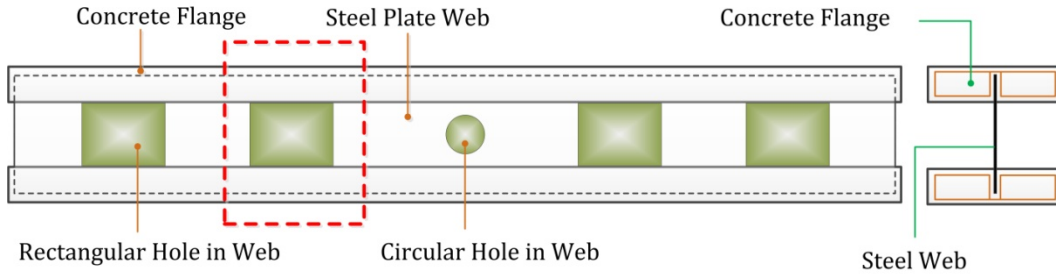


Figure 2-37: Geometry of composite girders with circular and rectangular hole (Abramski et al. 2010).

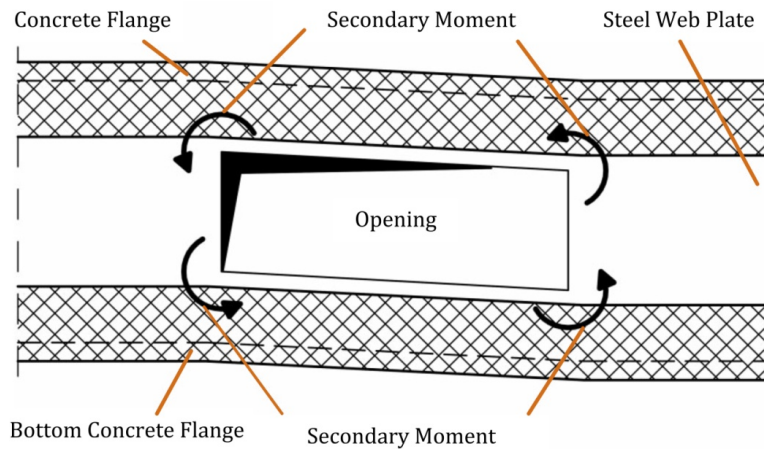


Figure 2-38: Secondary bending moment resulting from the shear force acting at opening (Abramski 2010).

Conventional headed stud—Kohlmeyer (2007) investigated the behaviour of composite I-shaped girders with rectangular openings in the beam web. A series of experimental tests, as shown in Figure 2-39, along with the numerical analysis were completed to study the load transfer mechanism between the connections components. Headed studs welded to top flange of steel I-shaped beam were used as the connection system between the concrete flange and the steel beam (Kohlmeyer 2007). According to the author, two different load transfer mechanisms between the connection's components were identified along the girder length: 1) regions located between the openings where the longitudinal shear forces between the concrete flange and steel web is dominant, 2) parts of the beam, located along the top and bottom edge of openings, where the pull-out force is significant (Kohlmeyer 2007, Abramski 2011).

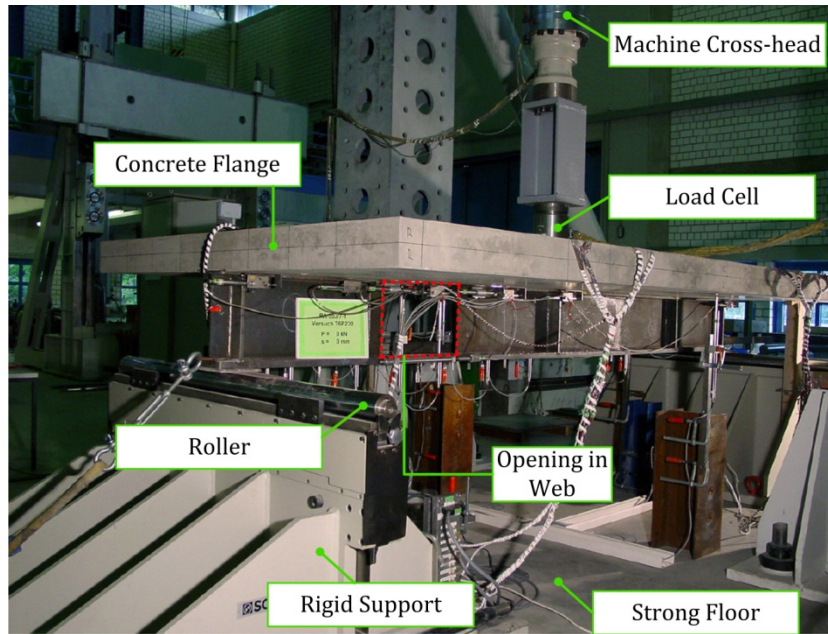


Figure 2-39: Composite girders with opening in web (Kohlmeyer 2007).

In order to capture the state of uniaxial stress and strain in the studs, pairs of linear strain gauges were attached to the shank of each headed stud, as shown in Figure 2-40. The strains along the studs were captured and transferred to stresses and uniaxial loads. The variation of the tensile load per a pair of studs against the total applied load to beam for different headed studs along the opening is shown in Figure 2-41. According to the diagram, higher pull-out loads were observed in the headed studs located at the far ends of the web opening.

While the use of the headed studs connection systems proved to be an effective composite connection system and is capable of enhancing the capacity of the composite connections in shear and tension, a significant welding is required in the fabrication and assembly process of the composite connection, introducing concerns with respect to cost, construction time and fatigue performance.

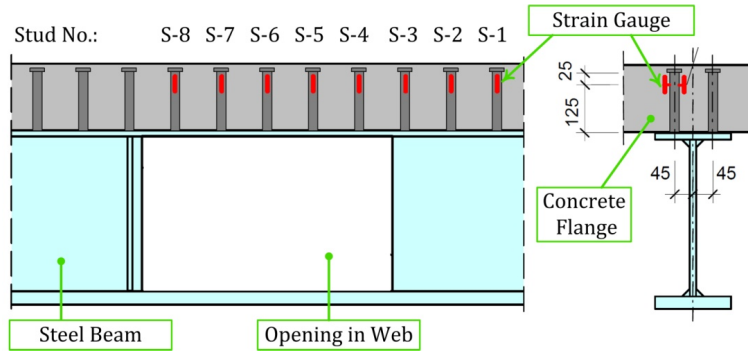


Figure 2-40: location of the strain gauges (Kohlmeyer 2007).

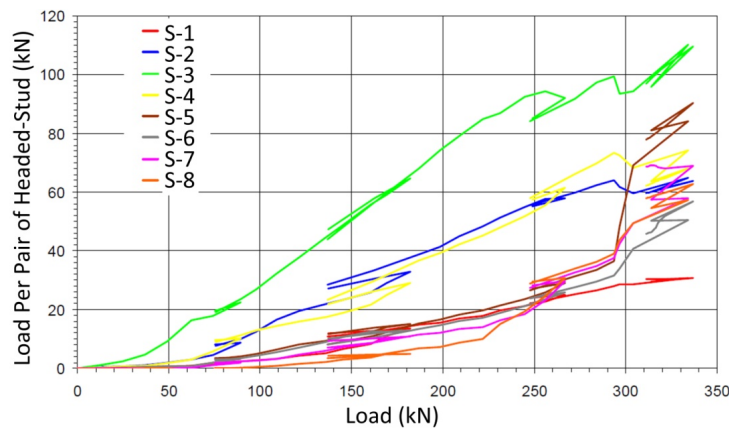


Figure 2-41: Variation of tensile loading in each headed studs against the total applied load (Kohlmeyer 2007).

Direct embedment of steel plate in NSC—The experimental response of a composite I-shaped girder—with 16 m span and 3 m width—constructed with concrete flanges and perforated steel web was investigated in Germany (Abramski 2010). The openings were cut through the web to accommodate the heating, ventilation, air conditioning, electricity, and etc. The composite beam consists of 200 mm high steel web (clear height) directly embedded into 100 mm thick slabs on both top and bottom sides. Two different techniques were proposed to transfer the forces between the steel web and concrete flanges: (1) Conventional horizontal headed studs (normal to web) welded to both sides of the embedded steel plate, (2) puzzle-shaped holes cut through the steel web which are located along the top and bottom edges of the embedded steel web, as shown in Figure 2-42. In order to improve the confinement and the mechanical interactions between concrete flange and embedded steel web, a series of spiral reinforcement were added to each puzzle-

strip holes, as shown in Figure 2-42. A series of tests were completed by them to investigate the response of the proposed connection subjected to the pull-out loading, as this is the governing load along the opening. The test setup for the pullout test used by Abramski et al (2010) is shown in the Figure 2-43 and Figure 2-44. A break-out failure in concrete flange was observed for the specimens subjected to the pull-out load. It was also reported that the addition of spiral springs to puzzle-strip holes improved the pull-out capacity of the connection around 29%. This enhancement in the pull-out load was achieved through the improvement in the mechanical interlock between the holes cut through plate and the surrounding concrete (Abramski et al. 2010).

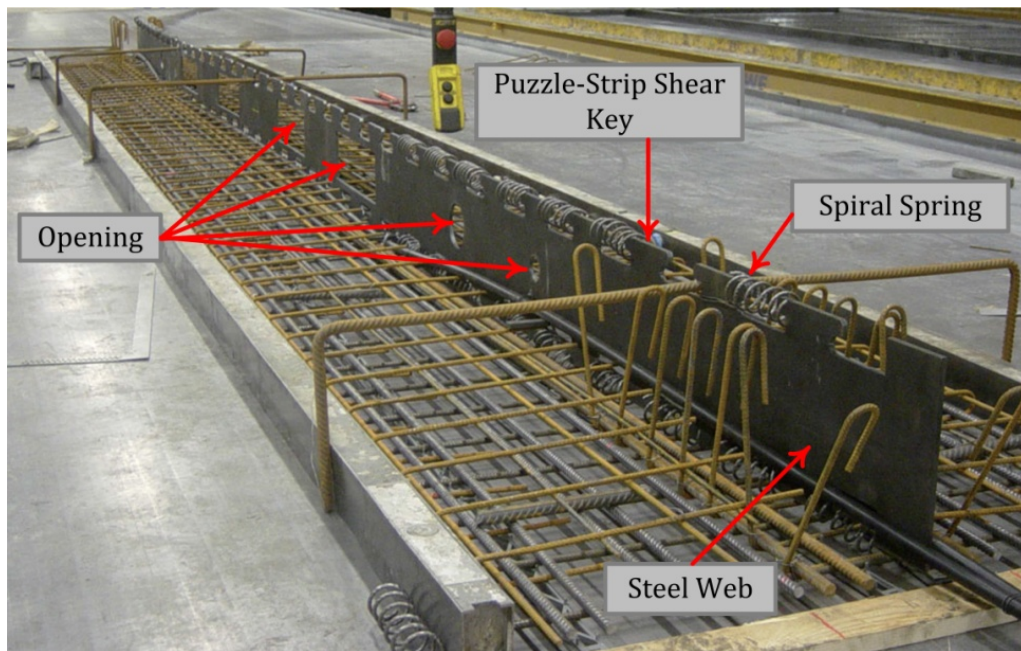


Figure 2-42: Composite beam with multiple opening in steel web (after Abramski et al. 2010).

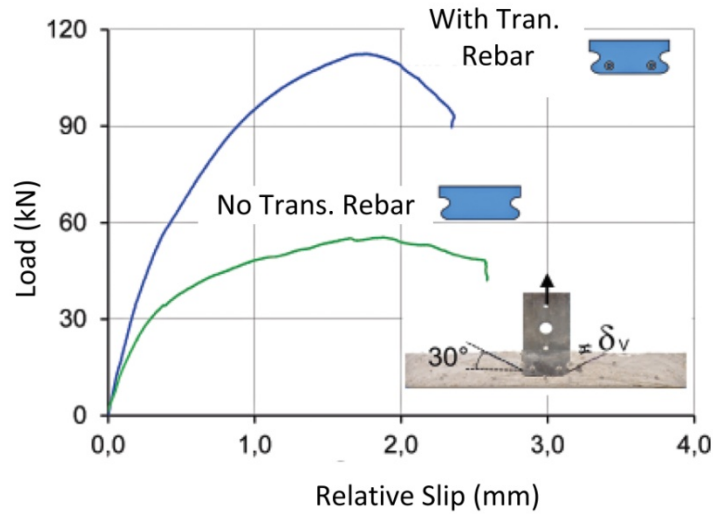


Figure 2-45: Variation of pull-out load against the relative slip for the composite connections constructed with embedded steel plate in normal strength concrete (Hegger et al. 2013).

Burger (2009) investigated the pull-out load-slip behaviour of the composite connection made of the embedded steel plate with Ω -shaped hole directly embedded in the normal strength concrete flange. Three different failure modes during the pull-out tests were observed: 1) concrete break-out failure, where a triangular shaped failure was observed in the concrete beam, as shown in Figure 2-46; 2) steel yielding failure, where a plastic deformation forms at the region with highest stress, as shown in Figure 2-47; and 3) combination of both failure modes. Unlike a brittle failure in specimens with break-out failure, a ductile mode was reported for those specimens with the steel yielding failure. It is indicated that the increase in the concrete cover at back side of the embedded plate was significantly enhanced the peak pull-out load of the connection system.

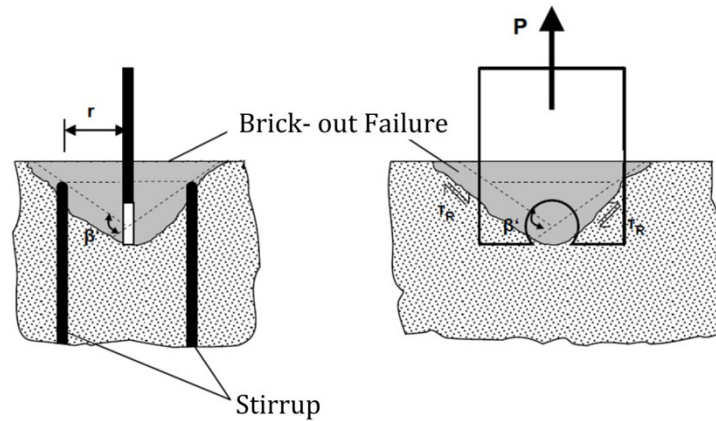


Figure 2-46: Schematic of the break-out failure in the pull-out test (Burger 2009).

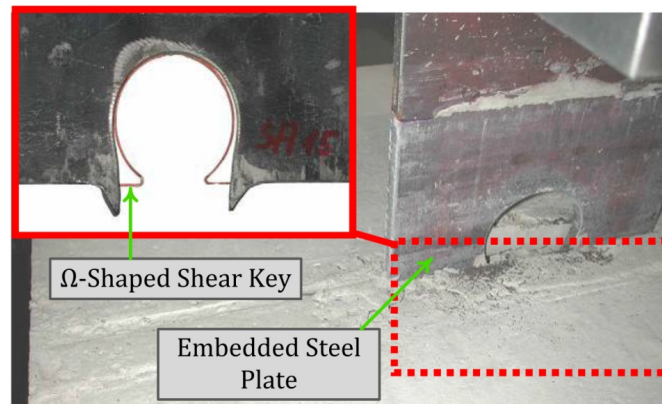


Figure 2-47: Plate yielding failure in the pull-out test (Burger 2009).

Direct embedment of steel plate in UHPC flange

Hegger et al. (2009) investigated the pull-out response of composite connection constructed with embedded steel plate in the ultra high performance concrete (UHPC) with a compressive strength of 175 MPa. A puzzle-strip configuration was selected for embedded steel plate, as shown in Figure 2-48.

The composite connection subjected to pull-out test after failure is shown in Figure 2-49. A shallow breakout failure was observed in all the specimens. According to Hegger et al. (2009), no significant enhancement in the pull-out load carrying capacity of the connection was found after the concrete cover at the bottom side of the concrete flange was increased by 20%. However a higher variation in the peak pull-out load (PPL) was observed for connection specimens with smaller cover size.

This variation is associated to the premature failure at the back of those specimens with smaller cover size.

The addition of the transverse reinforcement passed through the embedded steel plate on the pull-out load-slip response of the composite connection was investigated by Hegger et al. (2013). According to them, a similar failure pattern was observed for specimens with and without transverse reinforcement. However the addition of transverse reinforcement to the connection was found to enhance the peak pull-out load by 105%. This improvement is associated to the direct contribution of the transverse reinforcement to the pull-out loading and the confinement of concrete flange.

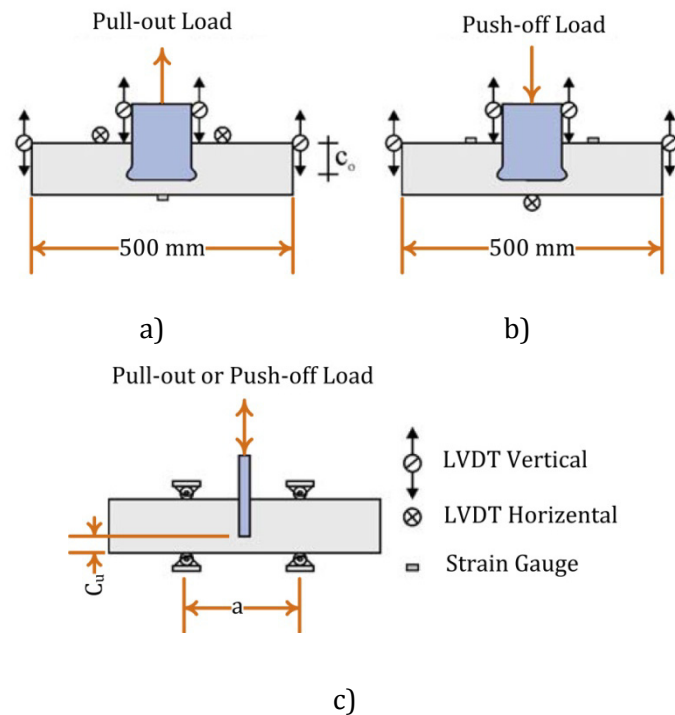


Figure 2-48: Overall configuration of composite connection: a) under pull-out loading, b) Under push-out loading, c) side view of composite connection (Hegger et al. 2009).

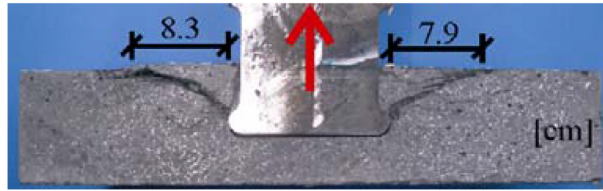


Figure 2-49: The composite connection under pull-out test after failure (Hegger et al. 2009).

The study of the composite connection constructed with the steel plate embedded in the concrete flange is important in several applications where the embedded plate experiences an in-plane compression load. The behaviour of this composite connection subjected to push-off load was studied by Hegger et al. (2009) and is shown in Figure 2-50. The variable parameter was the concrete cover underneath the embedded steel plate. It was reported that an increase in the cover from 20 mm to 30 mm resulted in 19% increase in the peak push-off load of the composite connection. Steeper crack angle was found for specimens with a larger cover.

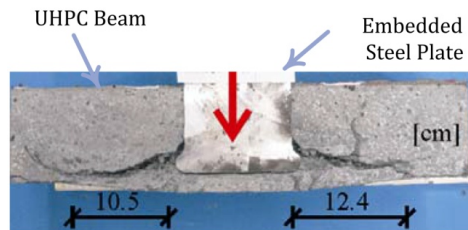


Figure 2-50: Composite connection under push-off test after failure (Hegger et al. 2009).

Chapter 3

3 Mechanical Properties of UHPFRC material: Experimental Program

3.1 Introduction

This chapter starts with the development of a unique UHPFRC mix, suitable for in-situ casting, using locally available material and between 0 and 5% volume-fraction of short steel fibers. Conventional moist curing without added heat or pressure was used to be representative of potential applications requiring in-situ casting. While numerous studies have investigated the compressive, flexural, and flexural-tensile strength of UHPFRC, emphasis on the role of the fiber volume-fraction and specimen size on these properties has not been widely considered. In addition, there is no research available which addresses the behaviour of UHPFRC subjected to direct shearing action. This chapter establishes the compressive response of UHPFRC using cylinder and cube specimens over a size range of 2. Flexural tests of un-notched prisms subjected to 4-point bending as well as shear tests of notched prisms were also completed over size factors of up to 4 and 2 respectively. In addition to the mechanical properties outlined above, the influence of UHPFRC mix composition and the energy imparted by the mixer on its rheological properties was also studied.

3.2 Mix Preparation and Development

A UHPFRC mix design using locally available materials was developed at the University of Alberta, designated as Alberta UHPFEC, based on several reference mix compositions (e.g. De Larrard 1994, Richard and Cheyrezy 1995, Habel et al. 2008). In establishing the Alberta mix, the proportions and preparation techniques were systematically varied and changes in the resulting compressive strength were used to guide further adjustments. A typical UHPFRC mix contains cement, crushed quartz sand, silica fume, superplasticizer, water and steel fibers which are briefly explained below.

3.2.1 Portland Cement

A locally produced type HE Portland cement, conforming to CAN/CSA-A3000-08, was adopted for the mix. Although other cement types were tried (Type GU, InterCem, etc.), the HE cement was found to have the best compatibility with the other mix components. The chemical properties of type HE cement that were provided by the suppliers are listed in Table 3-1.

Table 3-1: Chemical analysis of type HE cement (ASTM C 25-06)

Property	Value (%)		
	Cement	Silica Fume	Quartz Sand
SiO ₂	21	98.9	92.3
Al ₂ O ₃	4	0.131	4.42
Fe ₂ O ₃	4.4	0.073	0.9
CaO	62	0.109	1.09
MgO	3.34	0.018	0.24
SO ₃	2.08	-	0.07
Na ₂ O	0.24	0.1	0.86
K ₂ O	0.52	0.008	0.68
C	-	0.047	-
S	-	0.039	-
Loss on Ignition	1.4	0.199	0.54
Insoluble Residue	0.33	-	-

Table 3-2 lists the physical properties of the high early strength concrete (type HE) cement along with the compressive strength at the ages of 3, 7, and 28 days provided by the Lehigh Inland Cement Limited.

Table 3-2: Physical properties of type HE cement

Property	Unit	Value
Blaine	m ² /kg	406
Retained on 45μ sieve	%	5.27
Autoclave Expansion	%	0.055
Sulphate Expansion	%	0.028
Vicat Initial Set	Min.	95
False Set	%	62
Air Content	%	8.13
3 Days	MPa	19.2
7 Days	MPa	25
28 Days	MPa	37.3

Mineralogical properties analysis of type HE cement are listed in Table 3-3. In order to reduce the demand for water and thus improve the compressive strength, several researchers proposed to use cement with a C₃A content lower than 8%. Cement with C₃A content of 3% was used in the current research.

Table 3-3: Mineralogical properties analysis of type HE cement

Property	Value (%)
C ₃ S	54
C ₂ S	19
C ₃ A	3
C ₄ AF	13.5

3.2.2 Silica Fume

Silica fume is an industrial by-product with a completely spherical shape which helps to improve the rheological characteristic of the mix. Its very small particles' size can fill voids between cement particles to achieve higher packing density and thus significantly improve the microstructure of UHPFRC mix (e.g. Mazanec et al. 2010). Furthermore, silica fume is a pozzolanic material which can form Calcium-Silicate-Hydrate (C-S-H) phases by pozzolanic reaction of silica fume with calcium hydroxide (e.g. Ma and Schneider 2002, Richard and Cheyrezy 1995). Based on the manufacturer's specified properties, the chemical composition and physical properties of silica fume are given in Table 3-1 and Table 3-4, respectively. A silica fume with low carbon content should be used in UHPFRC, as the higher carbon contents increase the demand for water. The carbon content of this SF was 0.04% which is well below the proposed average of 0.5% by other researchers (e.g. Scmieth et al. 2003).

Table 3-4: Physical properties of silica fume (CAN/CSA-A23.5-M86)

Property	Unit	Value
Specific Surface Area	m^2/g	18 - 20
Specific Gravity	-	2.2
Bulk density (Undensified)	kg/m^3	250-300
Bulk Density (Densified)	kg/m^3	700
Fineness (Average Diameter)	μm	≤ 0.1
Percent Passing 45 μm	%	99 - 100
Particle Shape	-	Spherical
Form	-	Amorphous

3.2.3 Sand

The most commonly used aggregates in UHPFRC mix are quartz sand, as its desirable matrix-aggregate bond improves its mechanical properties. High-purity crushed quartz sand, commercially available in the Canadian market, with a maximum size of 1 mm was used in this research. The percentage of particles of sand retained on sieves 8, 16, 20, and 30 was respectively 3.1, 82.4, 12.3, and 2.1. Five different sand to cement ratios (S/C), S/C = 0.44, 0.5, 0.56, 0.6, 0.66, were used

to improve the packing a density of granular particles in UHPFRC matrix and enhance the compressive strength.

3.2.4 Superplasticizer

Superplasticizer is necessary to lower the water/binder ratio without sacrificing the mix workability. It also contributes to enhance durability and workability of UHPFRC(e.g. Aïtcin et al. 2000, Richard and Cheyrezy 1995). Five different types of commercially available superplasticizers (SP) were investigated in this study through a trial batch technique. A polycarboxyl-based SP with density of 1100 ± 20 kg/m³ and 30% solid content showed the best consistency for mix workability and allowed the highest compressive strength among the SP and cement combinations considered. Only mixes with this selected SP are presented in this thesis.

3.2.5 Water

A very low water to binder ratio is required for UHPFRC to gain improved mechanical properties and to avoid drying shrinkage and to improve the mechanical properties (e.g. Schmidt et al. 2003, Graybeal 2006). In this research water to binder ratios (W/B) were increased from 0.15 to 0.21 with an increment of 0.1. The optimum water to binder ratio by weight was selected to be 0.18.

3.2.6 Steel Fibers

Straight, smooth, steel wire fibers, manufactured by Bekaert Corporation, and made from hard-drawn wire with a tensile strength of 2500 MPa and elasticity modulus of 210 GPa were used, as shown in Figure 3-1. Fibers with a very high tensile strength are required in UHPFRC mix, as they are expected to transfer significant tensile stresses during the crack bridging processes in the cracked part of prism specimens. The fibers had a nominal diameter of $d_f = 0.2$ mm, a nominal length of $l_f = 13$ mm and a shape factor (l_f/d_f) of 65. No reserved tensile strength and ductility after the peak tensile strength point was reported for this type of fiber. Steel fibers are lacquered with thin brass coating to prevent corrosion during casting and curing.



Figure 3-1: Short steel fibers, $l_f=13$ mm and $d_f=0.2$ mm.

3.3 UHPFRC Mix Composition

The mix from this study is compared to the other published reference mixes in Table 1. It is observed that a higher silica fume to cement ratio was used in the Alberta mix. Further, the sand to binder ratio was smaller for the Alberta mix. These differences are both attributed in part to the selected use of 1 mm downgraded sand aggregate in the Alberta mix whereas the reference mixes typically had uniform particle sizes with a maximum dimension of 0.5 mm.

Table 3-5: UHPFRC composition normalized by mass of cement

Components	Current Study	Ref-I [†]	Ref-II [‡]	Ref-III [‡]
Portland Cement (HE)	1.00	1.00	1.00	1.00
Silica Fume (SF)	0.35	0.26	0.25	0.31
Fine Sand	0.56	0.70	1.10	0.75
Added Water	0.19	0.23	0.17	0.18
Superplasticizer (SP) *	2.10%	1.50%	1.6%	1.3%
Total Water ^{**} /Binder ^{***}	0.18	0.20	0.14	0.14
Compressive Strength (MPa)	140	121-128	130-160	165

* Solid content of SP, **Total water=Added water + water from SP, ***Binder=cement+SF

[†]Habel et al. (2006), [‡]Richard and Cheyrezy (1995), [‡]De Larrard and Sedran (1994)

3.4 Mixing, Sampling and Curing

3.4.1 Mixing

A high performance pan mixer was used to achieve a homogenous UHPFRC product which leads to improved strain hardening response and enhances its average compressive, shear and tensile strength. The mixer has a rotating tilted mixing pan with selectable speed, an eccentrically placed counter-rotating mixing tool (i.e. rotor) with separately adjustable speed and a stationary scraper tool, which prevents material build-up at the walls and floor of the pan, as shown in Figure 3-2.



Figure 3-2: High performance mixer with inclined pan.

The electronic control panel for the mixer continuously records the power usage during mixing as well as variations in mix temperature. The mixing sequence and mixer speed were established through trial batches, and the final procedure is reported in this section. The quartz sand, cement and SF were initially dry mixed for 3 minutes, as the fine cementitious material tends to agglomerate and form chunks once the water was added. Next, all of the mixing water was gradually added over a 30 second period to distribute the water uniformly throughout the mix (point I in Figure 3-3).

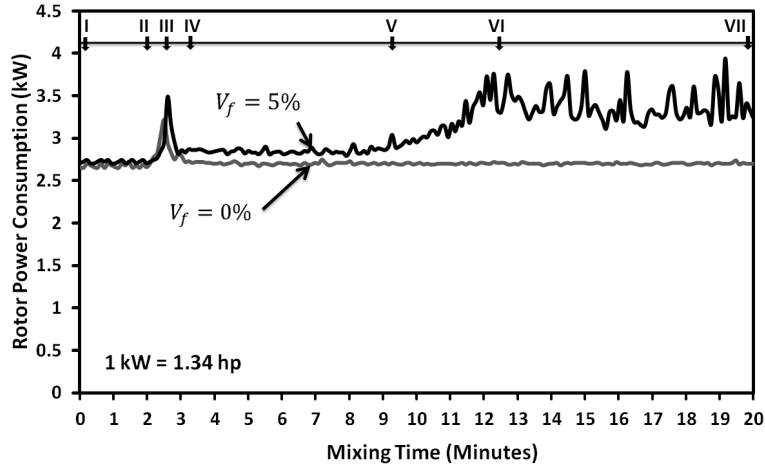


Figure 3-3: Material addition and corresponding power consumption during the UHPFRC mixing.

After about 2 minutes from the start of adding the water (point II), 50% of the SP was added over 30 seconds. The remaining SP was added one minute later (point IV) and the mixing continued for an additional 6 minutes. Compared to a direct SP addition method where the SP was dissolved in the water at the beginning, higher consistency and compressive strength was achieved by using this stepwise addition of SP to mix after the water was added. Other researchers proposed to add SP at a different stage. For example, Tue et al. (2008) proposed to add SP gradually. Wille et al. (2011) added whole SP at once after the water was added. Finally, the steel fibers were added 9 minutes from the start of mixing (point V). Fibers were slowly added over a period of 2 minutes to prevent fiber balling, as shown in Figure 3-4. The total mixing time was 20 minutes from the start of adding water to the mix. The minimum required mixing time is dependent on the energy imparted by the mixer, the fiber volume-fraction (V_f), and the chemical and physical characteristics of the mix components. The temperature at the start of mixing was about 17°C and at the end was between 18.5-21.5°C for V_f up to 3% and between 26.5-28.5°C for $V_f = 4-5\%$.

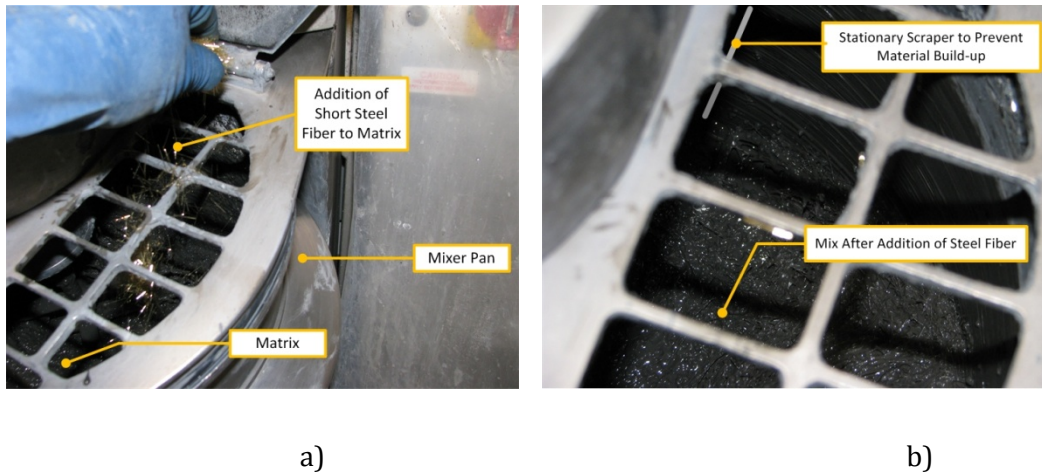


Figure 3-4: a) Addition of steel fibers to mix, b) Finished UHPFRC mix.

3.4.1.1 Mixer Energy

The power consumption of the mixer rotor is presented in Figure 3-3 for the cases of two identical mixes varying only by the fibre-volume fraction (i.e. $V_f = 0$ and 5%). The mass and volume of each mix were 13.5 kg and 4.5 litres respectively. All batches were mixed using a constant rotor speed of 30 Hz, and thus the energy input to the rotor varies in Figure 3-3 depending on the mix viscosity at different times in the mixing sequence. According to recent research (e.g. Schießl et al. 2010) once water is added to a mix, water bridges are immediately formed between adjacent grains, attempting to cover as much grain as possible. The mix appeared to be wet but not liquid in this stage (point I to II). Once the SP was added to the mix, the capillary forces between the small particles tend to increase rapidly until the maximum power consumption is reached (e.g. Schießl et al. 2010, Goldszal and Bousquet 2001). See point II to III. In this period the mix seems to be completely wet. At the peak point (point III), most of the particles are partially surrounded by water, which tends to decrease the capillary forces. As a result, the power abruptly drops until a plateau is reached (point III to IV). This plateau can be attributed to the observed homogenized mix which had a creamy appearance. The increase in power consumption occurring after point V in the mix with $V_f = 5\%$ resulted from the gradual addition of the fibers. This was followed by fluctuations in the energy consumption, which were more pronounced in the mixes with higher fiber volume fraction. The peak power consumption at point VI was found to linearly increase

with increasing V_f , as shown in Figure 3-5. Compared to the plain mix without fibers, the peak energy level was 24% higher for the mix with $V_f = 5\%$.

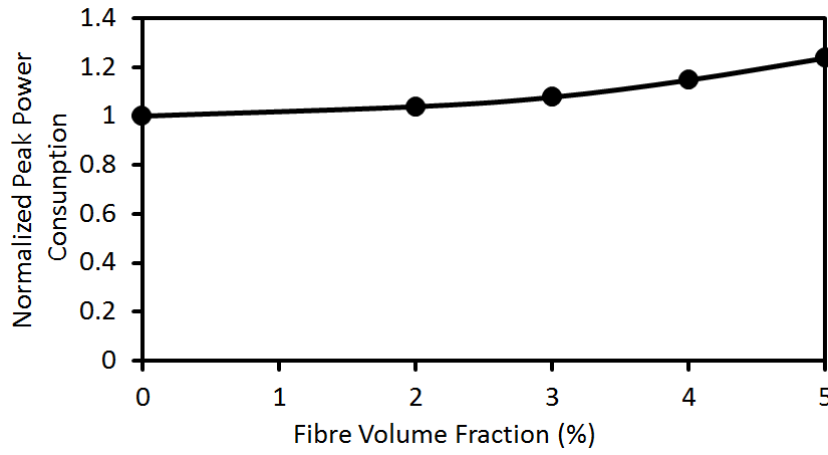


Figure 3-5: Relation between normalized peak power consumption of mixer and fiber volume fractions.

3.4.1.2 Workability

An objective of this study was to develop a self compacting mix with V_f between 0 and 5%. During development of the matrix composition using mixes with $V_f = 0\%$, the slump flow of the fresh concrete was measured using a mini-slump cone adapted from Kantro (1980) on a flow table. The truncated cone had a height of 57 mm and lower and upper diameters of 38 and 19 mm, respectively, as shown in Figure 3-6.

The workability of the mix is characterized by the size of the initial pat formed after lifting the cone and after the flow table was dropped twenty times within 20 seconds with an amplitude of 12.5 mm. A similar test procedure was completed by other researchers (e.g. Goldszal and Bousquet 2001). The test was repeated on 300 mixes with $W/B = 0.18$. An initial pat size of 84 mm with a coefficient of variation (COV) of 11% was observed for the $V_f = 0\%$ mix reported in this thesis. An average pat size of 96 mm with a COV of 10% was recorded at the end of dropping. These values suggested self-compacting characteristics for the matrix.

A series of slump tests were carried out to investigate the influence of the water/binder (w/b) ratio on workability of UHPFRC. All the results were

normalized with respect to pat diameter, d_p , of mix with $W/B = 0.18$. As presented in Figure 3-6, the tap diameter tends to linearly increase with the increase in w/b ratio from 0.16 to 0.21.

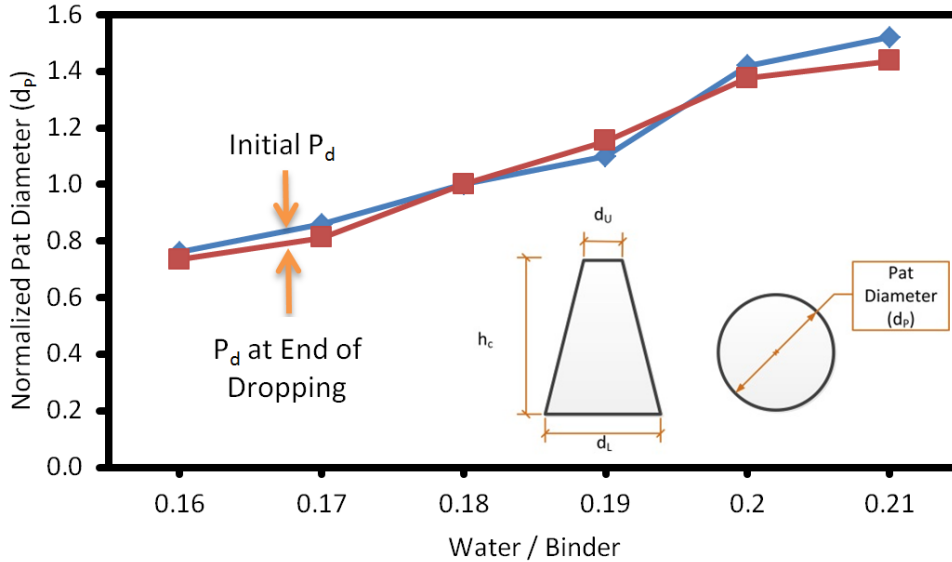


Figure 3-6: Pat diameter of UHPFRC matrix and slump test in accordance with ASTM C 230/ C 230M-03.

Based on Wille et al. (2010), the mini-slump cone test cannot be used reliably for the mixes with steel fibers. Instead, a fiber factor was used to evaluate the workability of the UHPFRC. A maximum V_f of 3 to 4 % was suggested by these researchers as an upper limit, to allow for a workable mix. In the current study it was visually noted that mixes with $V_f \leq 4\%$ present a proper level of workability in terms of both casting and finishing. A maximum addition of 5% was achieved based on the capabilities of the mixer used.

3.4.2 Placement

The fresh mix was poured into prisms in three equal layers from one end of prism to the other with an average rate of 75 mm/sec (See Figure 3-7). Consistent method of casting was used, as this would influence the fiber orientation and mechanical properties of UHPFRC. The steel fibers tend to align in the flow direction of fresh UHPFRC mix which is mainly influenced by the flow profile developed by the

frictional restraint provided by the surfaces of mould (Grenier 2006 and 2007; Reineck and Frettlöhr 2010).

Cube and cylinder molds were filled up in one stage. Even though the mix was considered self-compacting based on a slump flow test, some molds were vibrated on a shaking table operating at a frequency of 150 Hz for 90 seconds (Each layer of prism samples was individually vibrated for 30 seconds) to further improve the mix consolidation. Of the smaller cubes (CU-50), cylinders (CY-50) and prisms (PF-50 and PS-50), half were vibrated during fabrication while the remaining similar samples were not vibrated to allow evaluation of the consolidation influence on the compression, flexural, and shear response. All larger prisms, PF-100, PF-150, and PF-200, were vibrated.



Figure 3-7: Top view of casting method.

3.4.2.1 Fiber Orientation

The fiber distribution pattern was visually investigated along the fracture surfaces after the compression, flexural, and shear tests were completed. Fibers were observed to be distributed in random directions in both cube and cylinder samples used for compression tests (See Figure 3-8), with some alignment occurring near specimen edges due to the so-called wall effect. However, the majority of the fibers were oriented parallel to the direction of the flexural-tensile strain (i.e. longitudinal direction) in both PF-50 and PF-100 due to the layered casting method described earlier. All the prisms were rotated 90 degrees around the longitudinal axis during the flexural and shear test.

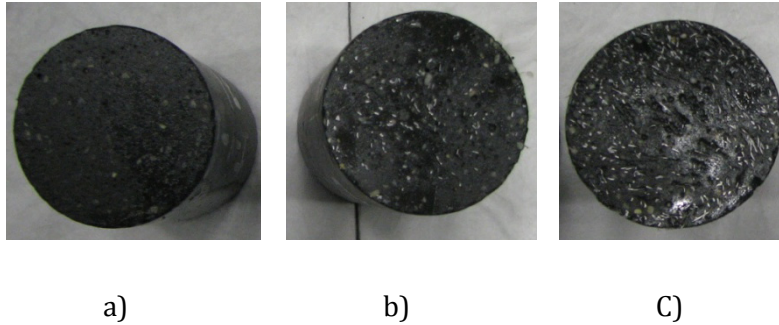


Figure 3-8: Fiber dispersion at the top surface of ground CY-50 cylinder specimen including a) $V_f = 0\%$, b) $V_f = 2\%$, and c) $V_f = 4\%$.

3.4.3 Curing

Conventional moist curing without added heat or pressure was used for all specimens to be representative of potential applications requiring in-situ casting. All samples were covered with plastic sheeting immediately after casting and then placed in a room with a controlled temperature of $23 \pm 2^\circ\text{C}$ and relative humidity of 100% to minimize potential surface shrinkage and cracking. Specimens were demolded 19-24 hours after casting and remained in the curing room until testing.

3.5 Specimen Geometry and Test Set-up

3.5.1 Compressive Strength

The compressive strength of 50 and 100 mm cube specimens, designated as CU-50 and CU-100, were determined in accordance to ASTM C109. The 50, 75, and 100 mm diameter cylinder specimens, designated as CY-50, CY-75, and CY-100, were tested according to ASTM C39. A 2600 kN capacity MTS Universal Loading Frame was used to perform the compression tests on both cubes and cylinder specimens according to ASTM C39-09a. All of the quality control specimens (CU-50) were tested subjected to quasi-static loading using the Forney machine (FX-700) with the capacity of 3600 kN at the concrete research laboratory at the University of Alberta. For each UHPFRC mix design, at least three specimens were cast and tested and the average of the results was used in the discussions below.

3.5.1.1 End Grinding

The cylinder end surfaces were not capped with sulphur capping compound, as the maximum strength of capping material was well below the peak compressive strength of UHPFRC. Instead, all cylinder samples were end-ground by a surface grinding machine at the concrete research lab of the University of Alberta to produce flat end surfaces. The concrete cylinder is held on a V-shaped jig which keeps the specimen perpendicular to the side of a grinding wheel and is passed against the revolving wheel. The ends were measured using a digital dial gauge checked at the end of the process to make sure neither end of the test specimens depart from perpendicularity to the axis by more than 0.5° (1 mm per 100 mm), proposed by the ASTM C-39 standard. This process helps to: (1) assure that both sample ends during the compression test experience uniform compressive stresses, and (2) improve the test results consistency. All the cylinder specimens were prepared a week before their scheduled compression testing time.

3.5.1.2 Loading Protocol

The displacement controlled loading rate applied to both cube and cylinder samples was 0.5 mm/min which is equivalent to a rate of 1 MPa/s . While this rate is higher than the value specified in the corresponding ASTM standards, other research showed that variations in the loading rate between 0.24 to 1.7 MPa/s resulted in less than 3.5% change in the compressive strength for UHPFRC (e.g. Graybeal 2008). The use of displacement control allowed the compressive response to be captured in the post-peak range.

The compressive test fixture is illustrated in Figure 3-9. The setup consists of top and bottom aluminum yoke which are temporarily held in place by bracing at distances of 50 mm, 75 mm, and 100 mm apart from each other in the CY-50, CY-75, and CY-100 samples respectively. The load was measured by a load cell attached to a MTS 2600 kN testing machine, while the axial deformation was measured with three linear variable displacement transducer (LVDTs) mounted on the yokes, with 120-degree separation between individual LVDTs. The full compression stress-strain curve, including the post-peak response, was determined from three identical

cylinder specimens. Average results were used to study the influence of fiber content, specimen size, and time development on compressive strength.

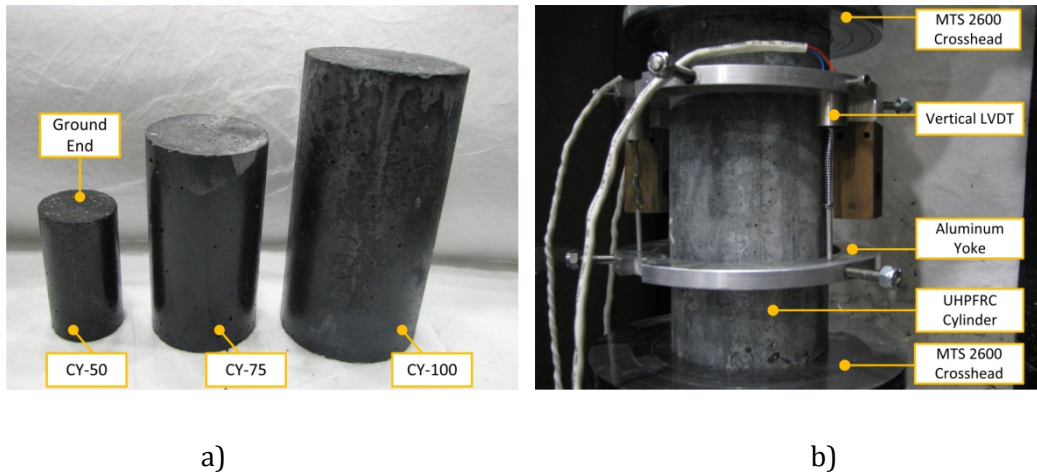


Figure 3-9: (a) Compression cylinder specimens including (right to left) CU-100, CU-75, and CU-50, (b) ASTM C39 compression test setup using a yoke with 3 LVDTs at 120° to measure axial stress-strain response.

3.5.2 Flexural Strength

The flexural properties of the UHPFRC were evaluated using un-notched prism specimens tested subjected to third-point loading in accordance with ASTM C1609 and ASTM C1018, as shown in Figure 3-10. As an alternative to the un-notched prism specimen, the notched one can be used. However the flexural behaviour of notched prism specimens was reported to be significantly influenced by the presence of notch, as it forces the crack to be formed in the cracked location (e.g. Chanvillard 2002, Habel 2004). The flexural tests are conducted in a MTS-1000 Universal Testing Frame equipped with hydraulic grips, having an actuator range of 150 mm and a maximum load capacity of 1000 kN. Two sets of casting were completed at two different time intervals. Considerable attention was given to the mixing and casting procedure since this would have a direct influence on the mechanical response. The only difference was the measurement method, where LVDTs only were used to measure the mid-span deflection during the first series of testing (Phase-I), and LVDTs and DIC system was both used in the second series of testing (Phase-II).

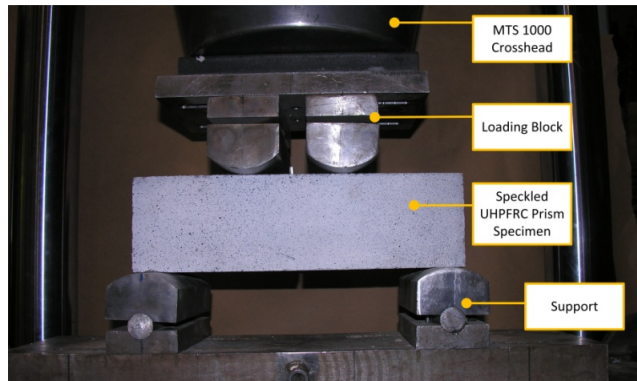


Figure 3-10: Test set-up of flexural test.

3.5.2.1 Specimen Size

Figure 3-11 shows the geometry and range of four different prism specimen sizes that were used to examine the size effect in flexure: 143 prisms had cross-section dimensions of 50×50 mm and a span of $L = 150$ mm, designated as PF-50; 38 prisms had cross-section dimensions of 100×100 mm and a span of $L = 300$ mm, designated as PF-100; 11 prisms had cross-section dimensions of 150×150 mm and a span of $L = 450$ mm, designated as PF-150; and 9 prisms had cross-section dimensions of 200×200 mm and a span of $L = 600$ mm, designated as PF-200. The complete list of prism samples (total of 201 prisms) is provided in Table 3-6.

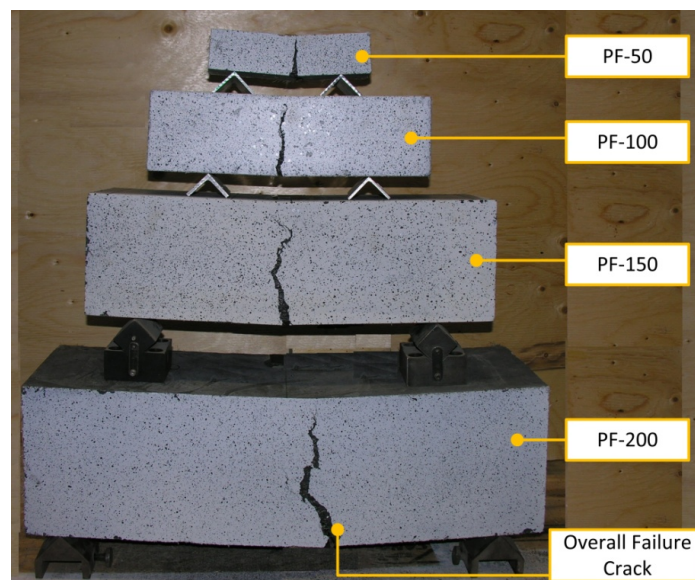


Figure 3-11: Flexural prism specimen samples including (top to bottom) PF-50, PF-100, PF-150, and PF-200.

Table 3-6: As-built prism specimen properties for flexural test

Specimen	Height (mm)	Width (mm)	Span (mm)	V _f (%)	V/N-V	SF/B	No. of Samples	
PF-50	50	50	150	0	V	0.22	3	
					NV		3	
					V	0.24	3	
					NV		3	
					V	0.26	20	
					NV		3	
				2	0.26	V	72	
						NV	3	
				3		V	3	
						NV	3	
				4		V	18	
						NV	3	
				5		V	3	
						NV	3	
PF-100	100	100	300	0		V	0.26	6
				2				6
				4				6
PF-150	150	150	450	0		V	0.26	4
				2				4
				4				3
PF-200	200	200	600	0	V	0.26	3	
				2			3	
				4			3	

3.5.2.2 Loading Protocol

All the flexural tests are conducted under displacement control. The specimen was loaded from the bottom with two semicircular cylinders spaced 150 mm, 300 mm, 450 mm, 600 mm apart and the top of the specimen was supported by two semicircular cylinders spaced 50 mm, 100 mm, 150 mm, and 200mm apart for PF-50, PF-100, PF-150, and PF-200 respectively. A relatively slow, quasi-static loading rate was used until a clear maximum peak load (MPL) was reached, then to speed up the test time, a higher loading rate is used to complete the test process. The loading

rates for different prism sizes are listed in Table 3-7, conforming to the requirements of ASTM C1609. The gap between the prism surfaces and bottom and top supports were filled with multiple thin steel shim plates to avoid the torsional stresses at samples. The proper shimming was found to be more critical in samples with no steel fibers.

Table 3-7: Rate of flexural loading

Prism Specimen	Rate of Loading (mm/min)	
	P<MPL	P>MPL
50	0.050	0.075
100	0.050	0.075
150	0.075	0.100
200	0.075	0.100

MPL: maximum post-cracking load

3.5.2.3 Instrumentation

MTS 1000 Load-Stroke Measurement

The MTS 1000 universal testing machine provides an accurate record of axial load force along with the overall stroke of the entire test set up. The results of axial deformation were not used in the development of the load-deflection response of UHPFRC prisms, as the softening of the test setup is also included in recorded deformation. Instead the axial deformation was measured with external LVDTs, which is explained below.

Standard Yoke System

A yoke was fabricated in accordance with JSCE G-552 (1999). As shown in Figure 3.12, the yoke was installed on both sides of the prism specimens to hold LVDTs, one on either side. This yoke ensured that the measured displacement reflect the net in-plane deflection at the neutral axis and eliminated any errors due to support settlement. A pair of LDVTs was mounted on both sides of the prism specimens to minimize the measured errors. The load and displacement histories were recorded with the aid of an electronic data acquisition system at a sampling rate of 5 Hz. All the LVDTs were calibrated prior to testing.

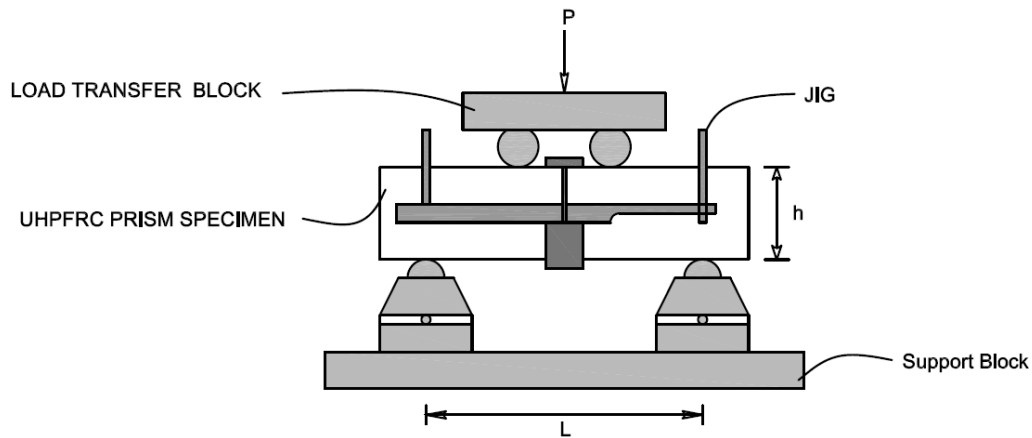


Figure 3-12: Schematic of flexural test setup.

Three-Dimensional Digital Image Correlation System

The digital image correlation (DIC) system is a pattern recognition technique where two images are compared to obtain the relative displacement between them. This method is widely used for full-field analysis of strain and displacements in solid mechanics by monitoring the motion of the speckle pattern over the surface of the specimen before and after the deformation. A three-dimensional DIC system with two high-resolution digital cameras was used in this research to perform a non-contact measurement of in-plane deformation and crack growth in the UHPFRC prism on the basis of the principle of digital image correlation. Figure 3-13 shows a typical setup of the DIC technique. The DIC method employs the results of actual object movements to generate the Lagrangian strain tensor at every single point on the surface of the prism specimen.

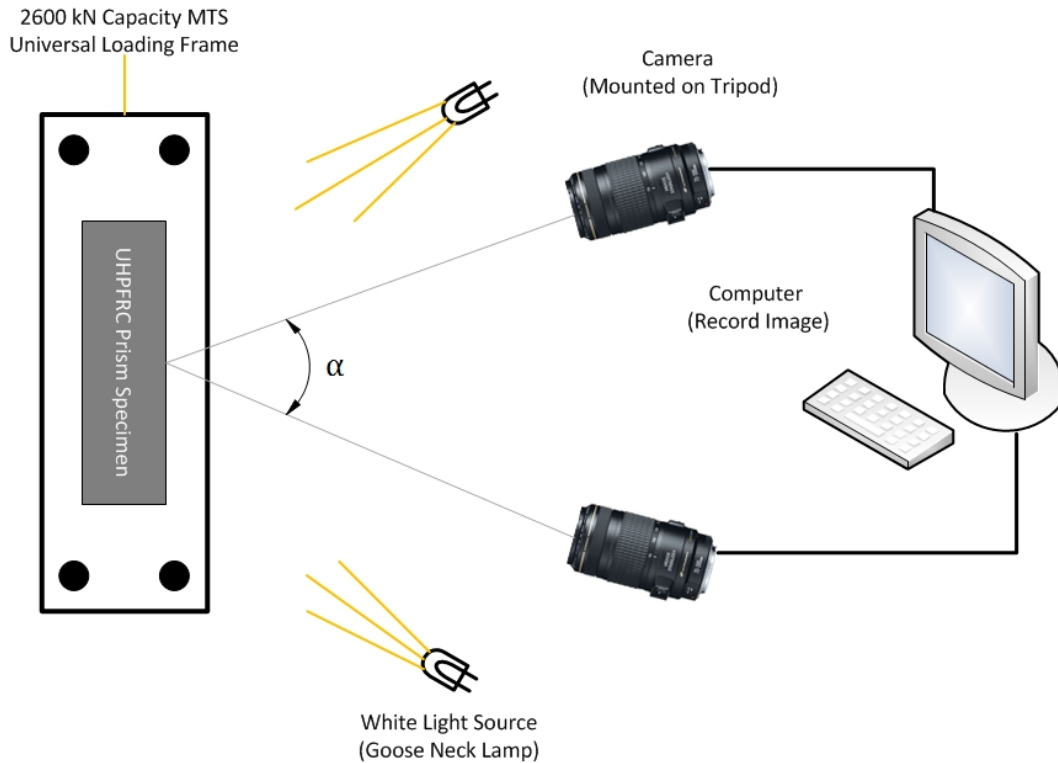


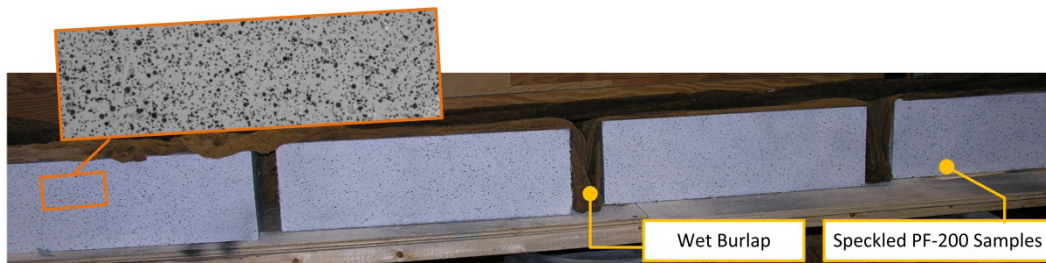
Figure 3-13: Experimental setup of digital image correlation (DIC) system.

Speckle Pattern

The Front face of each prism specimen was painted with a flat white latex paint, as shown in Figure 3-14(a). A random speckle pattern was then applied to the painted surface of the specimen using a flat black spray paint, as shown in Figure 3-14 (b), to produce small circular black dots covering approximately 50% of the specimen's surface. All the specimens were cured under wet burlap and plastic immediately after painting was completed. The mean speckle diameter was measured to be approximately as 3 mm and the spacing was 3-5 mm. Each of the dots in the camera is approximately 4-5 pixels in size, which is ideal for commercial software. The finer patterns are very sensitive to defocus and make the deformation tensor most sensitive to change during the image processing analysis (Correlated Solutions Inc. 2010).



a)



b)

Figure 3-14: a) Painted specimen, b) Black speckling on the front surface of prism.

Digital Camera

Two 5-Megapixel digital cameras from Point Grey Research with 35 mm focal length lenses (Fujinon Corporation 1:1.4/35 mm) and a maximum resolution of 2448 (vertical) x 2048 (horizontal) pixels are employed to photograph the surface throughout the test at specified intervals. Cameras were placed at an approximate distance of L_c from the prism specimens to capture the full length of specimen. See Table 3-8. Measurement resolution was increased by decreasing the area of the captured image. The captured images are completely composed of shades of gray, varying from white at the strongest to black at the weakest intensity. Two 250 W halogen lights were mounted on poles next to the two cameras and provided adequate and even light for the images (see Figure 3-13).

Table 3-8: Location parameters of camera

Prism Specimen	L_c	Angle between cameras (α)
PF-50	1.5	16
PF-100, PF-150, Pf-200	2.8	9

Image Acquisition

Vic-Snap software (Correlated Solutions Inc., 2009) recorded pairs of images every 1 second during the test on the prism with $V_f=0\%$ and every 3 seconds on the prism specimen with $V_f = 2$ and 4% . At the same time, applied load and data from LVDTs were recorded.

Image Processing and Analysis

After the test was completed, an automated digital image processing software package, Vic-3D digital image correlation software from Correlated Solutions, was used to correlate images and to extract the displacement field for each load increment in a 3D spatial field. For each individual flexural test, a reference image was selected at a preload force of 0.5 kN and each subsequent image was correlated from the reference one. The images at each load increment are then divided to small subsets of gray level data. Each subset from the loaded image is selected and mapped to the reference image. The gray levels for each of the pixels in the original subset are then compared with the gray levels at their mapped location in the second image using a cross-correlation error function and the parameters of the mapping function are optimized to reduce the error function to its minimum using an optimization technique. This process is repeated for all of the other subsets in the area of interest, resulting in a full-field map of the surface displacements. Additional information of the DIC method, including correlation parameters and resolution, can be found in the Correlated Solutions Inc. manual. (2009).

Mid-Span vertical deflection

The vertical deflection at mid-span of the flexural prism specimen was calculated as follows:

$$\delta = \delta_{ms} - 0.5(\delta_{sl} + \delta_{sr}) \quad (3-1)$$

Where δ_{ms} is the mid-span vertical deflection from the DIC measurement point. See Point M-M in Figure 3-14. δ_{sl} and δ_{sr} are the vertical deflections from the DIC measurement point located at mid-height of the prism specimen at the left (Point S-L) and right support (Point S-R) respectively.

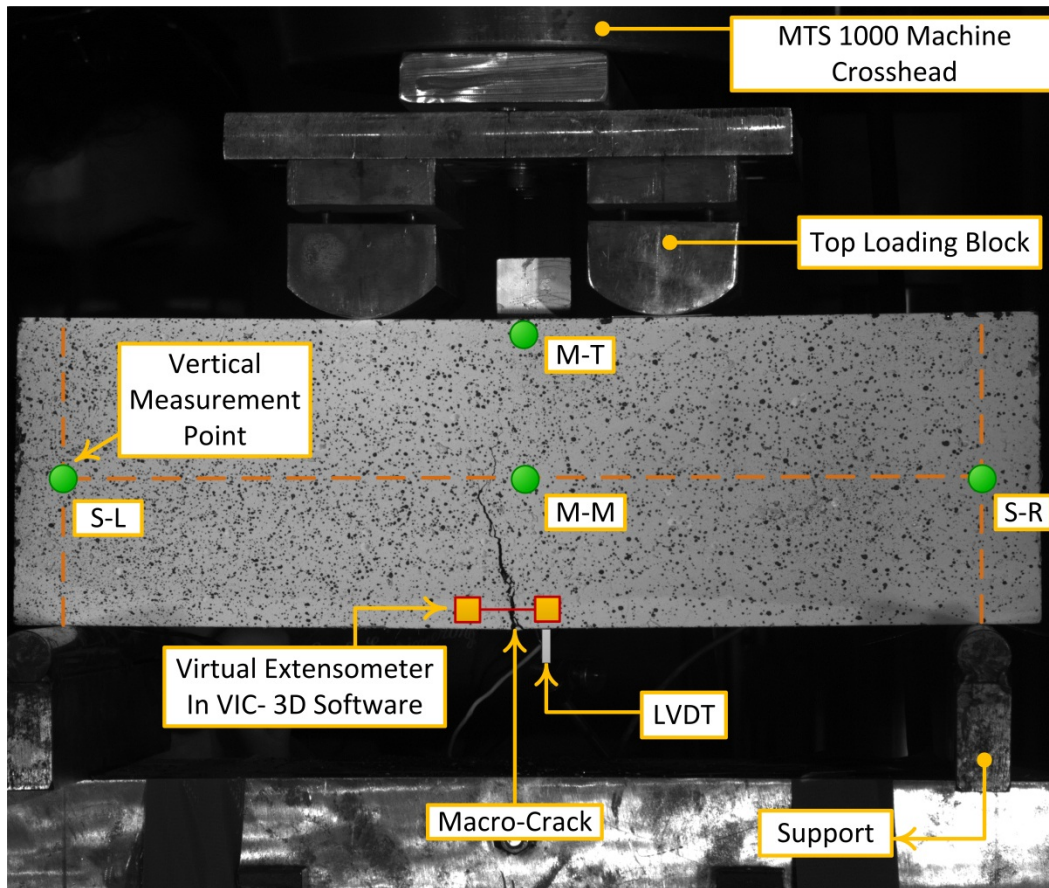


Figure 3-15: Vertical measurement points and virtual extensometer location in the VIC-3D software.

LVDT Measurement

A thin rectangular aluminum plate was epoxied on the top surface of the prism specimens at the mid-span locations to provide a measurement support for vertical LVDTs. See Figure 3-16. A pair of vertical LVDTs was mounted on a magnetic base with a high degree of movement that helped to position the LVDTs in right position. Two LVDTs with ± 12.5 mm of travel were used. Figure 3-16 illustrates the test setup and LVDT location at the back side of prism samples.

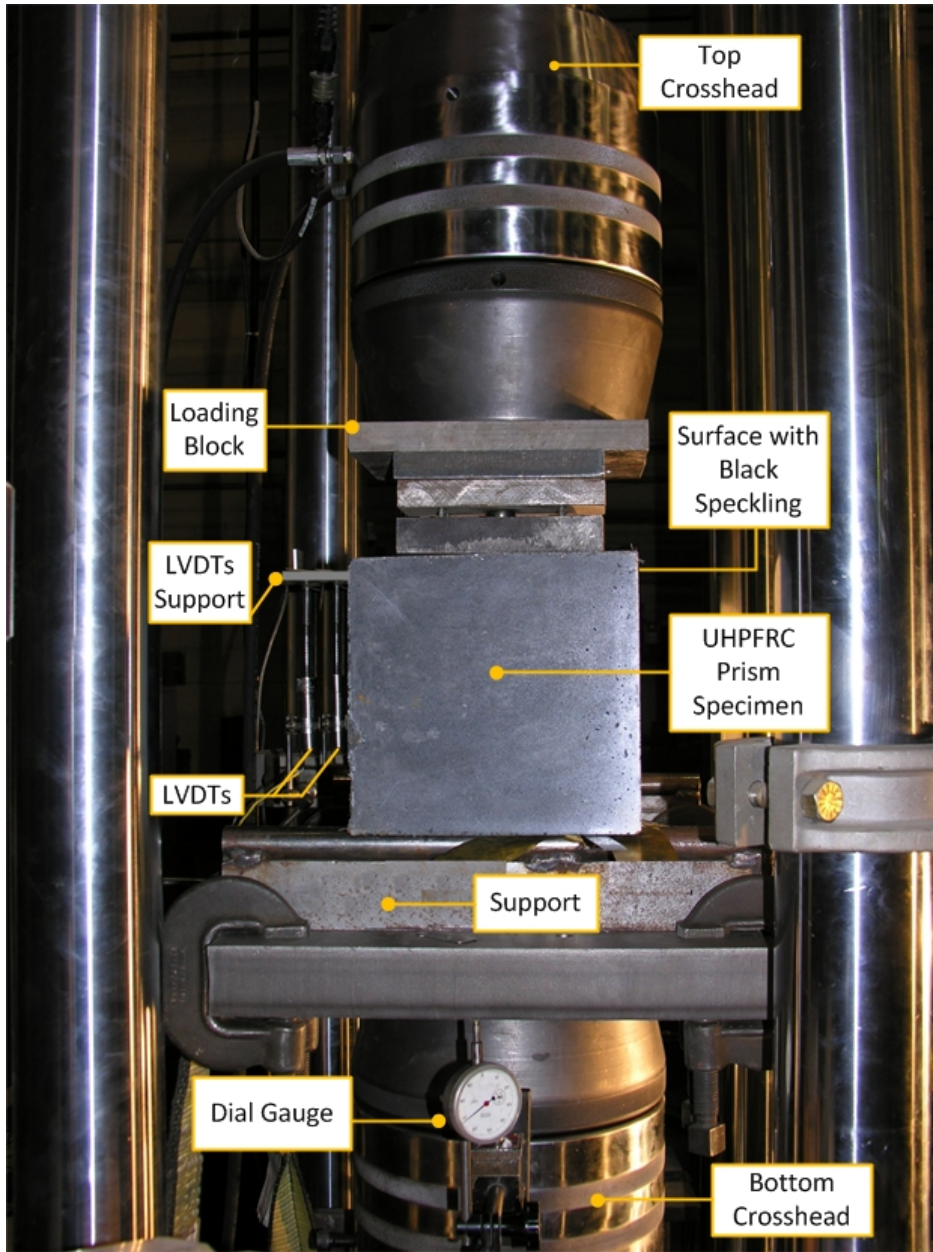


Figure 3-16: Side view of ASTM C1609 flexural test setup with two LVDTs mounted on back side of prism specimens.

3.5.3 Shear Strength

The direct shear strength of UHPFRC was measured through a test procedure adapted from section 2.1.4 of JSCE-G 553-1999 standard (1999). The shear tests were performed on prism specimens of two different sizes, width×height×length, of 50×50×150 mm, designated as PS-50, and 100×100×300 mm, designated as PS-100. All the specimens are listed in Table 3-9. Two double knife-edged loading blocks, which were respectively 50 and 100 mm apart for PS-50 and PS-100 prism specimens were used to apply two equal point loads on the specimen. Each specimen was supported by a pair of knife edges on the bottom side. The prism specimens were notched all the way around using a diamond cutter to make two planes with reduced cross-sectional areas ensuring that the fracture plane occurred in the prescribed locations. The schematic of fracture sections are illustrated in Figure 3-17 (b). To avoid the torsional effect, all the gaps between the plane of edges and UHPFRC surfaces were filled with shim plates. The nominal heights of the notched sections, h_n , were 30 and 50 mm for PS-50 and PS-100 respectively.

Table 3-9: As-built prism specimen properties for direct shear

Specimen	Height (mm)	Width (mm)	Span (mm)	Notch Depth (mm)	Notch Thickness (mm)	V_f (%)	V* or N-V**	No. of Samples
PS-50	50	50	150	30	3	0	V	3
							NV	3
						2	V	3
							NV	3
						3	V	3
							NV	3
						4	V	3
							NV	3
						5	V	3
							NV	3
PS-100	100	100	300	50	5	0		3
						2	V	3
						4		3

*V: Vibrated Mix Design; **N-V: Not-vibrated Mix Design

3.5.3.1 Loading Protocol

All the direct shear tests are conducted under displacement control. Loading was applied under displacement-control at a rate of 0.01 mm/s as an equivalent rate for 0.075 MPa/second as per JSCE-G553-1999 (1999). As illustrated in Figure 3-17 (a), the mid-part deflection at the bottom side of the prisms was measured through two LVDTs which are mounted on both sides of the prism.

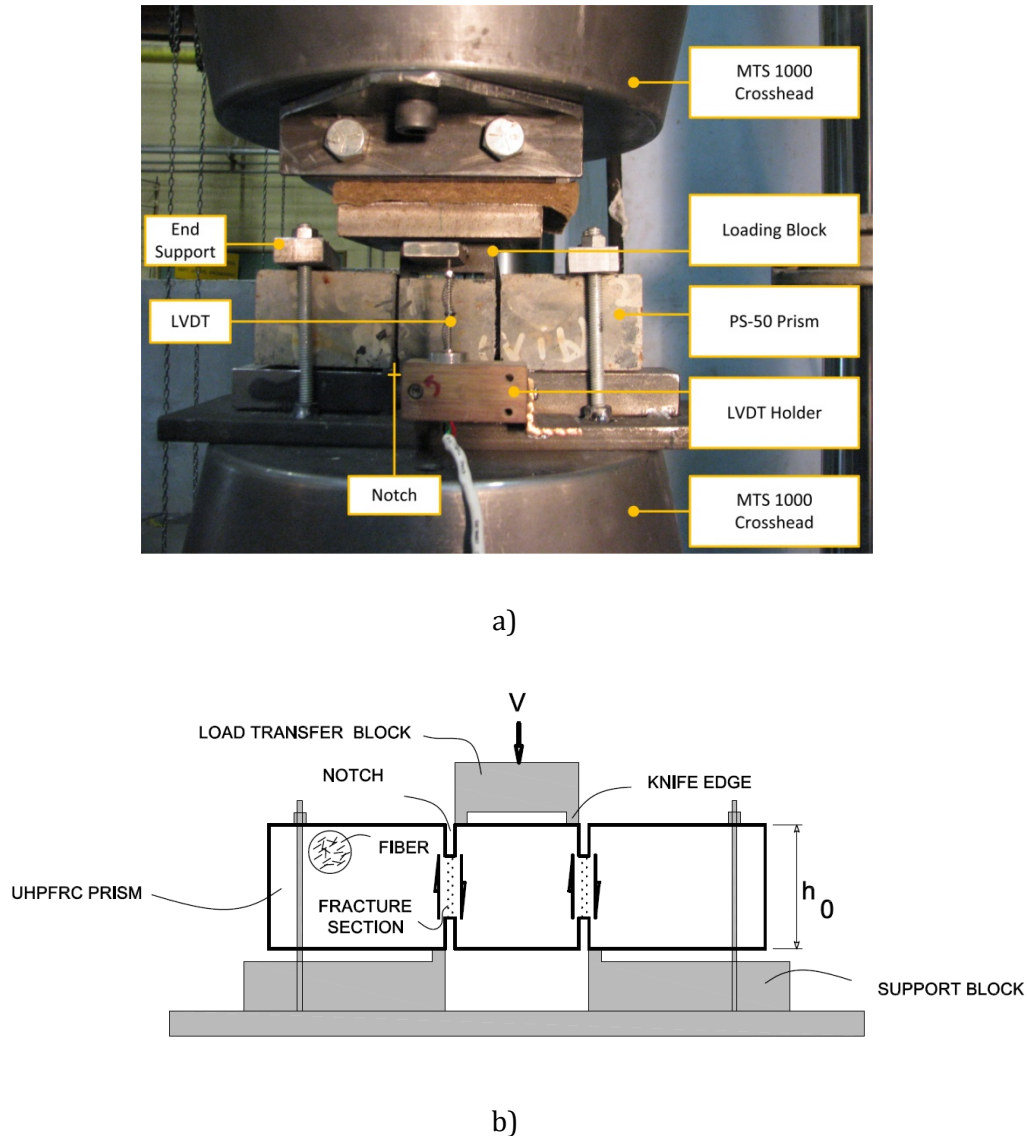


Figure 3-17: a) Direct shear test set-up in MTS 1000 machine, b) Schematic of test set up.

Chapter 4

4 Mechanical Properties of UHPFRC Material: Test Results and Discussion

4.1 Introduction

A detailed understanding of the mechanical properties of the UHPFRC material is required to efficiently use its available capacity and satisfy the performance requirements of structural members. While numerous research studies have investigated the compressive and flexural-tensile strength of this type of concrete, emphasis on the role of the fiber volume-fraction, V_f , and specimen size on these properties has not been widely addressed (Richard and Cheyrezy 1995, Chanvillard and Rigaud, Graybeal 2003, Rossi and Arca 2005, Graybeal 2006). In addition, there is no research available which addresses the behaviour of UHPFRC subjected to direct shearing action. This chapter establishes the compressive response of UHPFRC using cylinder and cube specimens over a size range of 2. Flexural tests of un-notched prisms subjected to 4-point bending as well as shear tests of notched prisms were also completed over a size range of 4 and 2 respectively. In all cases, three companion vibrated 50 mm cube specimens (CU-50) tested in compression at either 28 days or the same days of test were cast from each mix. The average strength of these cubes served as a reference strength parameter to allow correlation between the other response parameters evaluated. A back-analysis technique was used to derive the equivalent tensile mechanical properties relative to the crack mouth opening displacement.

4.2 Compression Response

The size dependent mechanical properties of the developed ultra-high performance

fiber reinforced concrete (UHPFRC) containing up to 5% volume-fraction of short steel fibers were investigated and the results are briefly discussed in the following subsections.

4.2.1 Stress-Strain Response

Typical compressive stress–strain curves of the UHPFRC are shown in Figure 4-1 for the three different cylinder diameters studied at fiber volume-fractions of $V_f = 0, 2,$ and 4%. The curves are offset horizontally to avoid overlap since the initial slopes of each curve are similar. The conditions of the specimens before loading and after failure are shown in Figure 4-2 (a-f) for CY-75 and CY-100 respectively. A brittle behaviour with a sudden drop in the load-carrying capacity of $V_f = 0\%$ mix was observed at a strain of 0.4% (see Figure 4-2 (b and e)). Similar results were reported by other researchers (e.g. Rossi et al. 2005; Graybeal 2008). Unlike the plain mix with a very brittle nature of compressive failure, mixes with steel fibers exhibited a strain hardening behaviour which is followed by a gradual rather than abrupt post-peak response, as shown in Figure 4-2 (c and f). This behaviour is mainly due to the fiber bridging effect that: 1) redistributes stress and involves the cracked part to sustain higher compression load; 2) retards the process of microcrack initiation and propagation. This leads to considerable axial deformations subjected to compression loading until the complete failure loading is reached. As presented in Figure 4-1, the hardening part of the curve is more pronounced for mixes with higher V_f , due to the improved stress transfer mechanism through the multiple microcracks. The slope of the post-peak softening branch in Figure 4-1 tends to decrease as V_f increases which would lead to higher energy absorption capacity.

The modulus of elasticity (E) of the UHPFRC was calculated using the initial linear part of the stress-strain response in compression between points located at approximately 10 and 40% of the maximum peak load. An average modulus of elasticity of $E = 40$ GPa was found for Alberta UHPFRC that is almost similar for all specimen sizes and fiber contents. Similar results were reported for UHPFRC by other researchers in North America (e.g. Graybeal 2006).

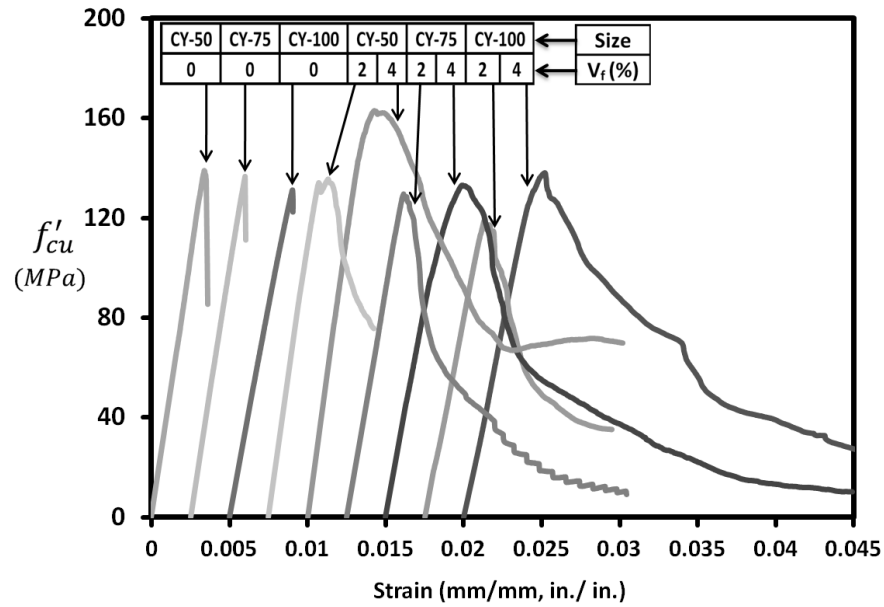


Figure 4-1: Typical stress-strain curves from compression tests of different cylinder sizes.

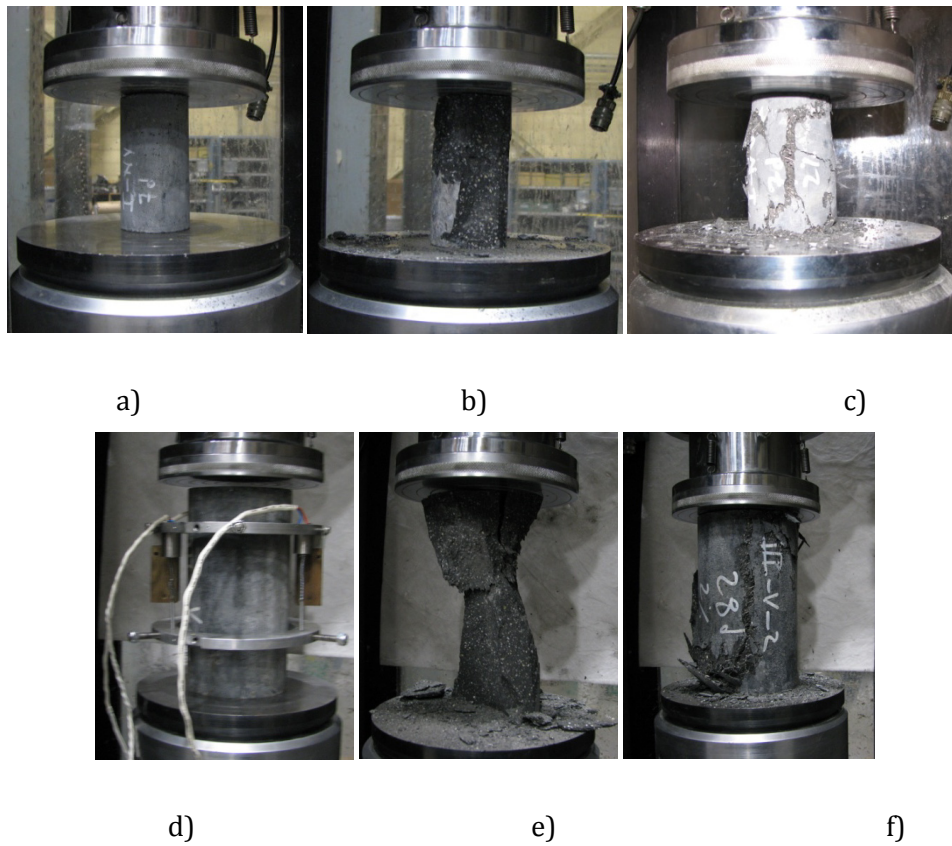


Figure 4-2: Typical failure mode for (a) CY-75 before loading, (b) CY-75 with $V_f = 0\%$, (c) CY-75 with $V_f = 2\%$, (d) CY-100 before loading, (e) CY-100 with $V_f = 0\%$, (f) CY-100 with $V_f = 2\%$.

4.2.2 Influence of Sand to Cement (S/C) ratio

The influence of five different sand to cement (S/C) ratios on the normalized compressive strength of UHPFRC CU-50 samples are shown in Figure 4-3 for three different SF/B ratios, i.e., SF/B = 0.22, 0.24, and 0.26. All the peak compressive strength of CU-50 was normalized by f'_{cu} of mixes with a sand to cement ratio of 0.56 and an SF/B = 0.26 which was found to have the highest compressive strength among other ratios. This is mainly due to an improvement in the packing density of granular particles in the matrix. (Pfeifer 2010). The ratio of S/C 1:0.56 was selected for the rest of this project.

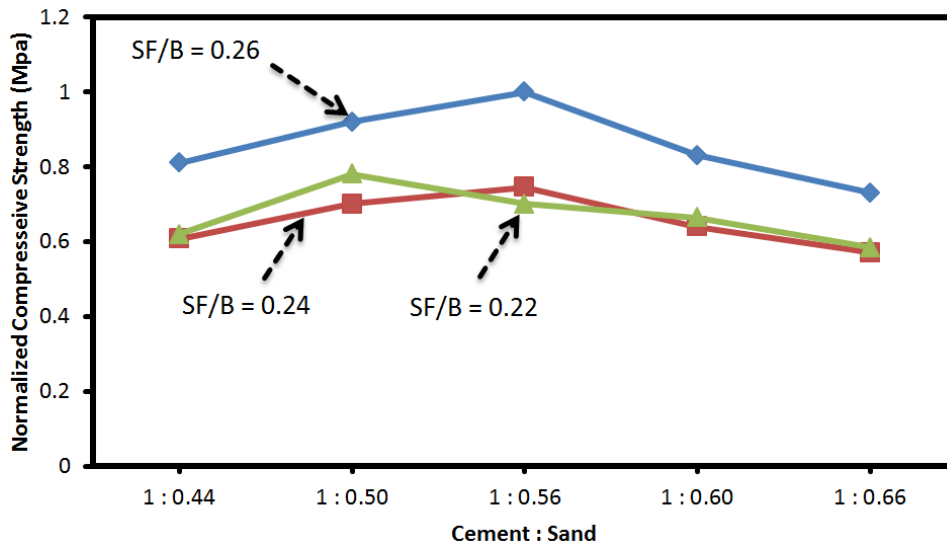


Figure 4-3: Influence of cement/sand and SF/B ratio on normalized compressive strength of the UHPFRC material.

4.2.3 Influence of Silica Fume to Binder ratio

While the typical mix design with a silica fume to binder (SF/B) ratio of 0.26 is given in Table 3-5, the influence of SF/B on the compression strength was also studied. Compression strength results for CU-50 specimens at different ages for SF/B ratios of 0.22, 0.24, and 0.26 are summarized in Figures 4-3 and 4-4. An average compressive strength of 100 MPa at 7 days was noted for mixes with all three SF/B ratios, as shown in Figure 4-4. The rapid strength gain was achieved through the use of a high volume of silica fume, which not only provides a rapid pozzolanic reaction,

but also further decreases the void space, as the very fine particles tend to pack between the larger particles (e.g. Pfeifer et al. 2010, Cohen et al. 1994). A more gradual increase in compressive strength of about 25% occurred between 7 and 28 days for mixes with SF/B = 0.22 and 0.24. The results were similar in the vibrated and non-vibrated specimens. However, for the mixes with SF/B = 0.26, increases in the compressive strength of 41 and 15% between 7 and 14 days were obtained for the vibrated and non-vibrated mixes respectively. This strength gain trend was followed by a strength plateau for these mixes, but as discussed later there was typically an increase in strength beyond 28 days. Based on these results, the SF/B = 0.26 was selected for the rest of the study (see Table 3-5), as it has the highest compressive strength.

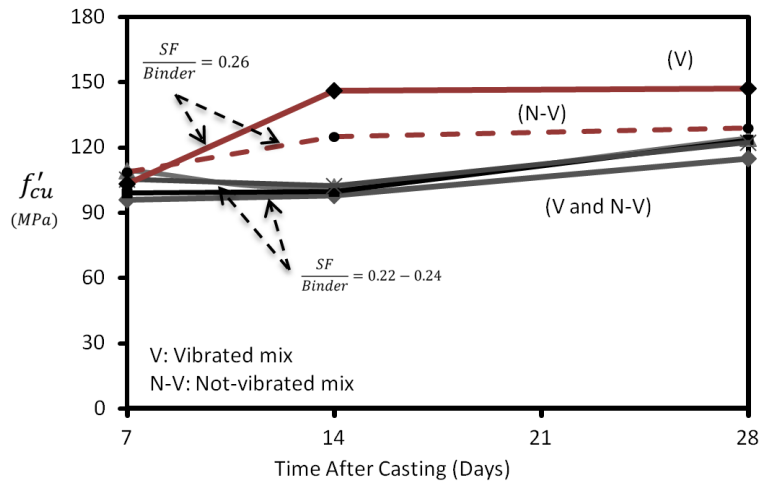


Figure 4-4: Influence of SF/B on the compressive strength of the UHPFRC material.

4.2.4 Influence of Fiber Volume-Fraction

Mixes with four different fiber volume-fractions were used to study the influence of V_f on the compressive strength of CU-50 specimens. Similar analyses were also completed for CU-100, CY-50, and CY-100. From multiple batches of each mix (minimum 3 replicate tests of each), the compressive strengths of CU-50 at 28 and 42 days are summarized in Table 4-1. Compared to the plain mix with $V_f = 0\%$, an increase in V_f from 2 to 5% was found to increase the compressive strength by 5.8 to 25% for CU-50 and 7 to 26% for CU-100 at the age of 28 days. A similar trend was observed for CY-50, CY-75, and CY-100 where averages of 5 and 15% enhancement

in compressive strength were noted for mix with $V_f = 2$ and 4%, as compared to the plain mix. Slight improvements in the 42 day compressive strength of CU-50 were found with changes in V_f except for the mix with 5% fiber, where there was a 21% increase in compressive strength compared to the plain mix. Figure 4-5 provides an overall view of the failure of CY-200 with $V_f = 0\%$, 2%, 4%. Unlike the plain mix with a brittle behaviour after the peak load, significant cracking after failure had occurred for mix with fiber.

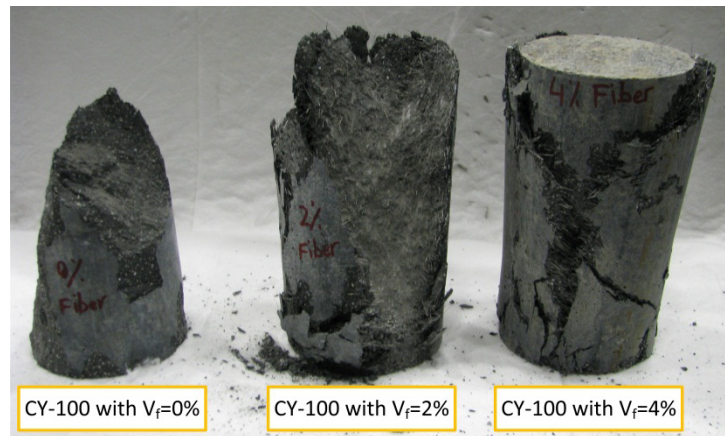


Figure 4-5: Compression failure in CY-200 specimens, left to right: $V_f = 0, 2,$ and 4.

Table 4-1: Compressive strength of CU-50 specimens

V_f (%)	Density (kg/m ³)	Age (Days)	Number of Specimens	f'_{cu} (MPa)	COV (%)	Increase in f'_{cu} *
0	2343	28	24	139	8.8	-
		42	9	164	3.1	-
2	2397	28	21	147	7.7	5.8
		42	9	170	4.1	3.7
3	2426	28	9	151	2.6	8.6
		42	3	172	14	4.9
4	2482	28	21	164	7.8	18.0
		42	15	175	4.7	6.7
5	2536	28	9	174	7.0	25.0
		42	3	198	1.0	21.0

* increase in f'_{cu} compared to $V_f = 0\%$ Mix.

4.2.5 Influence of Consolidation

The influence of consolidation on the compressive strength of CU-50 is shown in Figure 4-6. The mixes with $V_f = 0-4\%$ are essentially self-compacting with minimal difference between the compressive strength of vibrated and non-vibrated mixes. However, in the case of $V_f = 5\%$ mix, it needs vibration to work well. While there was no substantial improvement (only around 2%) in the compressive strength of vibrated mix over the non-vibrated one at the ages of 7 and 21 days, a 13% improvement was found at the age of 28 days. This improvement is most likely attributed to reduction in volume of entrapped air which leads to a UHPFRC matrix with higher homogeneity.

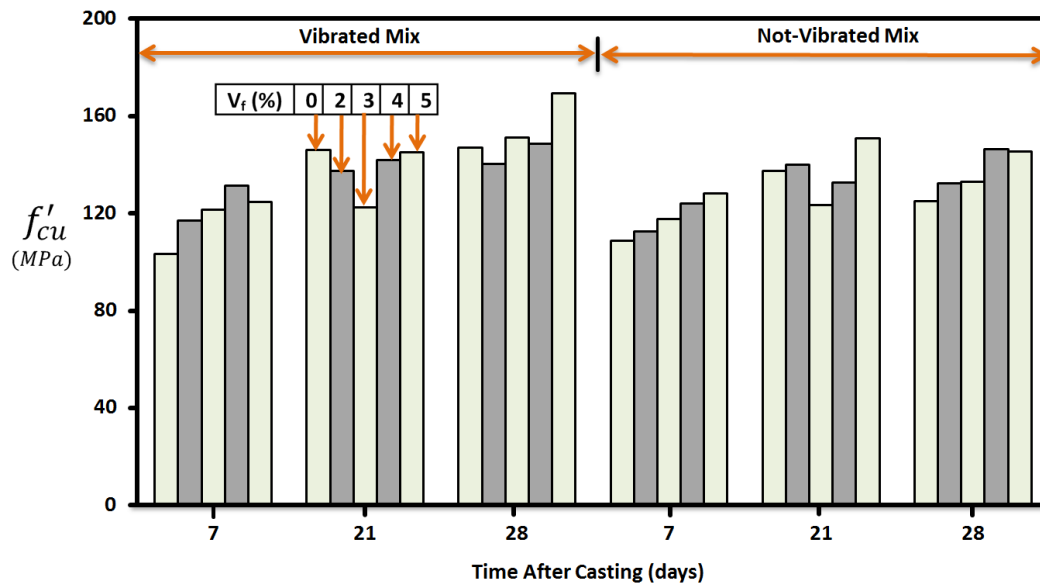


Figure 4-6: Influence of consolidation on the compressive strength of the CU-50 specimens.

4.2.6 Influence of Specimen Size and Shape

Understanding the influence of size effects on the compressive strength of UHPFRC is important when extrapolating the results from laboratory scale specimens to the scale of real structural members. The 28 day compressive strengths of vibrated CU-50 and CU-100 as well as CY-50, CY-75, and CY-100 samples for different fiber-volume fractions are summarized in Figures 4-7 and 4-8.

A size effect is apparent, where lower compressive strengths were obtained as the specimen size increased, which is reported in other research (e.g. Graybeal 2006, Graybeal and Davis 2008). The experimental results demonstrated that the cube samples consistently have higher strength than cylinder samples of the same maximum cross-section dimension, as shown in Table 4-2. This trend related to specimen shape is similar to that observed for conventional concretes. This influence of specimen size on the compressive strength was found to be of similar magnitude for V_f between 0 and 5%. The result is in agreement with published studies on $V_f=2\%$ UHPFRC (e.g. Graybeal 2006).

The conversion coefficients and the corresponding coefficients of variation (COV) that relate the compressive strength of cubes and cylinders are provided in Table 4-2. The results show that both CY-75 and CY-100 have the same compressive strength. As a simpler alternative to CY-100 and CY-75, the CU-50 can be used as it provides enough pairs of smooth surfaces and requires lower capacity test equipment.

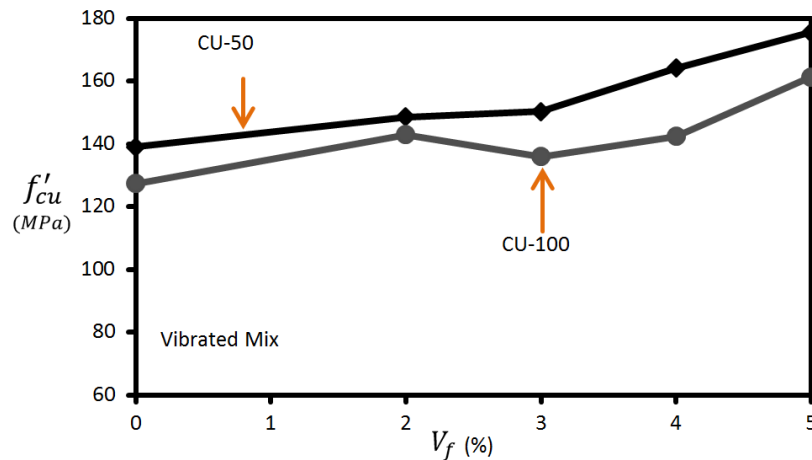


Figure 4-7: Influence of V_f on the average 28 days compressive strength of the CU-50 and CU-100 specimens.

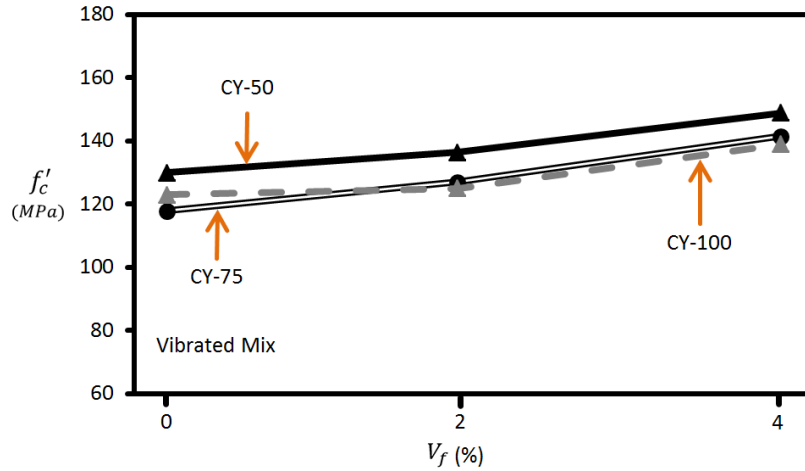


Figure 4-8: Influence of V_f on the average 28 days compressive strength of the CY-50, CY-75, and CY-100 specimens.

Table 4-2: Compressive strength conversion factors between cylinders and cubes

To Convert	To CU-50	To CY-75	To CY-100
CU-50	1.00	0.87 (4.6%)	0.88(5.3%)
CU-100	1.09(5%)	0.96(3.1%)	0.96(4.0%)
CY-50	1.09(1.5%)	0.95(5.1%)	0.96(3.9%)
CY-75	1.15(4.5%)	1.00	1.01(6.6%)
CY-100	1.14(5.4%)	0.99(6.4%)	1.00

() = Coefficients of variation of the conversion factor

4.2.7 Time Development

The evolution of the compressive strengths with time up to 180 days for CU-50 specimens with $V_f = 0$ and 5% are illustrated in Figure 4-9. The Weibull cumulative function was used in this study to describe the relationship between the compressive strength and time after casting.

$$f'_{cu,t} = f'_{cu,60} \left[1 - \exp \left(- \left(\frac{t-t_0}{4} \right)^\mu \right) \right] \quad (4-1)$$

where $f'_{cu,t}$ is the compressive strength of CU-50 at time t (days) after casting, $f'_{cu,60}$ is the compressive strength of CU-50 at 60 days. The above expression is valid for $t_0 > 0.9$ (day). The shape factor (μ) was independently calibrated for the two different V_f values: $\mu = 0.5$ and 0.6 were selected for $V_f = 0$ and 5% , respectively. Each of the above parameters is dependent on the curing condition as well as initial and final set time of UHPFRC mix (e.g. Graybeal 2006).

The typical set time of the UHPFRC was 8 hours based on the Vicat needle method. To allow extended working time, the use of a commercially available hydration stabilizer admixture (SA) was added to some mixes. A ratio of SA to binder of 3 ml/kg was adopted in this study, which extended the set time to 24 hours. The strength evolution of the mix with and without SA is shown in Figure 4-10. The mix with SA exhibits slower initial rate of strength gain compared to the mix without SA, but had the same strength after 2 month. In addition, it took similar times for the mix with and without SA to reach the maximum compressive strength.

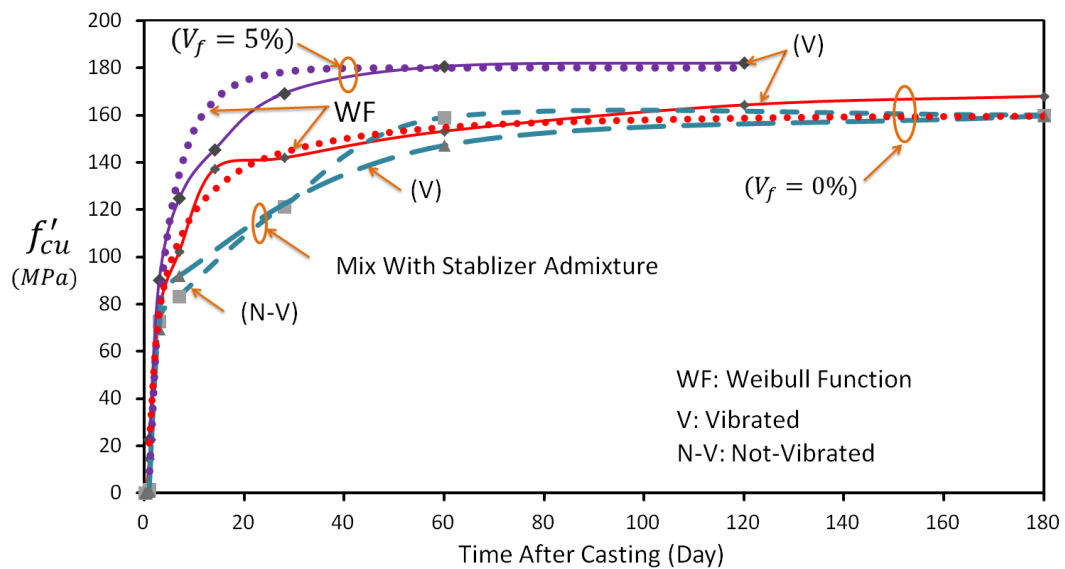


Figure 4-9: Time development of the CU-50 compressive strengths.

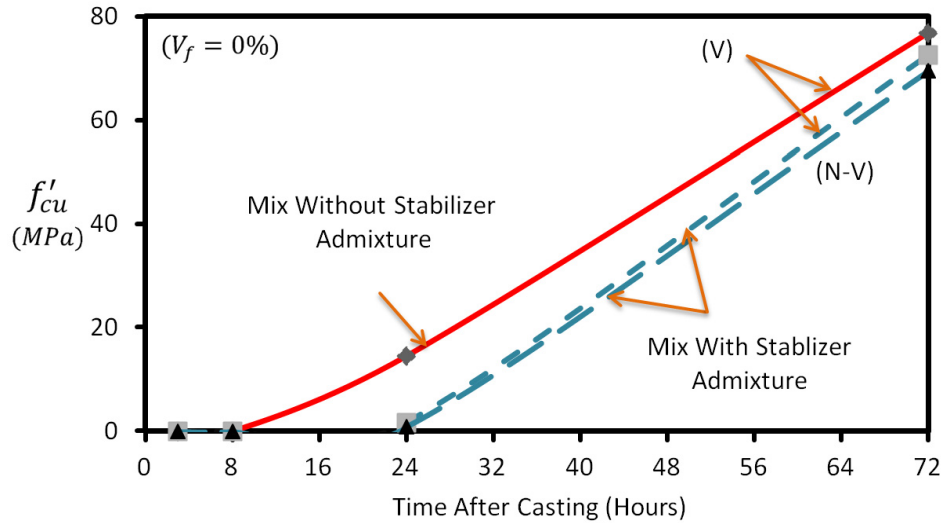


Figure 4-10: Time development of CU-50 compressive strengths during the first 72 hours.

4.3 Flexural Response

4.3.1 Overview of Flexural Test Results

The flexural testing was completed at two different time stages. The ASTM C1609-10 test setup with two LVDTs mounted on both sides of standard yoke was used to measure the mid-span deflection (δ) of prism specimens in the first phase (Phase-I). See Figure 4-11. A digital image correlation (DIC) system along with a pair of LVDTs mounted at the back side of prism specimens was used to measure the mid-span deflection (δ) at the second series of casting (Phase-II).

The results of δ extracted from DIC and LVDTs (Phase-II) were compared and it was found that the LVDT results tend to show higher values as compared to DIC results. See Figure 4-11. This difference is more pronounced in PF-150 and PF-200 prism specimens. The difference between LVDTs and DIC is due most likely to the fact that the DIC displacements were modified to remove rigid body motion (RBM) from the relative displacement. However the results of LVDTs were not corrected to accommodate for RBM and local flexibility at the supports. In addition, the LVDTs support was epoxied to the top side of the prism and dislocate, once the main crack reached this part and this could have deviate the results. Furthermore, in the case that the mid-span crack did not form at the mid-span, the LVDTs reading may not

exactly represent the vertical displacement, as the recorded information includes both horizontal and vertical components.

The results of PF-50 specimens with $V_f = 0\%$, 2%, 4% from Phase-I (LVDTs) are compared with results of geometrically similar specimens tested in Phase-II (DIC) and very close agreement was found.

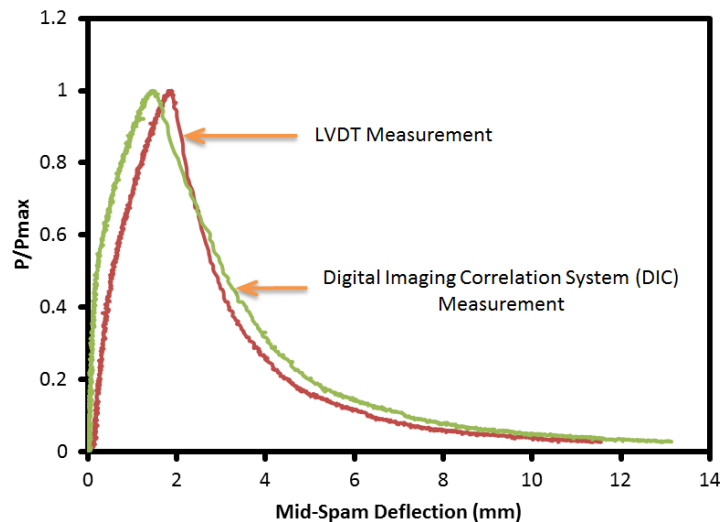


Figure 4-11: Normalized load-deflection response of the PF-200 specimen: comparison of LVDT and DIC measurement.

4.3.2 Load-Deflection Response

Typical load vs. deflection curves of the flexural tests of PF-50 specimens are illustrated in Figure 4-12 for mixes with $V_f = 0$ to 5%. A horizontal offset is used to avoid overlap. A highly brittle response with very rapid drop in the load after reaching the MPL was observed for plain mixes with no fiber. The curves show that the addition of short steel fibers to UHPFRC significantly improves the load-deflection behaviour from a brittle response at cracking for the plain mix to a ductile response for the mixes with fibers. This resulted from the formation of a single failure crack in the $V_f = 0\%$ specimens while multiple fine cracks formed in the constant moment region for mixes with fibers with a dominant macro crack only forming near the failure load.

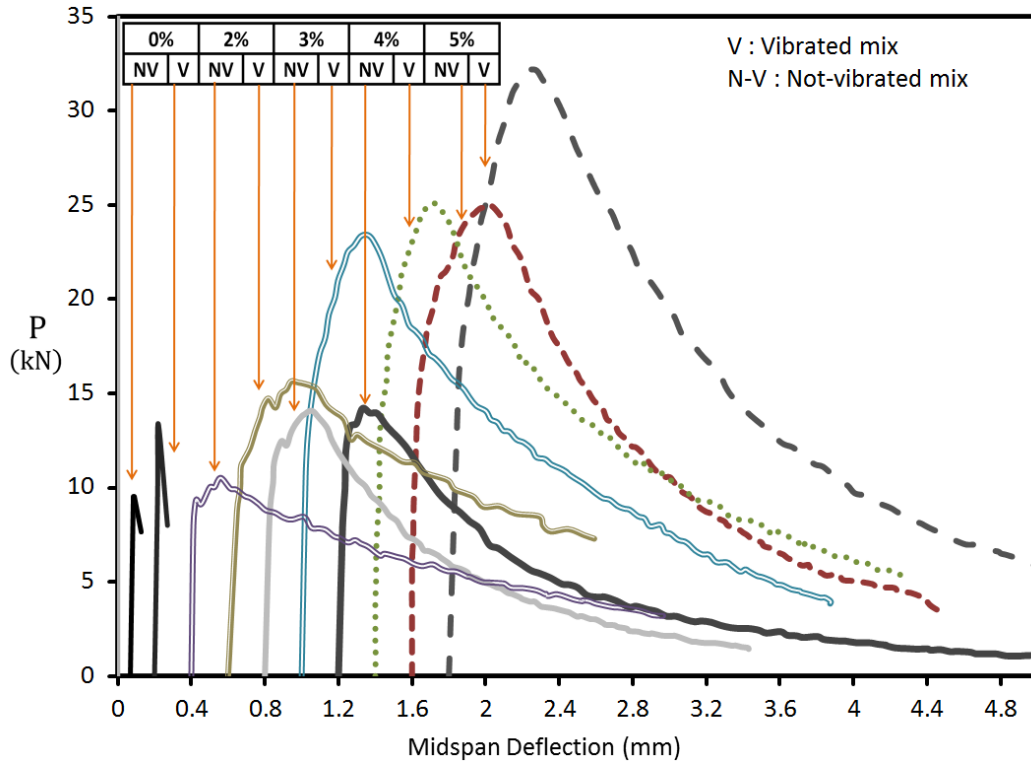


Figure 4-12: Comparison of the flexural load-deflection response of the PF-50 specimens with different V_f .

Figure 4-13 summarizes the average experimentally obtained flexural load-deflection curves of PF-50, PF-100, PF-150, and PF-200 with $V_f = 2\%$ and 4% . No significant variation in initial stiffness was found with change in specimen size and V_f . This means that the modulus of elasticity is size independent. For all different specimen sizes, higher MPL was found for mixes with higher V_f which is associated to contribution of short steel fibers to tensile capacity of UHPFRC mix. The trend from load-deflection results confirmed that the softening branch of larger prism specimens experience a steeper softening branch as compared to smaller prism sizes.

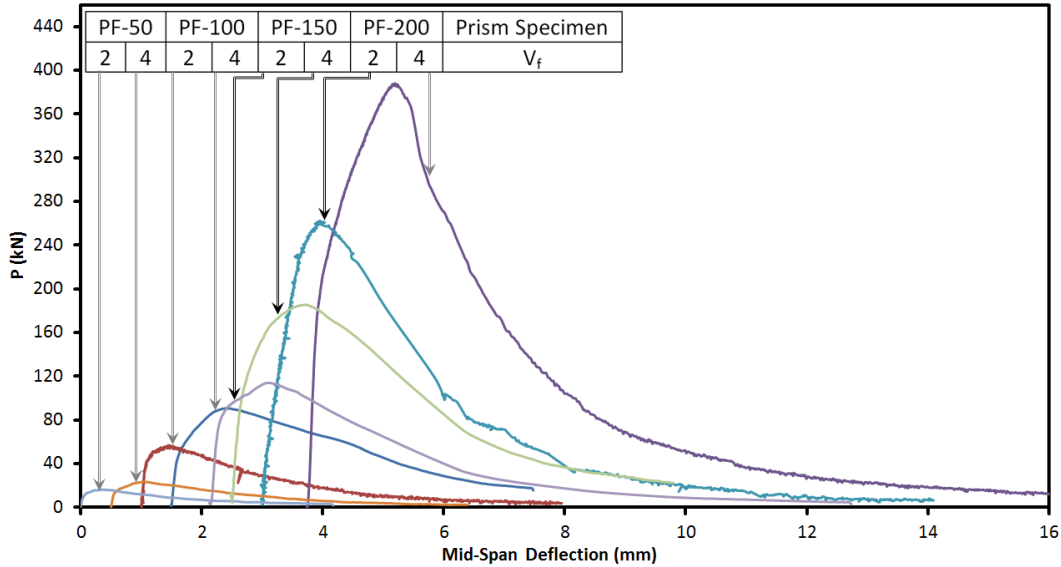


Figure 4-13: Comparison of the flexural load-deflection response of the PF-50, PF-100, PF-150, and PF-200 specimens with $V_f = 2\%$ and 4% .

4.3.3 Stages in Flexural Fracture of UHPFRC

The overall behaviour of UHPFRC prism specimens subjected to flexural loading along with stress distribution in the cross section in different stages are described by the plot of load versus mid-span deflection shown in Figure 4-14. This figure depicts the entire history of the test which is a continuous fracture process and can be divided into three distinct stages.

4.3.3.1 Linear-elastic Behaviour

In the first stage, the load displacement relationship for all the mixes with $V_f = 0-5\%$ was nearly linear up to the limit of proportionality (LOP), where cracking was first observed. See curve I-II in Figure 4-14. The LOP point proposed by ASTM C1018 as the point where the nonlinearity in the flexural load-deflection begins is more suitable for UHPFRC compared to the ASTM C1609 criteria at first cracking (a point where the slope is zero) since UHPFRC features stable deflection hardening. The pre-existing cracks in the UHPFRC matrix before the LOP point remain nearly unchanged (e.g. Bernard 2000). No permanent deflection was observed during this stage. This was confirmed by unloading a few PF-50 prism specimens to track the deflection of a specific point located at mid-height the mid-span of prism samples.

The result of DIC measurement indicated that the sample was returned to its original position after the load was removed.

The LOPs were reached at a small deflection, δ_{LOP} , which are shown in Figure 4-15 for different prism specimens, PF-50, PF-100, PF-150, and PF-200 with $V_f = 0\%$, 2%, and 4%. A linear increase in δ_{LOP} was found with an increase in V_f from 0% to 4%, for all the specimen sizes except for PF-50 samples where an almost similar δ_{MPL} was observed for mixes with $V_f = 2\%$ and 4%.

4.3.3.2 *Pseudo Strain Hardening Behaviour in Tension*

Beyond the LOP point, the second stage, the pseudo strain hardening response was observed. See curve II-III in Figure 4-14. During this stage, the flexural strength continued to increase for additional applied displacement with multiple microcrack formations occurring. This phenomenon is attributed to formation of multiple microcracking during the inelastic deformation process. A microcrack initiates in UHPFRC matrix once the maximum principal stress exceeds the elastic tensile strength. As a microcrack forms in the UHPFRC matrix, the crack faces are immediately bridged by steel fibers which retard the uncontrolled propagation of crack. The stress between the UHPFRC matrix and steel fibers are transmitted through the strong interfacial bond strength between steel fibers and the matrix (e.g. Naaman 2008). Upon the formation of a microcrack, the stress concentration will be relieved. This would lead to initiation of another crack of very small width in a new position at a higher load which propagates more rapidly compared to the last one, as the UHPFRC experiences higher stress concentration at this stage.

The formation of multiple microcracks is repeated in the constant moment region several times until they join with each other to form a dominant macrocrack near the failure load. See Point III in Figure 4-14. This phenomenon would lead to strain hardening behaviour which is influenced significantly by the fiber content (e.g. Naaman 2000, Habel 2004, Rosi 2002). Figure 4-15 presents the changes in deflection at maximum peak load (MPL), δ_{MPL} , against the changes in V_f for different prism specimens, PF-50, PF-100, PF-150, and PF-200. The deflection at MPL, δ_{MPL} , was found to linearly increase with an increase in V_f from 0% to 4%, for all the

specimen sizes except for PF-50 samples where an almost similar δ_{MPL} was observed for mixes with $V_f = 2\%$ and 4% .

4.3.3.3 Softening Behaviour

After MPL was reached (point III), the descending branch of the curve for mixes with fibers showed gradual softening with the shape influence by V_f . In contrast, the plain mix exhibited a very sudden failure after the formation of the first crack, as the aggregate bridging is the only source of bridging which is very weak compared to the fiber bridging mechanism. Development of cracks in the softening stage was observed to be quite unstable.

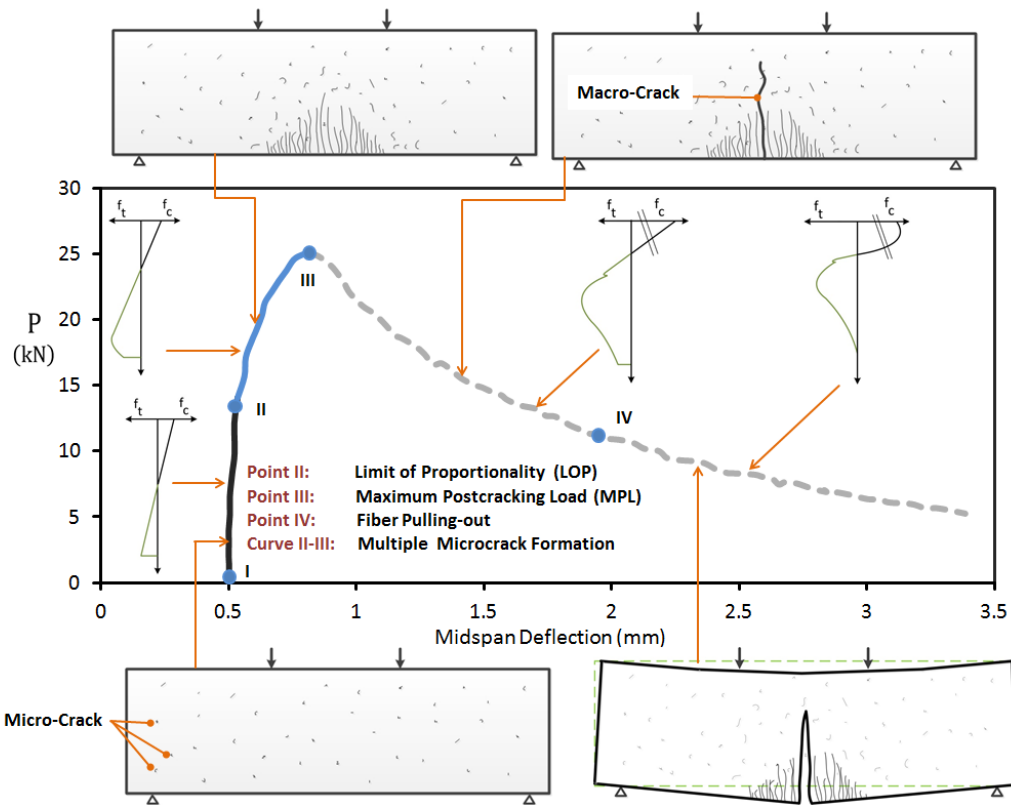


Figure 4-14: Different stages in the flexural fracture of the UHPFRC material: Linear Stage (Curve I-II); Hardening Stage (Curve II-III); Softening Stage (Curve II-III).

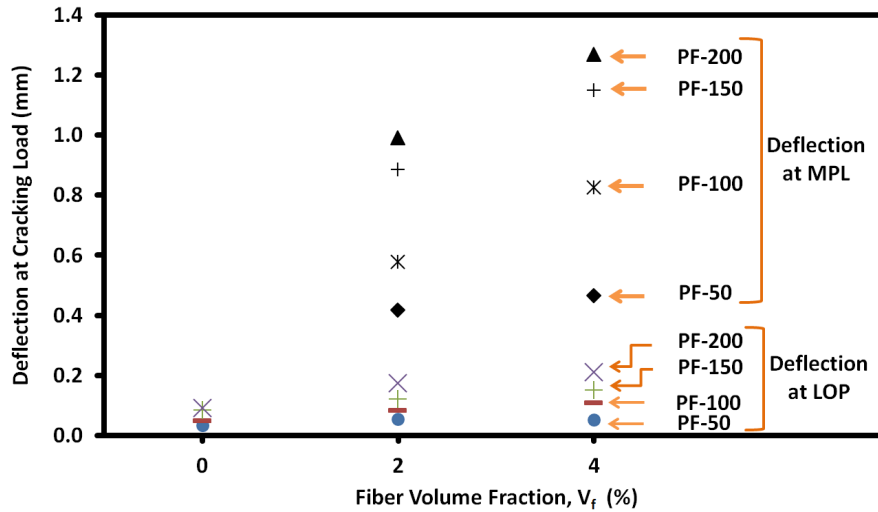


Figure 4-15: Mid-span deflection at cracking load for different prism specimen sizes.

4.3.4 Cracking and Peak Strength

The measured load-deflection test results were further analysed to evaluate the influence of V_f , SF/B, and specimen size on the flexural first crack strength (FCS) and the flexural peak load equivalent strength (PLES), which corresponded to the LOP and MPL. The FCS and PLES were solved as the peak tensile stress values after assuming an equivalent elastic stress-strain response over the cross-section height and normalizing the result by the square root of the 28 day CU-50 compressive strength.

$$FCS = \frac{3LOP}{h^2 \sqrt{f'_{cu}}} \quad (4-2)$$

$$PLES = \frac{3MPL}{h^2 \sqrt{f'_{cu}}} \quad (4-3)$$

where h is the prism width and height.

4.3.4.1 Influence of SF/B

From Figure 4-16 it is observed that, there are respectively 8 and 15% increases in FCS and PLES for vibrated and non-vibrated mix with increasing the SF/B ratio from 0.22 to 0.26. Note that FCS and PLES are similar for plain mixes. The improvement

in FCS with increasing SF/B ratio is most likely attributed to the physical and chemical enhancement in packing density of the UHPRC matrix. This is because the SF particles are small enough (1/20 of cement particles) to be dispersed throughout the available spaces between larger cement particles. These results indicate that the FCS was mainly affected by the matrix characteristics, but not by fiber content.

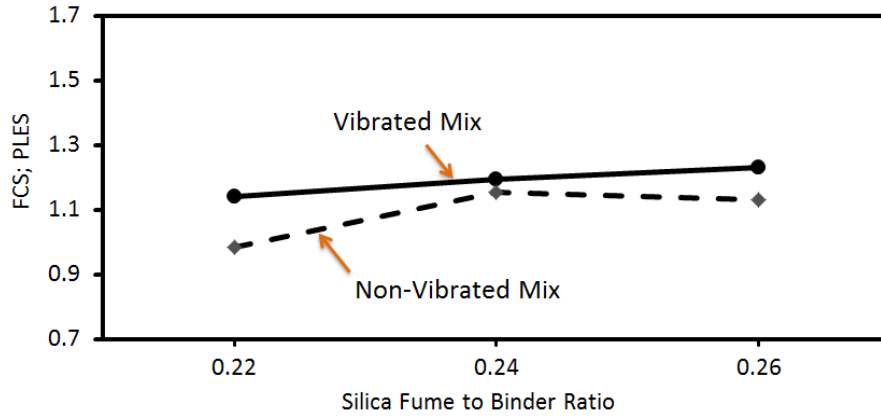


Figure 4-16: Influence of fiber content, SF/B ratio and size effect on the: (a) first crack strength (FCS); and (b) peak load equivalent strength (PLES).

4.3.4.2 Influence of Fiber Volume Fraction

Figure 4-17 shows the influence of specimen size on the FCS of UHPFRC with three different fiber volume fractions, i.e. $V_f = 0, 2, 4\%$. As presented in this figure, the addition of 2% fiber to the mix increased the FCS by 2%, 6%, 13%, and 43% for PF-50, PF-100, PF-150, and PF-200 respectively. Similar results were observed for mixes with $V_f=4\%$, where compared to the plain mix there were 20%, 33%, 37%, and 70% increases in FCS for PF-50, PF-100, PF-150, and PF-200, respectively.

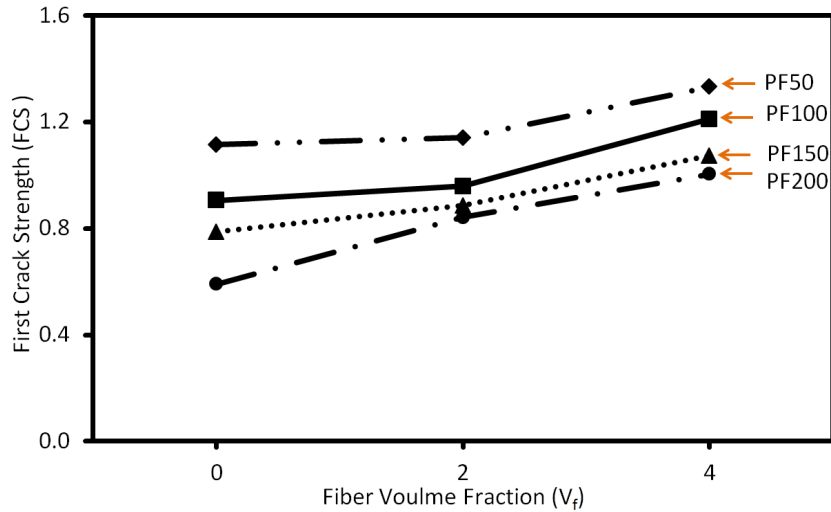


Figure 4-17: Influence of three different fiber content and specimen size on FCS of UHPFRC.

An increase in V_f from 2 to 5% resulted in a linear increase in PLES of PF-50 from 40 to 107% compared to the plain mix. See Figure 4-18. This is most probably because additional steel fibers with smaller fiber spacing can more efficiently control the development of microcracks and retard the crack propagation. Similar test results have been reported by other researchers (Kang et al. 2010, Van 2004, Romualdi et al. 1963).

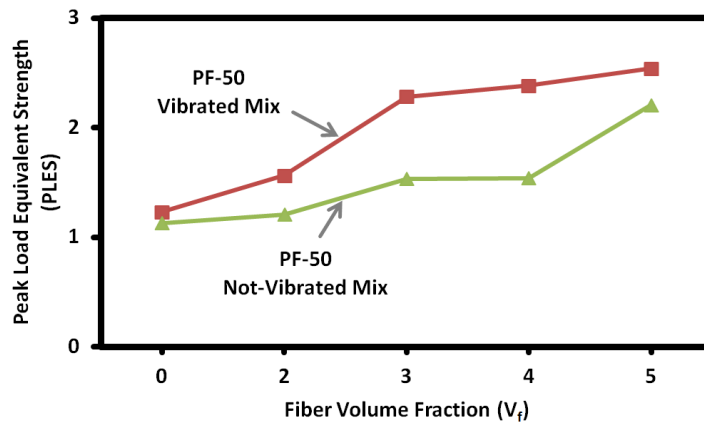


Figure 4-18: Influence of consolidation on the peak load equivalent strength (PLES) of PF-50.

4.3.5 Influence of Size Effect

To evaluate the influence of the size effect on flexural strength, results for the PF-100, PF-150, and PF-200 specimens with $V_f = 0, 2, \text{ and } 4\%$ are respectively compared to the PF-50 results in Figure 4-17. The FCS was decreased by an average value of 12, 21, and 31%, as the specimen size was increased from 50 mm to 100 mm, 150 mm and 200 mm respectively. This influence of prism height on the FCS is in agreement with the findings of other research on UHPFRC (e.g. Graybeal 2006, Reineck and Frettlöhr 2010, Chanvillard and Rigurad 2003, Reineck and Greiner 2007).

Similar results were observed for PLES, where average decreases of 15%, 24%, and 33% was noted for PF-100, PF-150, PF-200 specimens respectively as compared to PF-50 prism specimens. There is no general agreement on why the PLES tends to show a larger decrease as the specimen size increases. For the specimens in this study, this size influence can be partially attributed to the fiber orientation in the prism, which is known to be affected by the specimen size and the fiber length. Previous researchers (Reineck and Greiner 2007) have noted that the fiber orientation has a two-dimensional pattern near the prism surface due to the so-called wall effects from the specimen edges or the pseudo boundaries created during the layered casting. The zone of this wall or boundary influence is related to the fiber length. Away from these boundaries, the fibers are isotropically distributed in a 3-dimensional pattern. The 3-D distribution is less favourable for flexural strength, since a smaller equivalent fiber quantity will be aligned in the direction of the flexural tensile stresses to accommodate the crack bridging forces. Compared to PF-100, the smaller PF-50 specimens will have a greater proportion of their cross-section containing the more favourable 2-dimensional fiber orientation, which results in larger PLES values.

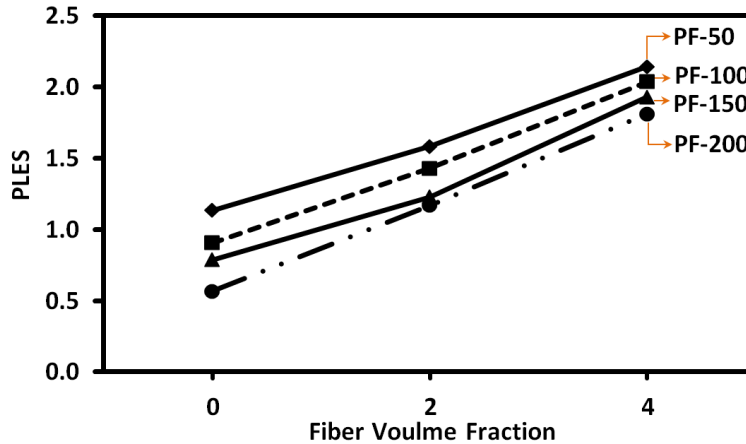


Figure 4-19: Influence of fiber content and specimen size on the PLES of UHPFRC material.

4.3.6 Influence of Consolidation

The influence of mechanical vibration on PLES of PF-50 prism specimens was experimentally investigated and the results are shown in Figure 4-18. While consolidation did not substantially enhance the PLES of plain UHPFRC, an average 37% improvement in PLES of vibrated UHPFRC mix with $V_f = 2-5\%$ was noted compared to the non-vibrated mixes with similar V_f .

4.3.7 Influence of Time Development

Additional flexural tests were completed on PF-50 prism samples at different ages (35 days, 125 days and 2 years) to study the development of flexural strength with time. Figures 4-20 and 4-21 illustrate the results of FCS and PLES from mixes with $V_f = 0\%$, 2%, and 4%. The FCS at the ages of 135 days was found to be 9%, 7%, and 15% higher than at the 35 days for mixes with $V_f = 0\%$, 2%, and 4% respectively, as shown in Figure 4-20.

Similar results were observed for PLES, where the PLES at the age of 125 days was 11%, 13%, and 9% higher than at the age of 35 days. Additional flexural testing was completed at the age of two years for plain mix and 21% and 23% improvements in FCS and PLES were found.

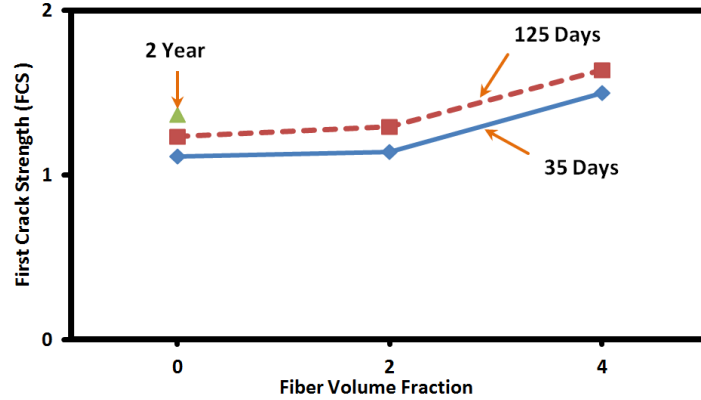


Figure 4-20: Time development of First Crack Strength (FCS) of PF-50 specimens.

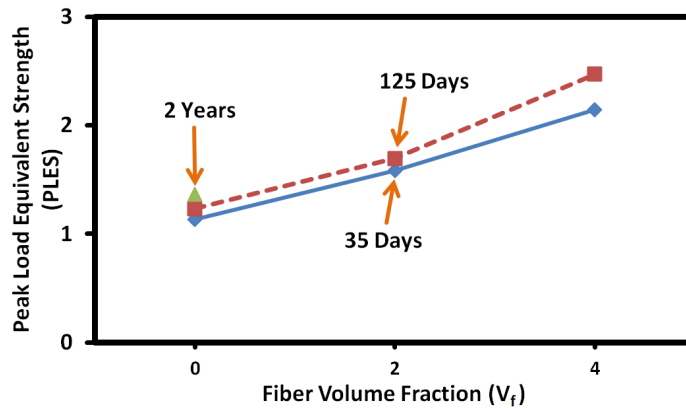


Figure 4-21: Time development of peak load equivalent strength (PLES) of PF-50 specimens.

4.3.8 Flexural Toughness Factor (FTF)

The flexural toughness factor (FTF) was determined for each prism test according to JSCE-G 552-1999 allowing comparison of the normalized energy absorption capacities. With L representing the prism span, the FTF was determined as:

$$FTF = \frac{L \cdot \Psi_{L/m}^h}{\left(\frac{L}{m}\right)bh^2} \quad (4-4)$$

where b is the prism width, h is the height and $\Psi_{L/m}^h$ (N.mm) is the flexural toughness determined as the area under the load-deflection curve from a deflection of zero to a value of L/m, where m is a constant number.

4.3.8.1 Influence of V_f

Figure 4-23 shows the variation of the FTF with V_f for PF-50 prism specimens using the typical value of $m=150$ as specified in the JSCE to reflect the serviceability limit states of deflection and cracking. A very poor FTF value of 0.25 MPa was observed for the $V_f = 0\%$ mix, since the only resisting source is the UHPFRC matrix which is extremely brittle in flexure. In contrast, the addition of a 2 to 5% volume-fraction of steel fiber was observed to significantly overcome the brittleness of the matrix and improve the toughness of the UHPFRC mix. This additional energy dissipation capacity would significantly improve the performance of the UHPFRC members subjected to seismic loading where huge inelastic deformation demands are required (e.g. Billington et al. 2004).

The FTF linearly increased as the fiber content was increased from 0 to 3% (refer to Figure 4-23). However, the rate of improvement decreased when the fiber content was increased from 3 to 5%. This improvement in FTF was achieved through the fiber bridging effect where the load carried by the cracked part was transferred to the steel fibers through the strong interfacial bond strength between the steel fibers and matrix. Thus, the larger the fiber contents, the slower the rate of propagation of the microcracks which would lead to a higher FTF. In addition, when microcracks approach steel fibers, they are often deflected along the fiber-matrix interface, which requires extra work to be done and, therefore, significantly enhances the FTF. Compared to the UHPFRC mix with $V_f = 2\%$, use of a 4% volume-fraction of steel fiber was found to increase the FTF by an average of 53%, 57%, 65%, and 63% for PF-50, PF-100, PF-150, PF-200 prism specimens respectively.

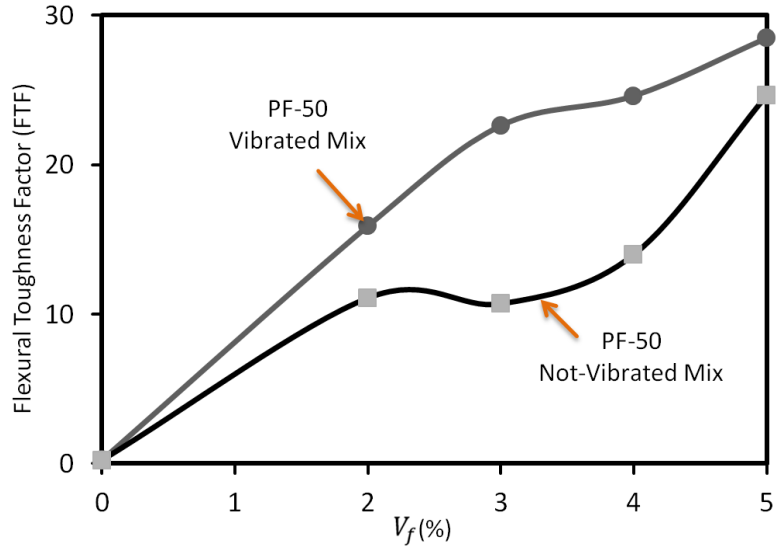


Figure 4-22: Influence of fiber volume fraction (V_f) and consolidation on the FTF of PF-50 prism specimens (L/150).

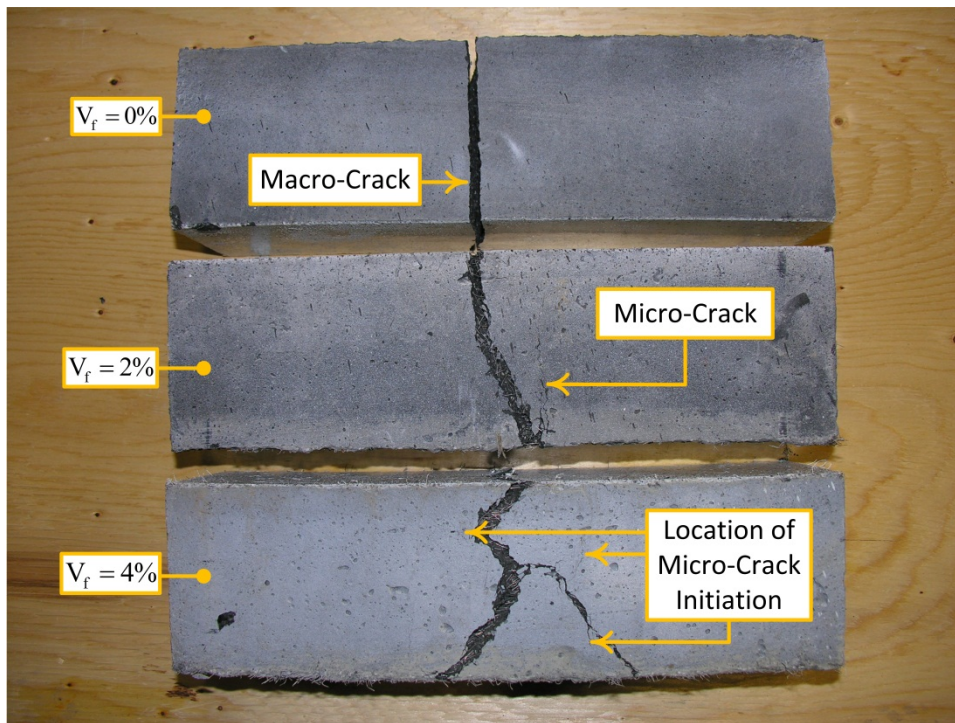


Figure 4-23: Crack development in PF-100 including (top to bottom) mix with $V_f=0\%$, $V_f=2\%$, $V_f=4\%$.

4.3.8.2 Influence of Consolidation

To investigate the influence of consolidation on FTF, a similar analysis was completed for non-vibrated PF-50 and the results are illustrated in Figure 4-23. The FTF of vibrated mixes was found to be significantly higher than the non-vibrated mix. This enhancement was more pronounced in the specimens with higher V_f content. This improvement in FTF is most likely due to the stronger interfacial bond strength between the steel fibers and matrix in the vibrated mix, which causes an efficient stress transfer mechanism from UHPFRC matrix to steel fibers.

4.3.8.3 Influence of Size Effect

The influence of specimen height and V_f on FTF of PF-50, PF-100, PF-150, PF-200 are shown in Figure 4-25 and Figure 4-26 for mixes with $V_f = 2\%$ and 4% respectively. For the mix with $V_f = 2\%$, the FTF was decreased by an average value of 16, 27, and 36%, as the specimen size was increased from 50 mm to 100 mm, 150 mm, and 200 mm respectively. Similar results were observed for the $V_f = 4\%$ mix, where the FTF was decreased by an average value of 14%, 22%, and 33% for PF-100, PF-150, PF-200 samples respectively compared to PF-50 prism specimens.

The $L/m = 150$ (L in mm) proposed by the JSCE standard code is often criticized for being much greater than the acceptable deflection/serviceability limits (e.g. Narataga et al.). Thus, the FTF for a wide range of this ratio, i.e. $m=300, 200, 150, 100,$ and 75 was calculated for PF-50, PF-100, PF-150, and PF-200 specimens and the results are shown in Figs. 4-25 and 4-26. Each of these indices represents different levels of serviceability in terms of deflection. As shown in these figures, the descending trends between FTF, V_f and size occur at all L/m ratios.

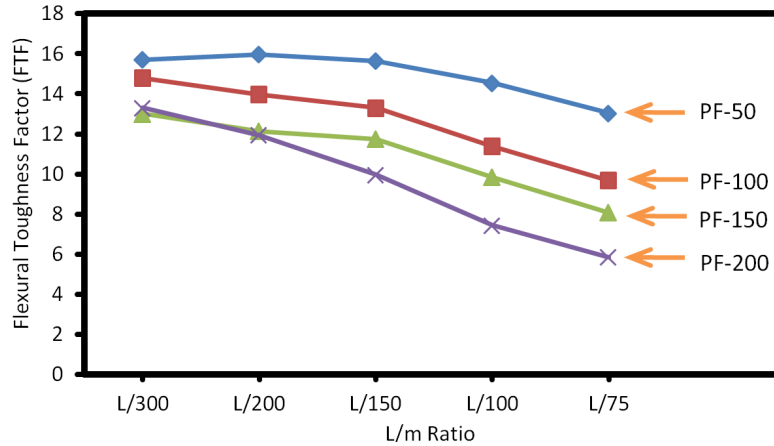


Figure 4-24: Influence of fiber volume fraction on FTF of specimens of different sizes including PF-50, PF-100, PF-150, PF-200 with $V_f=2\%$.

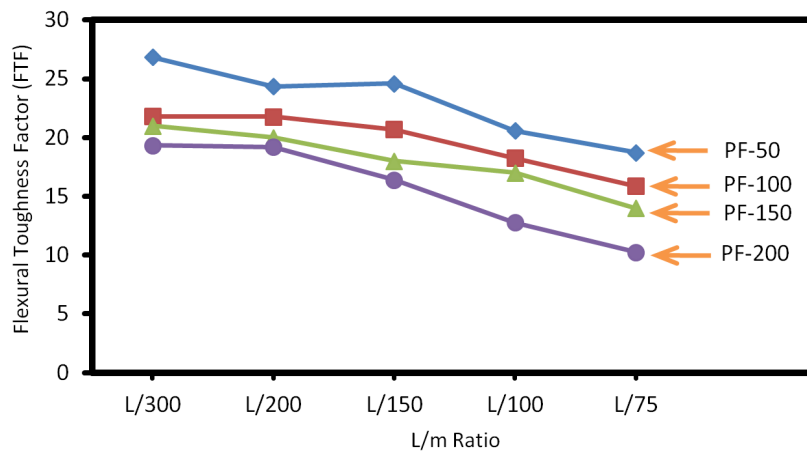


Figure 4-25: Influence of fiber volume fraction on FTF of specimens of different sizes including PF-50, PF-100, PF-150, PF-200 with $V_f=4\%$.

4.4 Direct Shear Response

4.4.1 Shear-Slip Relationship

Experimental test results of PS-50 samples from the direct shear test program are shown in Figure 4-27 with a horizontal offset to avoid overlap. The brittle behaviour of plain UHPFRC is evident from its low deformation capacity, catastrophic load reduction with explosive nature, and low shear strength. Figure 4-28 shows shear failure mechanism at the end of testing for UHPFRC mixes with and without fibers,

highlighting the catastrophic failure in samples without fiber. No descending branch in load-slip response can be observed for plain mixes. These indicate that the $V_f=0\%$ mix is unsuitable in applications where significant shear stresses are expected. In contrast, the mixes with 2 to 5% steel fibers showed a more ductile behaviour through large post-peak deformations. The curves in Figure 4-27 show that the cracking strength, the peak shear strength, and the strain hardening behaviour in shear were all influenced by the fiber content. The increase in V_f from 2 to 3% did not improve the maximum shear load, but instead reduced the softening slope, thereby leading to a higher shear toughness capacity. Unlike the mix with $V_f=2$ and 3% that showed a softening behaviour immediately after the peak, the mix with $V_f=4$ and 5% fiber volume-fraction exhibited a region of hardening behaviour followed immediately by a softening branch.

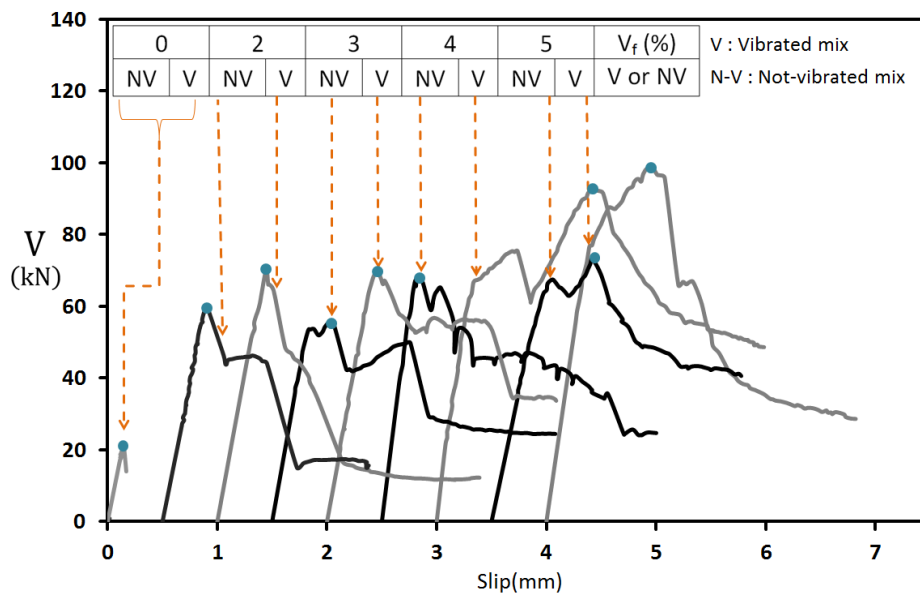


Figure 4-26: Typical shear load slip curves for PS-50 specimens.

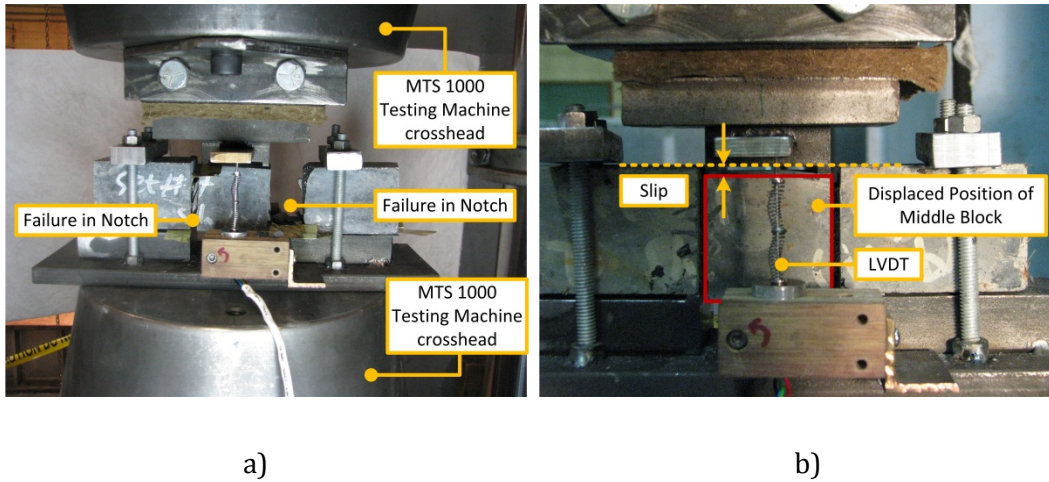


Figure 4-27: Failure of PS-50: (a) without fiber, (b) with fiber.

4.4.2 Stages in Shear Fracture of UHPFRC

The experimentally measured quasi-static load-deflection curve of UHPFRC subjected to direct shear loading is demonstrated in Figure 4-29. The shear cracking and macroscopic behaviour of UHPFRC subjected to shear loading are also shown in this figure. Based on the experimental results, three stages of crack development can be distinguished which includes the linear stage, strain hardening stage, and softening stage. Each of these stages are explained in detail in the subsequent sections.

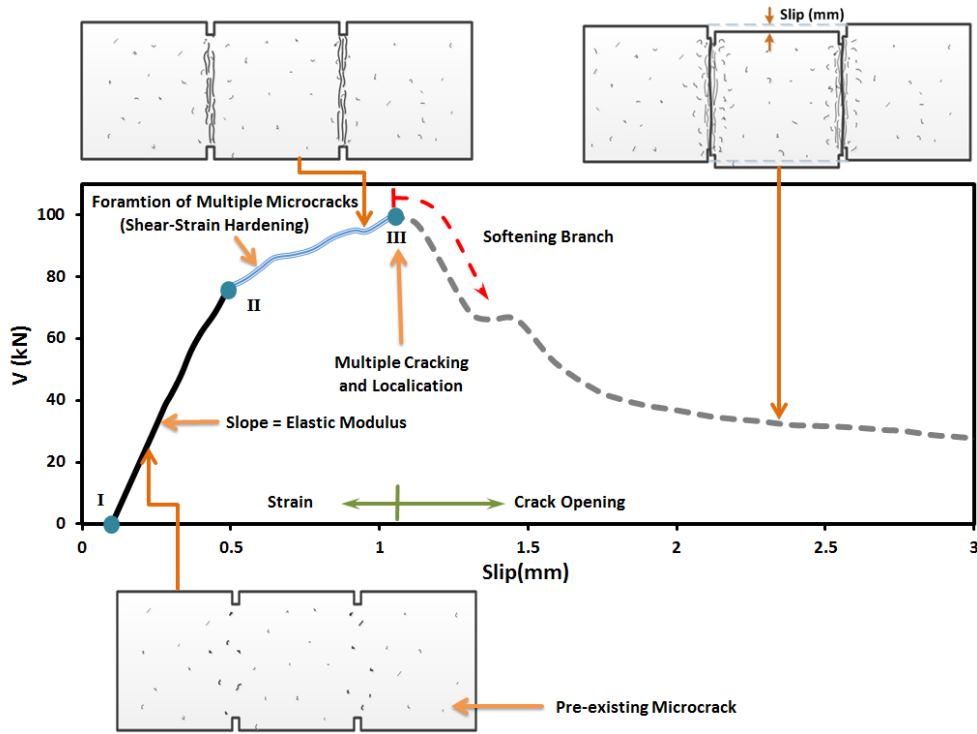


Figure 4-28: Typical shear load-slip curves for the UHPFRC material.

4.4.2.1 Linear-Elastic Behaviour

In this stage, the prism is un-cracked and an almost linear-elastic load-slip relationship in shear up to a well-defined cracking point was observed for the UHPFRC specimens (curve I-II). The major part of shear strength in all the mixes with different V_f is achieved in this stage, but with a very small part of corresponding deformations, as compared with the shear deformation at the peak shear load. No visible microcracks appear before reaching point II, so this stage can be considered as linear elastic with a modulus of Elasticity E . The shear slip factor (SSF) can be calculated based on equation 4-5.

$$SSF = \frac{slip}{h_{eff}} \quad (4-5)$$

where h_{eff} is the reference height after accounting for notch and is assumed to be 30 mm and 50 mm for PS-50 and DPS-100 prism samples respectively. The first-cracking shear load, SSF_{cr} , corresponding to the loss of linearity of elastic behaviour, V_{cr} , was reached at a SSF around $SSF_{cr} = 1\%$ for both PS-50 and PS-100.

4.4.2.2 Pseudo Strain Hardening Behaviour

Once the shear stresses along the notch exceed the shear capacity of the UHPFRC, a series of multiple microcracks form which are bridged by steel fibers. Subsequent to the formation of microcracks, the shear stresses are transferred by a combination of fiber pull-out resistance and matrix shear strength. Steel fibers are capable of transferring a higher load after the formation of the first microcrack which allows the formation of a new crack. This phenomenon is called a pseudo strain hardening, as no true plastic microstructural deformation is formed. A gradual reduction in the shear stiffness of the UHPFRC matrix was observed in this stage. In prism specimens with $V_f = 0\%$, the microcrack tends to rapidly develop into a macrocrack over the full depth of the notched region. Thus the notched region of prism samples suddenly fractures in a brittle manner with a very sudden drop in load carrying capacity. However, in the specimens with $V_f = 2\%-5\%$, the presence of short steel fibers significantly stabilizes the cracking process and enhances the ductility of the UHPFRC. As a result, several microcracks form during this stage until the peak shear load (maximum point of curve) is reached which is followed by the formation of the macrocrack along the notch (See Point III in Figure 4-28). The curves in this figure show that hardening is more pronounced for mixes with $V_f = 4\%$ and 5% , as compared to mixes with less V_f .

While no clear trend in the improvement of SSF corresponding to peak load, SSF_{peak} with increasing fiber volume content was observed, the incorporation of higher V_f was found to increase both V_{peak} and SSF_{peak} . This improvement is related, in part, to the pullout and dowel action of the fibers during shear cracking.

4.4.2.3 Softening Behaviour

The post-peak response of UHPFRC in shear is characterized by a softening branch (See Figure 4-28). In this stage, additional deformation localizes in a macrocrack and results in larger crack width until it becomes visible to the naked eyes.

The post-peak response in shear is mainly influenced by the combined contribution from the fiber bridging effect and the secondary load transfer mechanism which

refers to bending and shear resistance (dowel action) of a portion of fiber between the cracked surfaces.

4.4.3 Peak Shear Strength

The measured test results from shear testing of UHPFRC were further analysed to establish the peak shear strength factor, k_v . This factor was solved as the peak shearing stress value applied to an imposed surface supporting no normal force. The k_v was normalized by the square root of the 28 day CU-50 compressive strength as shown in Eqn. 4-6.

$$k_v = \frac{V_{peak}}{A_{eff} \sqrt{f'_{cu}}} \quad (4-6)$$

$$A_{eff} = w_{eff} \times h_{eff} \quad (4-7)$$

where V_{peak} is the shearing force necessary to cause failure along a surface and A_{eff} denotes the cross-sectional area along which failure occurs after accounting for the notch. The influences on shear stress factor from different parameters are discussed in the following sections.

4.4.3.1 Influence of Silica Fume to Binder Ratio

The influence of three different SF/B ratio, i.e., SF/B = 0.22, 0.24, and 0.26, on the shear strength of PS-50 is illustrated in Figure 4-30. While no significant change in k_v was observed with an increase in the SF/B ratio for non-vibrated mixes, a 45% increase in k_v was observed for the vibrated mixes as the SF/B ratio increased from 0.22 to 0.26. This improvement is attributed, in part, to microstructural improvements of UHPFRC matrix by reducing the mix porosity to a minimum value (e.g. Sarkar and Aitchen 1987).

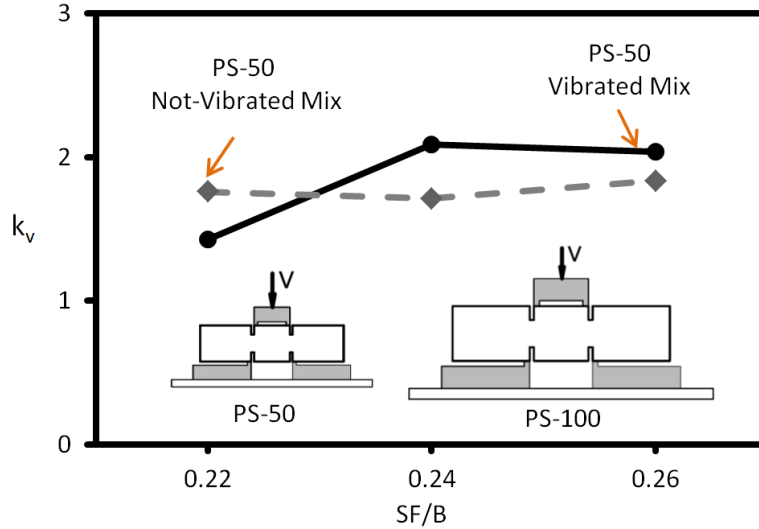


Figure 4-29: Variation of peak shear strength factor, k_v , with SF/B for PS-50 specimens.

4.4.3.2 Fiber Volume-Fraction

The peak shear strength factor, k_v , for vibrated and non-vibrated UHPFRC mixes with $V_f = 0-5\%$ are shown in Figure 4-31. An almost linear increase in k_v was noted for PS-50 samples with $V_f = 0-4\%$ followed by a plateau, where the shear strength attained a constant value. Compared to the plain UHPFRC mix, the use of vibrated mix with $V_f = 2-5\%$, resulted in an 150 to 260% increase in shear strength. The non-vibrated mix displayed a similar trend in which the k_v was an average of 16% lower than the vibrated one.

No limits for the minimal and maximal V_f are defined in the current codes of practice for UHPFRC in North America and Europe. As an initiative recommendation for minimal fiber content, sufficient V_f must be provided in UHPFRC to transfer shear stresses greater than the force carried by the UHPFRC matrix prior to shear cracking in order to prevent a brittle failure in structural elements.

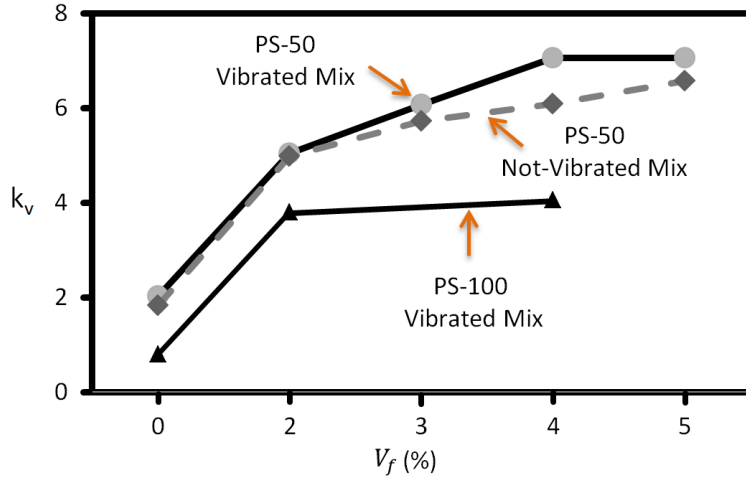


Figure 4-30: Variation of k_v against V_f for vibrated and non-vibrated PS-50 and vibrated PS-100.

The shear slip factor at peak shear strength (SSF_{peak}) for vibrated and non-vibrated PS-50 samples with $V_f = 0-5\%$ are shown in Figure 4-32. It is observed that the SSF_{peak} value for PS-50 samples linearly increases with the addition of steel fibers to plain UHPFRC mix. The addition of $V_f = 2\%$, 3% , 4% , and 5% to plain mix was found to increase the SSF_{peak} by average values of 121%, 174%, 277%, 279%. The non-vibrated mix displayed a similar trend in which the SSF was an average of 17% lower than the vibrated one.

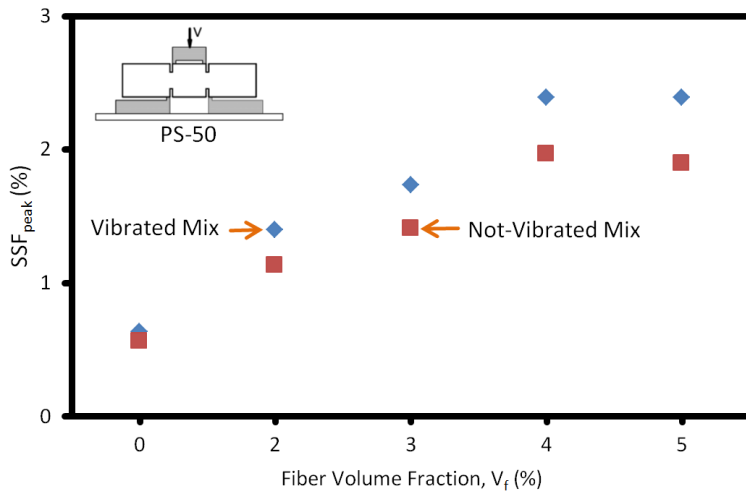


Figure 4-31: Relationship between SSF_{peak} and V_f for PS-50 with $V_f = 0-5\%$.

4.4.3.3 Influence of Size Effect

In order to understand the influence of size effects on the shear strength of UHPFRC, a series of prisms over a specimen size range of 2 with $V_f = 0, 2,$ and 4% were cast and the results are shown in Figure 4-33. Decreases of 25% and 43% in shear strength were respectively noted for mixes with $V_f = 2\%$ and 4% as the specimen sizes doubled. These results indicate that the influence of specimen size on shear strength increases as the V_f changes from 2% to 4%.

The SSF_{peak} for vibrated mixes with $V_f = 0, 2,$ and 4% are shown in Figure 4-33 for both PS-50 and PS-100. Similar to the trend observed for PS-50, the addition of steel fibers to plain mix causes an almost linear increase in SSF_{peak} which is slightly lower than values for PS-50.

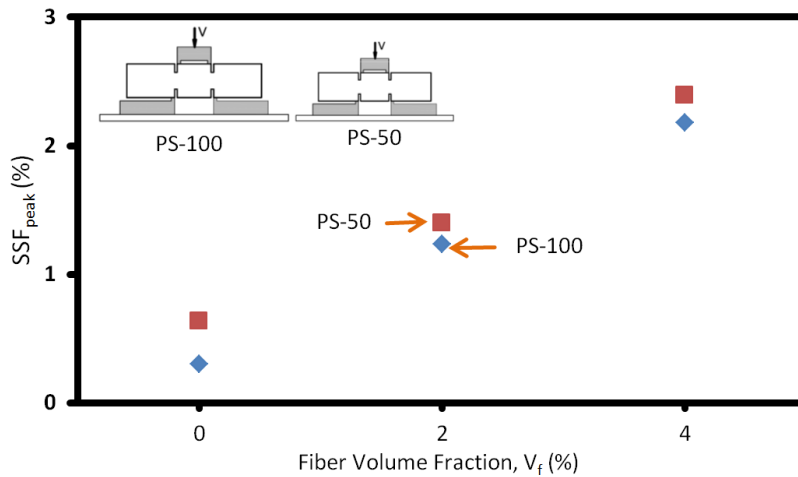


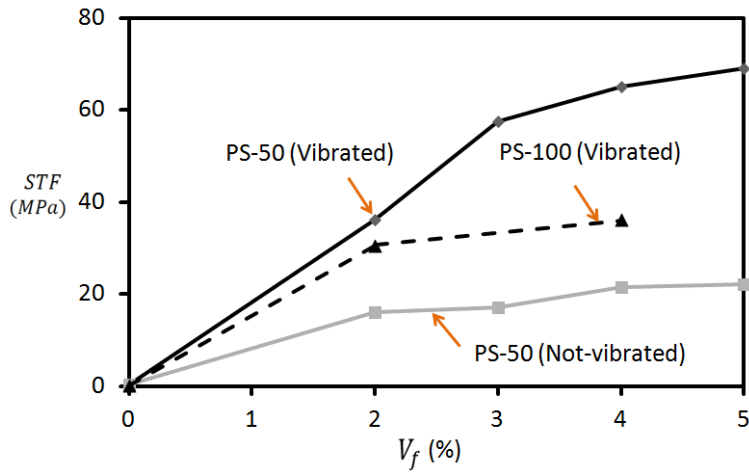
Figure 4-32: Variation of SSF_{peak} against V_f for PS-50 and PS-100.

4.4.4 Shear Toughness Factor (STF)

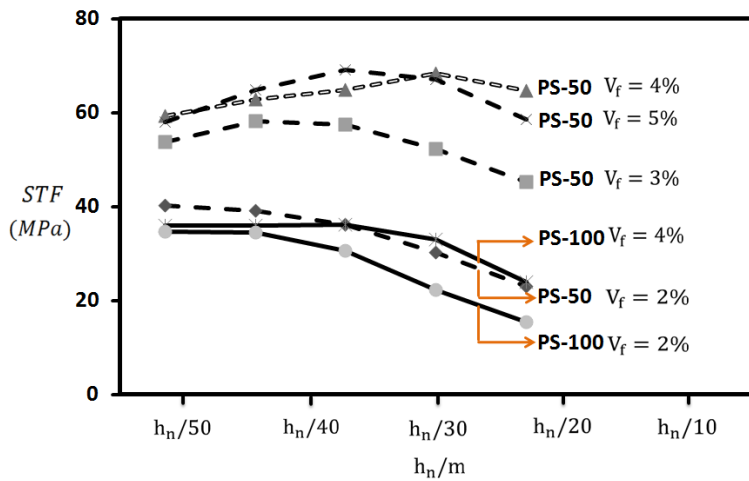
STF represents the capability of the UHPFRC to prevent structural members from brittle failures in shear. The STF originally proposed by Higashiyama and Banthia (2008) was used to evaluate the energy absorption capacity of UHPFRC. This factor is characterised by the area under the experimental shear load-slip curve and is given as

$$STF = \frac{\Gamma}{\left(\frac{h_n}{m}\right)w_n h_n} \quad (4-8)$$

where Γ (N.mm) is the shear toughness (area under the curve) up to deflection of h_n/m (h_n in mm). Five different values of h_n/m , $m = 50, 40, 30, 20,$ and 10 were used to evaluate the influence of V_f on STF of prism specimens over a size factor of 2. The results are summarized in Figure 4-33(a and b). The STF values have a descending trend as the h_n/m ratios increase, except for PS-50 with $V_f = 4\%$ where a plateau was reached, as shown in Figure 4-33(b). This is because, compared to the other mixes, the mix with $V_f = 4\%$ tends to show a more gradual decrease in shear load in the softening branch, which provides a higher value of Γ .



a)



b)

Figure 4-33: (a) Influence of V_f , consolidation, and specimen size on STF of PS-50 ($h_n/30$); and (b) variation of STF with different h_n/m for PS-50 and PS-100 specimens.

4.4.4.1 Influence of Fiber Volume-fraction

Very Low STF values were observed for both vibrated and non-vibrated plain mixes. This is mainly due to lack of a second mechanism with equal or higher shear strength that can sustain the shear stresses after the initiation of macrocrack in UHPFRC matrix. This low STF was observed to be significantly improved by addition of steel fibers to the mix. The higher the fiber content, the slower the rate of microcrack propagation and thus higher STF. While no significant improvement in STF was observed for the non-vibrated mix with a change in fiber contents, increases of 59, 79, and 91% in STF were noted for the vibrated mix containing 3, 4, and 5% fiber as compared to the mix with 2% volume-fraction of fiber. The higher values of STF (energy-absorbing capability) for mix with $V_f=4$ and 5% are attributed to the large number of fibers in the fracture zone, which significantly restrains crack propagation in fracture surfaces.

4.4.4.2 Consolidation

The influence of consolidation on STF is shown in Figure 4-34 (a). A 160% improvement in STF was noted for the vibrated mix with 2% fiber over the non-vibrated one. This results from the improved bond between fiber and UHPFRC matrix as the air voids around the fibers are reduced. Higher improvements were noted for vibrated mix with 3-5% fiber over the similar non-vibrated mix where an average increase of 235% in STF was obtained.

4.4.4.3 Influence of Size Effect

The influence of specimen size on the STF was studied and a clear size effect was observed. The test results showed that the STF decreased by 27 and 64% for vibrated mix with $V_f = 2$ and 4% respectively as the specimen size doubled. It was noted that the influence of prism height on the STF increases as the fiber volume-fraction increased from 0 to 4%. Compared to PS-50, the STF of PS-100 increases slightly for the change in V_f from 2 to 4%.

4.5 Equivalent tensile strength (ETS)

Direct tensile test (DTT) is the most reliable test setup to characterize the tensile strength of UHPFRC. This test generally requires more sophisticated equipments than used in the flexural test. Thus, in the absence of DTT, the equivalent tensile behaviour can be achieved from flexural tests. The first objective of this section is to quantify the contribution of short steel fibers to the flexural-tensile resistance of un-notched UHPFRC prism specimens. The second aim of this chapter is to study the influence of specimen size on the flexural-tensile strength of UHPFRC.

To extract the equivalent post-cracking tensile strength (ETS) of UHPFRC from the experimentally obtained flexural response of the prism specimens, equilibrium of the cracked section was established based on the stress pattern proposed by AFGC (AFGC 2002). The concept of the model proposed by AFGC is illustrated in Figs. 4-35.

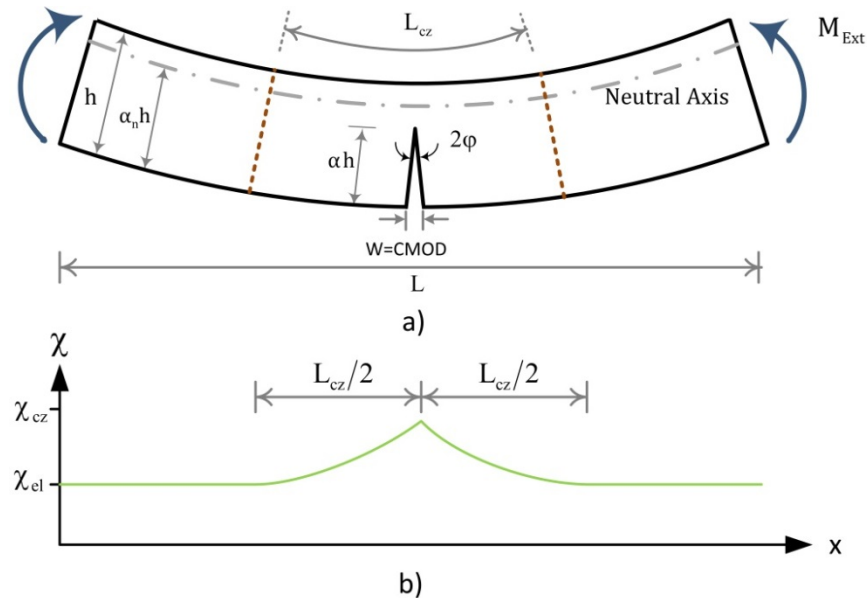


Figure 4-34: a) disturbed zone in crack UHPFRC beam, and b) Variation of curvature along the beam (after Casanova and Rossi 1996).

The analytical model proposed by AFGC uses kinematic assumptions of compatibility between the uncracked and cracked parts of the cross-section while simultaneously satisfying the equilibrium of forces and moments. See Figure 4-36 (c). The uncracked part of the cross section is assumed to behave in a linear-elastic

manner where Hooke's law applies to both the compressive zone and a small region of tensile strains below the neutral axis. See Figure 4-36 (b). The tensile force in the cracked section is sustained by the steel fibers crossing the crack and is treated as a non-uniform tensile stress distribution. See Figure 4-36 (a & b).

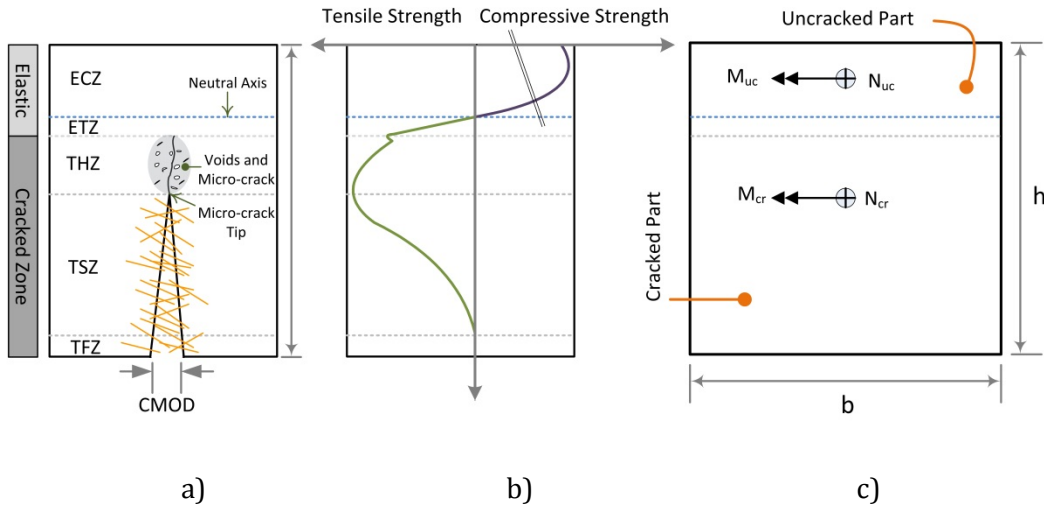


Figure 4-35: Full response of UHPFRC prism specimen under flexure and compression: (a) Geometry and situation; (b) Stiffness (c) Stress profile and definition of maximum stress softening.

The process of crack development generally consists of the following four stages which are illustrated in Figs. 4-35 (a) and described below.

- Stage I:* The first stage, linear elastic zone (LEZ), represents general elastic behaviour in both elastic compression zone (ECZ), and elastic tension zone (ETZ), without microcrack formation in UHPFRC matrix. Instead, one localized crack takes place in the constant moment region. The Kirchhoff hypothesis of normal to the mid-plane remain straight and normal as the flexural loading is applied was used. A linear stress distribution across the cross section was considered for this stage which is characterized by elastic modulus, E . By assuming linear strain distribution across the depth and ignoring shear deformation, the stress-strain relationships in Figure 4-36 (b) is used.

- *Stage II:* The next stage, tension hardening zone (THZ), is the initiation of several microcracks around the first microcrack in UHPFRC matrix until the PETS is reached.
- *Stage III:* This stage, tension softening zone (TSZ), refers to the evolution of the failure, which is governed by the fiber bridging. The shape of the softening curve depends on the fiber content in the fracture zone and the fiber alignment along the prism specimen. The fibers in this stage start pulling out while others could possibly rupture. The stress distribution in this stage is shown in Figure 4-36 (b). A non-linear stress distribution (ETS-CMOD) curve is used for tension part.
- *Stage IV:* The final stage, traction free zone (TFZ), defines failure when the CMOD reaches the ultimate crack opening width, e.g., half of the fiber length. The new fictitious crack surfaces with no load bearing capacity are formed in this stage.

4.5.1 Analytical model for ETS-CMOD

A rectangular section of width b , height h , and length L is considered. This section can be divided into two parts: (1) the uncracked part where there is a compressive force in ECZ as well as a small tensile force in ETZ and (2) the cracked part where the fibers are bridging the crack and carry the tensile force in THZ and TSZ. **Error! Reference source not found.** The uncracked part is assumed to behave in accordance with engineering beam theory: plane section remains plane so that there is a linear distribution of the axial strains in the un-cracked section. The normal force and moment equilibrium of the cracked section requires that:

$$N_{ext} = N_{uc} + N_{cr} \quad ; \quad N_{ext} = 0 \quad (4-9)$$

$$M_{ext} = M_{uc} + M_{cr} \quad (4-10)$$

The resulting normal force in un-cracked part (ECZ and ETZ) can be expressed as follows:

$$N_{uc} = \frac{E\chi_m b h^2}{2} [(1 - \alpha_n)^2 - (\alpha - \alpha_n)^2] \quad (4-11)$$

The relative height of the neutral fiber is as follows:

$$\alpha_n = \alpha - \frac{\sigma_w(w)}{E\chi_m h} \quad (4-12)$$

where χ_{cz} is the curvature of the cracked zone and can be determined by Eqn. 4-13.

The normal force in the cracked part:

$$N_{cr} = \frac{\alpha b h}{w_0} \int_0^w \sigma_w(w) dw \quad (4-13)$$

Resistance moment in the un-cracked part:

$$M_{uc} = \frac{E\chi_m b h^3}{3} [(1 - \alpha_n)^3 - (\alpha - \alpha_n)^3] + h\alpha_n N_{uc} \quad (4-14)$$

Resistance moment in the cracked part:

$$M_{cr} = \alpha h N_{cr} - \frac{(\alpha h)^2 b}{w} \int_0^w w \sigma_w(w) dw \quad (4-15)$$

4.5.1.1 Kinematic Hypothesis of Non-linear Hinge

The deformed configuration of a UHPFRC prism subjected to flexural loading is shown in Figure 4-35(a). The prism behaves linear-elastically in both ends with a curvature of χ_{el} , while the middle zone, L_{cz} , experiences a parabolic variation of curvature called χ_{cz} .

$$\chi_{el} = \frac{M}{EI_{uc}}; I_{uc} = \frac{bh^3}{12} \quad (4-16)$$

$$\chi_{cz} = \frac{M}{EI_{cr}} \quad (4-17)$$

A kinematic assumption originally proposed by Casanova and Rossi (1996) was adopted in this method to characterize the hinge zone. Several researches showed that the length of the disturbed zone, L_{cz} , increases with an increase in the crack length. Based on several FEM analyses, the L_{cz} was found to be approximately a linear function of crack length.

$$L_{cz} = 2\alpha h \quad (4-18)$$

A parabolic relation between χ_{el} at the cracked section and χ_{cz} at a distance of $L_{cz}/2$ away from the macrocrack was developed (Rossi 2005).

$$\chi(x) = a_0x^2 + a_1x + a_2 \quad (4-19)$$

$$a_0 = \left[\frac{4}{(L_{cz})^2} (\chi_{cz} - \chi_{el}) \right]; \quad a_1 = \left[\frac{4}{L_{cz}} (\chi_{cz} - \chi_{el}) \right] \quad a_2 = \chi_{cz} \quad (4-20)$$

The angular rotation ϕ is

$$\phi = \int_0^{\frac{L_{cz}}{2}} \chi(x) dx = \frac{\chi_{cz} + 2\chi_{el}}{3} \alpha h \quad (4-21)$$

Thus the crack width can be determined by Eqn. 4-22.

$$w_{CMOD} = \frac{2(\chi_{cz} + 2\chi_{el})}{3} (\alpha h)^2 \quad (4-22)$$

4.5.2 Iterative Process

As these integrals are not explicit, an incremental analysis approach is used. The trapezoidal rule was implemented to approximate the tensile stress function in the cracked area.

$$\int_0^{w_{i+1}} \sigma_w(w) dw = \int_0^{w_i} \sigma_w(w) dw + \left(\frac{\sigma_w^i(w) + \sigma_w^{i+1}(w)}{2} \right) (w_{i+1} - w_i) \quad (4-23)$$

The axial component can be expressed incrementally between two successive steps of cracking:

$$N_{cr}^{i+1} = N_{cr}^i \frac{\alpha_{i+1}}{\alpha_i} \frac{w_i}{w_{i+1}} + \alpha_{i+1} b h \left(\frac{\sigma_w^i(w) + \sigma_w^{i+1}(w)}{2} \right) \left(1 - \frac{w_i}{w_{i+1}} \right) \quad (4-24)$$

where $\sigma_w^i(w)$ at step $i = 1$ is equal to CETS described and is illustrated in Figure 4-37. The moment in the cracked part can also be expressed incrementally between two successive steps of cracking:

$$M_{cr}^{i+1} = M_{cr}^i \left(\frac{\alpha_{i+1}}{\alpha_i} \frac{w_i}{w_{i+1}} \right)^2 + \alpha_{i+1} h N_{cr}^{i+1} \left(1 - \frac{w_i}{w_{i+1}} \right) - \sigma_w^{i+1}(w) \left(1 - \frac{w_i}{w_{i+1}} \right)^2 \frac{b(h\alpha_{i+1})^2}{2} \quad (4-25)$$

Having the $\sigma_w^i(w)$ and w_i completely defined at step i , it is possible to evaluate the step by step crack height (αh), depth of neutral axis ($\alpha_n h$), curvature χ_{cz} as well as

the corresponding equivalent tensile stress (σ_{cr}) at step i+1. See Figure 4-36. To this aim, a MATLAB code was developed to implement the algorithm presented above.

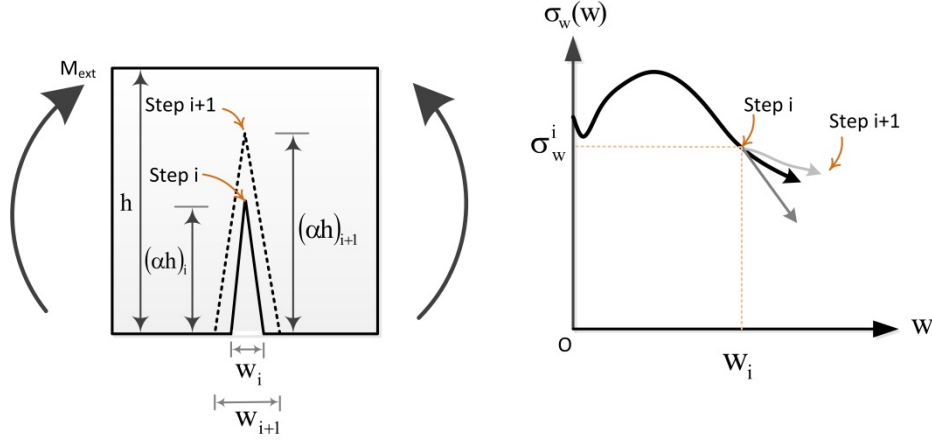


Figure 4-36: Situation of CMOD and equivalent tensile strength at two different steps.

4.5.3 Correlation between Deflection and Crack Width

The crack mouth opening displacement (CMOD) at the base of the macrocrack was determined by calculating the expansion between the two DIC measurement points. However, this data measurement may not be feasible in all the laboratories. Thus it is essential to relate the load mid-span deflection to CMOD for prism specimens of different sizes. As illustrated in the Figure 4-38, the slope of CMOD – δ curve is zero before the initiation of macrocrack. After this point, there is a disturbed zone where the relationship is quadratic. However, this phase is relatively short and can be neglected. After this stage, the rate is almost constant, regardless of the specimen size. If the mid-span deflection at the cracking point, δ_{cr} , is known, CMOD can be estimated using the following equation:

$$CMOD = v(\delta - \delta_{cracking}) \quad (4-26)$$

where δ is the mid-span deflection derived from either LVDTs or DIC system, $\delta_{cracking}$ is mid-span deflection at cracking, and v (*upsilin*) is

$$v = \frac{CMOD}{\delta} \quad (4-27)$$

The change in CMOD against δ is plotted for PF-50, PF-100, PF-150, and PF-200 in Figure 4-37 for mixes with $V_f = 2\%$. The curves are offset horizontally to avoid overlap, as the slopes of some curves are similar. Unlike the PF-50 samples with a smaller ν factor, the PF-100, PF-150, and PF-200 presented a similar ν factor. The ν factors for mixes with $V_f=2\%$ and 4% are plotted in Figure 4-38. Similar ν factors were observed for PF-50 with $V_f = 2\%$ and 4%. However the ν factor for larger specimens was found to decrease as the fiber content was increased from 2% to 4%. This is most probably because the higher fiber content would result in smaller spacing between fibers which increases load transfer and interaction between fibers. This phenomenon would lead to the formation of more microcracks and thus retard the expansion of CMOD. Average values of $\nu = 1.24, 1.48, 1.53,$ and 1.52 were found for PF-50, PF-100, PF-150, and PF-200 respectively. Based on the assumption of a perfect hinge mechanism at the crack, AFGC code (2002) recommended a value of 1.2 which does not account for the influence of prism sizes on this factor.

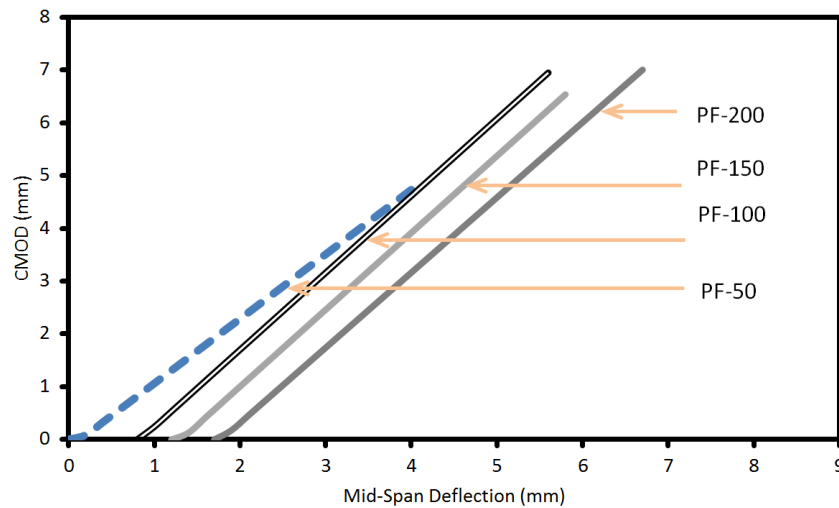


Figure 4-37: Variation of CMOD against mid-span deflection for prism specimens.

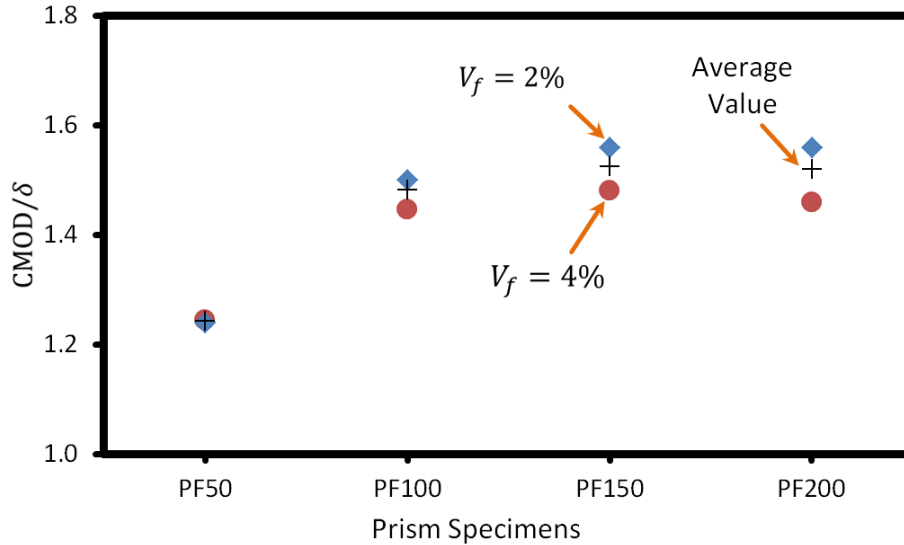


Figure 4-38: Values of v (*upsilin*) for prism specimens with $V_f = 2\%$, $V_f = 4\%$, and average v value.

4.5.4 Cracking Equivalent Tensile Strength (CETS)

The CETS of UHPFRC is found to be lower than the FCS derived from flexural tests (e.g. Chanvillard 2006, abc 2009, abc 2010). A modification factor (ξ_{SF}) originally proposed by CEB-FIP (1990) and adopted by AFGC is used to predict the CETS. The ξ_{SF} was developed using both experimental test results and fracture mechanics concept.

$$CETS = \xi_{SF} \cdot FCS ; \xi_{SF} = \frac{\alpha_{fl} \left(\frac{h}{h_0}\right)^{0.7}}{1 + \alpha_{fl} \left(\frac{h}{h_0}\right)^{0.7}} \quad (4-28)$$

where ξ_{SF} is modification factor and accounts for variation in specimen height. α_{fl} is a factor representing the concrete brittleness and increases with increasing brittleness of the concrete. A value of $\alpha_{fl} = 2$ is proposed for UHPFRC. The h is the overall height of the prism and $h_0 = 100$ mm. Chanvilard and Riguid (2003) studied the influence of steel fiber ($V_f = 2\%$) and specimen size on the tensile mechanical properties of DUCTAL concrete. It was found that the ratio of FCS to cracking tensile strength directly obtained from direct tension tests decreases as the specimen height increases which implies that the tensile strength is highly size dependent (e.g. Chanvilard and Riguid 2000).

4.5.5 ETS-CMOD Curve

The proposed algorithm was implemented in MATLAB to establish the ETS-CMOD curve from experimentally measured load and mid-span deflection. The results of ETS-CMOD for PF-50 with four different fiber volume fraction, i.e., $V_f = 2\%$, 3% , 4% , and 5% are shown in Figure 4-40. The initial drop in the ETS-CMOD curve immediately after the first cracking point can be explained by physical phenomena and numerical instability in the model. From a physical point of view, the fibers are only mobilized after a certain CMOD occurs and they do not all immediately act as reinforcement to bridge the cracks. Consequently the ETS decreases immediately after concrete cracking and subsequently increases as the fibers are engaged to act as reinforcement. Computational errors can also occur with the stepwise solution approach, as was observed when the crack length was fairly small. To offset this potential source of error, a weighting process was introduced (AFGC 2002) to stabilize the ETS-CMOD curve as follows:

$$ETS_i = \frac{2(ETS)_i + (ETS)_{i+1}}{3} \quad (4-29)$$

The results of the inverse analysis technique were verified by using the resulting ETS-CMOD relationship to predict the load-deflection behaviour of the prisms using a cross-sectional flexure model based on engineering beam theory. There was good agreement between all the model and test results.

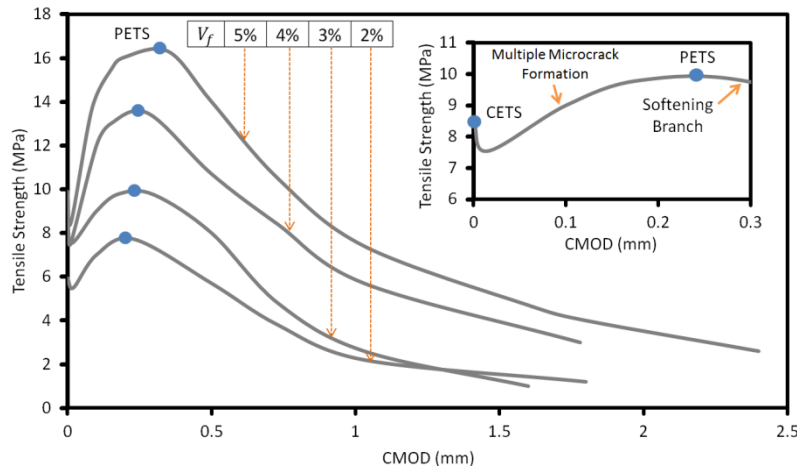


Figure 4-39: Equivalent tensile strength-CMOD response of PF-50 prism specimens with different fiber volume fraction.

4.5.6 Peak Equivalent Tensile Strength (PETS)

The technique described in the past section was used to study the influence of four different specimen sizes and five different fiber volume fractions on the PETS of UHPFRC. Each of these are described in the following sections.

4.5.6.1 Influence of V_f on PETS

The influence of four different fiber volume fractions, $V_f = 0\%$, 2%, 3%, 4%, and 5% on PETS of PF-50 prism specimens were investigated and the results are shown in Figure 4-41. An almost linear increase of 22%, 64%, 76%, and 116% in PETS was observed after the addition 2%, 3%, 4%, and 5% of steel fibers to UHPFRC matrix. This is because a higher number of short steel fibers are present in fracture zone to bridge the macrocrack. The non-vibrated mix displayed a similar trend in which the PETS was an average of 27%, 59%, 50%, and 30% lower than the vibrated one for mixes with $V_f = 2\%$, 3%, 4%, and 5% respectively. This lower strength is most likely due to: 1) weaker bonds between steel fibers and the surrounding matrix in the non-vibrated mix which would result in weaker pullout efficiency, 2) Fewer fibers were oriented in the direction of principal loading. The later one was visually observed by investigating the fractured zone of both vibrated and non-vibrated samples. It was found that compared to the non-vibrated mix, more fibers were aligned along the longitudinal direction of prism in the vibrated mix. This improved alignment configuration is most probably because the steel fibers tend to align themselves along the flow of mix during casting. The flow of casting was along the longitudinal direction of prism specimens and is further discussed in Figure 3-7.

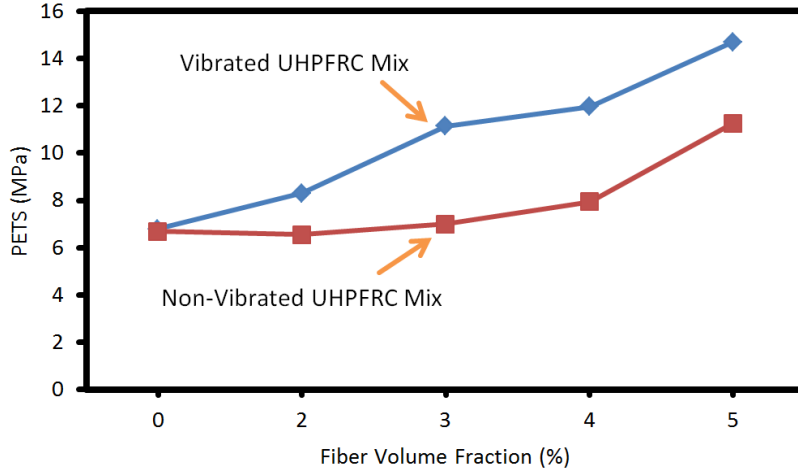


Figure 4-40: Effect of fiber volume fraction on PETS of UHPFRC.

4.5.6.2 Influence of Specimen Size

In order to gain a better understanding of the influence of specimen size on the mechanical properties of UHPFRC in tension, the average PETS from four different specimen sizes, PF-50, PF-100, PF150, and PF-200 with $V_f = 0\%$, 2%, and 4%, are compared in Figure 4-42. The mix with $V_f = 2\%$ and 4% exhibited averages of 11% and 55% respectively, higher than the mix with no fiber content. Similar experimental observations are reported by other researchers (e.g. abc et al. 2008, abc 2010).

As presented in Figure 4-42, the PETS of UHPFRC mixes with different V_f tend to decrease as the specimen size increases. This indicates that the PETS is influenced by the size of specimen which may be explained in the same way as for flexural behaviour in section 4.4.4. The percentage of decrease in PETS for PF-100, PF-150, and PF-200 compared to PF-50 prism specimen are depicted in Figure 4-43. An almost linear decrease in PETS with higher rates at higher fiber contents were observed for all the V_f except for PF-200 with $V_f = 0\%$ where the rate of decrease in PETS is much higher.

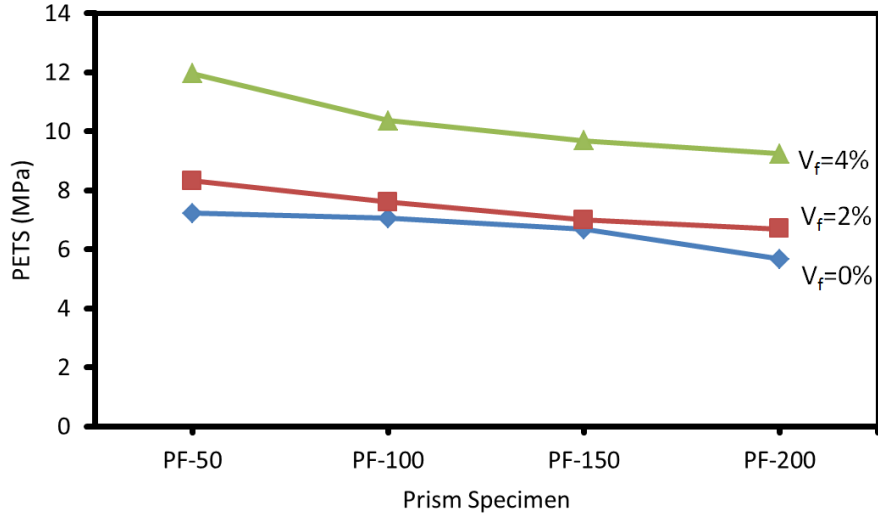


Figure 4-41: Influence of specimen size on PETS of UHPFRC with $V_f = 0, 2\%$, and 4% .

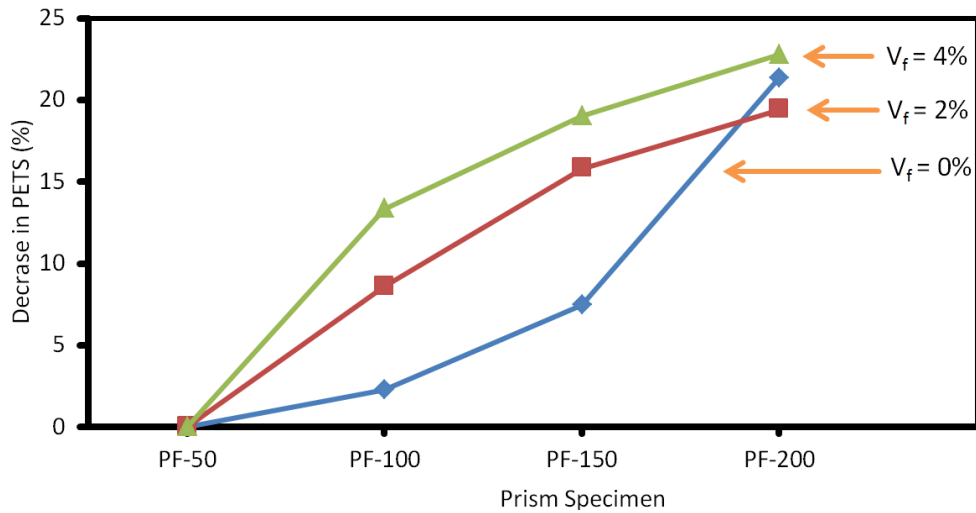


Figure 4-42: Relationship between the decrease in PETS and UHPFRC prism specimens with $V_f = 0\%, 2\%$, and 4% .

4.5.6.3 CMOD at PETS

The crack mouth opening displacement (CMOD) at PETS for mixes with $V_f = 2\%$ and 4% are plotted in Figure 4-44 for PF-50, PF-100, PF-150, and PF-200 samples. It is noted that the PETS is attained at relatively small CMOD which are shown in this figure. This very low fictitious crack width can be interpreted as a result of a desirable interaction between steel fibers and the UHPFRC matrix which efficiently retards the coalescence of multiple microcracks into one single macrocrack.

Compared to mixes with $V_f = 2\%$, higher CMOD values were found for mixes with $V_f = 4\%$, as shown in Figure 4-44.

The results of DIC analysis show that no crack opening occurs until a significantly high level of tensile stress is reached: around 80-90% of PETS. Before this point, the cracks are barely visible with naked eye. This would indicate that in UHPFRC material, a high percentage of tensile strength is achieved with a homogeneous pseudo-plastic material behaviour, with no localisation of deformation in a single crack. Compared to mixes with $V_f = 2\%$, the CMOD of mixes with $V_f = 4\%$ at the PETS was found to be 18%, 55%, 62%, and 31% higher for PF-50, PF-100, PF-150, and PF-200 respectively.

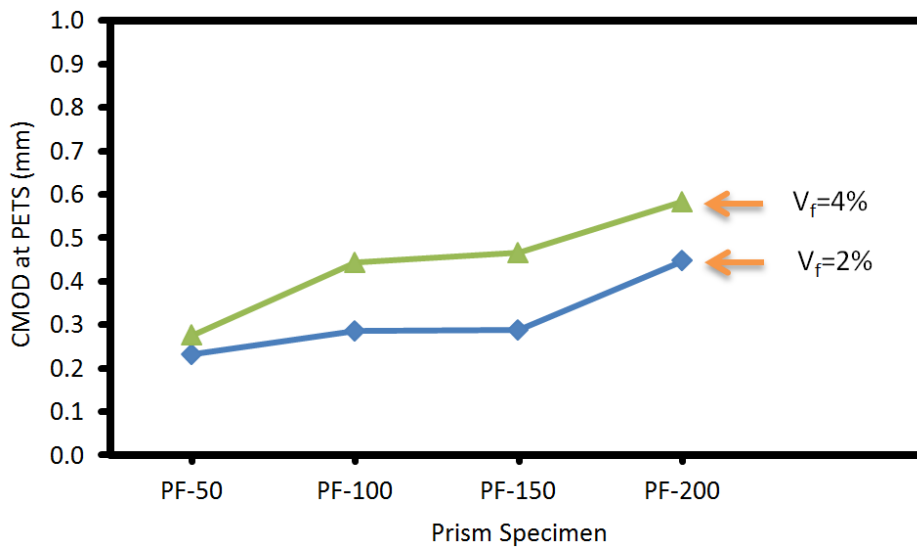


Figure 4-43: Relationship between the CMOD and prism specimen size for two different fiber volume fractions.

Chapter 5

5 Composite Connections: Experimental Program

5.1 Introduction

The primary objective of this chapter is to provide an overall understanding of a novel composite connection system constructed with a cast-in embedded steel plate in the concrete flange. Two different generations of concrete were used for the concrete flange: ultra-high performance fiber reinforced concrete (UHPFRC) and fiber reinforced concrete (FRC) material. A total of 42 laboratory tests were completed in the I. F. Morrison Structural Engineering Laboratory at the University of Alberta. This series of tests provides a good understanding of the behaviour of the composite connections subjected to the pull-out loading. The configurations of the composite connections were selected to include an extensive range of the design parameters. The primary variables included the configuration of the steel tension key (STK), size of STK, embedded length of cast-in steel plate, addition of double headed stud (DHS), thickness of cast-in plate, and generations of concrete, i.e., UHPFRC material with $V_f = 0, 2, 4\%$ and FRC material with $V_f = 1\%$. Furthermore, the details of the composite connections, fabrication procedures, test set-up, physical instrumentation, digital imaging correlation (DIC) system, and the testing procedure are discussed in this chapter. All the tests were complemented by ancillary material tests including steel coupon test, mechanical properties of the UHPFRC and FRC material in compression and flexure.

5.2 Description of Pull-Out Specimen

A series of preliminary finite element analyses were completed to investigate the influence on the composite connection's load-slip response from several parameters including the loading and boundary conditions, geometric dimensions of the connection's components, and other parameters that may influence the response of

the proposed connections. The developed FEA model allowed a detailed understanding of the stress and strain distribution in the pull-out composite connection's components and helped to rationally select the relevant parameters and configurations for experimental program. An emphasis in the FEM analysis was to develop connection systems which are expected to present a more enhanced response than the earlier configurations with conventional concrete materials (Hegger et al. 2009, Abarmiski 2011). The final configuration of the proposed connection system is presented in the Figure 5-1. The proposed connection system consists of a concrete beam, cast-in embedded steel plate, reinforcement cage, and double headed stud.

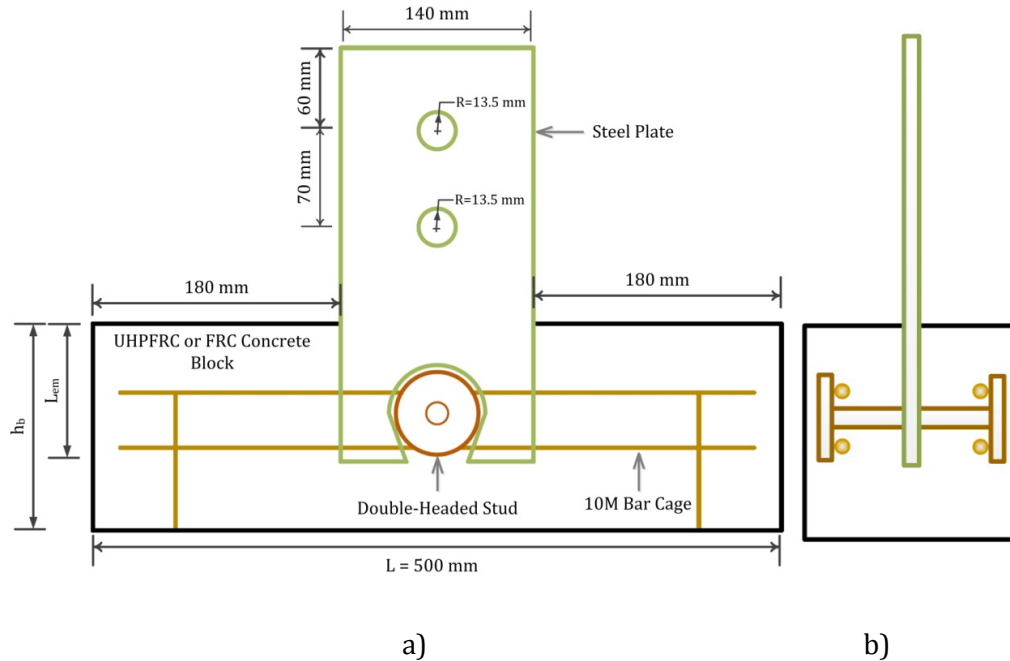


Figure 5-1: Overall geometry and configuration of the pull-out specimen, a) Front view, b) Side view.

5.3 Specimen Nomenclature

The composite connections are named by five characters in the format presented below to facilitate the discussion about the various composite connection specimens. The first characters represent the tension key configuration, which includes circular tension key, puzzle-strip tension key, or omega-shaped tension key. The second character represents the types of the concrete used for the beam:

ultra-high-performance fiber-reinforced concrete (UHPFRC) material, and fiber reinforced concrete (FRC) material. The third character symbolizes the size of the tension key (height or radius). The last two characters refer to the plate thickness and fiber volume fraction (V_f) respectively. A complete list of the connections specimens constructed with UHPFRC and FRC material are provided in the Table 5-1 and Table 5-2.

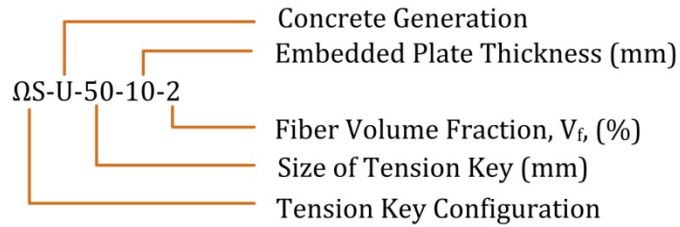


Table 5-1: Details of composite connections with UHPFRC material

Item	Designation	V_f	Shear Key Configuration	d_h or h_h (mm)	DHS	L_{em} (mm)	t_p (mm)
1	ΩS [†] -U-50-10-2	2	Ω-Shaped	50	A	100	9.53
2	ΩS-U-70-08-2	2	Ω-Shaped	70			8.00
3	ΩS-U-70-10-0	0	Ω-Shaped	70			9.53
4	ΩS-U-70-10-2	2	Ω-Shaped	70			9.53
5	ΩS-U-70-10-2 ^{††}	2	Ω-Shaped	70	N/A		9.53
6	ΩS-U-70-10-4	4	Ω-Shaped	70	A		9.53
7	ΩS-U-70-12-2	2	Ω-Shaped	70			12.7
8	ΩS-U-70-16-2	2	Ω-Shaped	70			15.9
9	ΩS-U-70-16-2	2	Ω-Shaped	70		150	15.9
10	ΩS-U-70-20-2	2	Ω-Shaped	70	A	100	19.1
11	ΩS-U-90-10-2	2	Ω-Shaped	90		9.53	
12	PS [‡] -U-70-10-2	2	Puzzle-Strip	70	A	100	9.53
13	PS-U-70-16-2	2	Puzzle-Strip	70			15.9
14	OS [‡] -U-50-10-2	2	O-Shaped	50	A	100	9.53
15	OS-U-70-10-2	2	O-Shaped	70			9.53
16	OS-U-70-16-2	2	O-Shaped	70			15.9

[†]ΩS: Omega-shaped Tension Key

[‡]PS: Puzzle-Shape Tension Key

[‡]OS: Circular-Shape Tension Key

A: Available

N/A: Not Available

Table 5-2: Details of composite connections with FRC material

Item	Designation	V_f	Shear Key Configuration	d_h or h_h (mm)	DHS	L_{em} (mm)	t_p (mm)
1	PS-F-70-10-1	1	Puzzle-Strip	70	A	100	9.53
2	OS-F-70-10-1		Ω -Shaped	70			9.53
3	OS-F-70-16-1		Ω -Shaped	70			15.9
4	CS-F-70-10-1		O-Shaped	70			9.53
5	CS-F-70-16-1		O-Shaped	70			15.9

5.4 Specimen Fabrication

Two different molds were used to cast the composite connections: $L \times W \times H = 500 \times 150 \times 150$ mm and $500 \times 200 \times 150$ mm steel molds. For composite connections made of UHPFRC material, a small high performance EIRICH mixer was used. The capacity of this mixer allowed one specimen along with three $150 \times 50 \times 50$ mm prisms and three 50 mm cubes to be cast at the same time. For composite connections made of FRC material, a 160 liter Gilson drum mixer with drum rotation of 20 rpm was used. The mixer capacity allowed two specimens along with three $100 \times 100 \times 400$ mm prisms and three 100 mm diameter x 200 mm long cylinders to be cast at the same time. The composite connection tests were conducted using two replicate test specimens for each type of composite connection. Four 10M vertical reinforcements were used to support the 10M bar cage. The horizontal reinforcements were tied to the mold at different locations to prevent the rebar cage from moving during the casting. A small clear concrete cover thickness of 10 mm was used for all the reinforcements and the double headed studs, as the UHPFRC material features an outstanding durability.

Special care was taken to keep the embedded steel plate perpendicular to the concrete beam, as the results of the preliminary FEA indicated that it would significantly influence the behaviour of the connection system and might result in a premature failure. To this aim, a pair of 100 mm angles was used to fix the embedded steel plate during the casting process. The embedded steel plate was attached to the form by clamping a pair of angles to both embedded steel plate and the sides of the mold to firmly secure the plate in its proper location prior to concrete placement. Special care was taken to ensure a consistent embedment

length was used for all the samples. The axis of each embedded steel plate was checked to be perpendicular to the formed surface.

5.5 Composite Connection Components

5.5.1 Concrete Beam

Two different generations of concrete, i.e., UHPFRC and FRC material were used to study their influence on the pull-out response of the composite connection systems.

5.5.1.1 Mixing Procedure

Ultra-High-Performance Fiber-Reinforced Concrete (UHPFRC)

The mixing sequence and mixer speed were adopted from the mix method explained in chapter 3 of this document, where a high performance pan mixer was used to achieve a homogenous product. The mass and volume of each mix were 15 kg and 5 liters respectively. All batches were mixed using a constant rotor speed of 30 Hz. The summary of the UHPFRC mix composition given in Table 5-3.

Table 5-3: UHPFRC composition normalized by the mass of cement

Components	Type	Weight
Portland cement	HS	1.00
Silica Fume (SF)	0.35	0.35
Fine Sand	d<1mm	0.56
Added water		0.19
Superplasticizer (SP)*	Glenium 3030	2.10%
Total Water†/Binder‡	0.18	0.18

* Solid content of SP

†Total Water=Added Water + Water from SP ‡Binder=Cement+SF

Multiple batches of UHPFRC mix are required to fill each connection specimen, as the small EIRICH mixer capacity was limited. To achieve a homogenous mix, each small batch was stored in a larger bucket and the concrete surface was immediately covered by a partially wet sponge to prevent any water evaporation. After all the small batches were completed, they were combined and the resulting new batch

was mixed for an extra 10 minutes to ensure all the smaller batches were completely mixed together and a homogenous product was gained.

For a typical large batch with $V_f = 2\%$, the energy input to the rotor at different times in the mixing sequence was recorded and compared for each single batch and a good consistence between them was found. In order to ensure the final mix was consistent, the workability of different batches were compared. The workability of the mix is characterized by the size of the initial pat formed after lifting the cone and after the flow table has been dropped twenty times within 20 seconds with an amplitude of 12.5 mm. A very good consistency between all the mixes of the different batches was observed.

Fiber Reinforced Concrete (FRC)

A 75 liter capacity drum mixer with a constant mixing speed of 60 rpm was sufficient for mixing the FRC material. Gravel was first mixed with all the sand for approximately 3 minutes. Afterwards, type HS cement was added and mixed dry for another 2 minutes before water was added. All the water, superplasticizer, and high range water reducer (HRWR) were mixed together before being added to the dry mix. The FRC became fluid after approximately 3 minutes of adding the water.

Hooked end Dramix steel fibers with yield strength of 1100 MPa, a length of 30 mm, and an aspect ratio of 55 were used in the current FRC mix. Fibers were added at around 3 minutes from the time of adding water to the mix over a period of 2 minutes. All mixes contained a fiber volume fraction of $V_f = 1\%$, as no significant improvement in flexural strength was found for mixes with higher fiber volume fraction (Adebar et al. 1997, Mirsayah & Banthia 2002, and Dinh 2009). The total time of mixing was about 10 minutes.

The air containments of the three different batches of FRC concrete were measured according to ASTM C231-09b and values of 2.4%, 1.6% and 2.9% were observed for castings A, B, and C respectively. The FRC slump was measured according to ASTM C143-10 standard during the casting and an average value of 118 mm was observed for all the three batches.

Table 5-4: FRC material composition

Components	Type	Weight
Cement	HS	391
Fine Aggregate	River Sand (4.75 mm)	796
Coarse Aggregate	Pea Gravel (14 mm)	990
Water		157
Steel Fibers	Double-ended Hooks†	78.6
Water Reducer	Mililiter/m ³	250
Superplasticizer	Mililiter/m ³	1800

†BEKARET Dramix ZP305

5.5.1.2 Placement

The overall view of the specimens before casting is shown in Figure 5-2. Both FRC and UHPFRC fresh mixes were poured into the molds in three equal layers from both ends of the molds, as the middle part of the mold was blocked by the embedded steel plate and the supporting angles. Companion cubes, cylinders, and prism molds were filled up in two equal layers. All the samples and companions were compacted using a vibrating table with a frequency of 90 Hz for around 120 seconds. The top surface of the specimen was screeded to a smooth finish. See Figure 5-3.

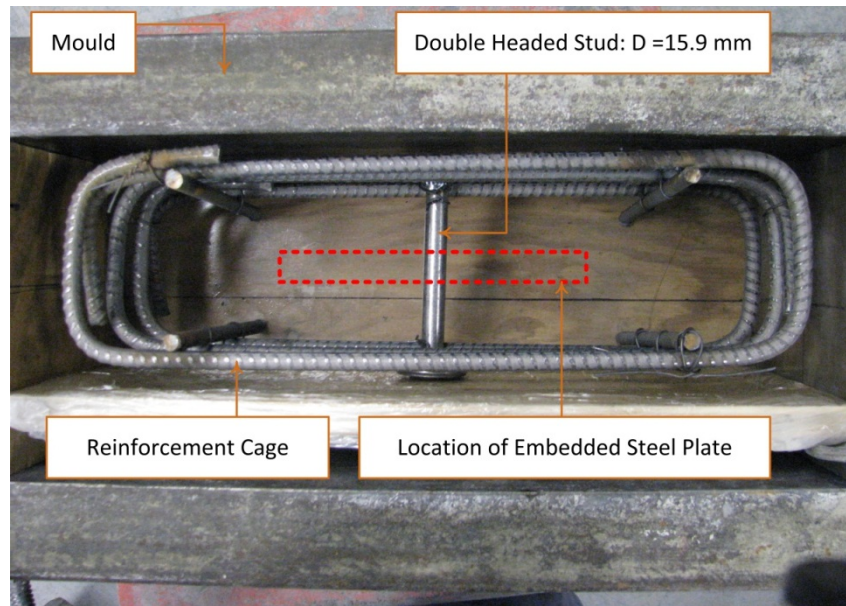


Figure 5-2: Top view of reinforcement cage, double headed stud (DHS) and formwork.

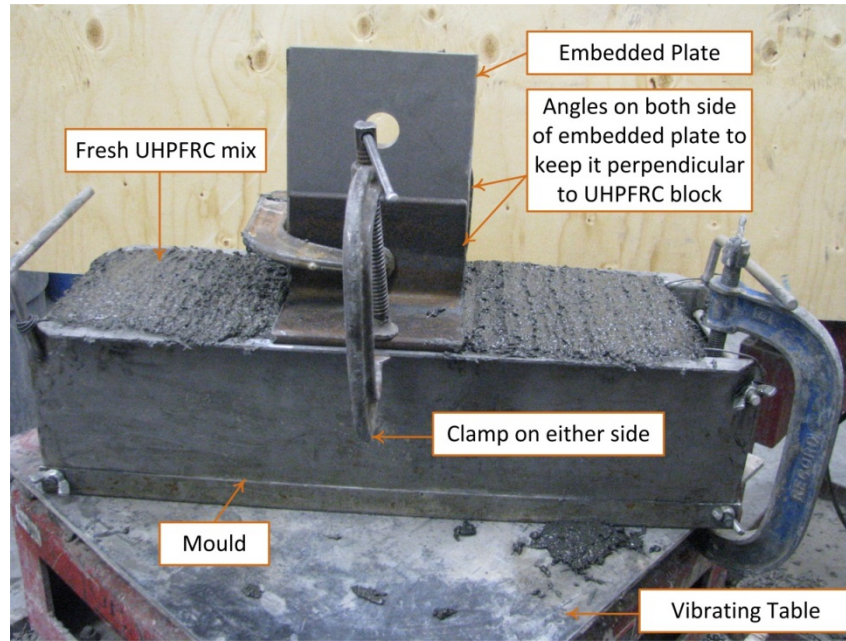


Figure 5-3: Composite connection after casting and screeding.

5.5.1.3 Curing

Conventional moist curing without added heat or pressure was used for all specimens to be representative of potential applications requiring in-situ casting. To minimize potential surface shrinkage and cracking, the top part of all the connection specimens and companion samples were covered immediately after casting with thin plastic sheeting to prevent water evaporation. The samples were cured under wet burlap. All the specimens were demolded around 19-24 hours after casting and remained in the curing room with a controlled temperature of $23\pm 2^{\circ}\text{C}$ and a relative humidity of 100% until testing.

5.5.2 Embedded Steel Plate

Perforated plates with different hole configurations were considered to study the influence on the composite connection response from a series of parameters including: thickness of embedded steel plate, depth of embedded steel plate, shape of tension key (hole cut through plate), and size of tension key. Some past research (Röhm 2009 and Rauscher 2011) investigated the influence of key shapes on the response of composite connections and accordingly three most efficient configurations were selected for this research: circular shaped hole, which is

designated as O-shaped tension key, omega shaped tension key, which is designated as Ω -shaped tension key, puzzle strip shear key which is designated as P-S tension key, as shown in Figure 5-4 and Figure 5-5. The symmetrical geometry of the P-S tension key helps to get two shear connector strips by one cut with no material wasted.

Two different grades of steel were used for the embedded steel plates. All the embedded steel plates with different thickness were cut from Grade 350WT steel plate by plasma cutting machine except for 8 mm samples, which were cut from Grade 300WT steel plates. All the surfaces of the plates were sand blasted after cutting was completed to remove the mill scale and provide a rough surface for bonding between concrete and steel. A pair of bolt holes with a diameter of 27 mm was drilled in all the plates. The embedded plates were connected to the thick clevis, which was gripped to the testing machine through two bolts.

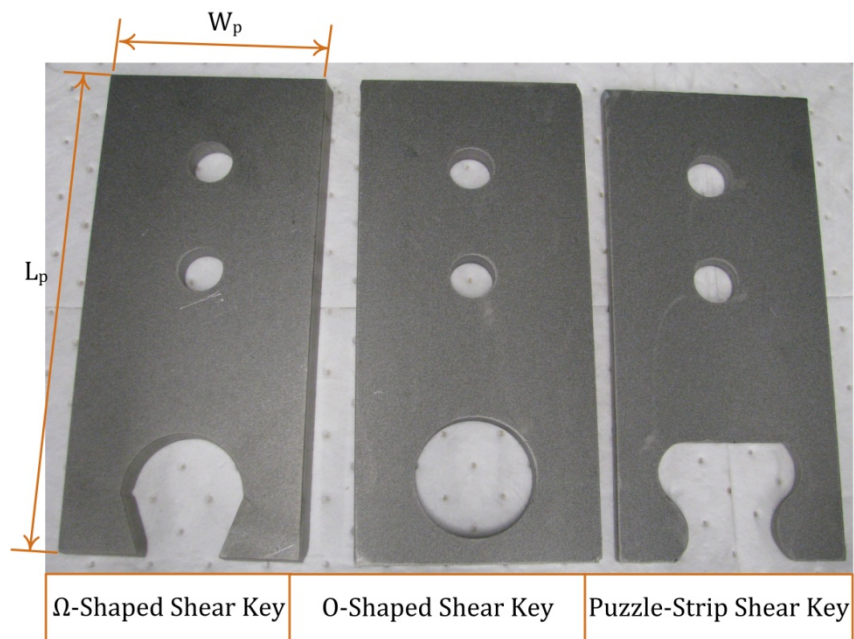


Figure 5-4: configuration of the embedded steel plate with different tension key configurations.

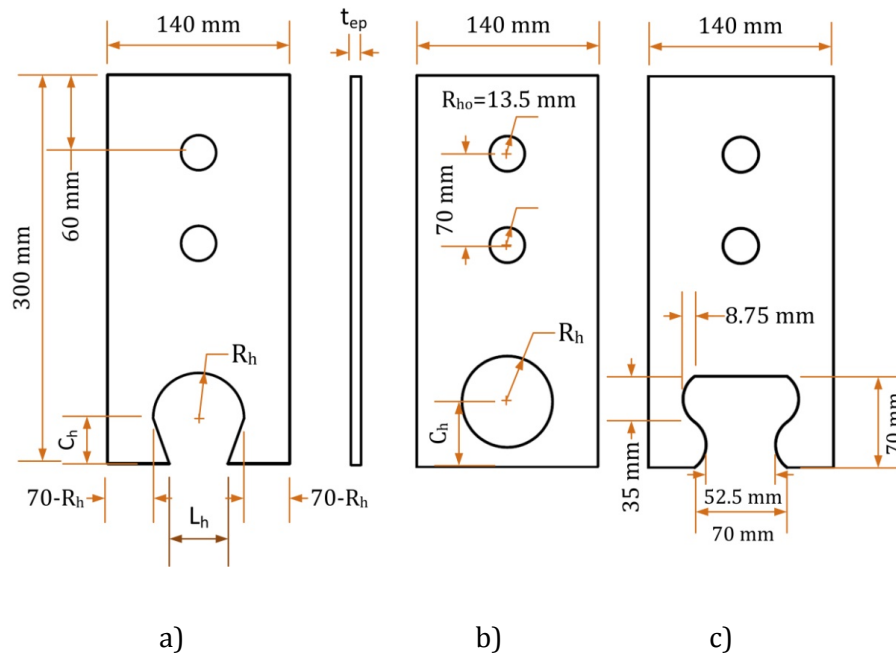


Figure 5-5: Geometry and configuration of the embedded steel plate: a) Ω-shaped tension key; b) O-shaped tension key; c) P-S tension key.

5.5.3 Double Headed Stud

Double headed studs (DHS) have been used in several applications where the anchorage requirements are difficult to achieve with conventional deformed reinforcing steel. It would also require less physical labour requirements and decrease the reinforcement congestion, particularly in the UHPFRC slender members.

In this research, a series of preliminary FEM analysis was completed to investigate the influence of the DHS on the response of the proposed connection system. According to FEM results, the use of DHS, passed through hole cut in the embedded perforated plate, was proved to improve the shear capacity of the concrete pin (CP) and prevent any premature failure in concrete pin subjected to the shear loading. In addition, significant splitting tensile stresses were observed in the concrete pin. Thus a DHS was used to provide resistance against the splitting tensile stresses and enhance the shear strength along the concrete pin. The proposed detailing is simple and speeds up the placement of the reinforcement on site.

The DHS that meets the requirements of CSA W59 or AWS D1.1/D1.1M was supplied by DECON and was fabricated with the integral head on one end and then a shop-welded head was attached to the other end. The geometry and the mechanical properties of the DHS is provided in the Figure 5-6 and Table 5-5 respectively. The head diameter is 4 times the stud diameter. Based on the manufacturer's specifications, the yield and ultimate tensile strength of DHS are 350 and 450 MPa respectively.

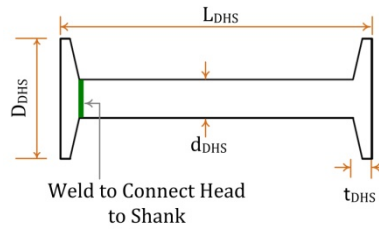


Figure 5-6: Geometry of double headed stud (DHS).

Table 5-5: Geometry of double headed stud

Sample	d_{DHS} (mm)	D_{DHS} (mm)	t_{DHS} (mm)	L_{DHS} (mm)
	15.9	50.2	7.9	130
Coupon Test	15.9	50.2	7.9	200

5.6 Ancillary Material Tests

Several ancillary tests were completed to characterize the mechanical properties of the constituent materials in the pull-out test specimens. The ancillary tests consisted of concrete flexural tests, concrete compressive tests, tension coupon tests of the embedded plates. The results of the ancillary material tests are reported in the next chapter of this thesis.

5.6.1 Concrete

5.6.1.1 Companion Compression Test

Compression tests were performed on the CU-50 specimens according to ASTM C109 for UHPFRC material and on CY-100 according to ASTM C39 for FRC material.

A Forney Testing Machine (FX700) was used to perform the compression tests at a standard loading rate of 1 MPa/s for CU-50 specimens. All the cylinders were end-ground in the Concrete Research Lab and tested in the MTS-2600 kN machine to capture stress-strain curves. A displacement controlled loading rate of 0.15 mm/min was used for the CY-100 FRC specimens. A summary of the compression tests for FRC and UHPFRC materials are provided in Table 5-6 and Table 5-7. A typical compression stress-strain response of FRC material is given in Figure 5-7.

Table 5-6: Summary of results of companion samples for composite connection made of FRC concrete

Specimen	f'_c	ϵ'_{cu} $\times 10^{-3}$	E (MPa)	d_{notch} (mm)	MPL (kN)	δ_{peak}	CMOD _{peak}	MOR (MPa)	ETS (MPa)
ΩS-70-10	46.5	3.2	20256	84	19.00	0.68	0.63	8.1	3.35
	46.0	3.6	20156	82	13.42	0.58	0.56	6.0	2.20
	41.5	3.1	20434	84	17.42	0.71	0.64	7.4	2.85
Mean	44.7	3.3	20282	83	16.61	0.66	0.61	7.2	2.8
ΩS-70-16	72	3.9	29808	84	18.1	0.65	0.58	7.7	2.10
	73.5	3.8	28715	82	12.42	0.58	0.54	5.5	1.90
	80	4.2	29615	84	15.81	0.72	0.70	6.7	2.48
Mean	75.2	4.0	29397	83	15.44	0.65	0.61	6.6	2.2
PS-70-10	40	3.1	21458	86	17.01	0.74	0.69	6.9	2.67
	42.2	3.3	21650	84	14.54	0.68	0.65	6.2	2.25
	35.2	3.3	20256	85	13.75	0.66	0.64	5.7	2.10
Mean	39.1	3.2	21121	85	15.10	0.69	0.66	6.3	2.3
OS-70-10	70.0	3.6	29675	82	15.22	0.74	0.70	6.8	2.40
	65.5	3.4	28451	83	14.44	0.61	0.58	6.3	2.30
	64.5	3.5	28115	82	13.43	0.66	0.60	6.0	2.20
Mean	66.7	3.5	28747	82	14.36	0.67	0.63	6.4	2.3
OS-70-16	79.5	3.8	29973	84	15.42	0.81	0.74	6.6	2.40
	71.5	3.6	28947	81	12.5	0.57	0.52	5.7	1.95
	68.5	3.7	27957	82	14.87	0.71	0.63	6.6	2.40
Mean	73.2	3.7	28959	82	14.26	0.70	0.63	6.3	2.3

Table 5-7: Summary of results of companion samples for composite connection constructed with UHPFRC material

Specimen Designation	V_f	f'_{cu} (MPa)	MPL (kN)	PLES	δ_{peak}	PETS (MPa)	CMOD _{peak}
ΩS-50-10	2	141.5	15.6	1.42	0.7	7.7	0.30
ΩS-70-08	2	148.0	16.5	1.51	0.5	7.8	0.27
ΩS-70-10	0	135.2	11.0	1.05	0.4	6.12	-
ΩS-70-10	2	145.5	15.2	1.36	0.38	7.5	0.23
ΩS-70-10	4	164.4	25.5	2.20	0.7	11.6	0.33
ΩS-70-12	2	138.6	15.4	1.40	0.45	7.3	0.26
ΩS-70-16	2	137.5	14.3	1.31	0.32	6.9	0.25
ΩS-70-16 [†]	2	153.0	17.5	1.64	0.65	8.1	0.31
ΩS-70-20	2	142.0	17.1	1.58	0.3	7.8	0.28
ΩS-90-10	2	148.5	17.3	1.61	0.26	7.9	0.30
PS-70-10	2	151.5	15.9	1.44	0.28	7.7	0.33
PS-70-16	2	144.4	18.4	1.67	0.38	8.2	0.31
OS-50-10	2	133.6	17.4	1.60	0.48	7.9	0.29
OS-70-10	2	154.5	14.2	1.34	0.46	7.1	0.35
OS-70-10 [‡]	2	151.5	13.8	1.32	0.47	6.9	0.32
OS-70-16	2	147.2	15.4	1.35	0.6	7.6	0.28

[†] Embedded length = 150 mm

[‡] Composite connection with no double headed Stud

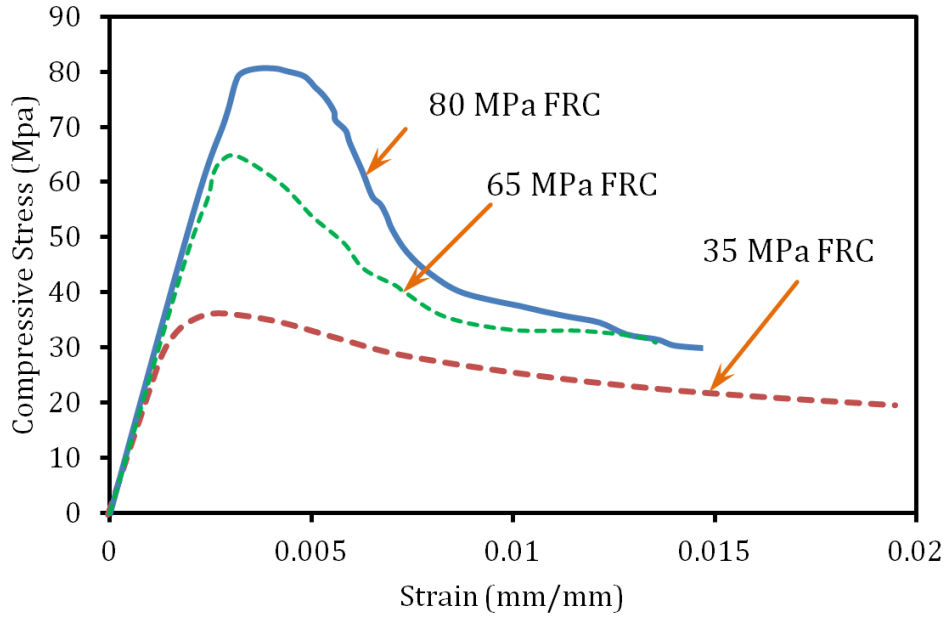


Figure 5-7: Compressive stress-strain behaviour of the FRC material.

5.6.1.2 Companion Flexural Test

Flexural prism tests were performed according to ASTM C1609-10 for each of the un-notched UHPFRC PF-50 prism (50 x 50 x 150 mm) and notched FRC PF-100 prism (100 x 100 x 300 mm). The detail of the flexural test method for the UHPFRC material was discussed in chapter 3. The geometry of the notched FRC PF-100 prism is provided in Figure 5-8. The displacement controlled loading rates for the UHPFRC PF-50 and the FRC PF-100 prism specimens are listed in chapter 3, conforming to the requirements of the ASTM C1609. The MTS load and stroke data and the LVDT output were captured by the DIC control computer in order to allow for the time synchronization. A summary of the average load-deflection curves for UHPFRC material with $V_f = 0, 2, 4\%$ and FRC material with $V_f = 1\%$ is illustrated in the Figure 5-9. According to this figure, the UHPFRC material with higher volume-fraction of randomly distributed short steel fiber tends to show a significantly higher flexural strength as compared to the FRC material. This phenomenon is most likely attributed to improved fiber bridging effect in UHPFRC material, which retards the formation and propagation of cracks.

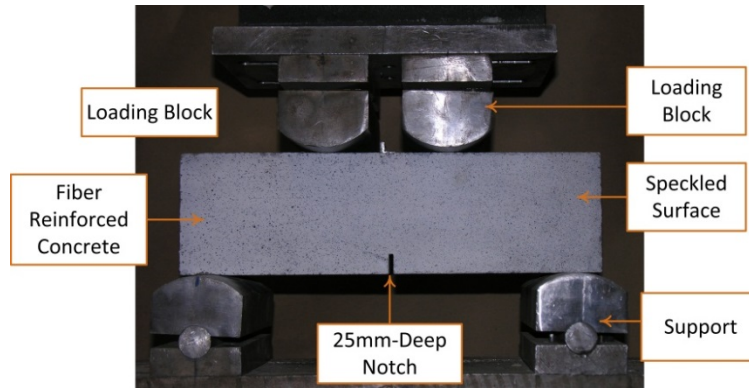


Figure 5-8: Flexural test set-up on notched PF-100 prism specimens.

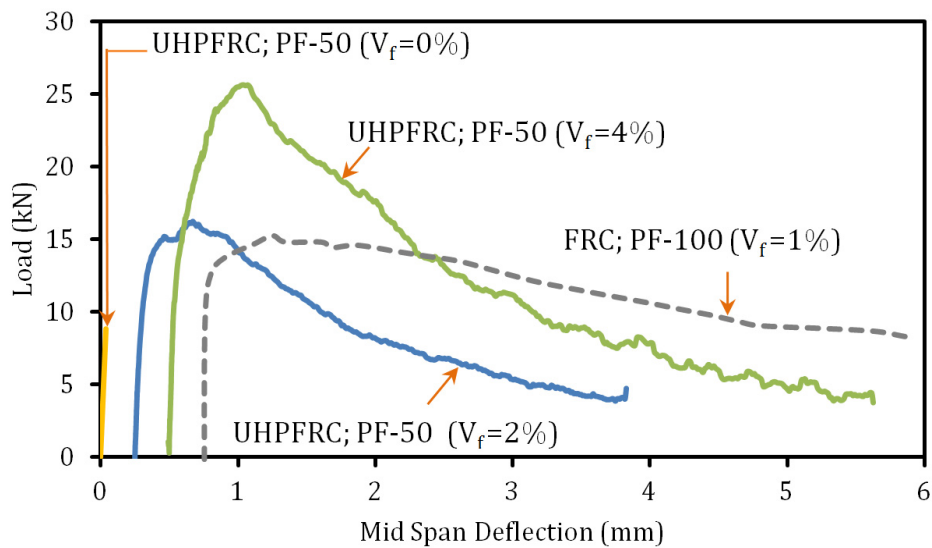


Figure 5-9: Flexural load-deflection responses of companion UHPFRC PF-50 and FRC PF-100.

5.6.1.3 Equivalent Uniform Tensile Stress

UHPFRC—The results of flexural tests and peak equivalent tensile strength (PETS) for each connection specimen are summarized in the Table 5-7. According to test results, an average 6.12, 7.6, and 11.6 MPa, were found for mixes with $V_f = 0, 2,$ and 4% respectively which is given in Figure 5-10. Higher rate of improvements in the PETS were found for those with higher fiber contents.

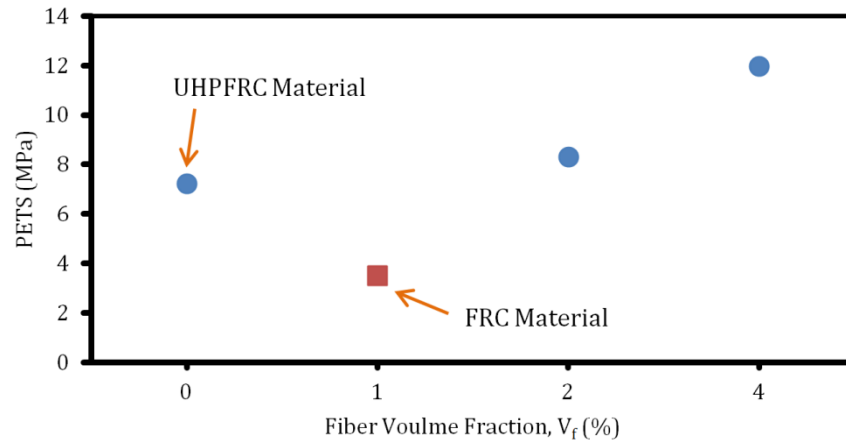


Figure 5-10: Variation of PETS of UHPFRC and FRC material against the change in fiber volume fraction (V_f).

FRC—A method developed by Armelin and Banthia (1997) was adopted in this research program to derive the equivalent tensile strength (ETS) against the crack mouth opening displacement (CMOD) for the FRC material as part of the structural companion material used in the composite connection prism. Figure 5-11 shows the ASTM C1609-10 flexural prism layout subjected to four-point loading, bending moment diagram, and deformation model for the FRC prism. The crack was assumed to form and the end of the notch.

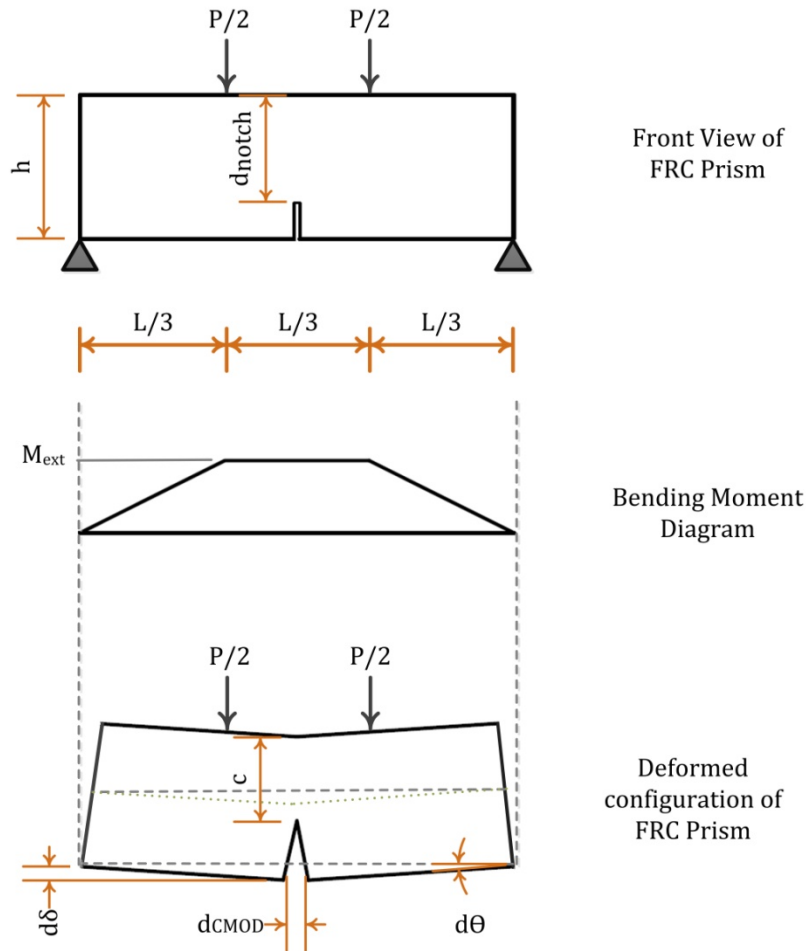


Figure 5-11: ASTM C1609-10 Flexural Prism Layout and Deformation Model (Adapted from Armelin and Banthia, 1997).

The strain and stress distributions along the depth of FRC beam is depicted in Figure 5-12. The tension and compression forces proposed by CSA A23.3-04 for reinforced concrete members are as follows.

$$T_r = \sigma_f (d_{notch} - c) b \quad (5-1)$$

$$C_r = \alpha_1 f'_c \beta_1 b c \quad (5-2)$$

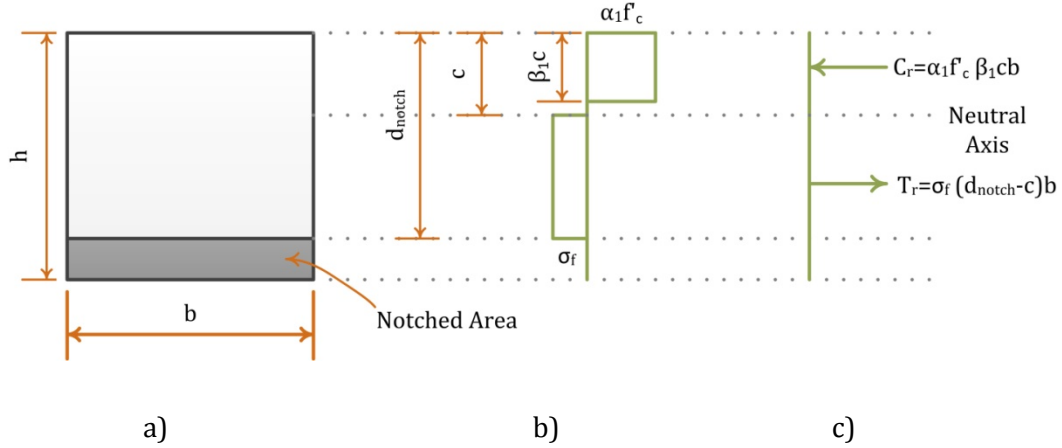


Figure 5-12: a) Cross section of prism, b) Stress distribution, c) Force Diagram in the cross section.

Equilibrium of the axial forces (along the prism length) as well as the flexural moment at the mid-span or cracked section requires that:

$$N_{ext} = T_r + C_r \quad ; \quad N_{ext} = 0 \quad (5-3)$$

$$M_{ext} = M_{int} \quad (5-4)$$

where the internal and external moments are as below.

$$M_{ext} = \frac{P}{2} a \quad (5-5)$$

$$M_{int} = \alpha_1 f'_c \beta_1 b c \left(\frac{d_{notch} + c(1 - \beta_1)}{2} \right) \quad (5-6)$$

where α_1 is a factor defining an equivalent concrete stress block at the ultimate condition and β_1 is an equivalent concrete stress block at the ultimate condition (Dinh 2010). After the depth of the neutral axis at each stage was determined from the equilibrium of internal and external moments, the equivalent tensile strength could be found as follows.

$$\sigma_f = \frac{\alpha_1 f'_c \beta_1 c}{d_{notch} - c} \quad (5-7)$$

The results of the flexural tests of the companion FRC prism specimens were used to derive the equivalent tensile strength (ETS) against the CMOD. The CMOD was

extracted from the DIC measurement systems. Typical results of ETS-CMOD for companion samples are given in the Figure 5-13. The peak equivalent tensile strength of the FRC material is compared against those for the UHPFRC material and is shown in the Figure 5-10. As given in this figure, the FRC material tends to show significantly lower PETS as compared to the UHPFRC material with 0-4% volume-fraction of steel fibers. This is mainly because the bond strength between steel fibers and matrix is substantially lower than that in the UHPFRC material.

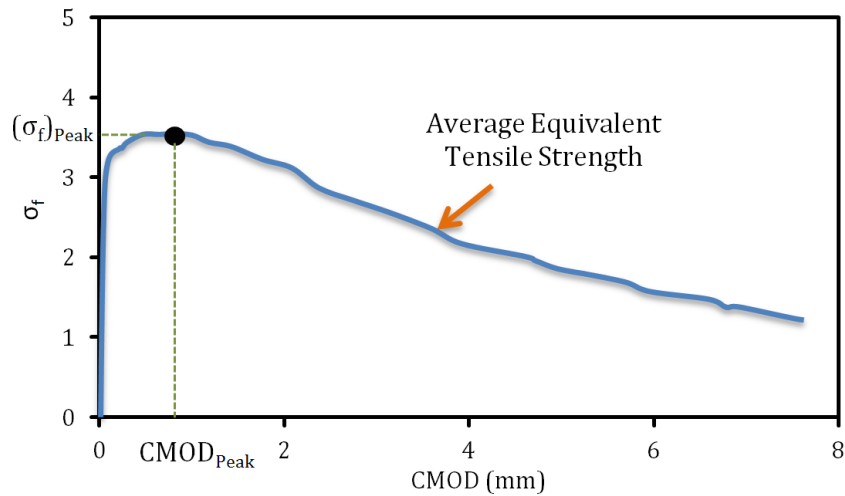


Figure 5-13: ASTM C1609-10 Flexural prism layout and deformation model (Adapted from Armelin and Banthia, 1997).

5.6.2 Embedded Steel Plate

All tension coupon tests were conducted according to ASTM standard A370-05 “Standard Test Methods and Definitions for Mechanical Testing of Steel Products” (ASTM 2005). Figure 5-14 depicts the dimensions of the tension coupons taken from random plate materials samples. All coupons used a 50 mm gauge length. A total of three tension coupons were taken from each plate. All the coupons were taken from extra material provided by the fabricator. The tension coupon tests were conducted in the MTS 1000 universal testing machine at the I.F. Morrison Structural Engineering Laboratory at the University of Alberta. Load measurement was done by an internal load cell integrated in the MTS 1000 test frame. An extensometer, mounted on the faces of the reduced section, with an initial gauge length of 50 mm was used during testing to capture the elongation of the coupon. The extensometer

was removed after the ultimate load had been reached to avoid possible damage. Figure 5-15 illustrates a coupon test with the attached extensometer. The test strain rate was incrementally increased from approximately 1 mm/min in the elastic range to 5 mm/min as the test approached rupture.

A digital image correlation (DIC) system was also used to track the axial deformation in coupon samples. One face of each coupon sample was painted with flat white paint, and subsequently speckled with black flat paint to create a random pattern of dots of varying size up to approximately 3 mm, which corresponded with the ideal dot size of at least 3-4 pixels through the software (Correlated Solutions Inc., 2009). Two 5.0 megapixel digital cameras with 35 mm focal length lenses were placed at a distance of approximately 700 mm from the samples in order to view the entire coupon face.

A total of 15 tension coupons were tested to determine the material properties of the steel parts of the composite connection specimen. Results of the tension coupon tests of the plates with different thicknesses generally showed a very small yield plateau, which is due to the excessive rolling of these thin plates. The three coupons produced practically identical stress-strain responses. Figure 5-16 shows the stress-strain curves of coupons TP-1. The test results for each of the coupon test are summarized in Table 5-8. The Elastic modulus of the embedded steel plate, E_s , was measured using the initial portion of the stress-strain curve. It was defined as the slope of the curve between the origin and a point at around 40 percent of the peak tensile stress. The measured modulus of elasticity are listed in Table 5-8.

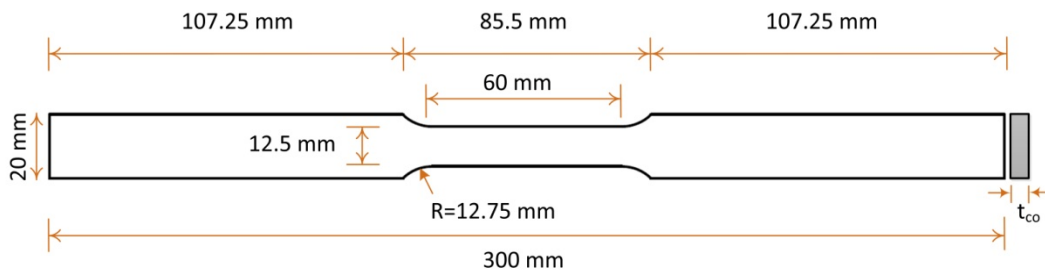


Figure 5-14: Dimensions of the tension coupon test taken from plate material.

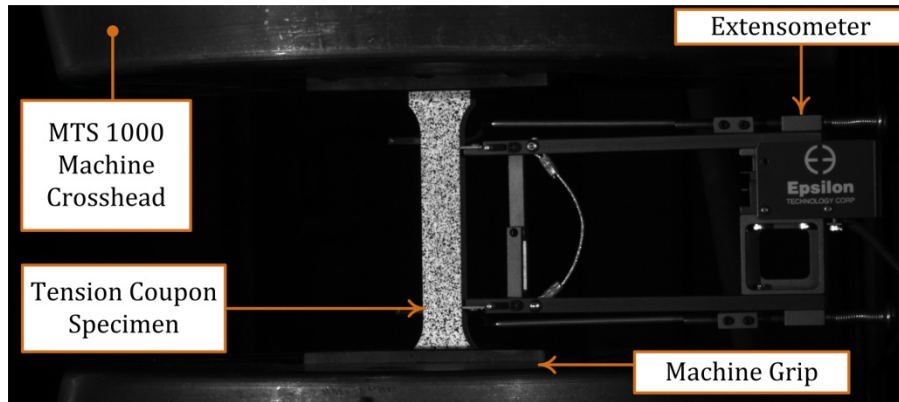


Figure 5-15: Coupon test with painted surface and extensometer.

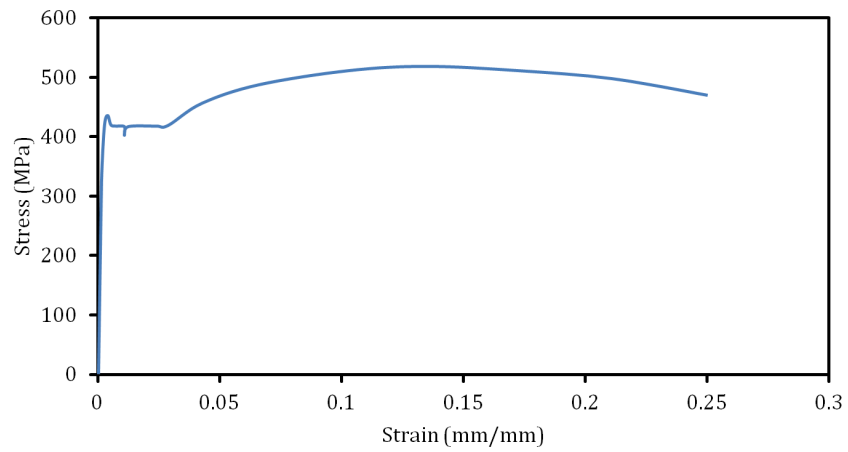


Figure 5-16: Typical Stress-strain curves of coupons test samples.

Table 5-8: Geometrical and mechanical properties of coupon tests

Coupon Test	Nominal Thickness (mm)	Width (mm)	Measured Thickness (mm)	E (MPa)	$F_{y,st}$ (MPa)	$F_{y,dy}$ (MPa)	$F_{u,dy}$ (MPa)
C-S-1	8	12.47	8.05	194,375	332	343	495
		12.51	7.96	215,862	317	320	470
		12.46	7.94	206,581	319	323	480
Mean		12.48	7.98	205,606	323	329	482
C-S-2	9.53	12.50	9.63	193,529	383	395	480
		12.43	9.44	185,427	373	395	478
		12.39	9.64	192,397	386	393	480
Mean		12.44	9.57	190,451	381	394	479
C-S-3	12.7	12.51	12.77	192,458	423	432	527
		12.49	12.76	181,218	425	437	523
		12.57	12.65	196,667	424	440	528
Mean		12.52	12.73	190,114	424	436	526
C-S-4	15.9	12.51	15.86	196,518	402	409	525
		12.48	15.82	184,000	399	401	518
		12.38	15.78	187,000	406	417	515
Mean		12.46	15.82	189,173	402	409	519
C-S-5	19.1	12.46	19.17	193,818	416	420	520
		12.35	19.19	205,000	418	423	512
		12.52	19.12	201,980	423	440	516
Mean		12.44	19.16	200,266	419	428	516

5.7 Pull-out Test Setup

An overall view of the test setup and a schematic diagram of the test assembly configuration are shown in Figure 5-17. The test setup was designed to simulate a typical composite connection subjected to the pull-out loading. The pullout tests were conducted in an MTS 1000 universal testing machine equipped with the hydraulic grips, and having a maximum load capacity of 1000 kN and an actuator range of 150 mm.

The concrete part of the composite connection system was tied to the bottom cross-head through a support plate. The support consisted of a horizontal thick plate

welded to a vertical stem plate, which was clamped by the lower grip of the machine, as shown in Figure 5-17.

The embedded steel plate was bolted to the clevis, which was held in the top grip of the machine. In order to prevent the slip of the assembly subjected to tensile load, a slip-critical connection was designed. The slip-critical joint was designed to transfer the designated load by the slip resistance of the clamped faying surfaces in accordance with CSA S-16-09 standard. A series of primary and secondary filler plates of different thickness were cut and machined at the Chemical Engineering Machine Shop at the University of Alberta to fill the gap between the clevis and the embedded steel plates, as shown in Figure 5-18.

The loading system for this test setup consisted of a pair of bearing transverse fastener plates which were placed against the hardened concrete surfaces (Fastener-B) to tie the concrete beam to the support plate. To ensure uniform contact, a thin layer of plaster was used between the Fastener-B and the concrete beam.

A pair of longitudinal fasteners, Fastener-A, were connected to the top part of Fastener-B to prevent any movement of the Fastener-B in the X-direction. All the fasteners were connected to the strong supporting plate by four high-strength pre-tensioned 20 mm ASTM-A495 bolts. Two rigid end supports were used at both ends of the concrete beam to enhance the axial stiffness of the concrete beam and prevent any premature flexural failure in the beam.

In all the tests, the embedded steel plate and the filler plates were first positioned and connected to the clevis through two 25 mm ASTM-A495 bolts. All the bolts were installed in the finger tight condition at this stage. The top crosshead was then slowly lowered until the concrete beam barely rested on the strong support plate. The beam was then shimmed (see Figure 5-17). This would significantly minimize the stress concentration caused by misalignment between the planes of the concrete beam's bottom face and the strong support plate surface. The two rigid end supports were clamped to the strong support plate using two pairs of high-strength clamps. To ensure a complete contact between the concrete beam and the support system,

the gaps were fully shimmed. After the specimen and the filler plates were centered and seated, all the bolts were pretensioned using the turn-of-nut method.

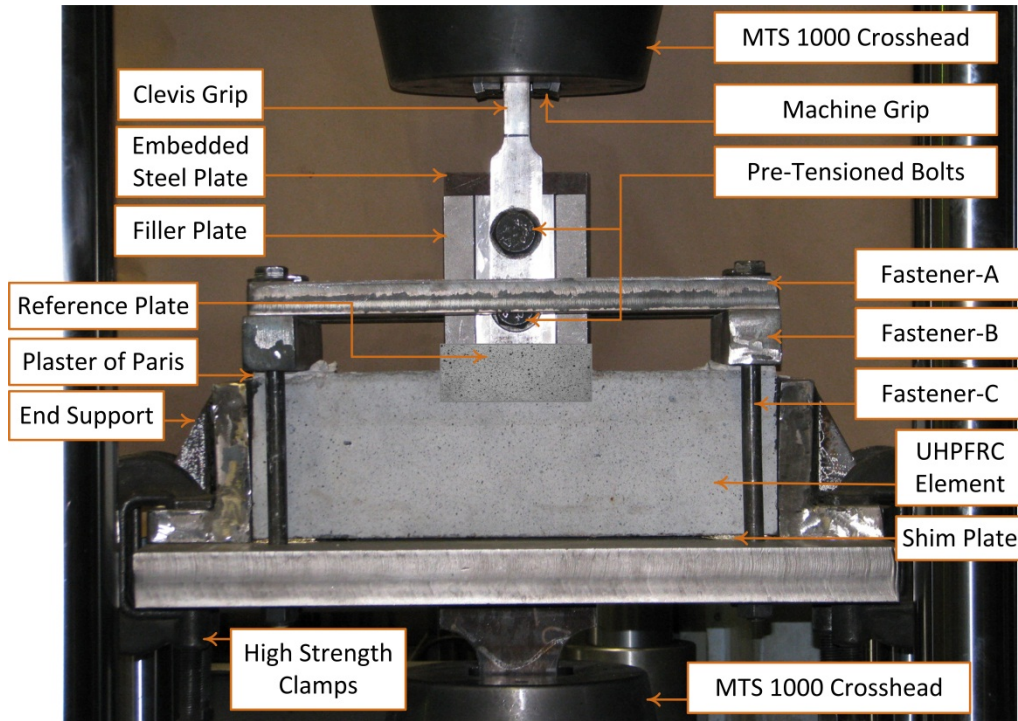


Figure 5-17: Geometry of Pull-out specimen under tensile loading in MTS-1000 machine.

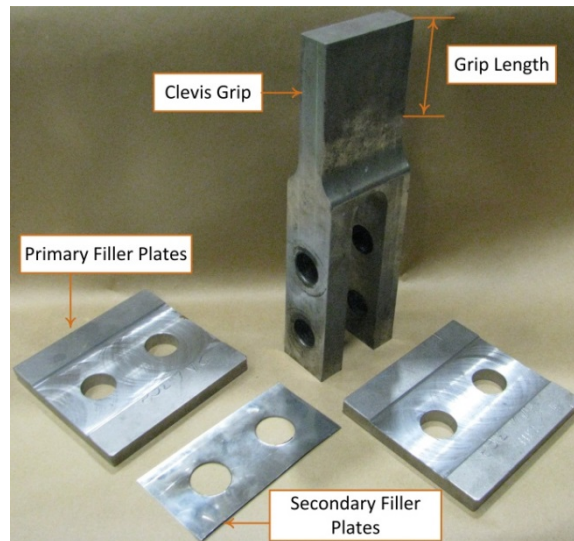


Figure 5-18: Clevis and filler plates to grip the embedded steel plate to top cross-head of MTS-1000 machine.

5.8 Instrumentation

The pull-out load applied to the composite connection specimens was monitored using the internal load cell integrated in the MTS 1000 test frame. Different instruments including the LVDTs and DIC system were used to measure the crack width, crack growth, and the relative slip between steel plate and the concrete beam. In between each test, all the instrumentations were checked for the accuracy and were re-calibrated when necessary.

5.8.1 External Instrumentation

Relative vertical displacement between the embedded steel plate and the concrete beam were taken by a pair of Linear Variable Displacement Transducers (LVDTs) with ± 25 mm of range, which were mounted on the both sides of the steel plate. The LVDTs layout is schematically illustrated in Figure 5-19 and Figure 5-20. A series of four LVDTs, HL-1, HL-2, HR-1, and HR-2, with gauge lengths of 10 mm, were mounted along the top side of the concrete beam to monitor the crack opening between the surface of the embedded steel plate and the concrete beam. In order to gain the net crack opening displacement, global out-of-plane deflection of embedded steel plate was recorded by a single LVDT, called HC LVDT. The readings from HC LVDT showed very small displacement, which was considered negligible.

5.8.2 Strain Gauges

The strain on the surface of the embedded steel plates at selected locations was measured with electrical resistance strain gauges. The corresponding stresses were calculated using the modulus of elasticity extracted from the tension coupon tests. The details of the instrumentation including the position and designation of strain gauges and LVDTs are shown in Figure 5-19 and 5-20. These locations were selected to obtain the steel strain at the tension critical sections. The strain gauges had an electrical resistance of $119.8 \pm 0.2 \Omega$ and were manufactured by Kyowa Electronic Instruments (model KFG-5-120-C1-11). The gauge length and width were 5.0 and 1.4 mm, respectively. The area was prepared using 400 grit sandpaper and cleaned with a conditioner and neutralizer. M-Bond 200 adhesive was used to attach strain

gauges to steel plates. A transparent acrylic lacquer was used to protect strain gauges against any possible damage during casting and testing.

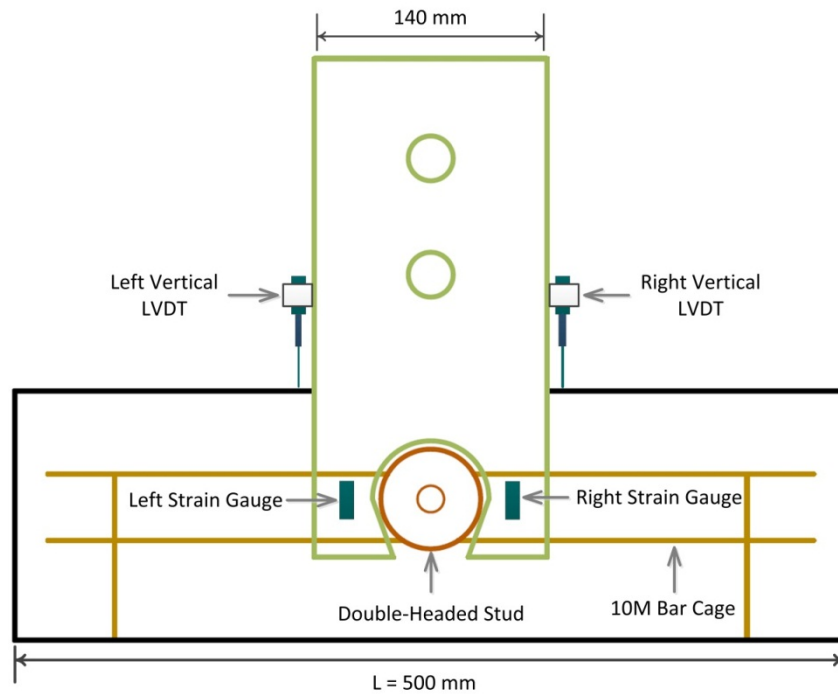


Figure 5-19: Front view of instrumentation including vertical LVDTs mounted on both side of steel plate and a pair of strain gauges mounted next to tension key.

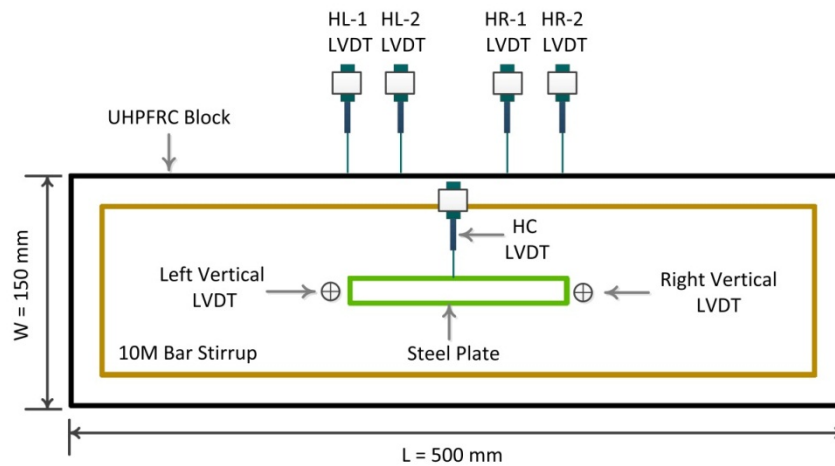


Figure 5-20: Top view of instrumentation including four horizontal LVDTs mounted on top back-side of steel plate and a pair of Vertical LVDTs attached to embedded steel plate.

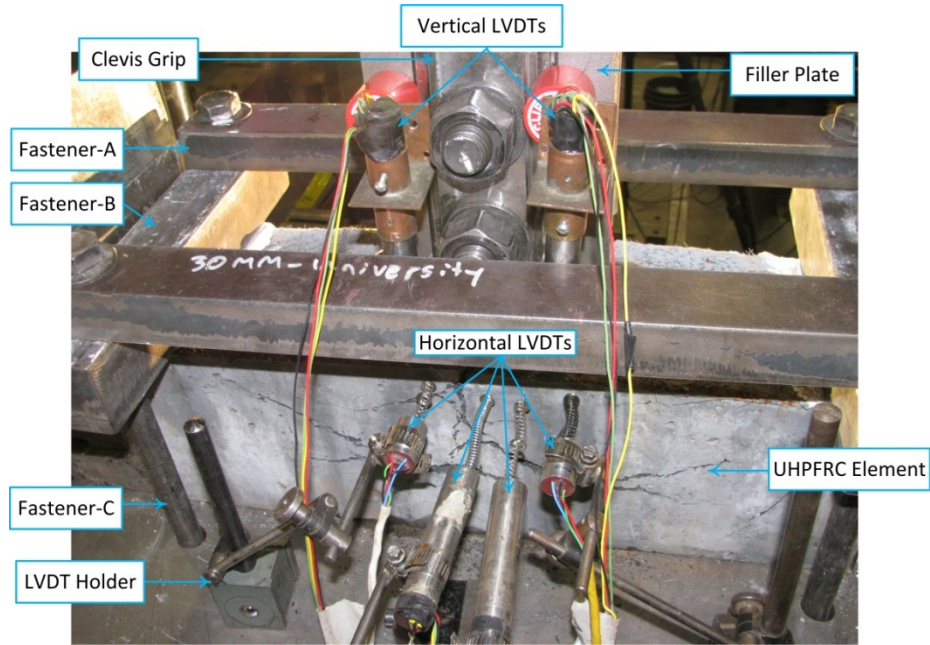


Figure 5-21: General view of the horizontal LVDTs mounted on back side of concrete beam and vertical LVDTs attached to embedded steel plate.

5.8.3 Data Acquisition

Data from the different instrumentations was captured using National Instrument system and built-in data acquisition system in DIC control system. The strain gauges along with MTS outputs were connected to National Instrument system which is controlled by Lab View 2009. All the horizontal and vertical LVDTs along with MTS load cells were connected to an internal data acquisition system in Vic-3D 2009. In order to allow for synchronization between the Lab View and DIC control system, the MTS load and stroke data were captured by both systems.

5.8.4 Digital Imaging Correlation System

The front face of the concrete beam in each composite connection was painted with a flat white latex paint, as shown in Figure 5-22. A random speckle pattern was then applied to the painted surface of the specimen using a flat black spray paint to produce small circular black dots covering approximately 50% of the specimen's surface. All the specimens were cured under wet burlap and plastic immediately after painting was completed to prevent the formation of microcracking. The mean speckle diameter was measured to be approximately 2-3 mm and the spacing was 3-

5 mm. Each of the dots in the camera is approximately 4-6 pixels in size, which is ideal for the commercial software. The use of finer patterns was proved to be more sensitive to defocus and make the deformation tensor most sensitive to change during the image processing analysis (Correlated Solutions Inc. 2010).

A digital image correlation (DIC) system was employed during the pull-out tests, as an alternative to classical extensometry technique using the LVDTs, to capture the crack initiation and propagation and measure the slip between the embedded steel plate and the concrete beam.

In order to track the slip between the embedded steel plate (Point RP-T) and the concrete beam (Point RP-B), a rectangular reference plate (150 x 50 mm) attached to a U-shape bracket was fabricated and clamped to the steel plate at two points near the steel concrete interface to represent the movement of the embedded steel plate. A similar speckled pattern was applied to the steel plate to be consistent with the pattern used for the concrete beam. Special care was taken to align the planes of the concrete block front face and the reference plate to prevent blurry images which would result in an inaccurate deformation tensor. The DIC system was set to record a pair of images every 3 seconds during the pull-out test.

In order to process the recorded images and extract the deformations, Vic-3D software was used (Correlated Solutions Inc. 2010). Rigid body motion was analytically removed by the software to account for any connection settlement during the testing. The results of DIC technique allowed for a detailed study of relative slip between the connection components, and the variation of crack width over the member length and its relation to the applied load.

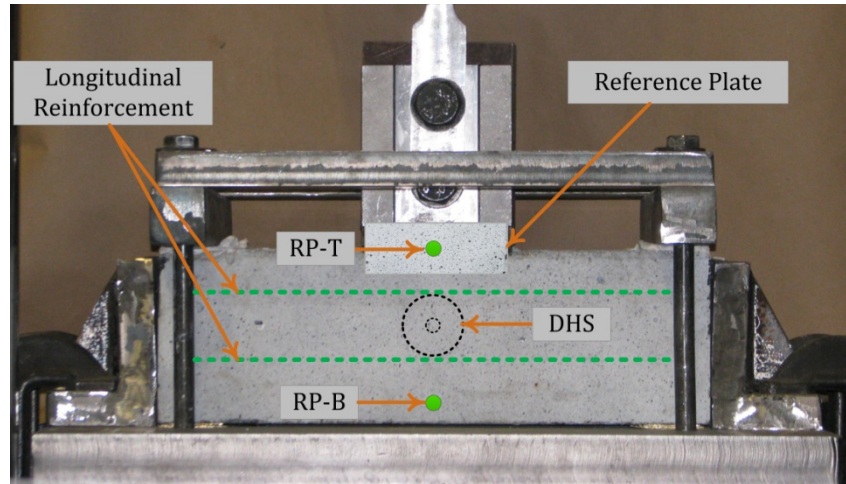


Figure 5-22: Front view of the painted concrete beam and the data extraction point for DIC.

5.9 Test Procedure

All pull-out tests reported in this thesis were conducted using an MTS 1000 universal testing machine. Displacement-controlled loading was used to apply the quasi-static tensile load at a rate of 0.2 mm/minute. All the composite connection specimens were loaded until the pull-out force on the descending branch of the load-displacement relationship is dropped below 70% of the peak value. Tensile loads as well as the feedback from the LVDTs and the strain gauges were continuously recorded during the tests. All the displacement and strain readings on both data acquisition systems were set to zero before the test was run. Digital images were continuously taken by the digital image correlation system cameras throughout the loading process of each test. To protect the MTS testing machine and pullout specimens from unforeseen events, upper and lower bound limits on displacements and loads were set.

Chapter 6

6 Composite Connections: Test Results and Discussion

6.1 Introduction

This chapter presents the experimental results of 42 large-scale composite connections constructed with embedded steel plates in the concrete beams. Two different generations of concrete, i.e. ultra-high performance fiber-reinforced concrete (UHPRFC) and fiber-reinforced concrete (FRC) were used for the concrete beam. Pull-out load slip response, failure mode, load-strain response of the embedded steel plate, crack formation and growth for each group of pull-out specimens are investigated. The influences on the pull-out capacity of the composite connections from several parameters including the embedded length of steel plate, plate thickness, configurations of holes cut through the embedded plate, concrete beam depth, and fiber volume-fraction are investigated. In addition, the behaviour of the composite connections constructed with UHPRFC material incorporating different fiber volume fractions (V_f), i.e. $V_f = 0\%$, 2% , and 4% are compared against composite connections with similar connection detailing made of FRC material. The pull-out ductility for each group of the connection system are also discussed.

Prior to casting, the dimensions of different connections' components were measured and the average measured dimensions for each specimen are listed in Table 6-1. All the connections were labeled according to their nominal dimensions, but all the calculations were based on the measured values. The effective embedment length of the steel plates and the position of double headed studs were kept at the design value since these values cannot be measured after casting was completed.

The composite connections were loaded under the displacement controlled loading in the MTS 1000 test frame until the failure. The use of displacement control allowed the pull-out response to be captured in both pre-peak and post-peak range. In all the cases, failure criteria was defined as a point where the pull-out force on the descending branch of the load-displacement relationship is dropped below 85% of the peak pull-out load (PPL).

The peak pull-out load (PPL) and the corresponding slip between the concrete beam and the embedded steel plate at peak (Δ_{peak}), along with the equivalent service slip ($\Delta_{\text{cr,e}}$) corresponded to 85% of the PPL is reported in the Table 6-1 to Table 6-3 for composite connections made of UHPFRC and FRC material. The deflection at failure (Δ_f) is also reported for all the connections in the similar tables. The summarized loads in this table are based on the applied loads from the MTS 1000 machine and include the 0.3 kN weight from both base plate and self-weight of the composite connection. The relative slip between the embedded steel plate and the concrete beam as well as the crack width are based on the DIC measurements, which is analyzed through the Vic-3D 2009 and have been corrected for the support settlement (Correlated Solutions Inc. 2009).

An overall view of the failure crack on the front face of each connection specimen is provided with the surface strain shadings to allow for a qualitative examination of the extent and location of the different cracks on the front surface of the concrete beam.

Table 6-1: Experimental results of composite connections system with Ω -shaped tension key

Specimen Designation	V_f (%)	h_h (mm)	t_p (mm)	L_{em} (mm)	f'_{cu} (MPa)	PPL (kN)	$\Delta_{cr,e}$ (mm)	Δ_{peak} (mm)	Δ_f (mm)	Λ	Failure Mode
Ω S-U-50-10-2	2	50	9.53	100	142	153	1.14	5.10	13.68	11.1	PF
						142					
Ω S-U-70-08-2	2	70	8		148	172	2.00	7.60	18.00	9.0	SYF
						180					
Ω S-U-70-10-0	0	70	9.53		135	78	0.15	0.24	0.33	1.2	BF
Ω S-U-70-10-2	2	70	9.53		145	177	1.33	5.10	11.37	7.4	PF+BF
						179					
Ω S-U-70-10-4	4	70	9.53		164	224	1.67	5.90	19.58	13.0	PF
						221					
Ω S-U-70-12-2	2	70	12.7		139	204	0.97	2.20	11.64	10.7	BF
						203					
Ω S-U-70-16-2	2	70	15.9		138	221	1.16	3.36	6.50	4.6	BF+SF
						213					
Ω S-U-70-16-2	2	70	15.9		150	153	340	0.88	6.30	18.00	19.5
				345							
Ω S-U-70-20-2	2	70	19.1	142	197	1.23	2.80	5.00	3.1	BF+SF	
					206						
Ω S-U-90-10-2	2	90	9.53	148	175	1.03	2.12	7.19	6.6	SP+PF	
					193						
Ω S-F-70-10-1	1	70	9.53	44.5	80	4.58	7.50	12.26	1.7	PF	
					87						
Ω S-F-70-16-1	1	70	15.9	75	139	1.04	2.90	3.31	2.1	BF	
					144						

Pull-Out Failure (POF), Breakout Failure (BF), Concrete Edge Failure (CEF), Steel Failure (SF),

$$\text{Ductility Factor: } \Lambda = \frac{\Delta_f - \Delta_{cracking}}{\Delta_{cracking}}$$

Table 6-2: Experimental results of composite connection systems with puzzle-strip tension key

Specimen Designation	V_f (%)	h_h (mm)	t_p (mm)	L_{em} (mm)	f'_{cu} (MPa)	PPL (kN)	$\Delta_{cr,e}$ (mm)	Δ_{peak} (mm)	Δ_f (mm)	Λ	Failure Mode
PS-U-70-10-2	2	70	9.53	100	151.5	202	1.07	2.34	4.40	3.2	BF
						167					
PS-U-70-16-2	2		15.9		144.4	216	1.03	4.1	6.45	3.0	BF+PF
						203					
PS-F-70-10-1	1		9.53		39.1	88	2.05	3.7	6.00	2.0	PF
						81					

Table 6-3: Experimental results of composite connection systems with O-shaped tension key

Designation	V_f (%)	h_h (mm)	t_p (mm)	L_{em} (mm)	f'_{cu} (MPa)	PPL (kN)	$\Delta_{cr,e}$ (mm)	Δ_{peak} (mm)	Δ_r (mm)	Λ	Failure Mode
OS-U-50-10-2	2	50	9.53	100	133.6	195	1.49	2.95	5.30	2.6	BF
						194					
OS-U-70-10-2	2	70	9.53		154.5	180	0.81	1.65	8.38	10.1	BF
						183					
OS-U-70-10-2 [‡]	2	70	9.53		151.5	154	0.72	1.6	3.06	4.23	BF+PF
						170					
OS-U-70-16-2	2	70	15.9		147.2	210	0.88	3.2	4.66	4.4	BF
						215					
OS-F-70-10-1	1	70	9.53		66.5	100	0.68	0.97	2.26	7.2	BF
						117					
OS-F-70-16-1	1	70	15.9		73	102	0.84	1.95	3.29	3.0	BF
						113					

‡ : No Double headed stud was used in this specimen

6.2 General Observation

The overall response of the composite connection specimen during the pull-out testing is provided in this section.

Compared to the composite connections constructed with FRC material, the connection specimens constructed with UHPFRC material demonstrated a significant enhancement in the pull-out load with a less degradation rate after the peak pull-out load. In addition, the use of UHPFRC material in the composite connection appreciably improved the deformability and ductility in the majority of the connection specimens. The composite connection constructed with the FRC material presented the similar behaviour but with a limited peak pull-out load (PPL), deformability, and ductility.

No concrete spalling was observed in the specimens made of UHPFRC and FRC material incorporating randomly distributed discontinuous steel fibers, except in the OS-U-70-10-0 specimen where the beam was constructed with plain UHPFRC material. According to the test results, the use of higher volume fraction of short steel fibers in the UHPFRC beam allowed a more gradual degradation in the pull-out load-slip response of the composite connection system after the PPL than those with the plain UHPFRC material.

The typical actual and idealized pull-out load-slip response of the composite connection systems at different stages of loading are described in Figure 6-1. Three distinct stages are evident: linear-elastic stage, post-cracking stage, and softening stage.

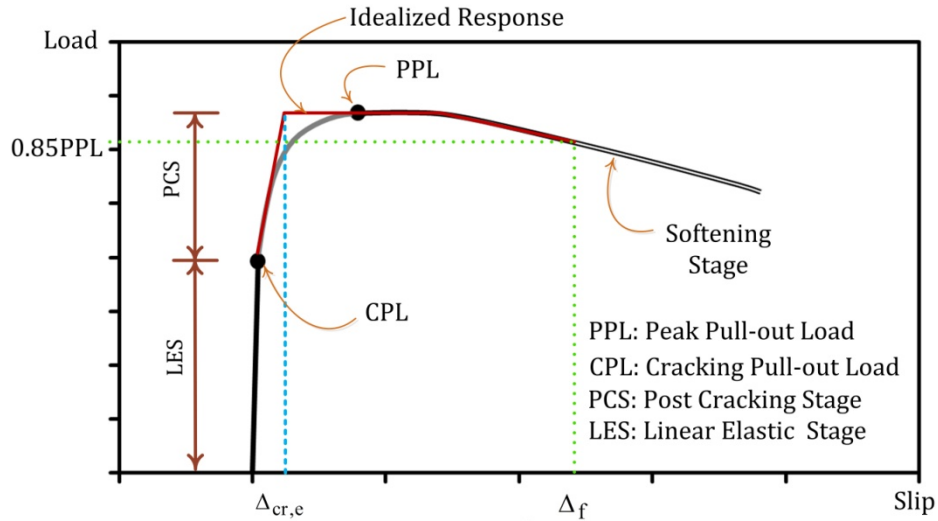


Figure 6-1: Typical pull-out load-slip response of composite connection system.

Linear-elastic stage: According to experimental test results, the composite connections constructed with UHPFRC and FRC material exhibited a quasi linear-elastic load-slip response in tension up to a cracking pull-out load (CPL). In this stage, no visible cracks were observed in the concrete beam (see linear stage in Figure 6-1). The cracking pull-out load (CPL) is defined as a load level where the load-slip curve began to deviate from the initial linear load-slip response.

The average CPL reached between 55%-70% and 70%-75% of the PPL for the composite connections constructed with UHPFRC and FRC material respectively. This indicates that the connection systems with UHPFRC material tend to show higher reserve strength that exist between the CPL and PPL as compared to those constructed with FRC material. No permanent slip was observed during the linear-elastic stage for all the connections constructed with FRC and UHPFRC material. According to test results extracted from the DIC measurement system, the CPL was reached at a small average slip of around 0.075 mm and 0.18 mm for the composite connections constructed with FRC and UHPFRC material respectively. The initial

stiffness of the connection systems constructed with both UHPFRC and FRC material in the elastic stage was compared and relatively similar values were found for both connection systems.

Post-cracking stage: beyond the CPL point, a non-linear response with lower stiffness was observed for the majority of the composite connections (see post-cracking stage in the Figure 6-1). During this stage, the pull-out load continued to increase for additional applied displacement until the PPL was reached. This phenomenon was more pronounced in the connection specimens constructed with UHPFRC material incorporating higher volume-fraction of randomly distributed short steel fibers. This is mainly because this material features a strain-hardening response in tension and shear, which leads to a significant increase in the deformation capacity of the connection system. This phenomenon is attributed to formation of multiple microcracks in the concrete beam during the inelastic deformation process. The formation of the microcracks in the UHPFRC concrete beam was observed to be repeated for several times until they joined each other and formed a single macrocrack. In contrast, the connection system constructed with FRC material presented a limited post-cracking stage, as compared to similar connections with UHPFR material.

Softening stage: A softening stage without a sudden drop in the load carrying capacity after the peak pull-out load was observed for all the connection specimens. The composite connections constructed with the plain UHPFRC material ($V_f = 0\%$) presented a significant fluctuation in the load-slip response after the formation of the main crack. In contrast, the connection specimens constructed with UHPFRC material (incorporating 2% and 4% fiber) presented a stable load-slip response with a gradual decrease after the PPL. This improvement is attributed to the fiber bridging effect, where the crack faces are immediately bridged by the steel fibers. This phenomenon significantly retards the uncontrolled propagation of the cracks and leads to a gradually load-slip response.

Ductility Factor: In the context of structural engineering, ductility factor in the connection systems is defined as the ability of the connection to undergo large displacements without significant loss of strength (ASTM 1964). Among the several

expressions proposed for the connection ductility, the following equation is adapted in this research.

$$\Lambda = \frac{\Delta_f - \Delta_{cr,e}}{\Delta_{cr,e}} \quad (6-1)$$

where Λ represents the ductility factor, Δ_f and $\Delta_{cr,e}$ are defined as the slip at the failure point and equivalent cracking load respectively (see Figure 6-1). The failure point is defined to be 85% of the PPL at the softening stage. The values for Δ_f , $\Delta_{cr,e}$, and Λ for all the composite connection systems tested in this research are given in Table 6-1 to Table 6-3.

According to test results, the connection systems constructed with the Ω -shaped tension key and UHPFRC material represented a higher ductility factor, as compared to those with circular and puzzle-shape strip holes. Compared to connection systems without DHS, higher ductility factor was found for those with DHS. The increase in the fiber contents from 0% to 2% and 4% in the connection systems constructed with UHPFRC material was found to linearly increase the connection's ductility factor. This is mainly because the UHPFRC material with higher fiber contents features a more enhanced hardening and softening response, which eventually leads to a more improved load-slip curve for the connection subjected to pull-out loading. In contrast a low ductility was found for the connection systems constructed with the FRC material, as the FRC material has negligible hardening response, as compare to the UHPFRC material.

6.3 Overview of Failure Mechanisms

This section describes the potential failure modes in the composite connections subjected to pull-out loading. Five distinct types of failure mechanism observed during the tests: pull-out failure (PF), steel yielding failure (SYF), splitting failure (SF), breakout failure (BF), and concrete side-failure (CSF). Breakout failure was the most common failure mode, occurring in the most of the connection systems. Although a small concrete cover was used for the double headed stud (DHS), no side blow out was observed in connections made of both UHPFRC and FRC material except for the Ω S-U-70-10-0 specimen, which was constructed with plain UHPFRC

material. This is explained by the fact that the fiber bridging mechanism in the UHPFRC and FRC material can sustain the quasi-hydrostatic pressure in the region of the head of the DHS and resist against the lateral bursting force.

6.3.1 Pull-Out Failure

Figure 6-2 shows a typical pull-out failure (PF) in the composite connections. In PF, the mechanical bond between the embedded steel plate and the concrete beam is lost and as such the embedded steel plate is pulled through the concrete beam without breaking out a major part of the surrounding concrete. This type of failure may happen when 1) the entire or parts of the concrete pin (surrounded by the steel tension key) fail subjected to direct shear load, 2) the concrete pin crushes under the high normal stresses along the interface between the concrete pin and the steel tension key, 3) a combination of the last two failure mechanism occur.

Prior to initiation of cracks along the interface between sides of concrete pin and surrounding concrete, both sides of pin experience tension-induced shear stresses until the CPL was reached. A higher CPL was observed for the connection specimens constructed with the UHPFRC material than FRC specimens. This is mainly because the mechanical property of the UHPFRC material in shear is appreciably higher than that for FRC material in the elastic range. In addition, compared to connection constructed with FRC material, more improved sliding friction between steel plate and the surrounding concrete exists in the specimens constructed with UHPFC material, which improve the pull-out load transfer mechanism. However this portion is very small as compared to the contribution of mechanical interlock and was neglected.

Once the shear stresses exceed the shear capacity of the concrete pin, a series of microcrack forms in the concrete pin. Subsequent to the formation of a crack, the shear stresses are transmitted by a combination of two mechanisms: the shear strength provided by the short steel fibers and the resistance to kinking of the DHS's shank which provides a significant resistance to the relative shearing displacement along the crack. A higher load capacity was observed for the connection specimens constructed with the UHPFRC material over those with FRC material, as the UHPFRC features significantly more improved shear strength than the FRC material after the

formation of cracks. This phenomenon is more pronounced for the UHPFRC with higher fiber content, as the results of direct shear test (Chapter 4) showed that the peak shear strength increased from 9.46 MPa for UHPFRC with $V_f = 0\%$ to 43 MPa and 54 MPa for UHPFRC with $V_f = 2\%$ and $V_f = 4\%$ while an average shear strength of 11 MPa was found for FRC with $V_f = 1\%$. After the maximum shear capacity of concrete pin reached the cracks width along the concrete pin increases and the pull-out load tends to gradually decrease. The subsequent behaviour is mainly influenced by the post peak behaviour of material in shear.

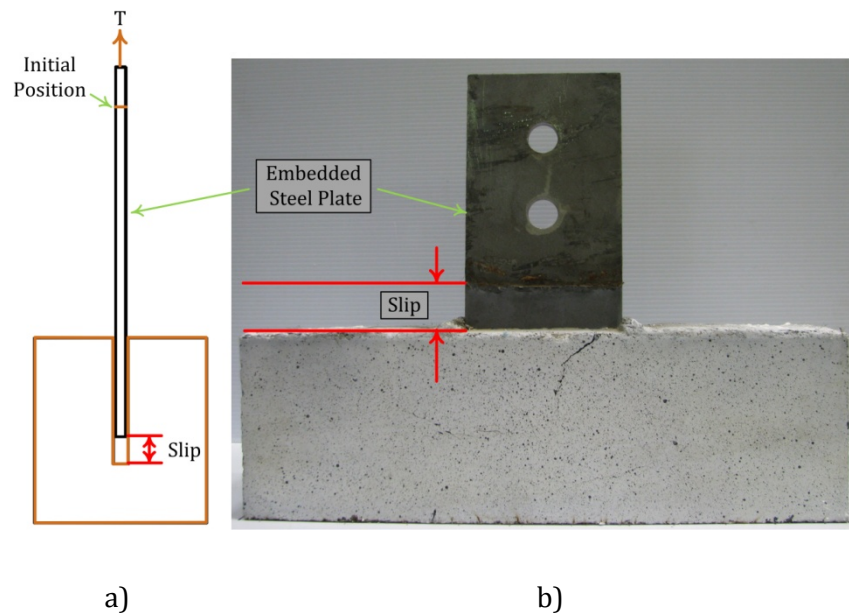


Figure 6-2: Pull-out failure, a) schematic side view of the connection specimen, b) front view of the connection specimen at the end of the test.

6.3.2 Steel Yielding Failure

The steel yielding failure is more frequent in the sides of the tension keys, where a relatively large amount of strain was localized in the small area of the steel plate. No visible cracks in the concrete beam were observed in the SYF. This failure mode represents an upper limit on the achievable load carrying capacity of a composite connection. A ductile load-slip curve results for the composite connection when loaded to failure. If the capacity is characterized by the steel yielding, the ultimate pull-out load can be calculated from the stressed cross sectional area of the embedded steel plate under direct tension loading as follows.

$$N_y = A_s \times F_y \quad (6-2)$$

where the N_y , A_s , and F_y are respectively the yielding pull-out load, net tensile cross-sectional area of steel plate, and measured yield strength of steel plate. Similar expression was used for the conventional headed studs subjected to pullout load.

6.3.3 Splitting Failure

A dominant vertical crack at the mid-span of concrete beam is referred to as the splitting failure (SF), as shown in Figure 6-3. According to test results, the main crack was formed after the initiation of a series of multiple microcracks at the mid-span and top side of the concrete beam. This crack was extended from the extreme tension fiber toward the mid-height of the specimen, where the flexural compression zone begins. The wider cracks results in less confinement to embedded plate, which notably lower the pull-out capacity of the connection. Once the splitting crack reach the compression zone, a series of horizontal cracks initiated from the splitting crack at the level of top and bottom rebars. The horizontal cracks propagated along the rebars and eventually directed toward the top reactions at both ends.

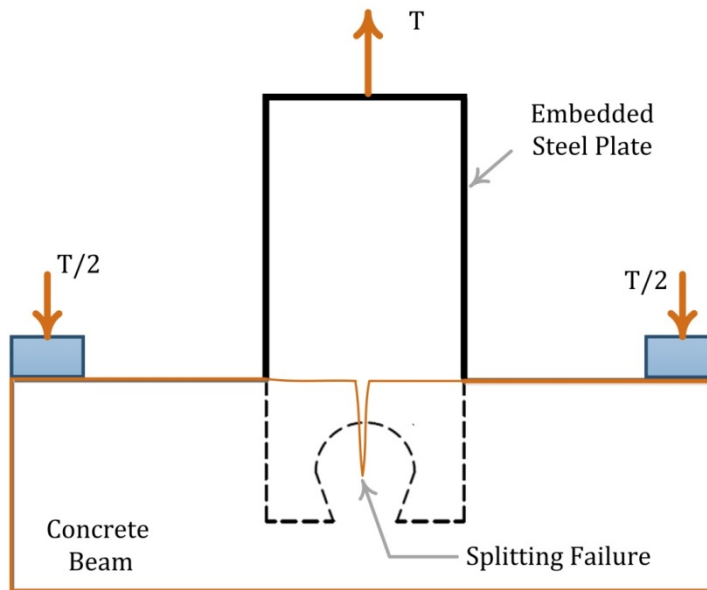


Figure 6-3: Schematic of splitting failure in the composite connection.

6.3.4 Breakout Failure

Break-out failure (BF) was found to be the most common failure mode in the majority of the composite connection specimens. The overall geometry of the four different types of the break-out failure is illustrated in the Figure 6-4. In this failure, a fractured concrete block surrounding the embedded steel plate tends to detach from the rest of the concrete beam.

According to test results, the overall configuration of the breakout failure including the crack pattern and the depth of the failure surface is significantly influenced by the concrete material (FRC or UHPFRC) used in the beam and the tension key configurations (Ω -shaped, O-shaped, and puzzle-strip). A cone-shaped failure was found for the composite connections constructed with the UHPFRC material. See Figure 6-4 (a-c). An almost triangular-shaped failure pattern was found for the composite connections made of the FRC material, as shown in Figure 6-4 (d). The specimens with Ω -shaped tension key tend to have the deepest failure pattern, where the failure surface is formed at the embedded end of the steel plate. The slope of the crack measured from the horizontal, lies between 30° to 40° and tends to increase with the increase in the depth of the concrete beam and embedded length of the steel plate. In the other words this angle is mainly affected by the state of stress in the concrete material around the embedded steel plate. According to the DIC test results, lower values for the depth of the concrete breakout surface was found for the connection system constructed with FRC material, as compared with those with UHPFRC material.

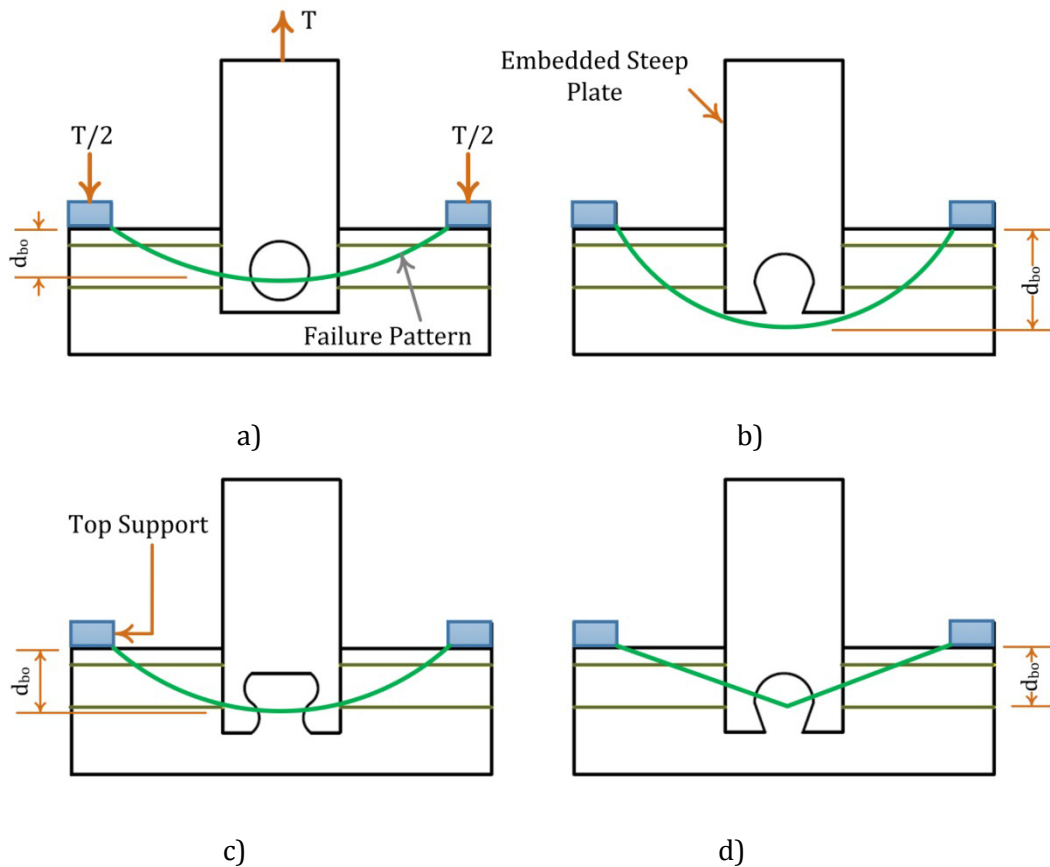


Figure 6-4: Breakout failure modes in the composite connections with different tension key configurations, a) O-shaped tension key in UHPFRC beam, b) Ω-shaped tension key in UHPFRC beam, c) puzzle-strip tension key in UHPFRC beam, d) Ω-shaped tension key in FRC beam.

6.3.5 Concrete Side Failure

The concrete side failure (CSF) is characterized by a pair of inclined cracks in one side of the concrete beam, which is parallel to the embedded steel plate. The inclined cracks extended from both sides of the embedded steel plate toward the supports, as shown in Figure 6-5. In this failure mode, the concrete surrounding the embedded steel plate displaced perpendicular to axis of the pull-out loading and formed two significant inclined cracks. A premature failure of this type was observed only at one side of the specimen when the embedded steel plate is not perpendicularly placed into the concrete beam. In this case, majority of the pull-out stresses should be sustained by one side of the connection.

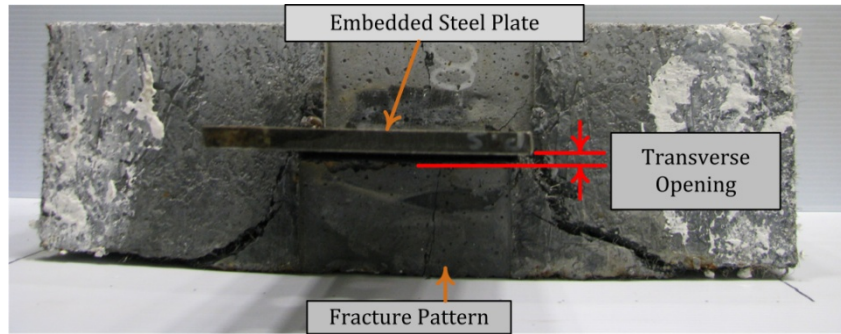


Figure 6-5: Concrete side failure in composite connection system.

6.4 Pullout Response of Composite Connection with Ω -shaped Tension key

In this section the influence on the pull-out response of the composite connection with Ω -shaped tension key from the size of the tension key, plate thickness, embedded length of plate, concrete generation, and fiber volume fraction was investigated. The results of DIC technique are used to highlight the deflection, crack width, and crack growth pattern during the pullout loading (Correlated Solutions Inc., 2009). The lists of all the composite connection with Ω -shaped tension key are reported in Table 6-1 along with the failure mode, load, deflection, and crack width information.

The complete detail of the companion samples with compressive strength, peak equivalent tensile strength (PETS), and crack mouth opening displacement (CMOD) at PETS for each individual mix design are provided in chapter 5. From multiple batches of each mix (minimum 3 replicate tests of each), the compressive strengths of 50 mm cubes at the day of test are summarized in Table 6-1.

6.4.1 Influence of Hole Diameter

The response of the composite connection constructed with Ω -shaped tension key with three different hole sizes, i.e. $h_h = 50$ mm, 70 mm, and 90 mm was studied in this section. A UHPFRC material with $V_f = 2\%$ was used for the concrete beam.

6.4.1.1 Specimen $\Omega S-U-50-10-2$

Crack diagram showing the condition of the composite connection after failure are given in Figure 6-6. In both specimens, the primary damage zone concentrated on the extreme tensile fiber at the top part of the concrete beam where a series of microcracks were formed. No significant slip between the embedded plate and the concrete beam was observed during the formation of microcracks. The slip between the embedded steel plate and the concrete beam started at a load level of 115 kN. The rate of slip was observed to be increased with an increase in the splitting crack width. This is because the splitting crack passes through the concrete pin and significantly decreases the mechanical interlock between CONCRETE PIN and the Ω -Shaped tension key.

The relation between the pull-out load and slip for the $\Omega S-U-50-10-2$ specimens is shown in Figure 6-7. The first part of the curve, i.e. linear elastic stage, represents a general elastic behaviour, without the formation of microcrack in the UHPFRC beam. At the end of the linear stage, the first microcracks appeared at the top part of the concrete beam and close to the mid-span, where the UHPFRC material experienced a cracking tensile strength. A cracking tensile strength of 6.2 MPa was recorded for the companion flexural specimens. The next stage, i.e., post-cracking stage, is the initiation of several microcracks around the first one in the UHPFRC beam until the peak pull-out load (PPL) was reached. The connection specimens continue to carry higher level of loads until a localized vertical crack formed at the end of this stage.

Although a series of flexural and tensile cracks was formed in the tensile zone (top side) of the beam, no sign of concrete crushing was found in the regions with highest compression zone (bottom side of the concrete beam). The variation of the compression strain in the bottom side of the concrete beam and at the mid-span during the test was determined by the DIC system and the results are given in Figure 6-9. The compressive strain at the extreme compression fiber was measured and a value of $130 \mu\epsilon$ was observed. This value is well below the strain at the peak compressive strength, $\epsilon'_c = 0.004$, which was found for UHPFRC $V_f = 2\%$.

The relation between the pull-out load and the splitting crack width at mid-span is illustrated in Figure 6-8. As presented in this figure, no further crack opening was

observed once the peak pull-out load was reached. Instead, the embedded steel plate was pulled out with a constant rate.

The possibility of two failure modes was investigated for this connection system: steel yielding failure (SYF) and pull-out failure (PF). The first mode is less likely, as the maximum tensile stress at the critical section of the steel plate subjected to PPL, given in Figure 6-7, is around 155 MPa which is well below the yielding stress of the steel plate derived from the coupon test ($F_{ys} = 373$ MPa). Thus the PF is more likely for this connection specimen in which the concrete tension key was failed under direct shear load.

Both specimens exhibited a graduate decrease in the load carrying capacity after the peak pull-out load reached. This is most probably because the short steel fibers in the UHPFRC beam can significantly contribute to the rate of degradation of the material.

The variation of compressive strain at the bottom side of the concrete beam is shown in the Figure 6-9. According to DIC test results, the compressive strain linearly increased with an increase in the slip until a strain level of $1.3E-3$ was reached. This strain level is well below the compressive strain of UHPFRC material at the peak (0.004). After this level, the strain decreased under the test was stopped.

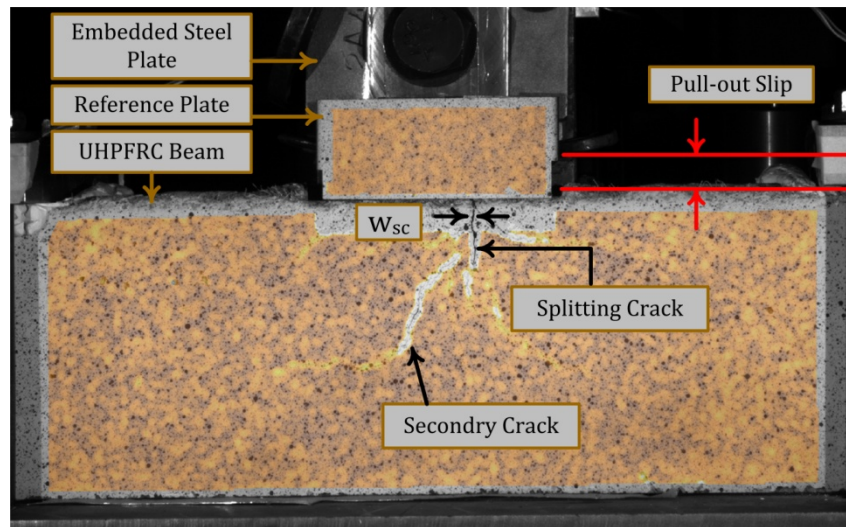


Figure 6-6: Overall failure of Ω S-U-50-10-2 specimen (Ω -shaped tension key, $h_h = 50$ mm, UHPFRC material with $V_f = 2\%$, plate thickness = 10 mm).

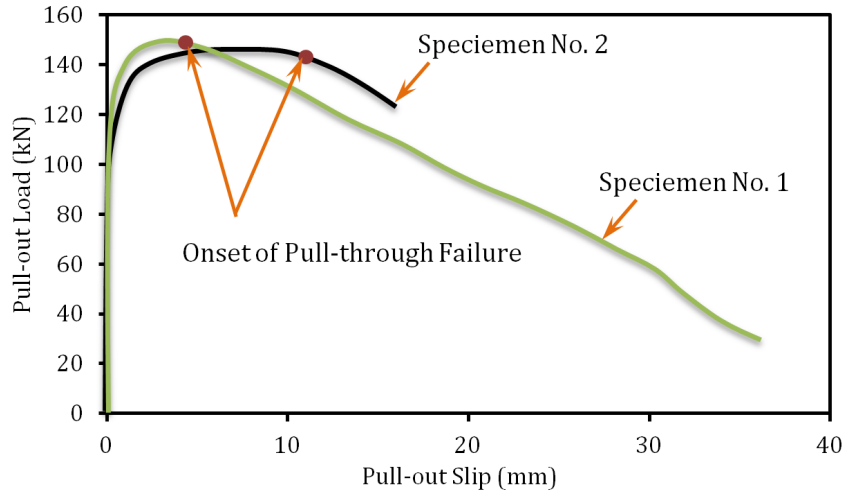


Figure 6-7: Pull-out load-slip response of Ω S-U-50-10-2 connection specimens.

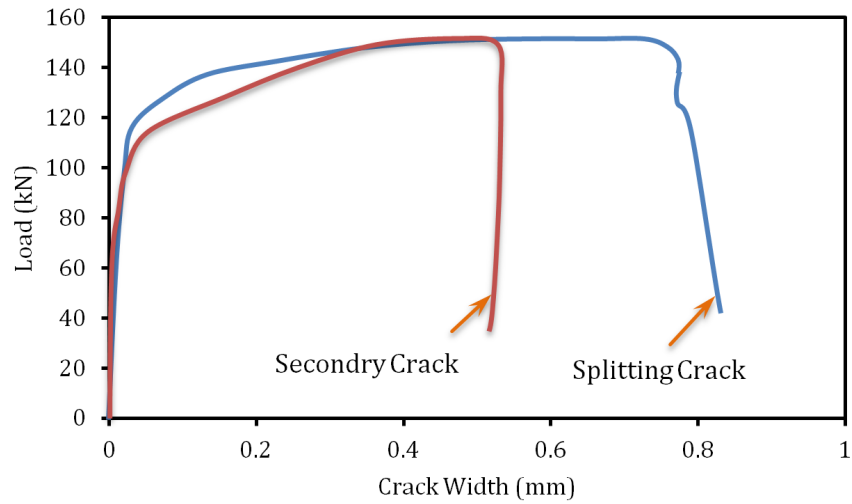


Figure 6-8: Failure cracks growth throughout testing of Ω S-U-50-10-2 specimen (First Specimen).

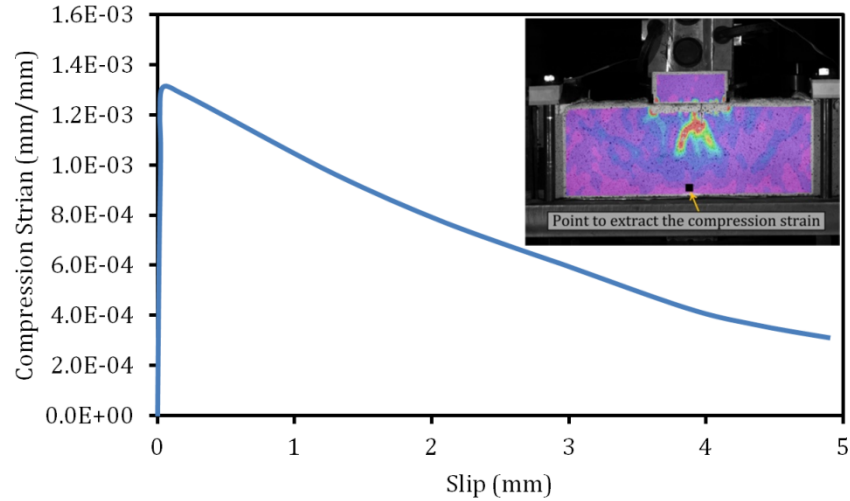


Figure 6-9: Variation of average compressive strain against slip for the $\Omega S-U-50-10-2$ specimen (First Specimen).

6.4.1.2 Specimen $\Omega S-U-70-10-2$

The crack pattern after the failure of the $\Omega S-U-70-10-2$ is given in the Figure 6-10. Unlike the $\Omega S-U-50-10-2$ specimen with a pull-out failure, a combination of splitting failure and breakout failure was observed in the $\Omega S-U-70-10-2$ specimens.

The variation of the splitting crack width at the level of the extreme tensile fiber and the breakout crack width at the mid-span of the beam were extracted from the data obtained from the digital image correlation (DIC) measurement system and depicted in Figure 6-11. For both specimens, a series of vertical microcracks near the mid-span of the beam initiated at a load level of 85 kN (see Figure 6-11). These cracks were then extended downward and gradually increased as the pull-out load increased. As a result the splitting cracks along with some secondary inclined cracks were formed in the mid-span of the beam where the tensile stress in UHPFRC beam is the maximum. An average splitting crack width of 1.15 mm at the PPL was observed (see Figure 6-12). Once the peak pull-out load was reached, the crack growth was rapid until the load level of 160 kN, where the splitting crack was stopped.

At a load level of 128.5 kN, a horizontal crack was initiated at the level of bottom horizontal reinforcement and propagated along the rebar. The breakout crack width at the PPL level was found to be 0.98 mm. The break-out crack growth was rapid

after the PPL and curved diagonally toward the inside edge of the loading plate at the top side of the beam, as shown in Figure 6-10.

No significant relative slip between the embedded steel plate and the concrete beam was noted up to a load level of 90 kN and 130 kN for first and second specimens respectively. After this stage, the embedded steel plate gradually pulled out until the PPL was reached. A higher rate of the slip between the embedded steel plate and the concrete beam was observed after the peak pull-out load was reached. This is most probably because the splitting crack leads to a significant degradation in the load carrying capacity of the concrete pin with an eventual failure in the concrete pin. Secondary cracks, with small width, propagated from the failure cracks to the inside face of the support plates after the peak pull-out load was reached (see Figure 6-10).

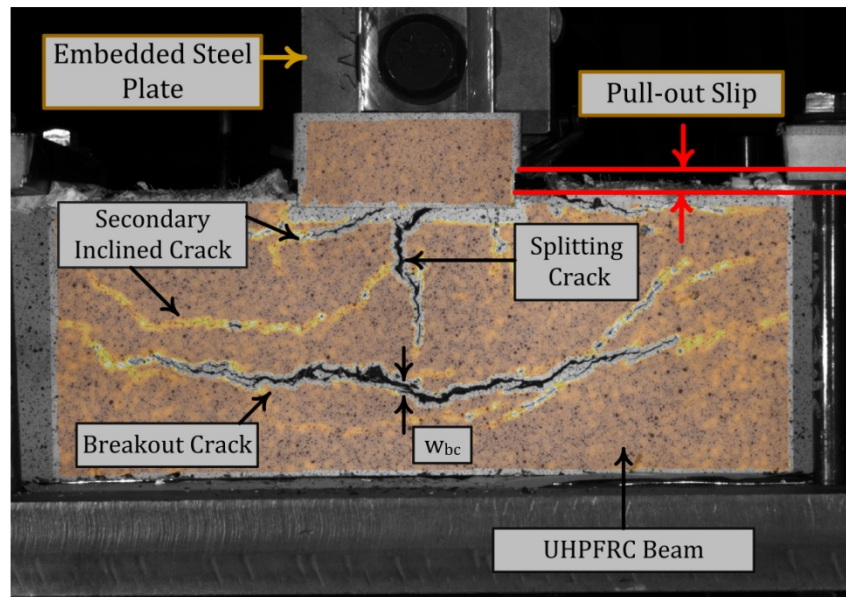


Figure 6-10: Overall failure of Ω S-U-70-10-2 specimen (Ω -shaped tension key, $h_h=70$ mm, UHPFRC material with $V_f=2\%$, plate thickness = 10 mm).

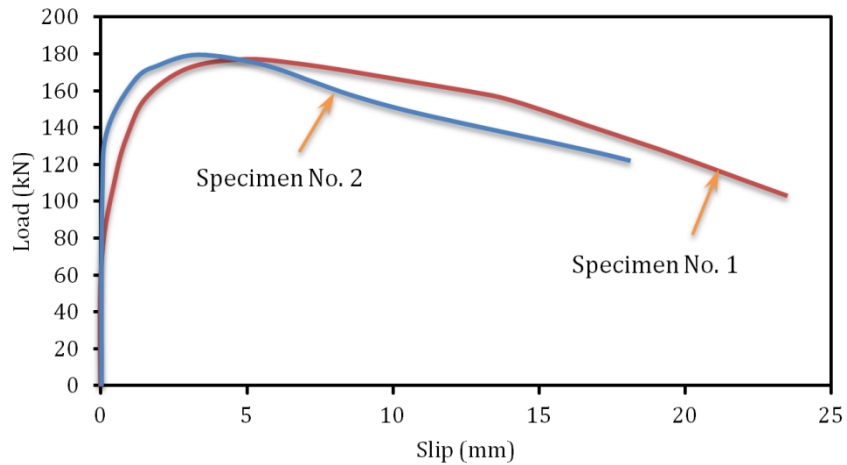


Figure 6-11: Load-slip response of $\Omega S-U-70-10-2$ specimens.

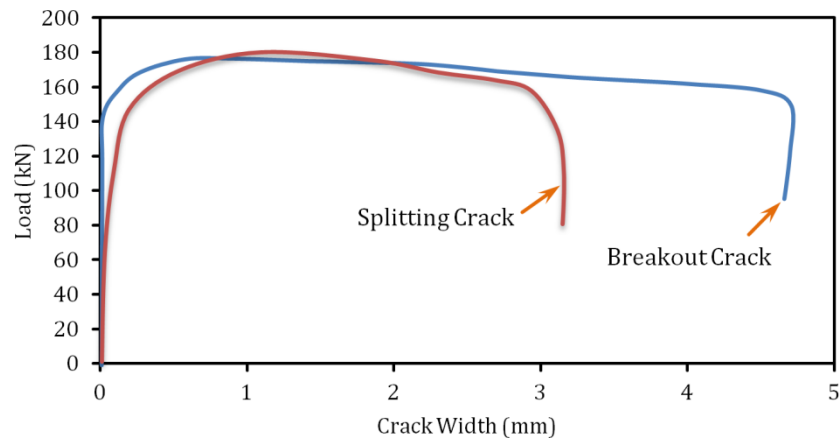


Figure 6-12: Failure cracks growth throughout testing of $\Omega S-U-70-10-2$ specimen (First Specimen).

6.4.1.3 Specimen $\Omega S-U-90-10-2$

The failure modes of the $\Omega S-U-90-10-2$ specimens are shown in Figure 6-13. According to Figure 6-13 (a), the first specimen was characterized as a shallow breakout failure. However a different failure mode was observed in the second specimen, where a combination of splitting failure and pull-out failure was observed.

Linear-elastic behaviour without microcrack formation in both specimens was observed up to a load level 119 kN and 123 kN respectively. For both specimens, a series of microcraks was formed at the extreme tensile fiber at the mid-span and at

the top of the beam, where the tensile stress in the UHPFRC material reached the peak equivalent tensile strength (PETS).

First Specimen: At a load level of 154 kN, an inclined crack at the level of double headed stud (DHS) was formed at the mid-height and mid-span of the beam. The slope of the crack with respect to the longitudinal axis of the concrete beam is approximately 45°. The crack was directed horizontally toward the left support at the level of top rebar. The right part of the crack also propagated from the level of bottom rebar toward the top support to form a breakout crack. The variation of the vertical crack against the pull-out load is given in Figure 6-15. The vertical crack formed at a load level of 172 kN at the mid-span of the concrete beam slightly propagated downward until the peak pull-out load was reached. A maximum splitting crack width of 0.05 mm was recorded by DIC system at the PPL. As given in Figure 6-15, a significantly higher rate of the splitting and the break-out crack was observed after the PPL was reached.

The slip between the embedded steel plate and the concrete beam started at a load level of 104 kN and gradually increased up to the PPL level. However, a higher rate of the slip was observed after the PPL, as shown in Figure 6-15, which is proportional to the rate of the break-out crack. A strain gauge mounted on the sides of the tension key recorded an average $\mu\varepsilon = 2950$ at 175 kN and $\mu\varepsilon = 3318$ at 153 kN (during softening stage), which is beyond the yield strain of the steel plate reported in chapter 5.

Second Specimen: A different failure cracks were observed in the second specimen, where the cracks were all localized around the embedded steel plate. According to the DIC test results, a series of vertical microcracks were initiated in the mid-span at the load level of 163 kN and gradually widened until they joined and formed a single crack at the PPL. More vertical cracks were formed next to the main crack after the PPL was reached. See Figure 6-13. Unlike the first specimen with a shallow break-out crack, no break-out failure was observed in this connection system. An average strain value of $\mu\varepsilon = 3170$ was recorded at the peak pull-out load (PPL) of the second specimen, which indicates that the embedded plate was yielded at both sides of the Ω -Shaped hole.

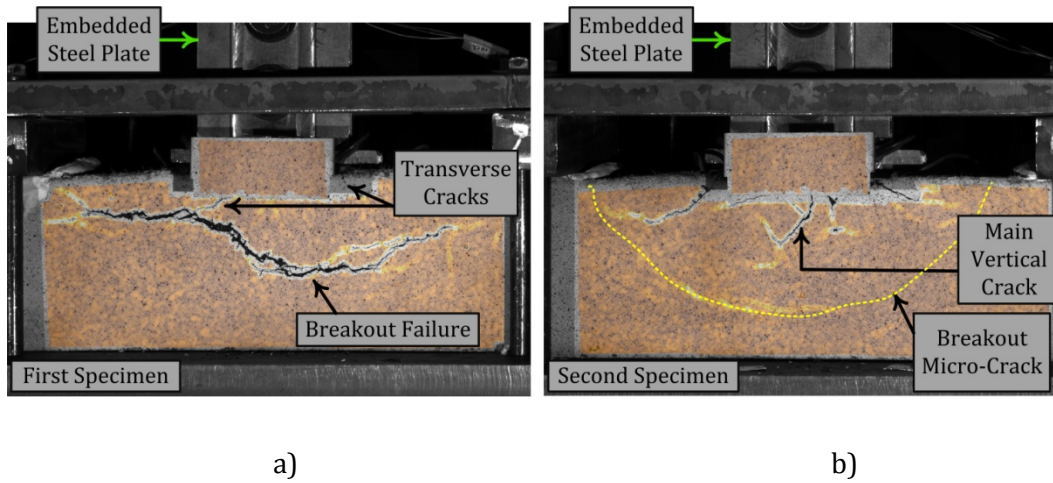


Figure 6-13: Overall failure of Ω S-U-90-10-2 specimen (Ω -shaped tension key, $h_h = 90$ mm, UHPFRC with $V_f = 2\%$, $t_{pl} = 10$ mm), a) First Specimen, b) Second Specimen.

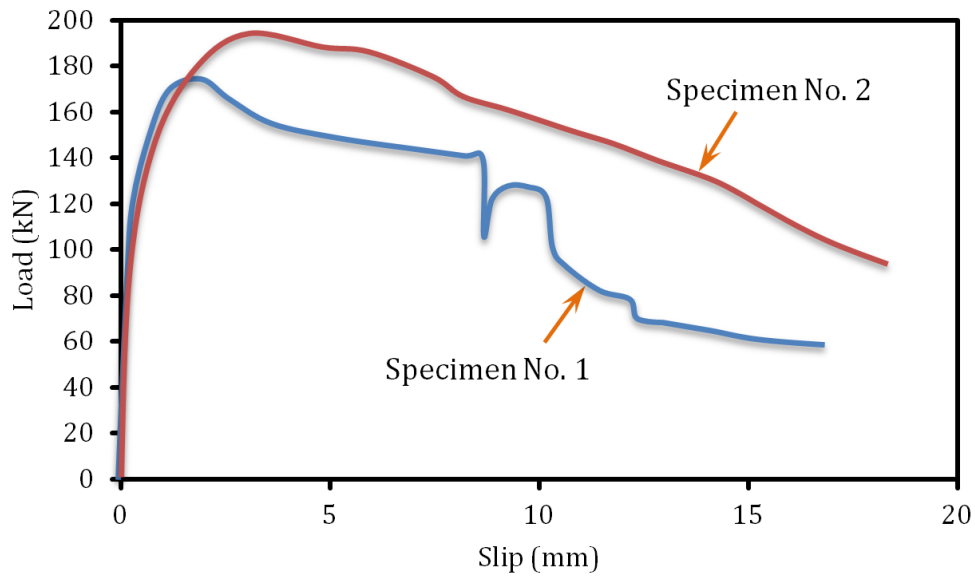


Figure 6-14: Load-slip response of Ω S-U-90-10-2 specimens.

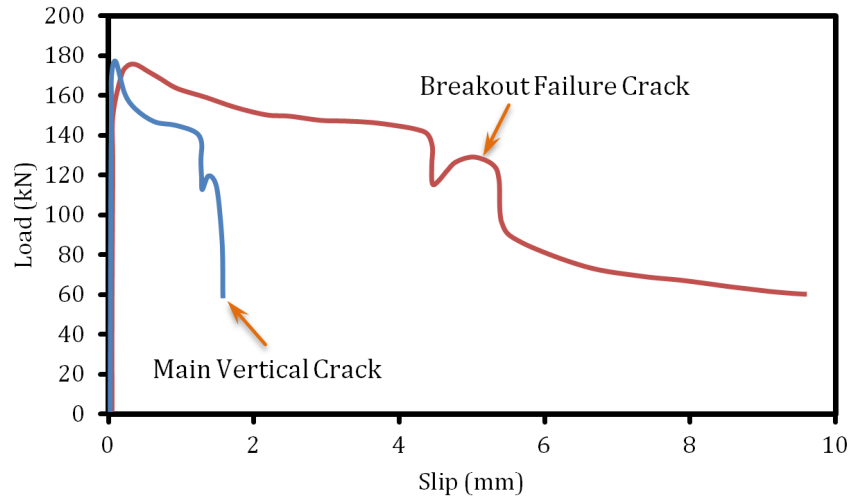


Figure 6-15: Failure cracks growth throughout testing of Ω S-U-90-10-2 specimen (first specimen).

6.4.1.4 Summary of Influence of Hole Diameter

Figure 6-16 shows a summary of the change in the peak pull-out load of the composite connection against the size of the Ω -shaped tension key. The average PPL values are shown with a solid line. Average improvement of 25% and 29% were observed as the tension key size was increased from 50 mm to 70 mm and 90 mm. This is mainly because the concrete pin under the pull-out load experiences a shear stress on its sides. Thus the increase in the hole size directly increase the shear strength provided by the concrete pin and enhance the pull-out load.

The extremely low crack width at the linear-elastic stage of the connection specimens offers a significant improvement in the permeability of the connection system under service conditions by preventing the ingress of detrimental substances (AASHTO T259 and AASHTO T260).

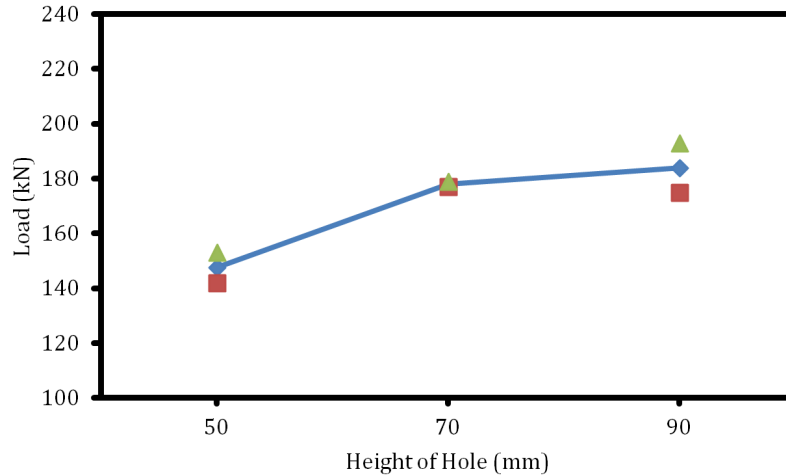


Figure 6-16: Influence of tension key diameter on load bearing capacity of composite connection with $V_f = 2\%$ and different tension key size.

6.4.2 Influence of Plate Thickness

The influence of different embedded plate thickness on the load carrying capacity of the composite connection constructed with UHPFRC material and the Ω -shaped tension key is discussed in this section. Five different plate thicknesses, i.e. 8, 9.5, 12.1, 15.9, and 19.1 mm were adopted in this study and the results of each test was discussed as follows.

6.4.2.1 Specimen $\Omega S-U-70-8-2$

Figure 6-17 shows the failure crack pattern in the $\Omega S-U-70-8-2$ specimen having an 8 mm Ω -shaped tension key. Both of the specimens were characterized by a steel yielding failure (SYF), where no significant loss of connection strength after the PPL was observed. The relationship between the pull-out load and slip is given in Figure 6-18. Similar load-slip responses were observed for both specimens during the test.

According to test results, a linear-elastic behaviour was observed for first and second connection systems up to a load level of 80 kN and 100 kN respectively. Then the crack width gradually increased until the peak pull-out load (PPL) was reached. Maximum crack widths of 0.4-0.5 mm were observed for longitudinal and transverse cracks at the PPL, as shown in Figure 6-17 and 6-19. No further growth in the crack width was observed after the PPL was reached. Instead the embedded

steel plate was pulled out with a higher rate compared to the rate before the peak load.

A steel failure was observed for both specimens, as the maximum tensile stress at the critical section of the steel plate is around 320 MPa which is close to yielding stress of the 8 mm steel plate derived from coupon test ($F_y=320$ MPa). Two strain gauges were placed on the east and west sides of the omega-shaped tension key to measure the longitudinal strain at the critical section of the embedded steel plate at various load levels. The strain gauge reached an average strain of 2700 $\mu\text{m}/\text{m}$ at an applied load level of approximately 172 kN before gradually becoming unbonded, as shown in Figure 6-20. The other gauge was not reading correctly after a load level of 95 kN, as it was most probably debonded during the pulling out process.

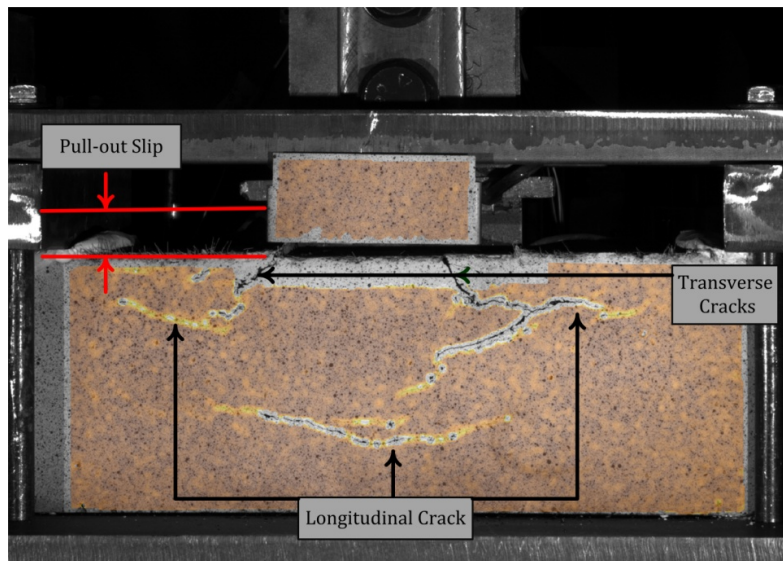


Figure 6-17: Overall failure of Ω S-U-70-8-2 specimen (Ω -shaped tension key, $h_h = 70$ mm, UHPFRC with $V_f = 2\%$, $t_{pl} = 8$ mm).

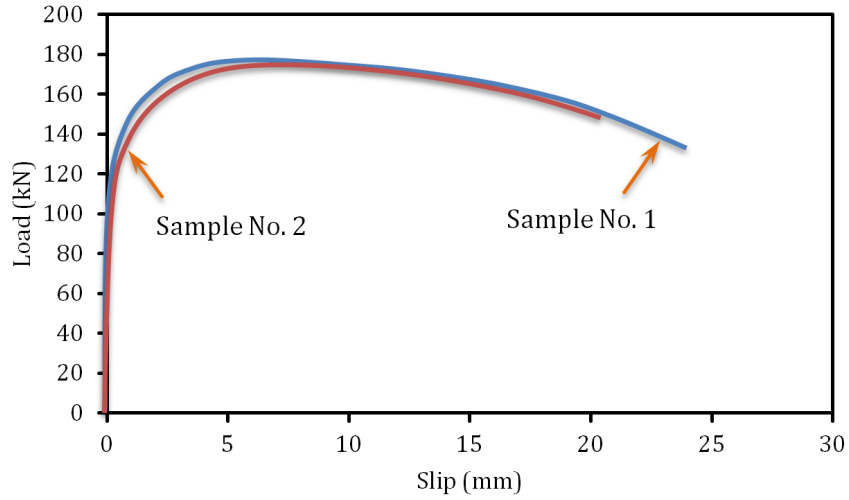


Figure 6-18: Load-slip response of Ω S-U-70-8-2 specimens.

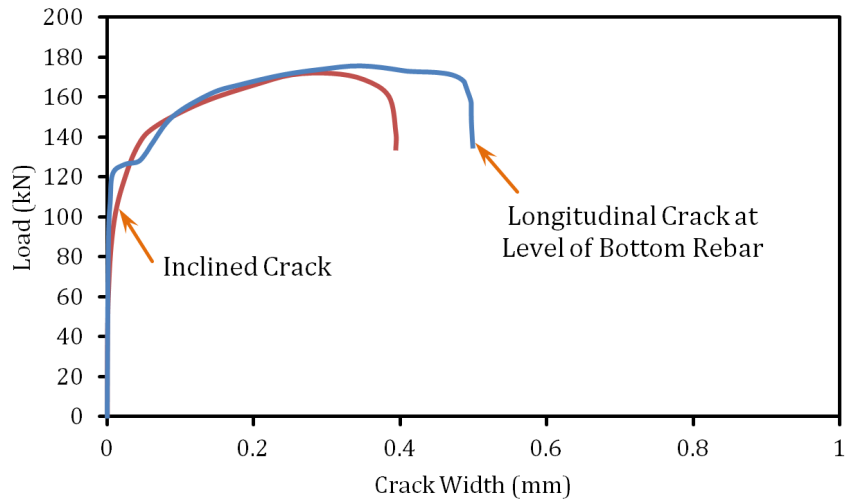


Figure 6-19: Failure cracks growth throughout testing of Ω S-U-70-8-2 specimen (First specimen).

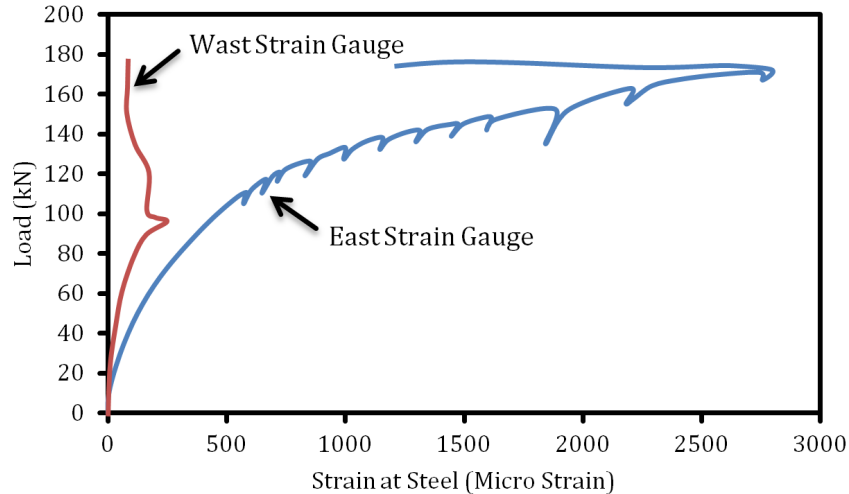


Figure 6-20: Load-steel strain response at mid-span for specimens of $\Omega S-U-70-8-2$ specimen (first specimen).

6.4.2.2 Specimen $\Omega S-U-70-12-2$

A typical failure crack pattern of the $\Omega S-U-70-12-2$ specimen is shown in Figure 6-21. A mixed failure mode was observed for both specimens. According to test results, a splitting crack was formed near the right end of steel plate at a load level 134 kN, which is significantly higher than the similar load level for the same connection with thinner embedded steel plate thickness, i.e. 8 mm or 10 mm. This is most likely due to a good mechanical bond between the tension key and the concrete pin, as the thicker plate provides larger contact strip between them.

The breakout crack was initiated at a load level of 152 kN at the mid span and at the level of bottom rebar. Upon the formation of the breakout crack, the splitting crack was directed toward the center of the specimen where the DHS is located. The overall trend of both splitting crack and the breakout crack during the entire test are given in Figure 6-23. The breakout crack was further developed and propagated toward the top reaction plates to form a conical breakout failure, as shown in Figure 6-21. According to graph provided in the Figure 6-23, the rate of crack growth in both splitting and break-out cracks was observed to increase once the PPL was reached.

No plate pull-out was observed until a load level of 145 kN and 162 kN for the first and second specimens respectively. After this stage, a gradual pull-out rate observed

until a PPL of 202.5 kN was reached, as shown in Figure 6-21. Beyond this stage, the rate of pull-out was increased until the test was stopped. This is because the crack significantly reduces the confinement provided to the concrete pin.

The relative slip between the embedded steel plate and the concrete beam at the PPL level was compared for connection systems with 12 mm thick plate against those with the thinner plates and significantly smaller value was found for connection system with 12 mm embedded steel plate.

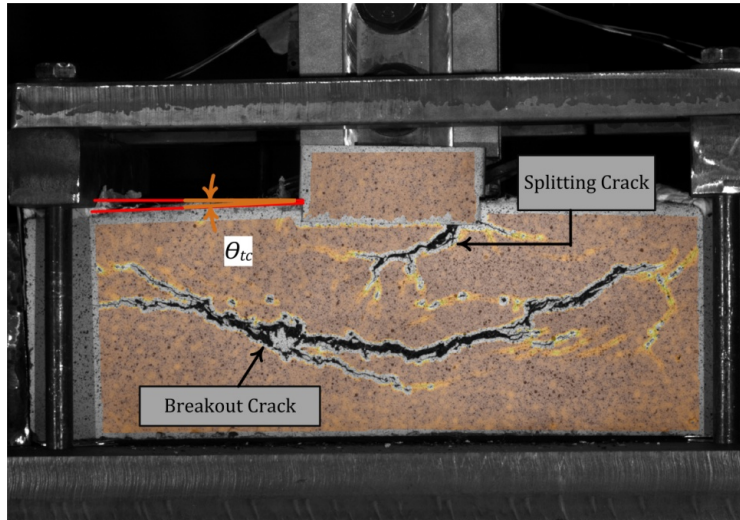


Figure 6-21: Overall failure of Ω S-U-70-12-2 specimen (Ω -shaped tension key, $h_h = 70$ mm, UHPFRC with $V_f = 2\%$, $t_{pl} = 12$ mm).

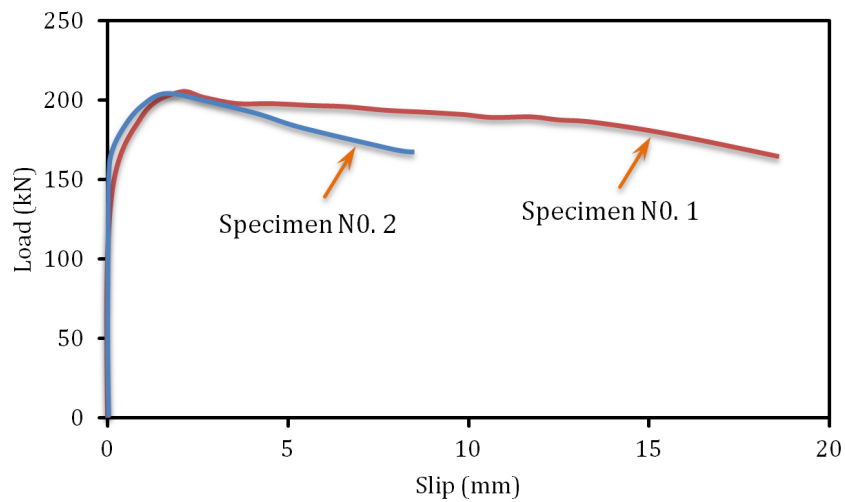


Figure 6-22: Load-slip response of Ω S-U-70-12-2 specimens.

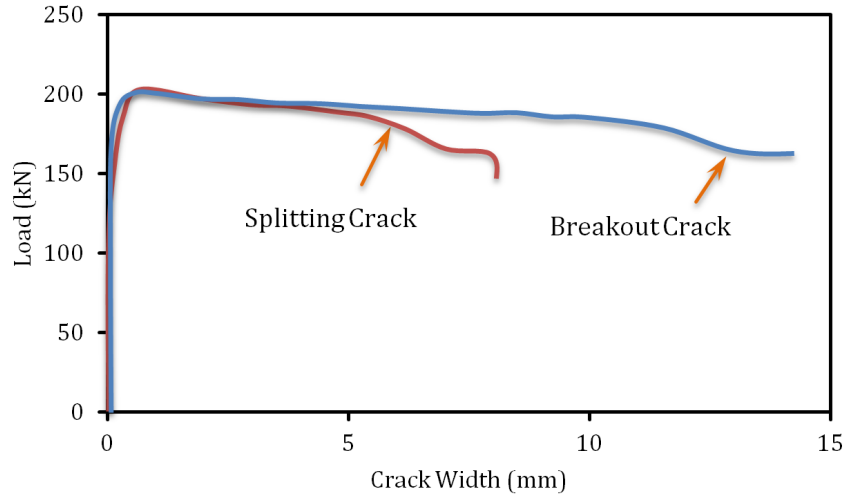


Figure 6-23: Failure cracks growth throughout testing of $\Omega S-U-70-12-2$ specimen (first specimen).

6.4.2.3 Specimen $\Omega S-U-70-16-2$

The failure in both $\Omega S-U-70-16-2$ specimens were characterized as a combination of the breakout failure and splitting failure, as shown in Figure 6-24. The change in the pull-out load is plotted against the slip between steel plate and concrete beam for $\Omega S-U-70-16-2$ specimens in Figure 6-25. Linear load deflection behaviour up to a load level of 100 kN was observed. This load level is 24% lower than the same connection with 12 mm plate. However compared to $\Omega S-U-70-12-2$ connection specimens, a higher PPL was observed for the $\Omega S-U-70-16-2$ connection, where 22% improvement in the PPL was observed. As given in Figure 6-25, the gradual increase in the load-slip response in the post-cracking stage was followed by a higher rate of slip between the embedded steel plate and the concrete beam in the softening stage. A series of sudden drop in the load-slip behaviour after the PPL level was observed for both specimens. This is because a huge energy was realized, once the breakout crack joined the inclined cracks. As shown in Figure 6-24, the breakout cracks were large enough to easily see through the full specimen width indicating a complete breakdown of the fiber bridging mechanism.

Figure 6-26 plots the pull-out load against the splitting and breakout crack. According to DIC results, neither splitting crack nor break-out crack was formed up to a load level 105 kN, where the first crack formed. After this stage, a gradual

growth in the splitting and break-out crack was observed until the peak pull-out load was reached. While no more significant growth in the splitting crack was observed after the PPL, the break-out cracks was observed to increase until the test was stopped, as shown in Figure 6-26.

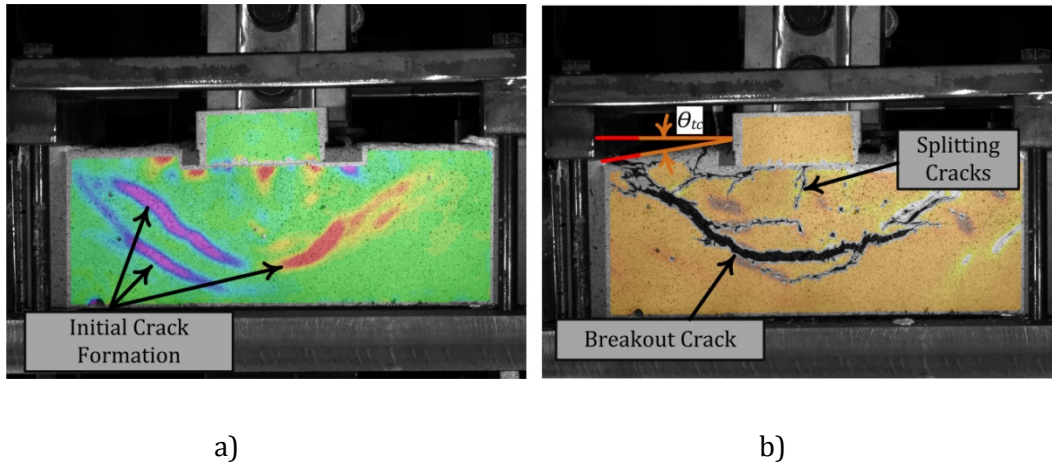


Figure 6-24: Overall failure of Ω S-U-70-16-2 specimens (Ω -shaped tension key, $h_h = 70$ mm, UHPFRC with $V_f = 2\%$, $t_{pl} = 16$ mm), a) First Specimen, b) Second Specimen.

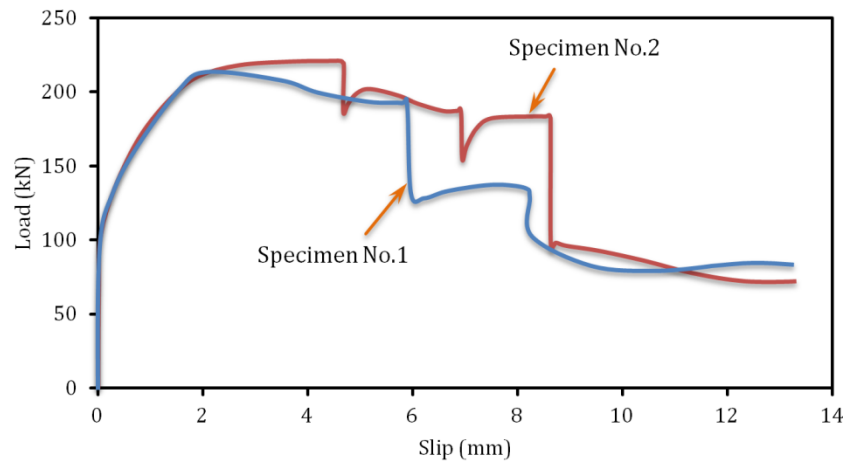


Figure 6-25: Load-slip response of Ω S-U-70-16-2 specimens.

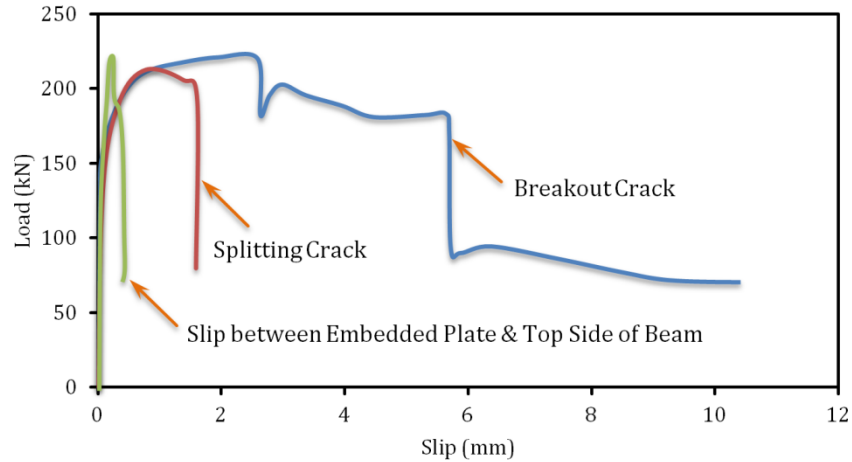


Figure 6-26: Failure cracks growth throughout testing of $\Omega S-U-70-16-2$ specimen (first specimen).

6.4.2.4 Specimen $\Omega S-U-70-20-2$

Similar failure mode was observed for both $\Omega S-U-70-20-2$ and $\Omega S-U-70-16-2$, where a combination of the breakout and splitting failure was observed, as shown in Figure 6-27. No significant crack growth was observed up to a load level of 126 kN. After this stage, both splitting and breakout crack width was gradually increased with an increase in the load until the maximum PPL was reached. While no significant growth in the splitting crack width was observed after the PPL was reached, the breakout crack was increased with a higher rate until the test was stopped, as indicated in Figure 6-28. The breakout crack was initiated at the mid-span of the beam and gradually propagated toward the left and right reaction located at the top side of the UHPFRC beam.

Almost no slip between embedded steel plate and top side of concrete beam was observed. This is mainly because there is a good mechanical interlock between the tension key and the UHPFRC beam. Instead the top side of the beam was observed to gradually rotate around the pivot (interface of the embedded steel plate and top side of concrete beam). According to Figure 6-28, a more stable load-slip response was observed for the $\Omega S-U-70-20-2$ specimens as compared with the $\Omega S-U-70-16-2$ specimen.

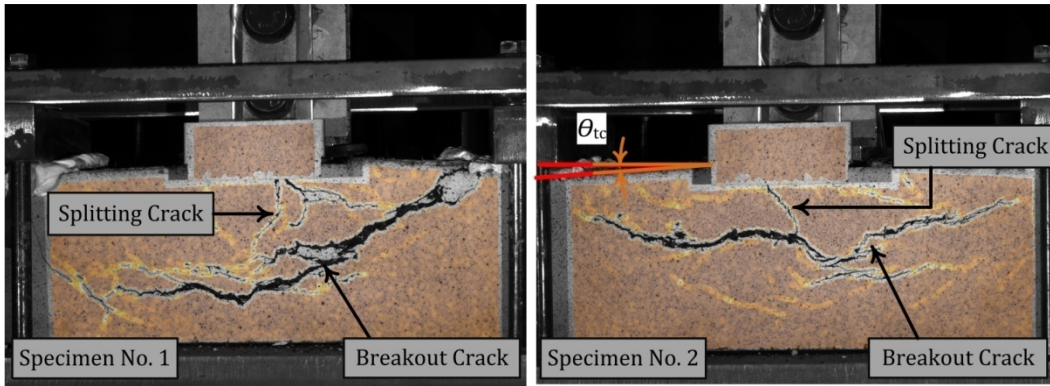


Figure 6-27: Overall failure of Ω S-U-70-20-2 specimen (Ω -shaped tension key, $h_h = 70$ mm, UHPFRC with $V_f = 2\%$, $t_{pl} = 20$ mm), a) First specimen, b) Second specimen.

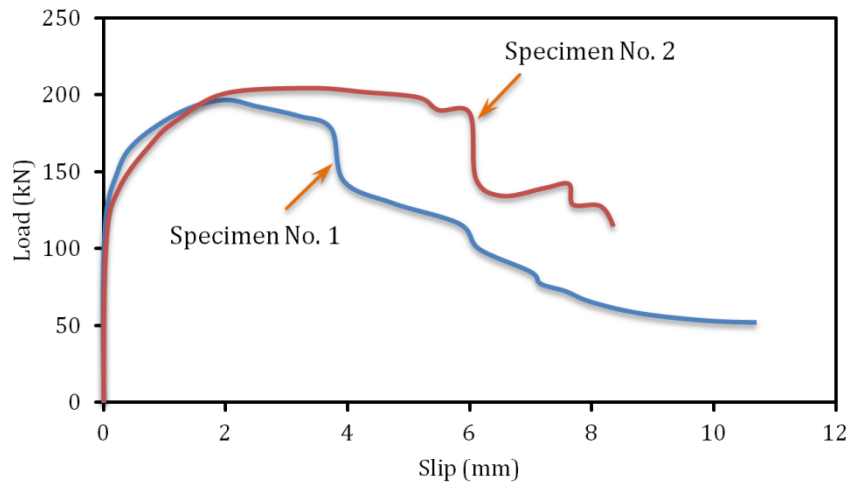


Figure 6-28: Load-slip response of Ω S-U-70-20-2 specimens.

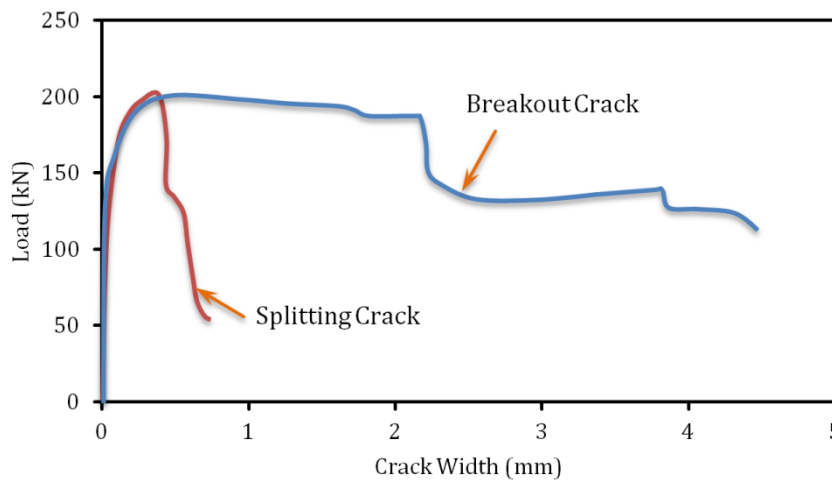


Figure 6-29: Failure cracks growth throughout testing of Ω S-U-70-20-2 specimen (First specimen).

6.4.2.5 Summary of Influence of Plate Thickness

Figure 6-30 shows the influence of embedded plate thickness on the PPL of composite connection with $V_f = 2\%$. Five different plate thicknesses, i.e. 8, 10, 12, 16, and 20 mm, were used in this study. Compared to the PPL of composite connection with 8 mm plate thickness, the use of 10, 12, 16, and 20 mm embedded steel plate in composite connection increased the PPL by 2%, 16%, 24%, and 15% respectively. This improvement is mainly because the increase in the plate thickness leads to lower bearing stress at the interface between the concrete pin and the embedded steel plate, which leads to higher PPL. The influence of plate thickness on the connection ductility was studied and the connection ductility tends to increase, as the plate thickness was increased from 8 to 12 mm. However further increase in the plate thickness was resulted in a decrease in connection ductility. This is due to drop in the load-slip response of the connection.

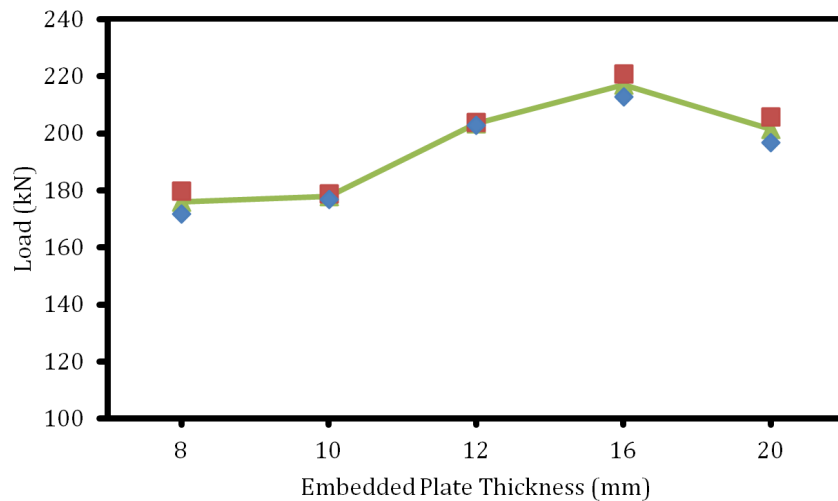


Figure 6-30: Influence of plate thickness on load bearing capacity of composite connection with $V_f = 2\%$.

6.4.3 Influence of plate embedment length

The influence of the embedded length of steel plate on the load PPL of the composite connection systems was experimentally studied. Two different embedment lengths were used: $L_{em} = 100$ mm and $L_{em} = 150$ mm. The dimension of the test specimens were selected in proportion to the embedment length of plate. The failure mechanisms of both connections are illustrated in Figure 6-31.

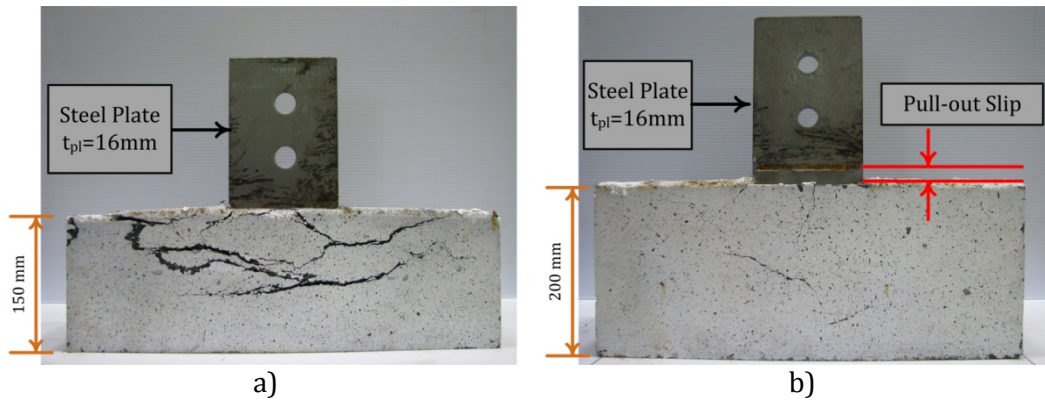


Figure 6-31: Crack pattern after failure for composite connection with UHPFRC: a) Ω S-U-70-16-2 specimen with embedded length of 100 mm, b) Ω S- U-70-16-2 specimen with embedded length of 150 mm.

6.4.3.1 Ω S-U-70-16-2; $L_{em} = 150$ mm

As shown in the Figure 6-32, the failure mode of the connection system with Ω -Shaped tension key was changed from a breakout failure for a specimen with embedded length of 100 mm to the pull-out failure for the Ω S-U-70-16-2 specimen with embedded length of 150 mm. Unlike the Ω S-U-70-16-2 with an embedded length of 100 mm, no significant loss of connection strength after the PPL was observed.

No significant crack growth was observed up to an average load level of 175 kN, which is 75% higher than the similar value for the same connection with embedded plate length of 100 mm. This improvement is attributed to the higher flexural stiffness provided by the deeper UHPFRC beam ($h_b = 200$ mm) over the connection system with 150 mm depth. The variation of the pull-out load against the crack width is given in the Figure 6-33. A splitting crack was first formed in the the mid span of the beam at a load level of 175 kN, where the tensile stresses exceeded the PETS of the UHPFRC material. This crack was gradually propagated until the PPL was reached. According to DIC results, a maximum 1.25 mm crack width was recorded for the splitting crack. At a load level of 205 kN, multiple microcracks initiated at the mid-height and mid-span of the UHPFRC beam along the rebars. These cracks were gradually propagated until the PPL, where a maximum crack width of 0.6 mm was reached. The results of DIC analysis indicated that compared with similar specimens with 100 mm embedded length, no significant crack opening

was observed in this connection system. This is mainly because the increase in the embedment length of steel plate changes the distribution of tensile stress over the surface of the potential failure path around the embedded plate and reduces the tensile stresses over the fracture surface.

The load-slip response for the Ω S-U-70-16-2 connection system is given in Figure 6-33. According to this graph, similar curves were observed for both specimens with an average peak pull-out load of 340 kN. The maximum tensile stress at the critical section of the steel plate under this load level was checked and a tensile stress of 305 MPa was found, which is well below the yielding stress of the steel plate derived from the coupon test ($F_{ys} = 409$ MPa). This implies that the behaviour of this connection system can be described by a pull-out failure in which the concrete tension key failed subjected to pull-out loading, which includes: 1) crushing of the concrete pin, as the small strip at the bottom sides of the concrete pin leads to a very high bearing stress, 2) shear failure of the larger sides of the concrete pin, as they experience a direct shear stress under the applied load.

The softening stage of this connection was compared against the similar connection system with 100 mm embedded plate and it was found that the connection systems with longer embedded plate length feature a significantly more stable softening stage with stable slipping rate and lower rate of degradation in the concrete beam. This is mainly attributed to lower level of the tensile stresses over the fracture, which prevents the premature failure.

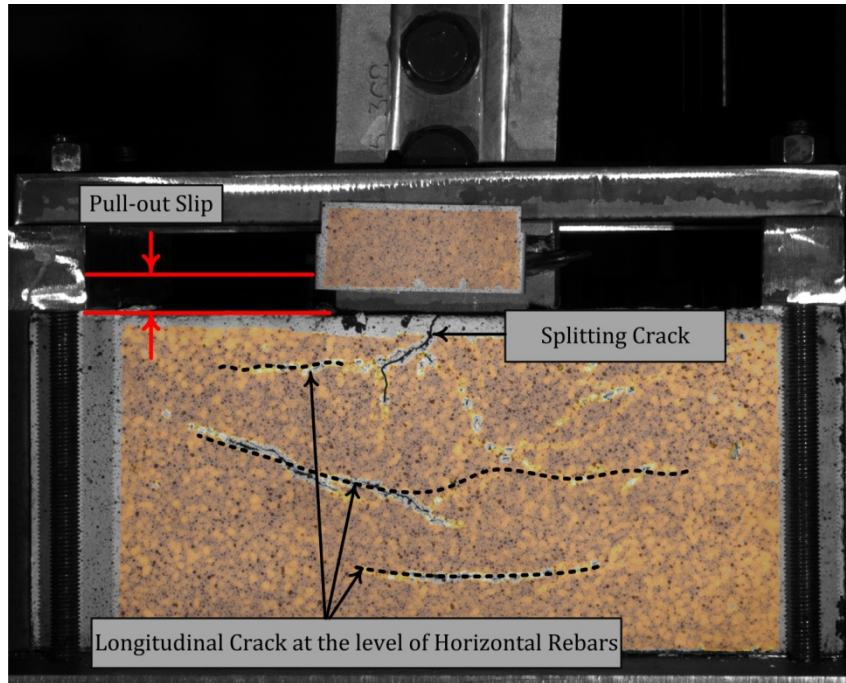


Figure 6-32: Overall failure of Ω S-U-70-16-2 specimen (Ω -shaped tension key, $h_h = 70$ mm, UHPFRC with $V_f = 2\%$, $t_{pl} = 16$ mm, embedded length of 150 mm).

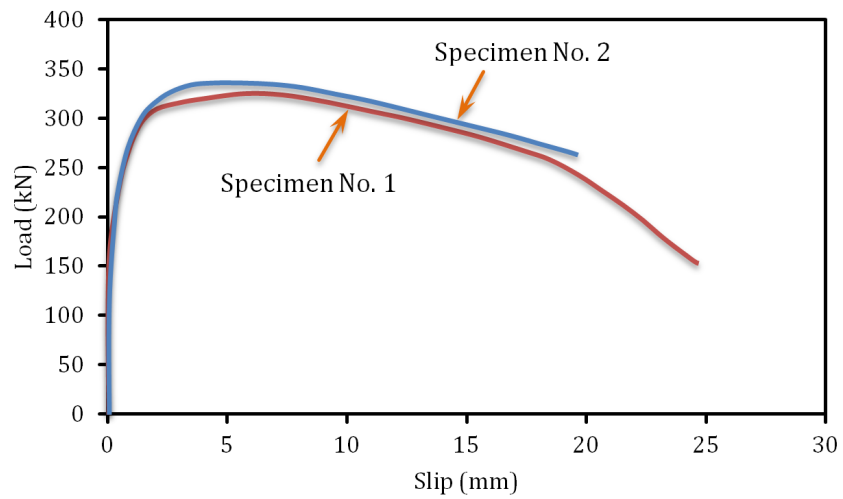


Figure 6-33: Load-slip response of Ω S-U-70-16-2 specimens.

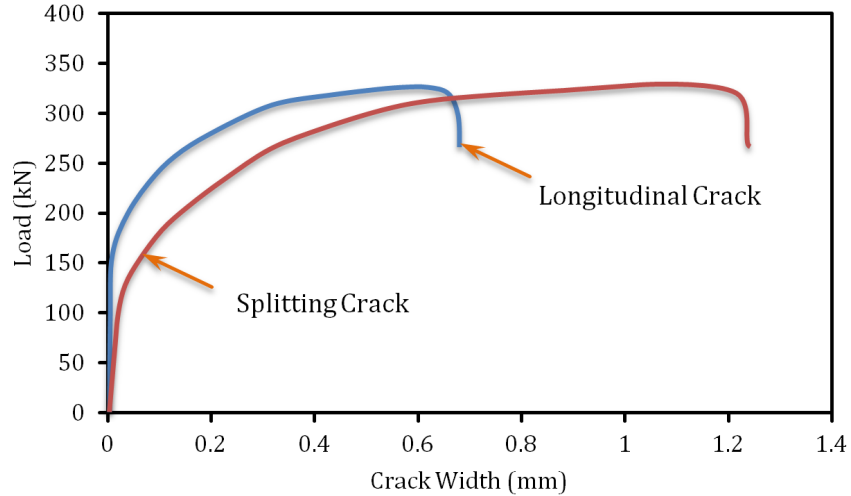


Figure 6-34: Failure cracks growth throughout testing of Ω S-U-70-16-2 Specimen.

6.4.3.2 Summary of Influence of Plate Embedded Length

The test results of the four connection specimens were used to evaluate the influence of embedment length of steel plate on the load bearing capacity of the composite connection. As shown in Figure 6-35, an average 55% improvement in the PPL of the composite connection was found as the embedded length of steel plate was increased from 100 mm to 150 mm. This is mainly attributed to the changes in the tensile stress distribution over the surface of the potential failure path which is already discussed.

The ductility factor for both connection systems was compared and it found that the increase in embedment length was resulted in 324% improvement in the ductility factor. This improvement is mainly attributed to a significant reduction in the average tensile stress over the fracture surface in the concrete beam, which prevents the sudden failure in the load-slip response of the connection. According to test results, a 324% increase in the connection ductility was observed as the embedded length was increased from 100 to 150 mm.

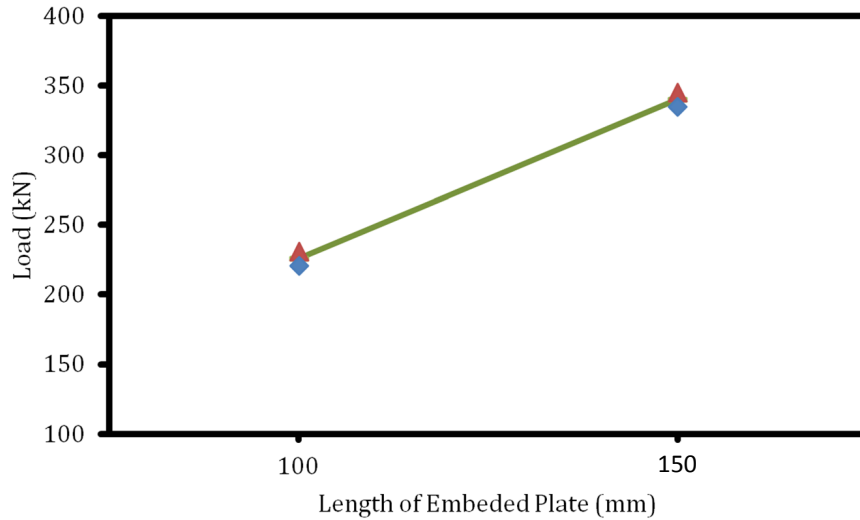


Figure 6-35: Influence of plate embedment length on load bearing capacity of composite connection with $V_f = 2\%$ and circular tension key.

6.4.4 Influence of Fiber Volume Fraction

UHPFRC Mixes with three different fiber volume-fractions, i.e, $V_f = 0\%$, 2% , and 4% , were used to study the influence on the pull-out response of the composite connections from different volume-fraction of randomly distributed short steel fibers. The UHPFRC with $V_f = 0\%$ is designated as $\Omega S-U-70-10-0$, with $V_f = 2\%$ is designated as $\Omega S-U-70-10-2$, and, with $V_f = 4\%$ is designated as $\Omega S-U-70-10-4$.

6.4.4.1 Specimen $\Omega S-U-70-10-0$ (Mix with $V_f = 0\%$)

The crack pattern of $\Omega S-U-70-10-0$ specimens after the failure is given in Figure 6-36. Both $\Omega S-U-70-10-0$ specimens were characterized as a breakout failure with multiple cracks on the front and back side of the specimen.

The variation of the pull-out load against the slip between the embedded steel and concrete beam is given in Figure 6-37. According to DIC test results, no relative slip between the embedded steel plate and concrete beam was observed until a load level of 45 kN was reached. After this stage a very unstable load-slip response was observed for both specimens during the post-cracking and softening stage. This is mainly attributed to the fact that there is no secondary mechanism (steel fibers) to

bridge the microcrack once the maximum principal stress in the UHPFRC matrix exceeds the elastic tensile strength.

Figure 6-37 plots the variation of the pull-out load against the transverse and breakout cracks. No microcracks were observed during the initial linear-elastic stage. At a load level of 40 kN, a pair of vertical cracks was formed along the edges of the embedded steel plate and gradually increase until the PPL was reached. A maximum transverse crack width and length of 1 mm and 18 mm was measured at the end of the test.

Immediately after the formation of the transverse cracks at the top of the concrete beam, a series of longitudinal microcracks were initiated from the DHS toward the end of the concrete beam at a load level of 45 kN. The rate of the crack propagation was found to be significantly higher than similar specimens constructed with the UHPFRC material incorporating short steel fibers. As the load increase, a series of micro-cracks was initiated around the DHS, which was resulted in a local side blow-out failure in the vicinity of the head of DHS. As a result, small concrete pieces were ejected from the front and back side of concrete. This is because the thin cover around the double headed stud with a thickness of 10 mm was not able to accommodate the quasi-hydrostatic pressure.

A series of secondary parallel cracks was formed below and above the main breakout crack at the higher load levels. The transverse cracks at top were further developed until they joined the breakout cracks. The maximum inclined crack width was observed to be less than 1 mm at the end of the failure. No significant slip between the embedded steel plate and the top side of concrete was observed. Instead the side was rotated around the pivot of the steel plate.

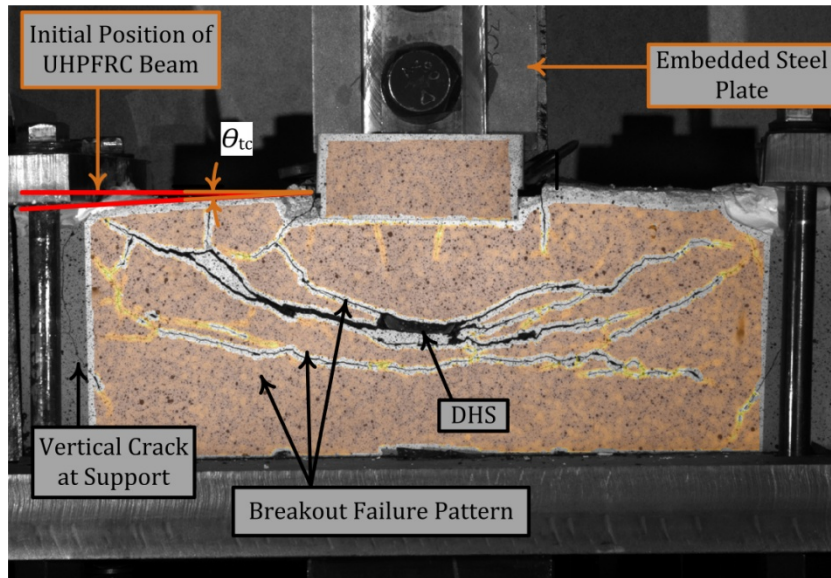


Figure 6-36: Overall failure of Ω S-U-70-10-0 specimen (Ω -shaped tension key, $h_h = 70$ mm, UHPFRC with $V_f = 0\%$, $t_{pl} = 10$ mm).

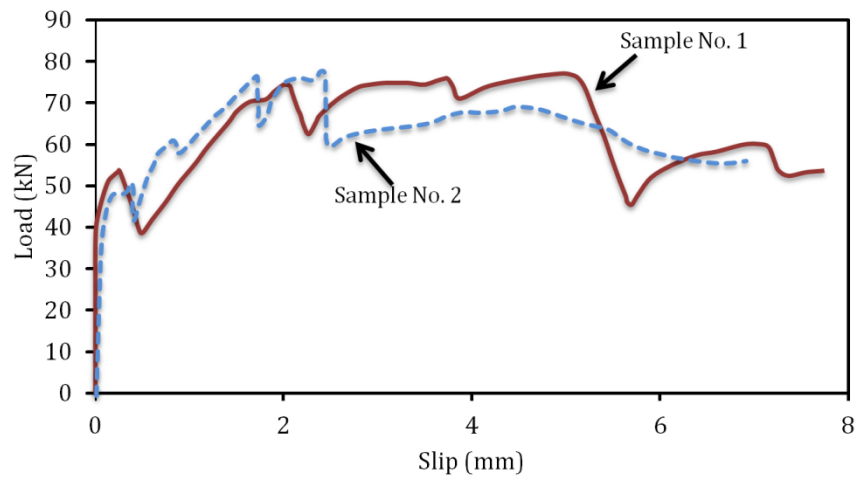


Figure 6-37: Load-slip response of Ω S-U-70-10-0 specimens.

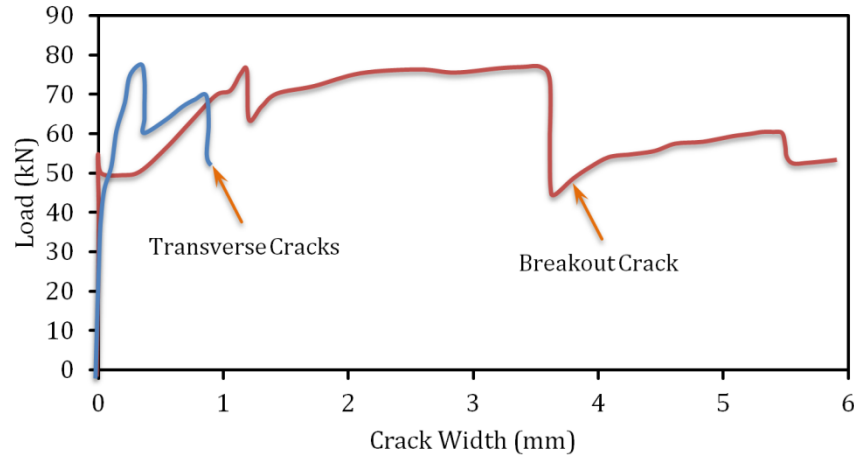


Figure 6-38: Failure cracks growth throughout testing of Ω S-U-70-10-0 specimen (first specimen).

6.4.4.2 Specimen Ω S-U-70-10-2 (Mix with $V_f = 2\%$)

The behaviour and failure pattern of this connection system was already explained in section 6.4.1.2.

6.4.4.3 Specimen Ω S-U-70-10-4 (UHPFRC material with $V_f = 4\%$)

The use of UHPFRC material with higher fiber contents allows developing a composite connection with a highly ductile response through the crack bridging effect provided by randomly distributed short steel fibers. The crack pattern of Ω S-U-70-10-4 specimens after the failure is given in Figure 6-39. Both specimens were characterized as a pull-out failure.

The pull-out load-slip response of the Ω S-U-70-10-4 specimens with $V_f = 4\%$ is shown in the Figure 6-40. A linear-elastic response up to a pull-out load of 150 kN was observed for this connection system, which is respectively 275% and 43% higher than the similar values observed for the mixes with $V_f = 0\%$ and 2%.

According to the DIC test results, no horizontal crack was observed until a load level of 80 kN was reached. At this load level, a horizontal crack was initiated at the level of the top rebar on the right side of the splitting crack and gradually propagated toward the reaction. The second horizontal crack was formed at the level of the bottom rebar, which is initiated from the end of the splitting crack and propagated

toward the left side. The horizontal cracks were further propagated along the rebars and stopped after the PPL was reached.

A single vertical microcrack was initiated at a load level of 185 kN at the mid span and at the top of the beam. This crack was further propagated with a higher rate as compared to the horizontal cracks until a splitting crack was formed at the mid-span of the beam. Variation of the splitting crack width against the pull-out load during the experimental test is given in Figure 6-40. According to test results, compared to connection system with $V_f = 0\%$, and 2% , a significantly more stable load-slip response before and after the PPL was observed for the connection system with $V_f = 4\%$.

The relation between the pull-out load and slip is given in Figure 6-41. No relative slip between the embedded steel plate and the concrete was observed in the linear-elastic stage. After this stage, a gradual slip was observed until the PPL was reached. Higher rate of slip was found for both specimens after the PPL level. The possibility of two failure modes was investigated for this connection system: steel yielding failure (SYF) and pull-out failure (PF).

Two strain gauges were placed on the east and west side of the omega-shaped tension key to measure the longitudinal strain at the critical section of the embedded steel plate during testing. The strain gauge reached an average strain of $550 \mu\text{mm}/\text{mm}$ and $625 \mu\text{mm}/\text{mm}$ at the PPL level. These values are well below the yielding strain of steel plate ($2000 \mu\text{mm}/\text{mm}$), which indicates that the steel failure did not happen. This indicates that the pull-out failure was most probably occurred during the test, in which the concrete pin (CP) failed under a combination of crushing of the concrete pin, and shear failure of the larger sides of the concrete pin.

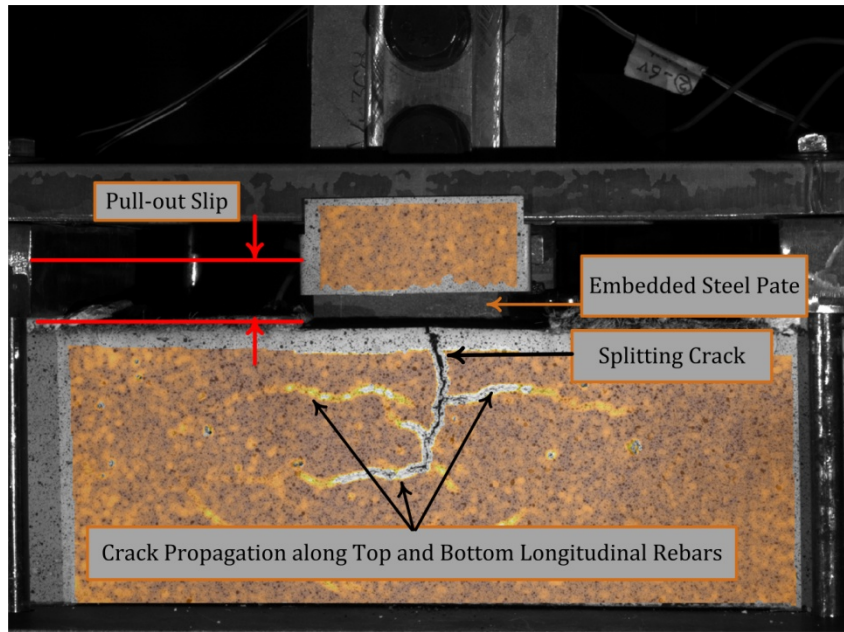


Figure 6-39: Overall failure of Ω S-U-70-10-4 specimen (Ω -shaped tension key, $h_h = 70$ mm, UHPFRC with $V_f = 4\%$, $t_{pl} = 10$ mm).

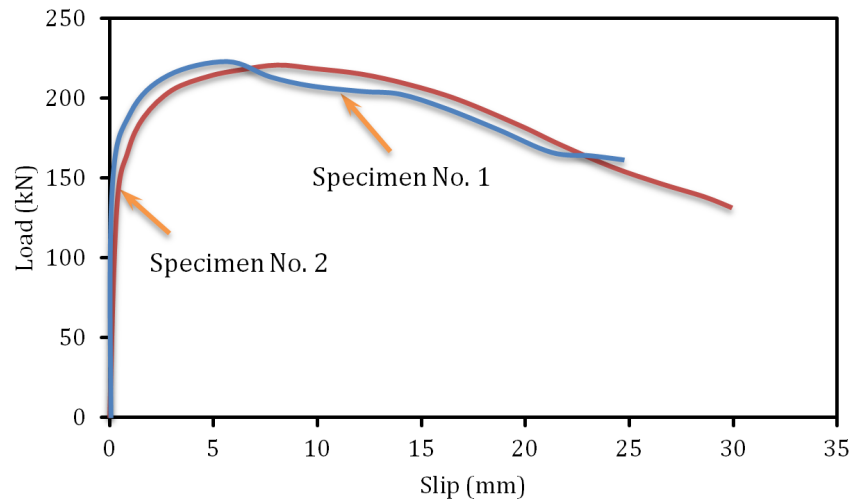


Figure 6-40: Load-slip response of Ω S-U-70-10-4 specimens.

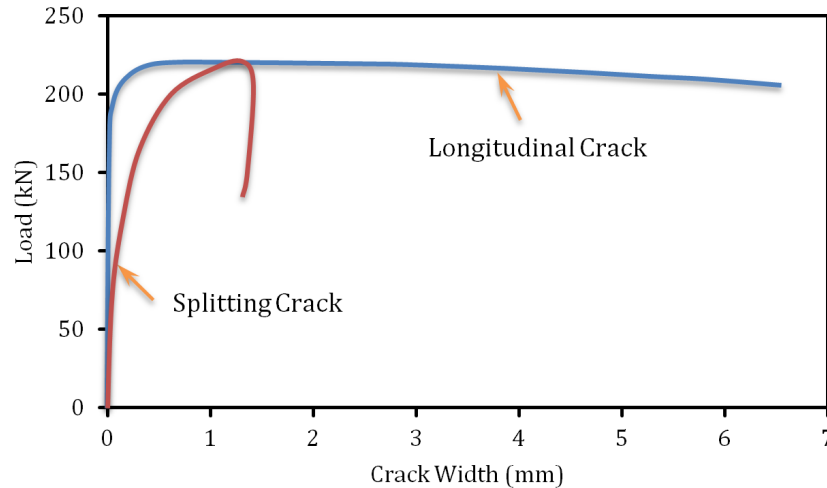


Figure 6-41: Failure cracks growth throughout testing of Ω S-U-70-10-4 specimen (first specimen).

6.4.4.4 Summary of Influence of Fiber Content

According to DIC test results, the composite connections constructed with plain UHPFRC material ($V_f = 0\%$), exhibited a larger fluctuation in the load-slip response than specimens with 2% and 4% volume-fraction of short steel fibers. In addition, the failure of the composite connections with plain UHPFRC material takes place at a very low slip deformation and is associated with a sudden drop in the pull-out load. In contrast, the composite connection constructed with the UHPFRC material with higher fiber contents was proved to have more desirable failure mode and can achieve significantly higher load and ductility.

Figure 6-42 shows the results of the changes in peak pull-out load (PPL) of the composite connection against the change in the V_f for the Ω S-U-70-10 composite connection. According to this graph, the increase in the fiber volume-fraction from 0% to 2% and 4% result in 130% and 187% improvement in the peak pull-out load of the connection systems. This significant improvement is mainly attributed to formation of multiple microcracking during the inelastic deformation of the concrete beam. As a microcrack forms in the UHPFRC matrix, the crack faces are immediately bridged by short discontinuous randomly-distributed steel fibers, which retard the uncontrolled propagation of the cracks in the concrete beam and eventually enhance the load-slip response of the connection system.

According to DIC test results, the addition of the fiber contents significantly enhanced the crack formation and propagation in the concrete beam by changing the cracking mechanism from a macrocrack to several microcracks. This phenomenon prevents ingress of detrimental substances.

Ductility—The composite connection constructed with the UHPFRC material with $V_f = 2\%$ and $V_f = 4\%$ exhibited 518% and 983% higher ductility factor than the connection system constructed with plain UHPFRC material. While the connection specimens with plain UHPFRC material failed by a brittle fracture failure associated with a lower ultimate strength, those with the UHPFRC material, incorporating short steel fibers, were gradually deteriorated by ductile yielding of UHPFRC materials. This significant enhancement in ductility suggests that the use of UHPFRC material can be effective in redistributing loads among the embedded steel plate and in improving composite action between steel plate and concrete beam. The brittle behaviour of plain UHPFRC is evident from its low deformation capacity, catastrophic load reduction with explosive nature, and low shear strength.

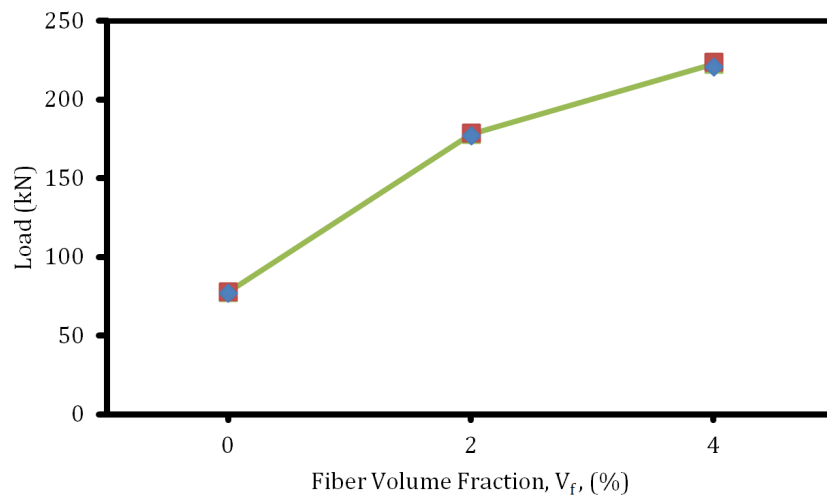


Figure 6-42: Influence of the fiber volume fraction ($V_f = 0\%$, 2% , and 4%) on the PPL of $\Omega S-U-70-10$ specimens.

6.4.5 Influence of Concrete Generation

The influence from two different generations of concrete, i.e. UHPFRC and FRC material on the pull-out response of the composite connection system are studied in this section. The connection system was constructed with the embedded steel plate

with two different thicknesses, i.e., 10 and 16 mm and a 70 mm Ω -shaped tension key. A UHPFRC material with $V_f = 2\%$ was used for the comparison of the performance with the FRC material.

6.4.5.1 Specimen $\Omega S-F-70-10-1$

An overall view of the $\Omega S-F-70-10-1$ specimen after failure is shown in Figure 6-43. The FRC concrete incorporating 1% volume-fraction of hooked ends steel fibers was used for the concrete beam. Both specimens were characterized as a pull-out failure.

According to DIC test results, a linear-elastic response up to an average load level of 64 kN was observed for both $\Omega S-F-70-10-1$ (FRC with $V_f = 1\%$) specimens, which is 30 % lower than the same value for the $\Omega S-U-70-10-2$ (UHPFRC with $V_f = 2\%$). Unlike the $\Omega S-U-70-10-2$ connection specimens with a hardening behaviour in the post-cracking stage, a small plateau was observed for $\Omega S-F-70-10-1$ specimens, which is followed by a hardening stage. The slope of the post-cracking stage of the $\Omega S-F-70-10-1$ specimens was observed to be significantly lower than that of the $\Omega S-U-70-10-2$ specimens. This is mainly because the response and failure mechanism of this connection system is directly influenced by the mechanical properties of the FRC material. According to past research, the mechanical properties of the FRC material in shear and tension are significantly lower than UHPFRC, which leads to lower stiffness and peak pull-out load in the connection system (Richard and Cheyrezy 1994, Graybeal 2006). According to DIC test results, higher rate of slipping between the embedded steel plate and the concrete beam during the post-cracking and softening stage was observed for connection system constructed with the FRC material over the similar connection system with the UHPFRC material.

According to the DIC test results, no splitting crack was found until a load level of 57 kN, where a horizontal crack was initiated at the mid-span of the beam. The crack was gradually propagated until the PPL was reached. A maximum splitting crack width of 0.2 mm at the end of the test was recorded by the DIC system. A breakout crack was formed at the level of the top rebar and gradually propagated toward top side of the concrete beam. A maximum breakout crack width of 0.2 mm at the end of the test was recorded by the DIC system, as indicated in Figure 6-45.

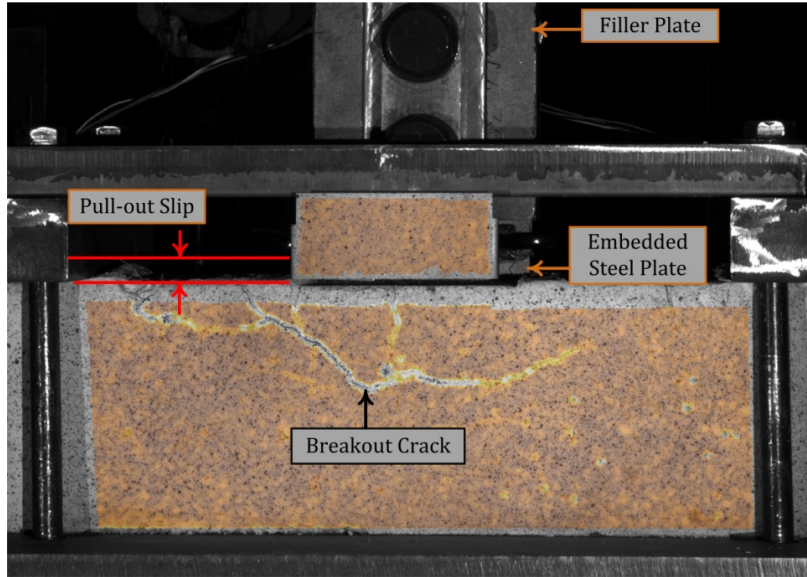


Figure 6-43: Overall failure of Ω S-F-70-10-1 specimen (Ω -shaped tension key, $h_h = 70$ mm, FRC with $V_f = 1\%$, $t_{pl} = 10$ mm).

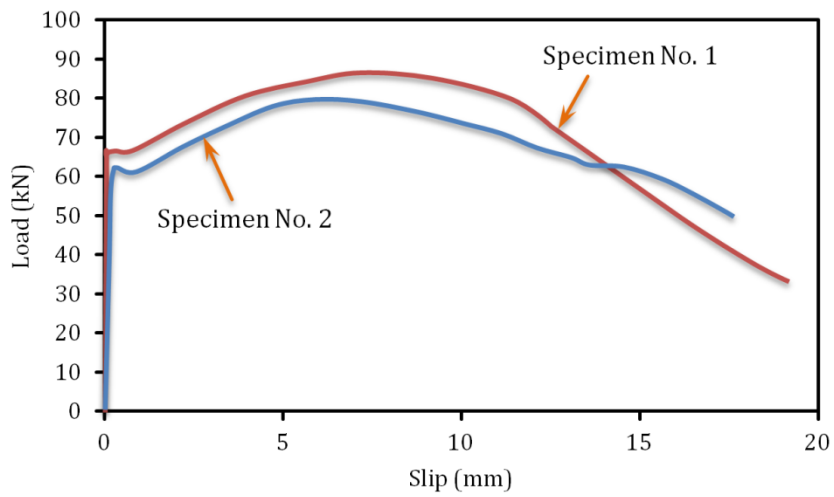


Figure 6-44: Load-slip response of Ω S-F-70-10-1 specimens.

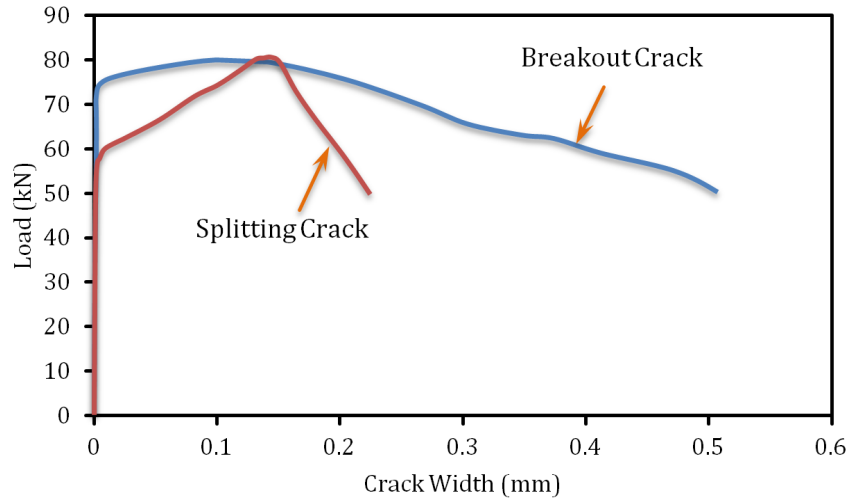


Figure 6-45: Failure cracks growth throughout testing of $\Omega S-F-70-10-1$ specimen (first specimen).

6.4.5.2 Specimen $\Omega S-F-70-16-1$

A general view of the $\Omega S-F-70-16-1$ composite connection system after the failure is shown in Figure 6-46. The connection system was constructed with FRC material and 16 mm embedded steel plate. Both specimens were characterized as a breakout failure.

The results of the pull-out load-slip response for the $\Omega S-F-70-16-1$ connection systems are given in Figure 6-47. A linear-elastic stage up to load levels of 84 kN and 122 kN was respectively observed for the first and second specimens. A post-cracking stage with higher stiffness, compared to $\Omega S-F-70-10-1$ specimens, was observed for the $\Omega S-F-70-16-1$ specimen until the average peak load of 142 kN was reached. A 70% improvement in the PPL was found as the embedded plate thickness was increased from 10 mm to 16 mm. This is most likely attributed to improved mechanical interlock between the concrete pin and the embedded steel plate.

The test results of the DIC measurements indicate that, the breakout crack was initiated at a load level of 92 kN, where a horizontal crack was initiated at the mid-span of the beam. This value is 55% higher than the similar value for the connection system with a plate thickness of 10 mm. The breakout crack was gradually propagated during the post-cracking and the softening stage until a maximum splitting crack width of 0.2 mm at the end of the test was reached. A splitting crack

was formed at the load level of 125 kN at the mid-span of the beam and propagated downward until a maximum value of 2.7 mm was reached, as shown in Figure 4-48. As the load increased, a pair of circular cracks was formed around the DHS head at both sides of the specimens.

Unlike the Ω S-U-70-16-2 specimens (UHPFRC with $V_f = 2\%$) with a deep breakout crack, a shallow triangle breakout crack pattern was observed in the Ω S-F-70-10-1 specimens (FRC with $V_f = 1\%$) constructed with the FRC material. This is mainly because a fracture localization induced by the stress concentration near the head of DHS was observed in the connection system constructed with that FRC material. This phenomenon significantly limits the load carrying capacity of the connection system subjected to pull-out loading. In contrast, a more enhanced pull-out load-slip and ductility was observed for the connection system constructed with UHPFRC material, as this material features a significant pseudo-strain hardening response under the tension and shear.

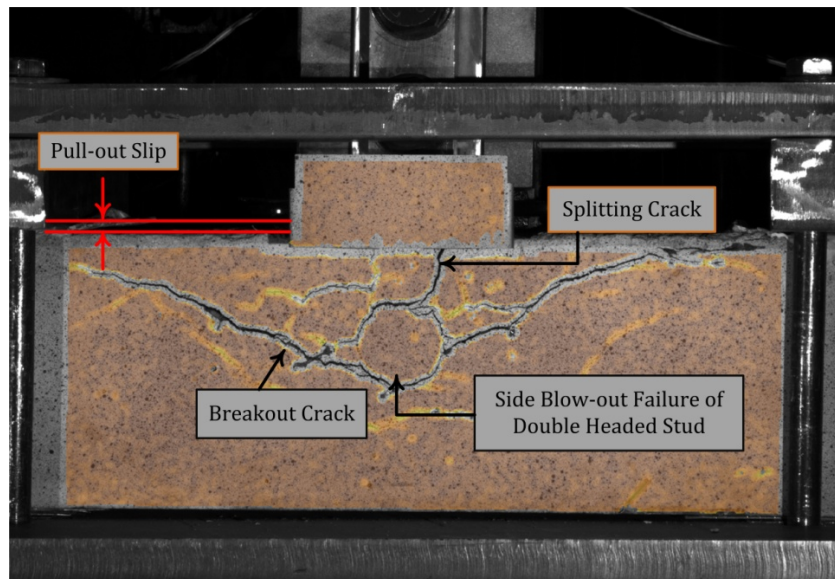


Figure 6-46: Overall failure of Ω S-F-70-16-1 specimen (Ω -shaped tension key, $h_h = 70$ mm, FRC with $V_f = 1\%$, $t_{pl} = 16$ mm).

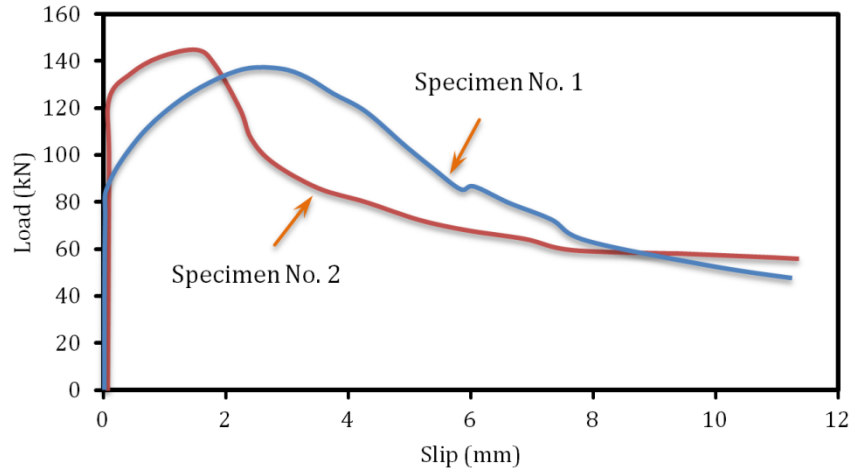


Figure 6-47: Load-slip response of Ω S-F-70-16-1 specimens.

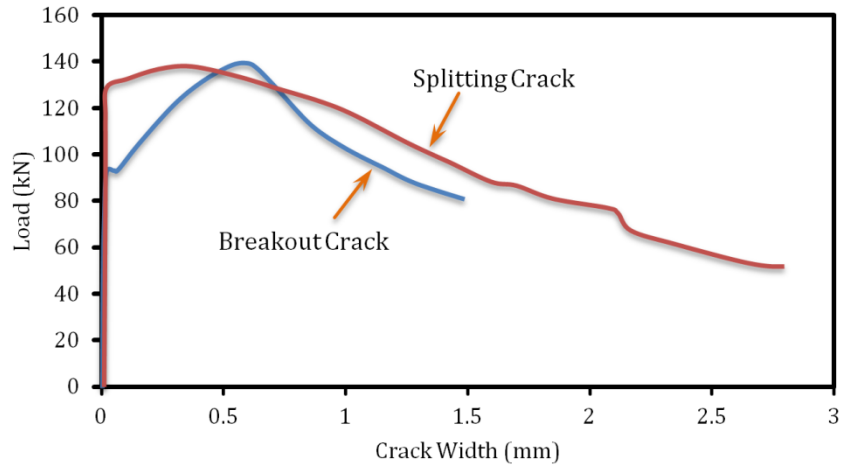


Figure 6-48: Failure cracks growth throughout testing of Ω S-F-70-16-1 specimen (first specimen).

6.4.5.3 Summary of Influences of Concrete Generation

The influences of two different concrete generations, i.e. FRC and UHPFRC material on the load carrying capacity of the composite connections with an Ω -Shaped tension key are summarized in Figure 6-49. The tests results indicate that compared to composite connection system with FRC material, the use of UHPFRC significantly increased the maximum peak pull-out load of the connection system by 114% and 54% for 10 mm and 16 mm embedded steel plate. This significant improvement is attributed to the pseudo-strain hardening response of the UHPFRC material in tension and shear which leads to a high mechanical properties.

The use of UHPFRC material was found to significantly improve the ductility of the connection systems with an Ω -shaped tension key. Compared to connection system with FRC material, 341% and 122% improvements in the connection ductility was found for those constructed with UHPFRC material incorporating 2% volume-fraction of randomly distributed short steel fibers.

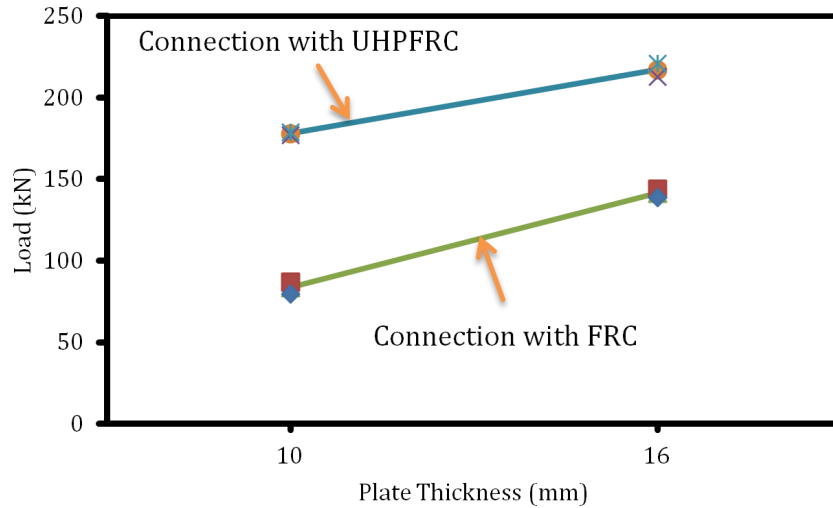


Figure 6-49: Influence of concrete generation on load bearing capacity of composite connection with Ω -Shaped tension key.

6.5 Pullout Response of Connection with Puzzle-Strip Tension key

In this section the influences of the embedded plate thickness and concrete generations on the pull-out response of the puzzle-strip tension key were studied. The results of the DIC technique are used to highlight the slip, crack width, and crack growth pattern during the pullout loading. The lists of all the composite connections with the puzzle-strip tension key are reported in Table 6-2, along with the peak pull-out load-slip response. The complete detail of the companion specimens with compressive strength, peak equivalent tensile strength (PETS), and crack mouth opening displacement (CMOD) at PETS for each individual mix design are provided in Tables 5-6 to 5-7.

6.5.1 Influences of plate thickness

6.5.1.1 Specimen PS-U-70-10-2

Figure 6-50 provides an overall view of the failure crack on the front faces of two repetitive specimens. Two different failure modes were observed in each specimen: 1) A breakout failure in the first specimen and 2) a concrete side failure (CSF) in the second specimen.

The pullout load-slip curves for both specimens are given in Figure 6-51. A linear load-slip response up to a load level of 96 kN was found for both specimens, which is followed by a non-linear stage for both specimens until an average PPL of 202 kN and 167 kN was reached.

First Specimen: Figures 6-50 (a) and 6-50 (b) respectively present an overall view of the failure cracks for the first specimen at the PPL and failure load level. The variation of the pull-out load against the splitting and breakout failure is plotted in the Figure 6-51. No crack was observed in the surface of the specimen up to a load level of 90 kN, where a longitudinal crack was initiated at the mid-span of the UHPFRC beam in the level of the bottom rebar. As the load increased, the longitudinal crack was diagonally propagated toward the top supports. A splitting crack was initiated at the mid-span and at the top side of the concrete beam at a load level of 134 kN. After the peak load was reached, a series of new horizontal crack were formed in the mid-span and at the level of top rebar and rapidly joined the splitting crack. The plate began to slip through once a load level of 95 was reached. No further growth in splitting crack was observed once the PPL was reached. Instead the breakout crack width at the level of top rebar rapidly increased. As presented in this figure, a strong mechanical interlock between the concrete pin and embedded steel plate was observed until the failure load was reached.

Second Specimen: The second specimen characterized by a CSF, which features a lower stiffness at the post-cracking stage. This lower stiffness is mainly attributed to the premature failure, where a concrete side failure occurred and prevented further increase in the pull-out load. This failure mode occurred as a result of the misalignment of the embedded steel plate, which leads to a 17% decrease in the PPL

of the connection system. A gradual decrease in the load-slip response of both specimens was observed during the softening stage. See Figure 6-51. The failure condition of second specimen is presented in Figure 6-50 (c). According to DIC test results, no crack was observed at the surfaces of the UHPFRC beam until a splitting crack was observed at a load level of 90 kN at the mid-span of the beam. This crack was propagated downward until the splitting crack reached the level of top rebar and slightly tilted toward the support. After the peak load was reached, a significant slip between embedded plate and UHPFRC beam was observed. The lateral deflection of the concrete beam at the back side of specimen was measured through four horizontal LVDTs and an average value of 8 mm was recorded. This value is significantly larger than an average value of 0.9 mm recorded for first specimen.

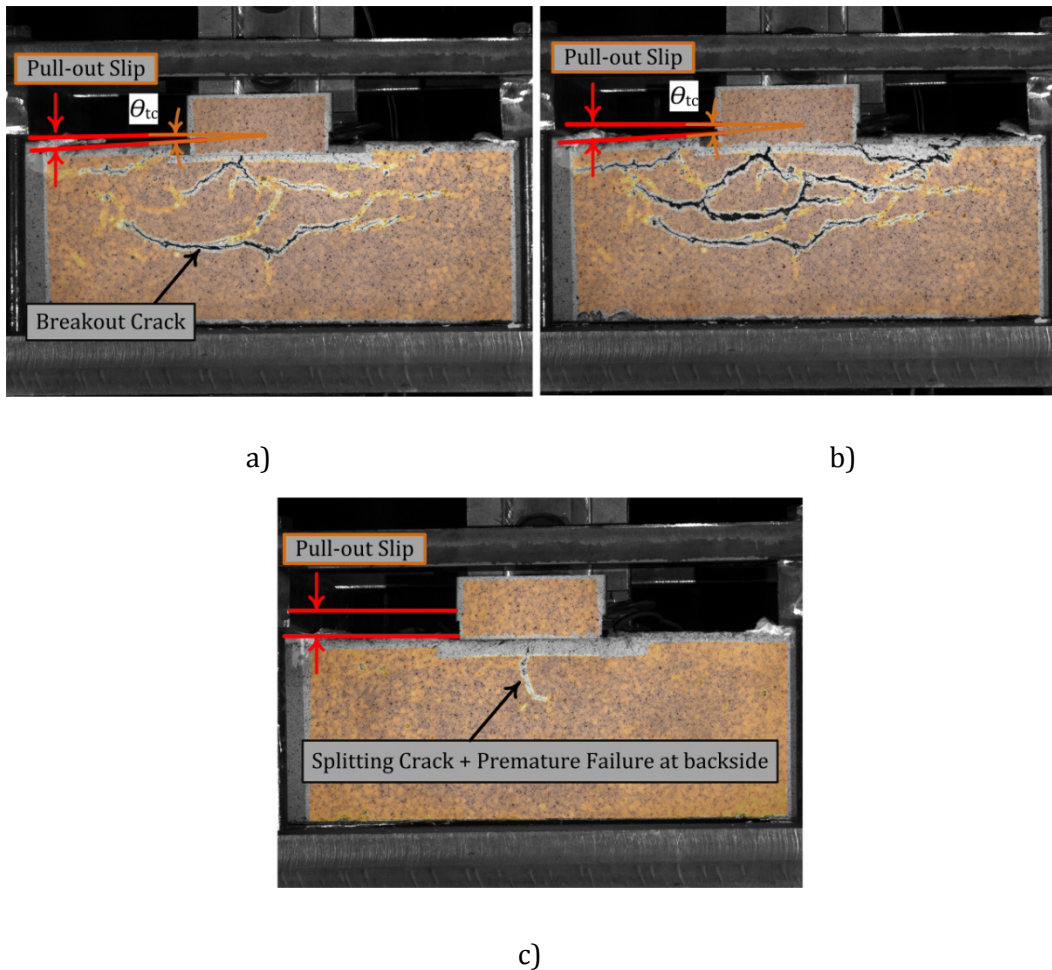


Figure 6-50: Overall failure of PS-U-70-10-2 specimen (Puzzle strip tension key, $h_h = 70$ mm, UHPFRC with $V_f = 2\%$, $t_{pl} = 10$ mm), a) First specimen at the PPL level, b) First specimen at the end of test, c) Second Specimen.

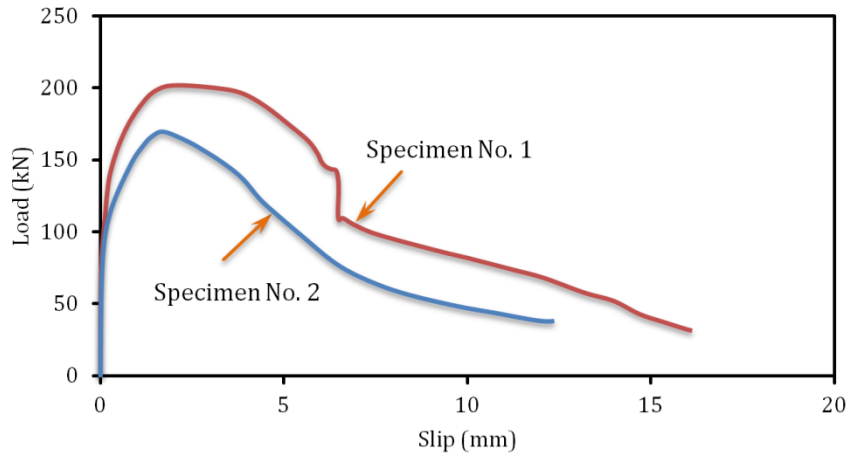


Figure 6-51: Load-slip response of PS-U-70-10-2 specimens.

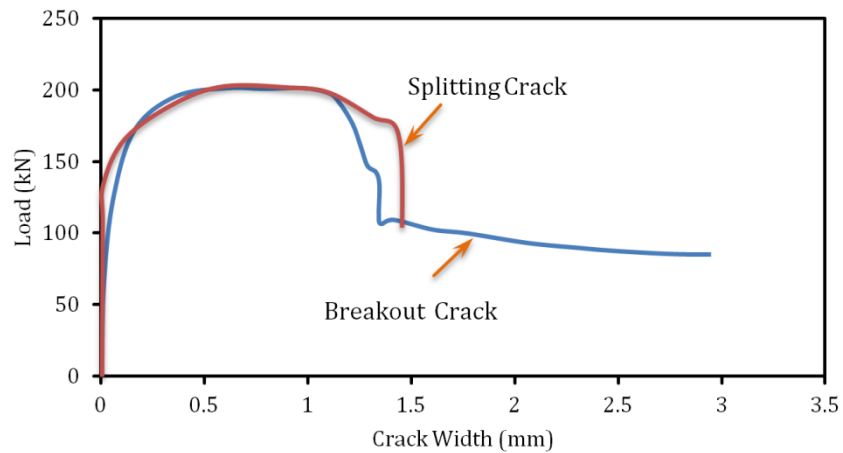


Figure 6-52: Failure cracks growth throughout testing of PS-U-70-10-2 specimen (first specimen).

6.5.1.2 Specimen PS-U-70-16-2

The overall view of the front face of PS-U-70-16-2 specimen is presented in Figure 6-53. A combination of breakout failure (BF) and pull-out failure (PF) was observed in both specimens.

The pull-out load-slip curve of the PS-U-70-16-2 specimen is given in Figure 6-54. An almost similar load-slip response was observed for both specimens until a load level of 120 kN was reached. After the cracking pull-out load, a gradual rate of slip between the steel plate and the concrete beam was observed. However this rate was significantly increased after the PPL was reached.

The variation of the cracks width against the pull-out strength is given in Figure 6-55. A series of multiple microcracks were observed at the mid-span and at the top side of the UHPFRC beam (where the tensile strength is max) at a load level of 130 kN. A single splitting crack was then formed at this location followed by the formation of a series of inclined microcracks along the both edges of embedded steel plate, as shown in Figure 6-53. These inclined cracks were then longitudinally directed toward the supports at higher level of load. No significant growth in the splitting crack width after the PPL was observed, as shown in Figure 6-55.

The results of the DIC analysis indicated that a longitudinal crack was formed at the level of the bottom rebar at a load level of 92% of the PPL and gradually propagated along the longitudinal rebar until the PPL was reached. A higher rate of crack growth was observed after the PPL until a crack width of 6.6 mm was reached at the end of the test.

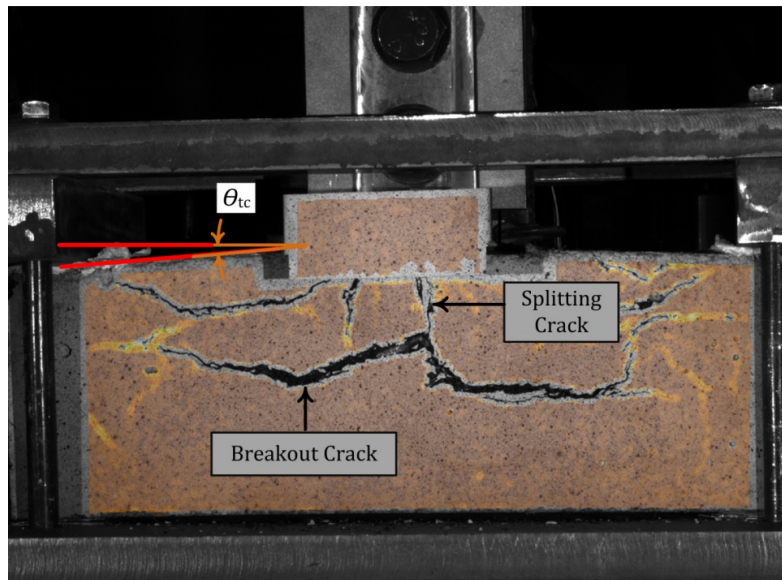


Figure 6-53: Overall failure of PS-U-70-16-2 specimen (Puzzle strip tension key, $h_h = 70$ mm, UHPFRC with $V_f = 2\%$, $t_{pl} = 16$ mm).

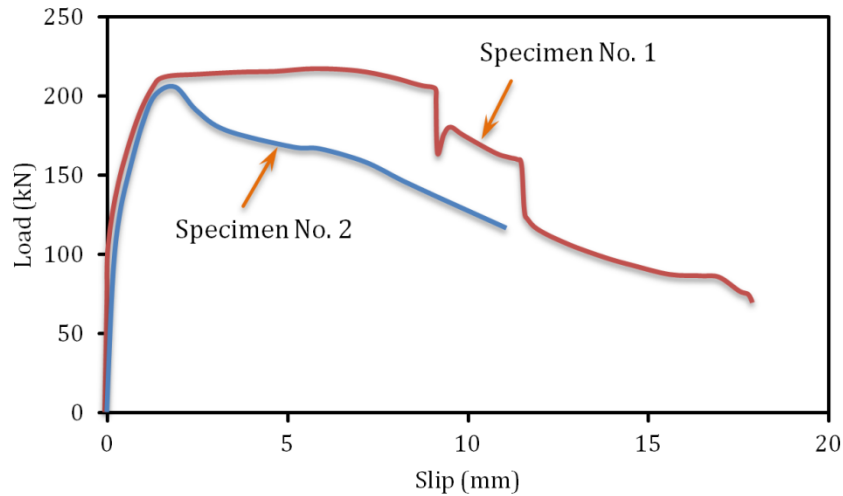


Figure 6-54: Load-slip response of PS-U-70-16-2 specimens.

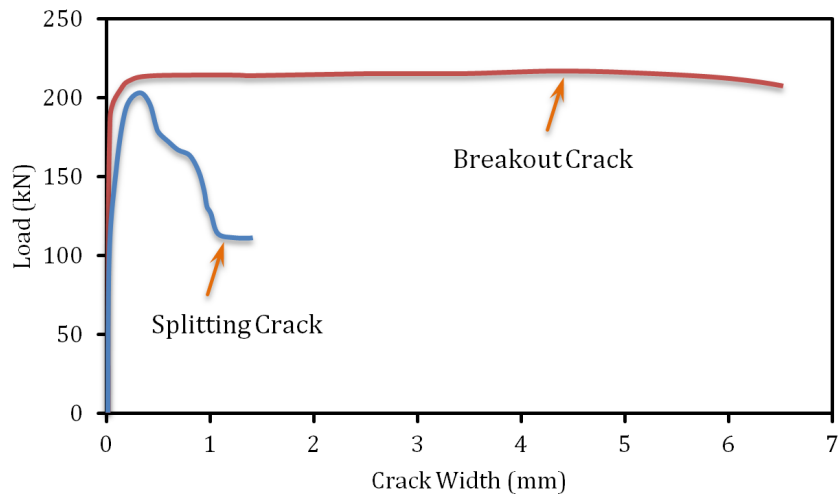


Figure 6-55: Failure cracks growth throughout testing of PS-U-70-16-2 specimen (first specimen).

6.5.1.3 Summary of influences of plate thickness

The influences of two different plate thicknesses, i.e. 10 and 16 mm, on the load carrying capacity of the composite connections constructed with the UHPFRC material with 70 mm puzzle-strip tension key are summarized in the Figure 6-56. The test results indicate that compared to composite connection with $t = 10$ mm, the use of $t = 16$ mm steel plate results in 14% increase in the maximum load bearing capacity of connection. According to test results, no improvement in the connection ductility was observed, as the plate thickens was increased from 10 to 16 mm.

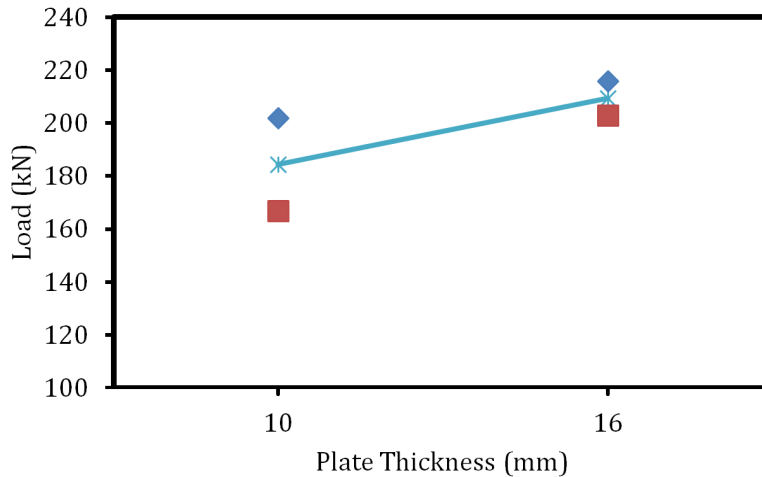


Figure 6-56: Influence of plate thickness on load bearing capacity of composite connection with puzzle-strip tension key.

6.5.2 Influence of concrete generation

In order to study the influence of two different generations of concrete on the behaviour of the composite connections constructed with the puzzle-strip tension key, a series of connection specimens was cast with the UHPFRC material incorporating 2% volume-fraction of randomly distributed short steel fibers and the FRC material containing 1% of double hooked steel. The results are discussed in this section.

6.5.2.1 Specimen PS-F-70-10-1

The failure condition of the PS-F-70-10-1 specimen constructed with FRC material with 1% of double-hooked fibers after the failure is given in Figure 6-57. A pull-out failure (PF) was observed for both specimens.

Figure 6-58 shows the pullout load-slip curves for both PS-F-70-10-1 connection specimens. A linear load-slip response up to a load level of 70 kN was noted for both specimens, which is followed by a non-linear post-cracking stage until the PPLs of 81 kN and 88kN were respectively reached for the first and second specimens. According to DIC test results, the slope of the post-cracking curve for the PS-F-70-10-1 specimen (FRC material incorporating 1% fibers) was significantly lower than that for the PS-U-70-10-2 specimen (UHPFRC material incorporating 2% fibers).

This is mainly due to the lower mechanical properties of the FRC material in the shear and tension.

The variation of the pull-out load against the crack width is given in Figure 6-59. A similar crack pattern during the test was observed for both specimens. Unlike the PS-F-70-10-1 specimen, an early slip between the embedded steel plate and concrete beam was started at an average load level of 70 kN, which is significantly lower than the similar values in the connection system constructed with the UHPFRC material. This is most probably because the bearing and shear capacity of the FRC material is significantly lower than that of the UHPFRC material.

According to DIC test results, a horizontal crack was initiated at the level of the bottom rebar at a load level of 70 kN and gradually increased until the PPL was reached. The second horizontal crack was formed at the level of top rebar and propagated toward the top reactions, as shown in Figure 6-57. As presented in the Figure 6-59, the first inclined crack was formed at an average load level 72 kN at the mid-span of the beam. Unlike the similar connection system constructed with the UHPFRC material, which features a gradual increase in the splitting crack width, a rapid crack growth was observed in the connection system with the FRC material.

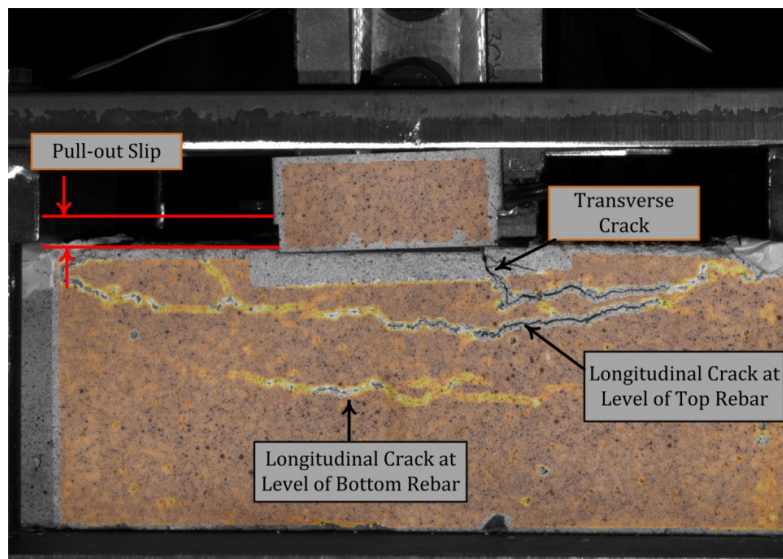


Figure 6-57: Overall failure of PS-F-70-10-1 specimen (Puzzle strip tension key, $h_h = 70$ mm, FRC with $V_f = 1\%$, $t_{pl} = 10$ mm).

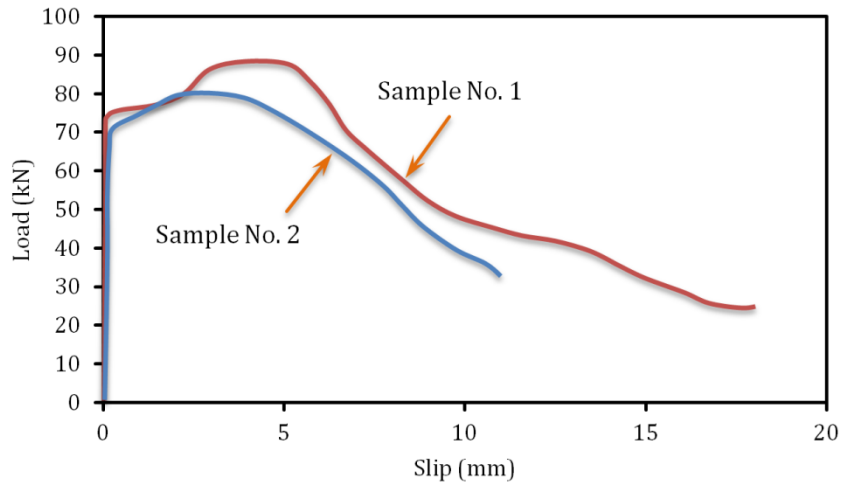


Figure 6-58: Load-slip response of PS-F-70-10-1 specimens.

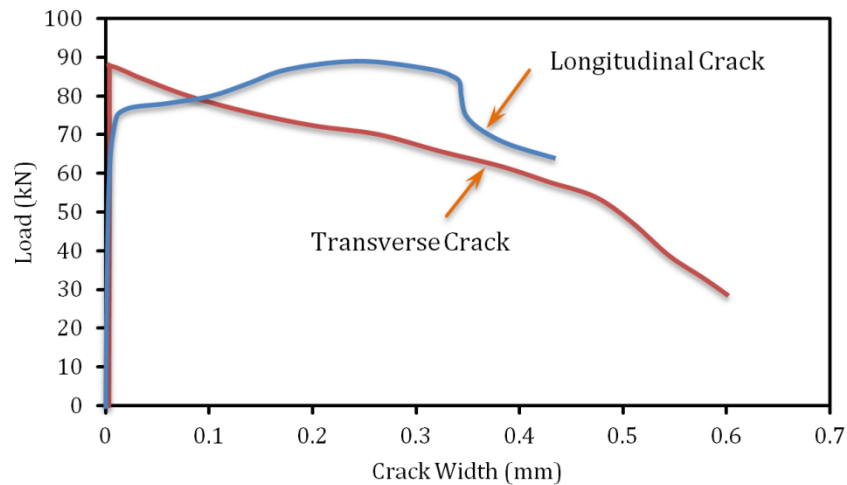


Figure 6-59: Failure cracks growth throughout testing of PS-F-70-10-1 specimen (first specimen).

6.5.2.2 Summary of Influence of Concrete Generation

A comparison between the pull-out load carrying capacity of the composite connections constructed with the FRC and UHPFRC material with similar puzzle-strip tension key is presented in Figure 6-60. An examination of this figure indicates that the use of UHPFRC material in the composite connections leads to 120% improvement in the maximum load carrying capacity of the connection system. According to tests results, the use of UHPFRC material in the connection system resulted in 56% improvement in the connection system ductility. This is mainly due

to the high mechanical properties of the UHPFRC material in tension and shears which can significantly improve the mechanical interlock between the concrete pin and the embedded steel plate.

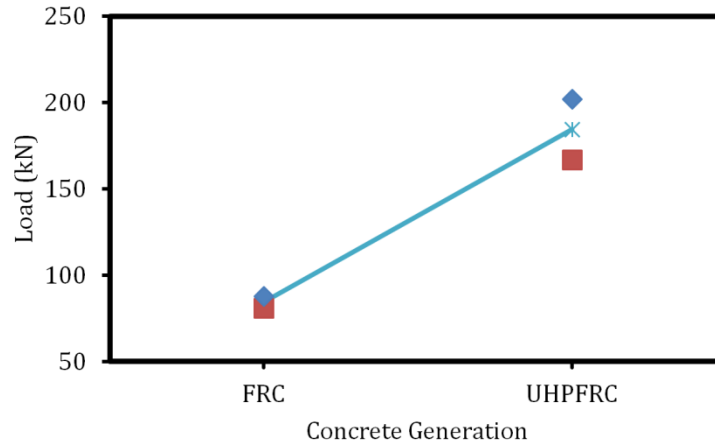


Figure 6-60: Influence of concrete generation on load bearing capacity of composite connection with $V_f = 2\%$ and puzzle-strip tension key.

6.6 Circular-Shaped Tension Key

In this section, the influences of tension key size, embedded plate thickness, double headed stud, and concrete generations (FRC and UHPFRC) on the behaviour of the composite connections constructed with the circular-shaped tension key are studied. The detail of all the specimens is listed in the Tables 6-3.

6.6.1 Influence of Tension Key Size

The test results of 4 specimens are used to evaluate the influence of circular hole size, i.e. 50 mm and 70 mm, on the pull-out load-slip response of the composite connections constructed with the UHPFRC material.

6.6.1.1 OS-U-50-10-2

The overall crack pattern after the failure of OS-U-50-10-2 specimen is shown in Figure 6-61. A breakout failure mode was observed for both OS-U-50-10-2 specimens, which was completely different than that observed for Ω S-U-50-10-2 specimen (with Ω -shaped tension key), where a pull-out failure was observed.

The pull-out load-slip curves for both OS-U-50-10-2 specimens are presented in the Figure 6-61. A linear-elastic load-slip response up to a load level of 100 kN was observed for both specimens, followed by a post-cracking stage. The peak pull-out load of 194 kN and 195 kN were observed for both specimens. An average 32% improvement in the PPL of the OS-U-50-10-2 specimens with the O-shaped tension key was found over the Ω S-U-50-10-2 specimens with the Ω -shaped tension key. This is most probably because the circular-shape configuration led to a lower bearing stress, which eventually prevents the pull-out failure in the connection system. Instead compared to the Ω S-U-50-10-2 specimens, a breakout failure was observed for the OS-U-50-10-2 specimens, which resulted in a higher PPL.

The variation of the splitting crack against the pullout load for the first specimen is depicted in Figure 6-62. No visible crack was observed up to a load level of 120 kN, where the first microcracks were observed at the mid-span and at the top of the UHPFRC beam. The formation of multiple microcracks is repeated in the maximum tensile region for several times until they join each other to form a dominant macrocrack near the PPL. As the load increased, the splitting crack was bent toward the top rebar. A maximum crack width of 1.8 mm was observed at the end of the test. A series of horizontal microcracks was initiated at the level of bottom rebar at a load level of 150 kN and gradually propagated toward the top reactions until the PPL was reached. A higher rate of break-out crack growth was observed after the PPL, as shown in Figure 6-63.

An outstanding bond between the tension key and the concrete pin was observed even after the breakout crack was formed. This is mainly due to a good mechanical interaction between the concrete pin, the circular shape hole, the double headed stud, which prevents a local failure between them.

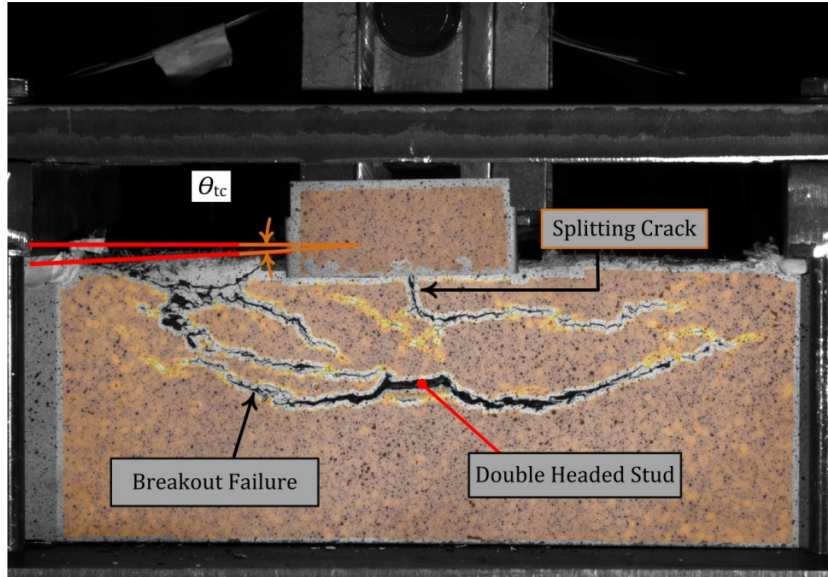


Figure 6-61: Overall failure of OS-U-50-10-2 specimen (O-shaped tension key, $h_h = 50$ mm, UHPFRC with $V_f = 2\%$, $t_{pl} = 10$ mm).

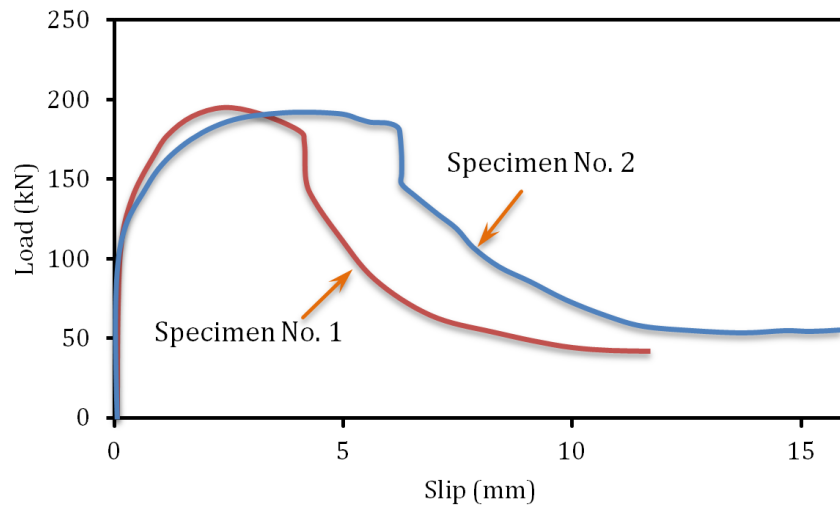


Figure 6-62: Load-slip response of OS-U-50-10-2 specimen.

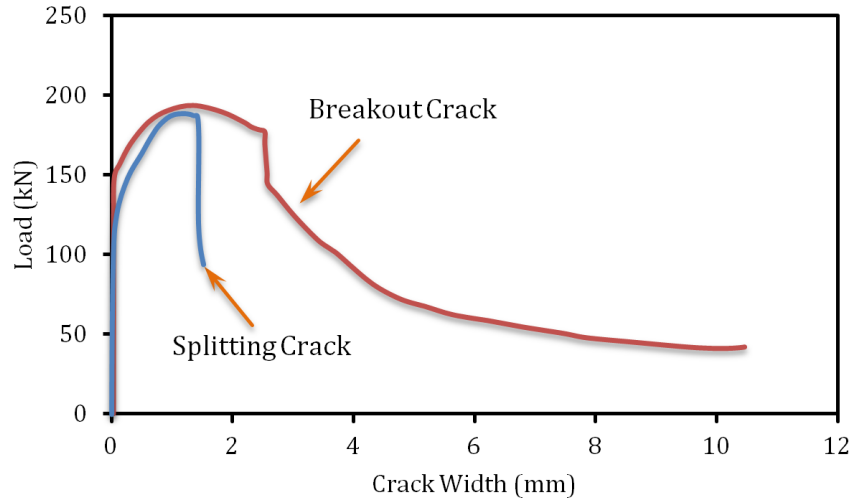


Figure 6-63: Failure cracks growth throughout testing of OS-U-50-10-2 specimen (first specimen).

6.6.1.2 OS-U-70-10-2

Figure 6-64 shows the condition of the failure in the OS-U-70-10-2 specimens at the end of the failure. Both specimens were characterized as a breakout failure with multiple cracks on the front and back side of the specimen.

Linear elastic load-slip behaviour was observed for both specimens up to an average load level of 130 kN, which is followed by a non-linear post-cracking stage until the PPL, as shown in Figure 6-65. Maximum peak pull-out load was occurred at an average slip of 2 mm for both specimens. After this stage a plateau was observed for the first specimen. However a softening behaviour with a lower rate of slip between the embedded steel plate and concrete beam was observed for the second specimen.

Figure 6-66 shows the variation of the pullout load against the transverse and breakout crack. No significant cracks were observed up to a load level of 130 kN, where a breakout crack was initiated at the mid-span and at the middle of the concrete beam. The breakout crack was gradually propagated until the PPL was reached. However the rate of crack growth was significantly increased after the PPL load.

A series of vertical microcracks were initiated at a load level of 152 kN at the mid-span and at the top of the beam, where the concrete beam experience the maximum

tensile stress. At the PPL, a single inclined macro-crack was formed at the mid-span. A maximum transverse crack width of 40 mm was observed at the end of the test.

Compared to other tension key configurations, i.e. Ω -shaped and puzzle-strip configurations, a much stronger mechanical interlock between the concrete pin and the embedded steel plate was observed. This is most probably caused by a larger bond area between the bottom part of the circular tension key and the concrete pin, which reduce the bearing stress.

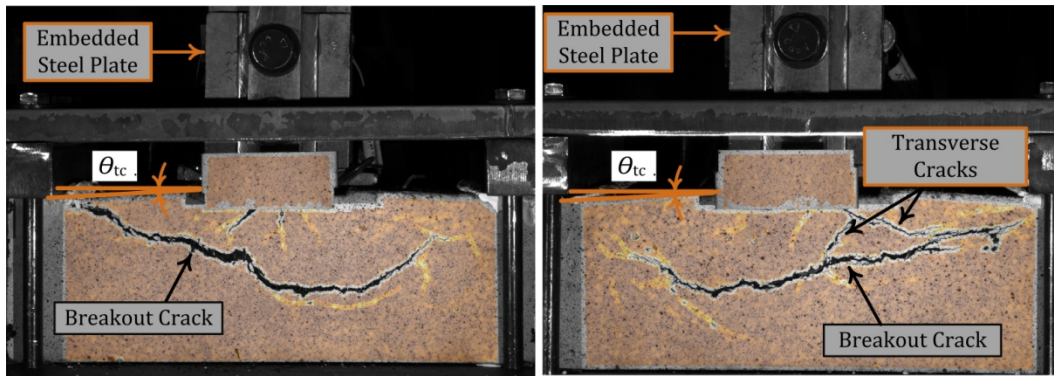


Figure 6-64: Overall failure of OS-U-70-10-2 specimen (Circular tension key, $h_h = 70$ mm, UHPFRC with $V_f = 2\%$, $t_{pl} = 10$ mm), a) First specimen, b) Second specimen.

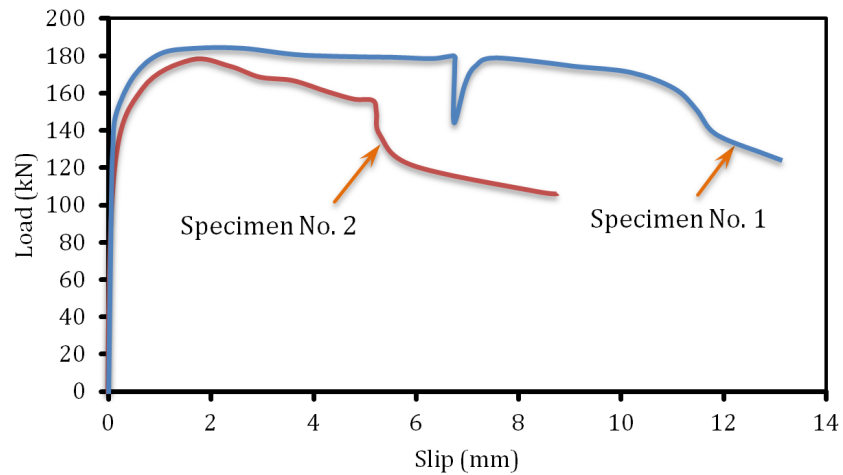


Figure 6-65: Load-slip response of OS-U-70-10-2 specimens.

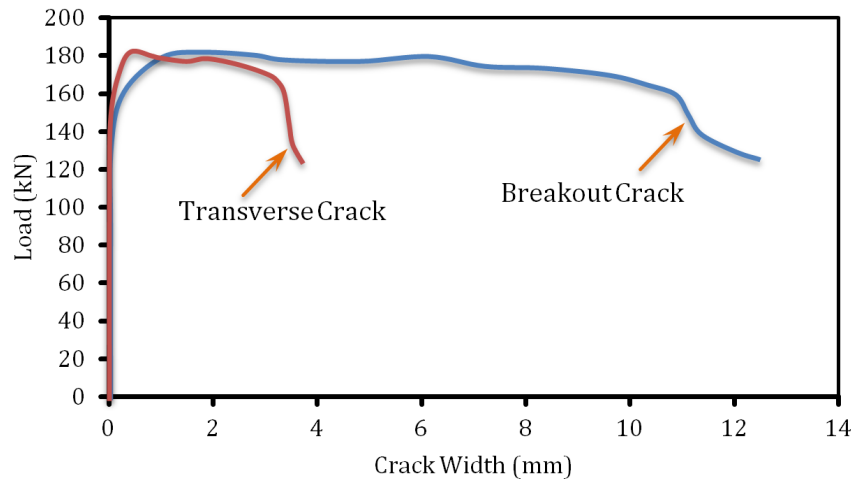


Figure 6-66: Failure cracks growth throughout testing of OS-U-70-10-2 specimen (first specimen).

6.6.1.3 Summary of Influence of Tension Key Size

A comparison between the load carrying capacity of the OS-U-70-10-2 composite connections constructed with the UHPFRC material with two different tension key diameters, i.e. 50 and 70 mm, are presented in the Figure 6-67. No improvement in the PPL of the connection was observed, as the tension key size was increase from 50 to 70 mm. However, a more stable load carrying capacity after the PPL point was reached for the connection system with larger hole size. The results of analysis indicated that the increase in hole diameter from 50 mm to 70 mm was resulted in 295% improvement in the connection ductility, which is mainly attributed to the less degradation rate in the load-slip response in the connection system. This improvement in the ductility would help to significantly enhance the energy absorption capability of the connection system and is appropriate in applications where the connection experience a huge cyclic load.

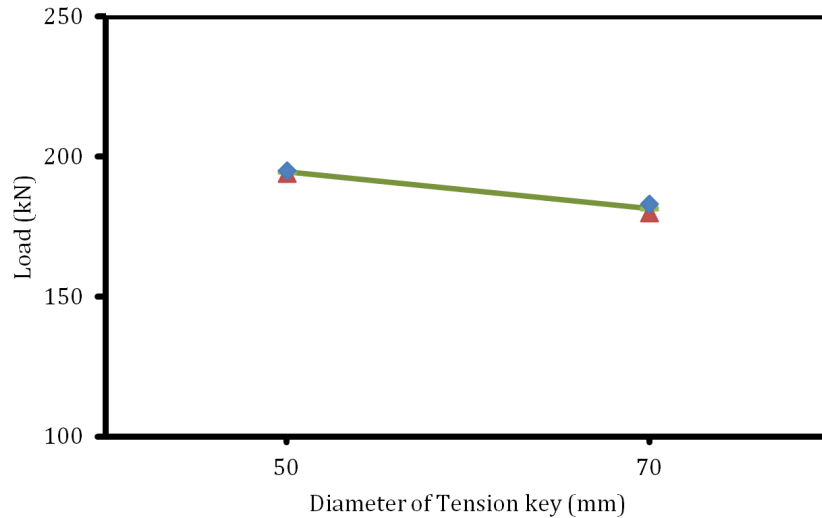


Figure 6-67: Influence of tension key size on load bearing capacity of composite connection with $V_f = 2\%$ and circular tension key.

6.6.2 Influence of Double-Headed Stud (DHS)

In order to study the influence of DHS on the pull-out load-slip response and ductility of the composite connection systems, two pairs of specimens with and without DHS were cast and tested. The responses of the connection specimens with double headed stud (DHS) are discussed in the section 6.6.1.2. The behaviour of the specimen without DHS is explained below.

6.6.2.1 OS-U-70-10-2 Specimen without Double Headed Stud

Figure 6-68 shows the crack pattern after the failure for the OS-U-70-10-2 specimen without double headed stud. A combination of breakout failure and the pull-out failure was observed for both specimens.

The pull-out load-slip curves for both OS-U-70-10-2 specimens are given in the Figure 6-69. A liner-elastic load deflection up to a load level of 117 kN was observed for both specimens, which is around 12% lower than the CPL for the OS-U-70-10-2 specimen with DHS. A post-cracking stage was observed for the first specimen, which is followed by a sudden drop in the pull-out loading. However the second specimen presented a larger post-cracking stage with a slightly higher peak load of 170 kN. Compared with OS-U-70-10-2 specimens with DHS, lower post-cracking stiffness was found for the OS-U-70-10-2 specimens without DHS. This is most

probably attributed to the lack of lateral confinement provided by the DHS to the concrete pin, which allows the concrete on both sides of embedded steel plate to deflect outward. A significant fluctuation in the load-slip response was observed in the second specimens without DHS, as shown in Figure 6-69, which significantly decrease the connection ductility and should be prevented.

The variation of the crack width against the pull-out load is given in Figure 6-70. No breakout crack was observed in the UHPFRC beam until an inclined crack was initiated at the mid-span of the beam at a load level of 128 kN. This crack was further propagated, with a high rate, along the top rebar until the PPL was reached. A maximum breakout crack width of 3.5 mm was observed at the end of the test.

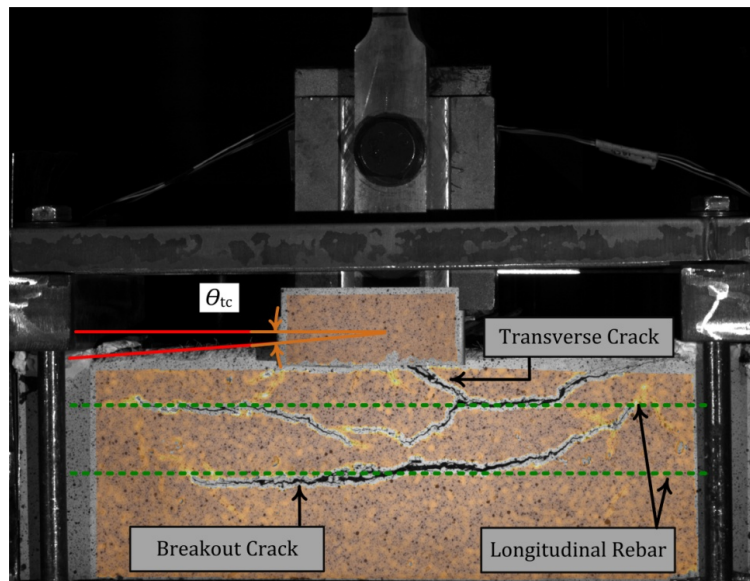


Figure 6-68: Overall failure of OS-U-70-10-2 specimen (Circular tension key, $h_h = 70$ mm, UHPFRC with $V_f = 2\%$, $t_{pl} = 10$ mm, No Double Headed Stud).

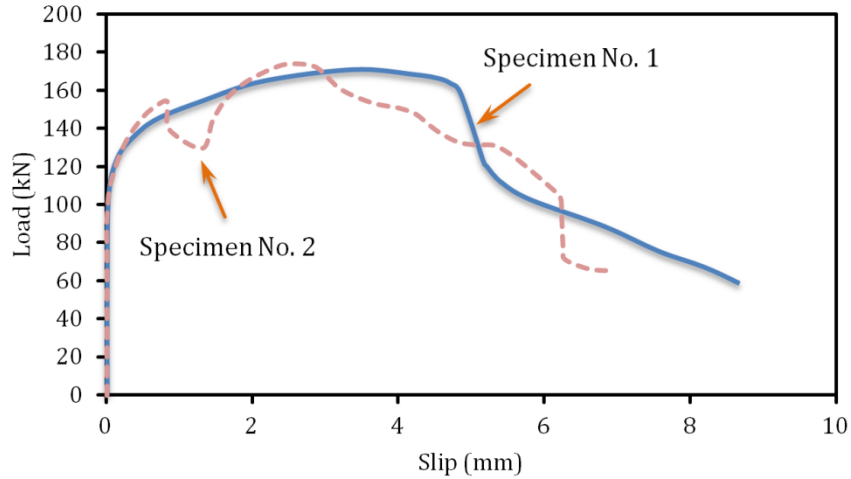


Figure 6-69: Load-slip response of OS-U-70-10-2 Specimen with no double headed stud (DHS).

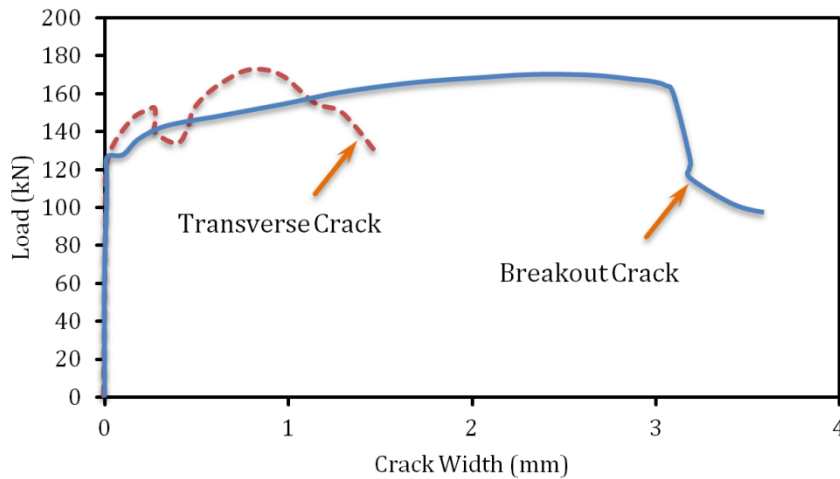


Figure 6-70: Failure cracks growth throughout testing of OS-U-70-10-2 specimen (first specimen).

6.6.2.2 Summary of Influence of Double-Headed Stud

The influence of the double headed stud (DHS) on the PPL of the OS-U-70-10-2 connection system is shown in the Figure 6-71. Compared to connection specimen without double headed stud, a 12% improvement in the PPL of specimens with double headed stud was found. In addition, the use of the DHS significantly improved the pre-peak and post peak response of the composite connection, which leads to a significant improvement in the ductility factor. According to test results, the use of DHS was resulted in 137% improvement in the connection system

ductility. This is because the DHS significantly enhances the lateral confinement to the concrete pin and prevents any sudden crack growth around the concrete pin. Compared with the composite connections without DHS, a lower scatter in the results was found for the specimens with DHS. See Figure 6-71.

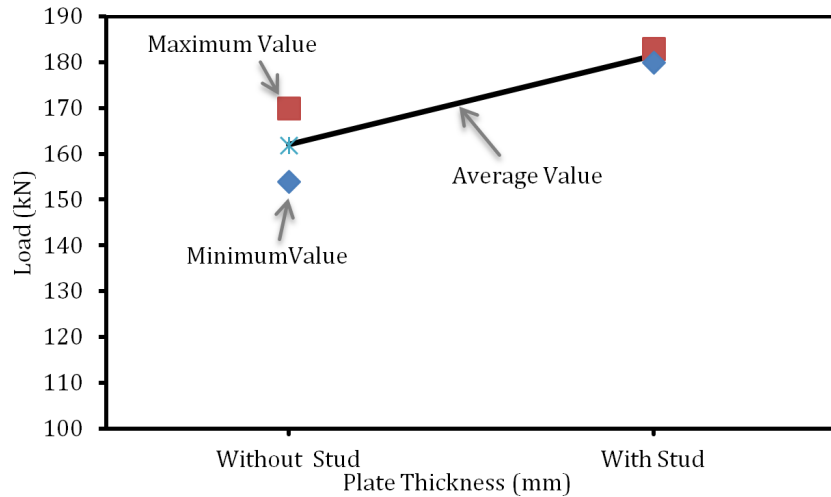


Figure 6-71: Influence of concrete generation on load bearing capacity of composite connection with $V_f=2\%$ and circular tension key.

6.6.3 Influence of Plate Thickness

6.6.3.1 OS-U-70-16-2

The crack pattern after the failure of the OS-U-70-16-2 specimen is presented in the Figure 6-72. Both specimens were characterized as a breakout failure.

The pullout load-slip behaviour of OS-U-70-16-2 composite connection is presented in Figure 6-73. According to DIC test results, no significant slip between the embedded steel plate and the concrete beam was observed until an average load level of 120 kN was reached. After this stage, a gradual slip between the plate and concrete beam was observed during the softening stage, which is followed by a plateau after the PPL level. A very sudden failure in the load-slip response was observed at the end of the plateau in the absence of the vertical reinforcements to intercept the breakout crack. A higher rate of breakout crack growth was observed after this stage until the test was stopped.

According to DIC test results, a series of microcracks were initiated at a load level of 115 kN at the mid-span of the concrete beam, where the cracking equivalent tensile strength (CETS) of the UHPFRC material was exceeded. The formation of the multiple microcracks is repeated in this region for several times until they joined each other and formed a single splitting crack at the PPL. As illustrated in Figure 6-74, the splitting crack was stopped after the peak load was reached.

A breakout crack was started at a load level of 140 kN at the mid-span of the beam and continued to widen until the PPL. The rate of crack growth after the PPL was significantly increased, which was followed by a sudden drop in the load carrying capacity of the connection system.

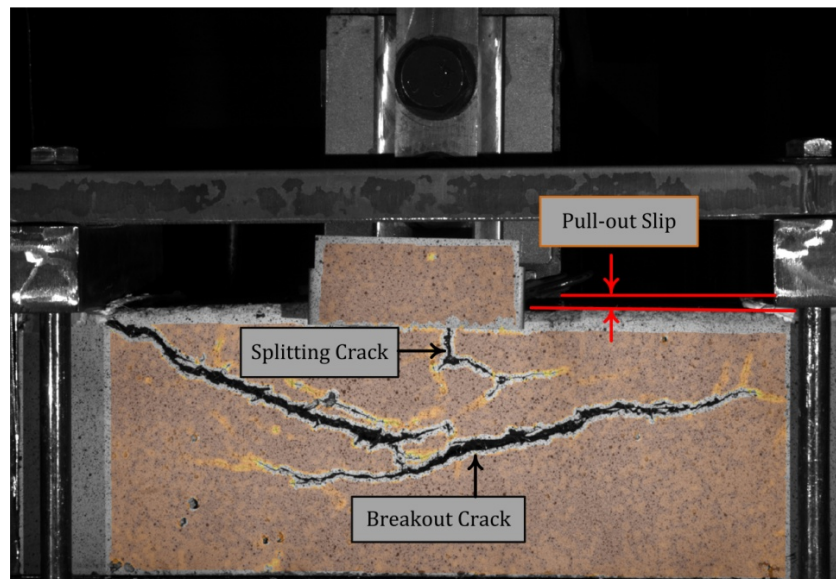


Figure 6-72: Overall failure of OS-U-70-16-2 specimen (Circular tension key, $h_h = 70$ mm, UHPFRC with $V_f = 2\%$, $t_{pl} = 16$ mm).

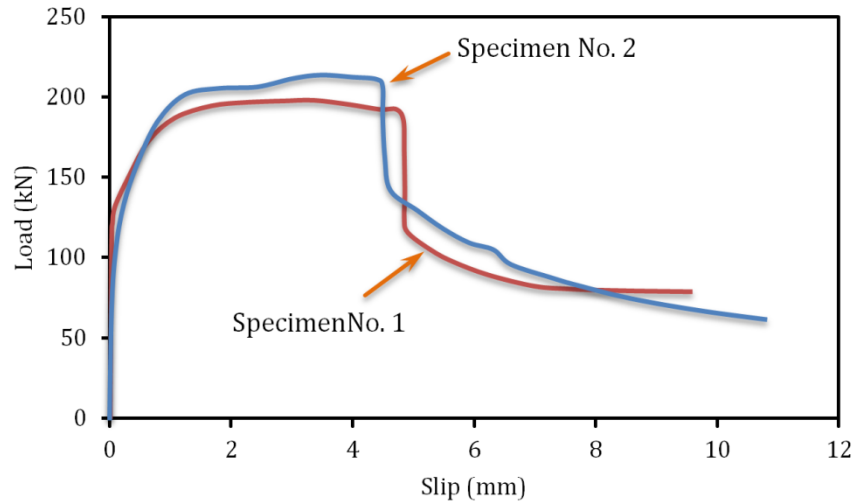


Figure 6-73: Load-slip response of OS-U-70-16-2 specimens.

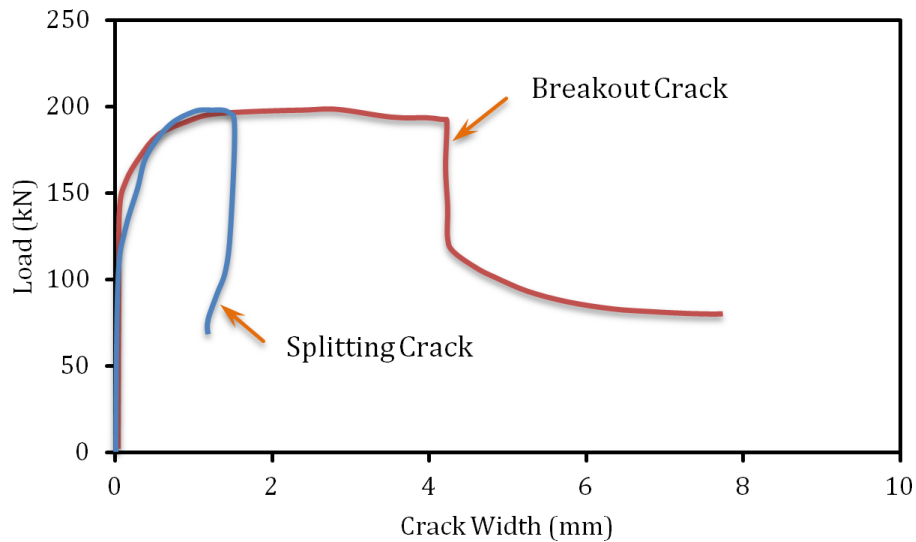


Figure 6-74: Failure cracks growth throughout testing of OS-U-70-16-2 specimen (first specimen).

6.6.3.2 Summary of Influence of Plate Thickness

The influence of two different embedded plate thickness, i.e. 10 mm and 16 mm, on the PPL of the composite connection constructed with the UHPFRC material are illustrated in Figure 6-75. An average 17% improvement in the peak pull-out load of the composite connections was observed as the plate thickness was increased from 10 mm to 16 mm. Instead a significant drop in the ductility factor was observed as the thickness increased. According to test results, the connection with thicker plate

tends to show an approximately 57% lower ductility over those with 10 mm plate, which is mainly attributed to sudden drop after the PPL was reached.

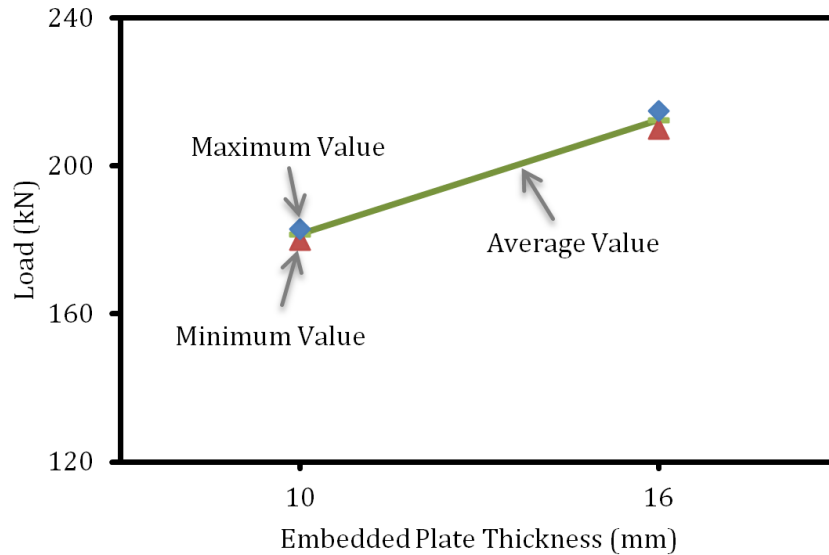


Figure 6-75: Influence of embedded plate thickness on load bearing capacity of composite connection with $V_f = 2\%$ and circular tension key.

6.6.4 Influence of Concrete Generation

In order to study the influence of concrete generations on the pull-out load carrying capacity of the composite connections constructed with circular tension key and two different thickness, i.e. 10 mm and 16 mm, a series of four specimens were cast and tested and the results are summarized in this section.

6.6.4.1 OS-F-70-10-1

The crack pattern after the failure of the OS-F-70-10-1 specimen is shown in the Figure 6-76. The break-out failure pattern was found to be different from the similar specimens constructed with the UHPFRC material. Figure 6-77 shows the relationship between the pullout load against the slip for the OS-F-70-10-1 specimens. A linear load-slip relationship was found for both specimens up to a load level of 90 kN, where a breakout crack was started from bottom side of the head of DHS. The crack was gradually propagated to both supports along with some parallel cracks.

After the CPL, two different load-slip responses were observed for this connection system. The first connection specimen featured a limited post-cracking response until the PPL of 100 kN, which was followed by a softening stage. The second specimen, on the other hand, presented a more enhanced post-cracking response up to a PPL of 117 kN, which was followed by a softening response.

Figure 6-78 illustrates the variation of the pull-out load against the break-out and splitting crack. While no significant splitting crack width (around 0.2 mm) was observed at the PPL, a 2.3 mm break-out crack was observed at the PPL.

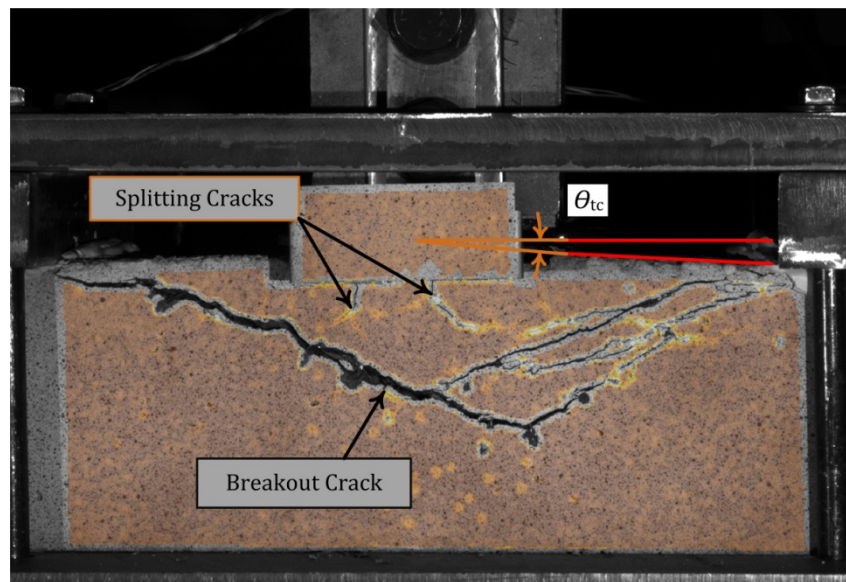


Figure 6-76: Overall failure of OS-F-70-10-1 specimen (circular tension key, $d_h = 70$ mm, FRC with $V_f = 1\%$, $t_{pl} = 10$ mm).

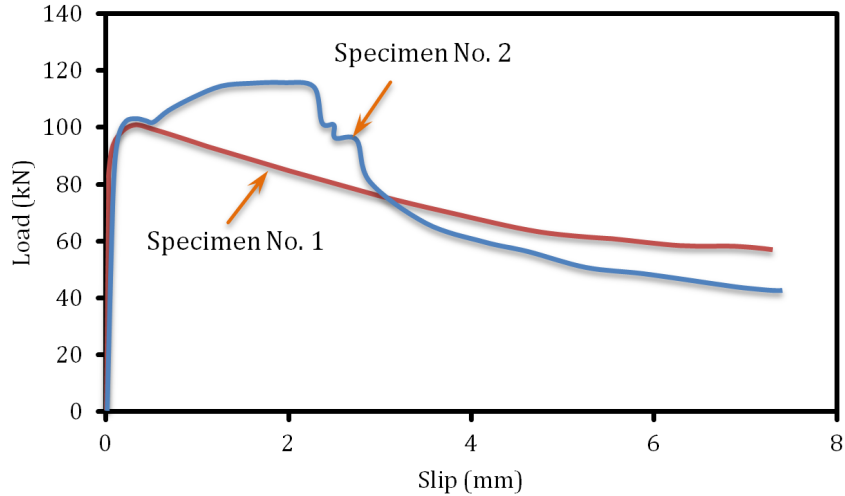


Figure 6-77: Load-slip response of OS-F-70-10-1 specimens.

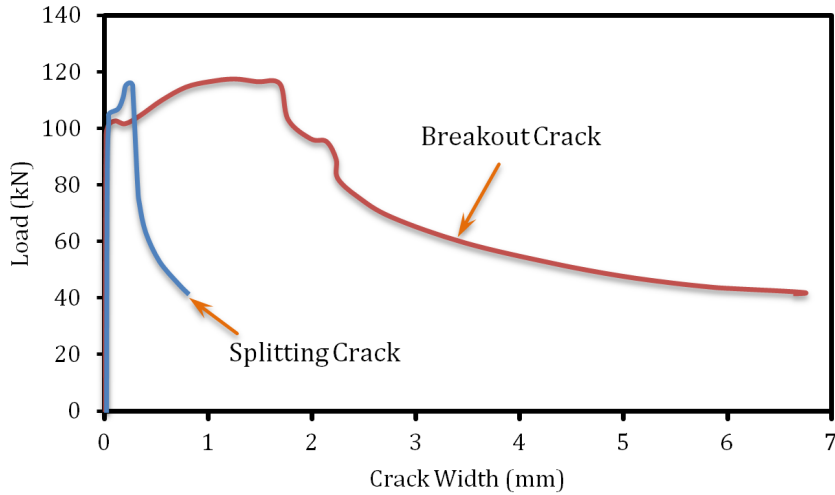


Figure 6-78: Failure cracks growth throughout testing of OS-F-70-10-1 specimen (first specimen).

6.6.4.2 OS-F-70-16-1

The pullout load-slip curve for OS-F-70-16-1 specimens are given in Figure 6-79. A linear behaviour up to a load level of 75 kN was observed for both specimens, which is 20% lower than the same value for the connection system with 10 mm plate. A pair of vertical crack was initiated at the mid-span and the top of the concrete beam at this load level (CPL). After the CPL, a post-cracking response was observed in both specimens, which was followed by a softening response until the failure.

The variation of the pullout loads against the splitting and break-out cracks for OS-F-70-16-1 specimens are given in Figure 6-81. A very small crack width of 0.35 mm at PPL was extracted from the DIC results for the vertical crack, which was stopped after the PPL was reached. However the break-out crack growth was found to be rapid until the failure load.

At a load level of 100 kN, the vertical crack at the mid-span of the beam propagated toward a horizontal crack at the level of the DHS and deviated toward the top reaction. A plateau in the load-breakout crack width was observed until the crack width around 3 mm reached, which was followed by the softening response, as shown in Figure 6-81.

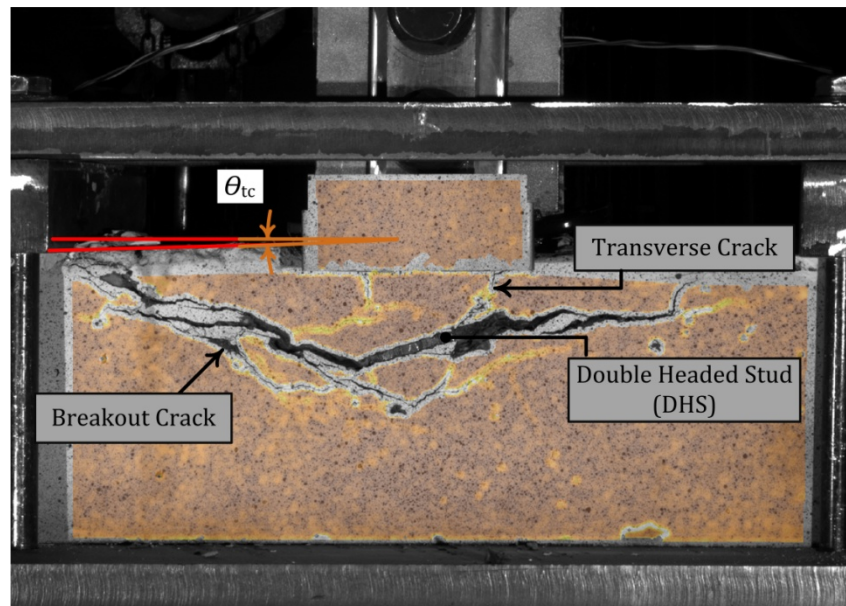


Figure 6-79: Overall failure of OS-F-70-16-1 specimen (Ω -shaped tension key, $d_h = 70$ mm, FRC, with $V_f = 1\%$, $t_{pl} = 16$ mm).

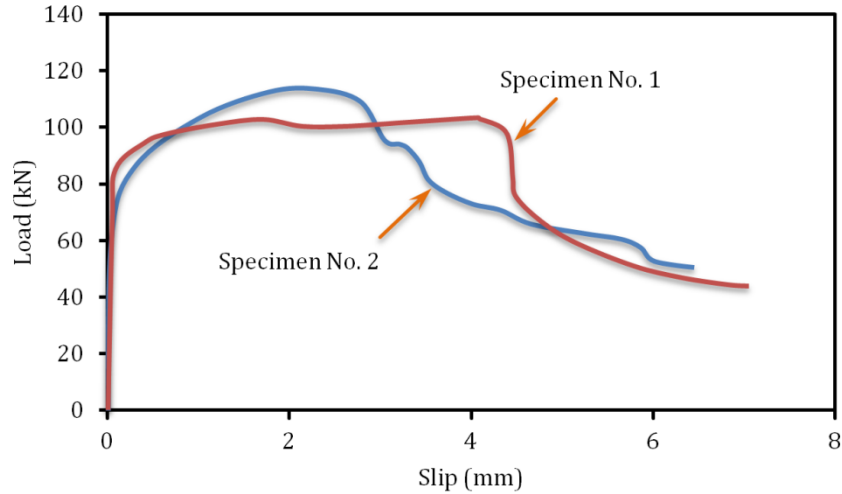


Figure 6-80: Load-slip response of OS-F-70-16-1 specimen.

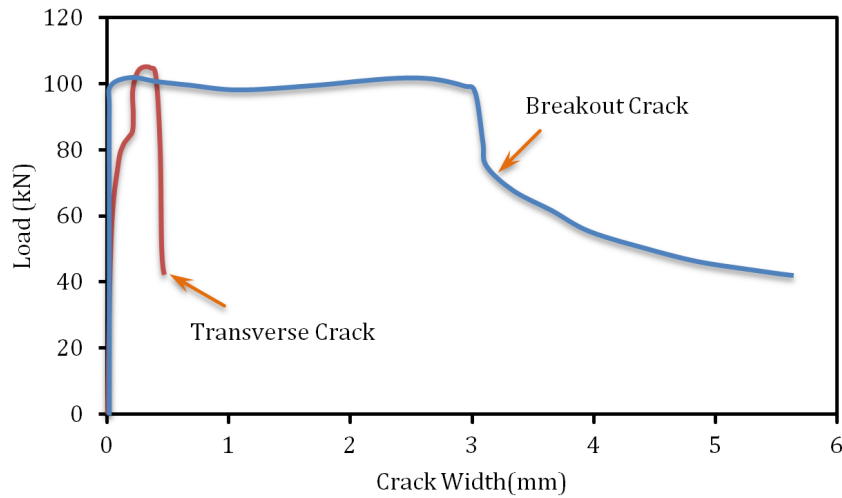


Figure 6-81: Failure cracks growth throughout testing of OS-F-70-16-1 specimen (first specimen).

6.6.4.3 Summary of Influence of concrete generation

In order to investigate the influence of embedded plate thickness on the PPL of the composite connections constructed with the FRC and UHPFRC material, the results of eight experimental tests are summarized in the Figure 6-82. According to this figure, the increase in the embedded plate thickness did not result in a higher PPL. In contrast, an average 17% improvement in the PPL of the connection systems constructed with UHPFRC material and 16 mm embedded steel plate was observed over those similar specimens with 10 mm plate. This is mainly associated to the

significant enhancement in the mechanical properties of the UHPFRC material in tension and shears which prevents the crack formation and propagation in the concrete beam.

According to test results, the use of the UHPFRC material in the composite connection systems with 10 and 16 mm plate was resulted in 62% and 123% improvements in the PPL of the connection system over the similar connections with FRC material. The test results show that compared to connection system constructed with FRC material, the use of UHPFRC material was resulted in 39% and 47% increase in the connection ductility for specimens with 10 mm and 16 mm embedded length. This significant enhancement in the ductility suggests that the use of UHPFRC material can be very effective in applications where a significant ductility is required.

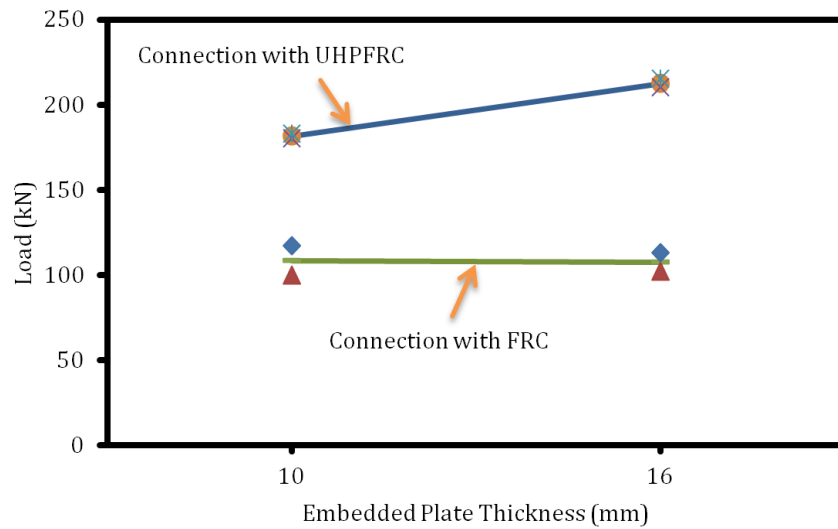


Figure 6-82: Influence of concrete generation on load bearing capacity of composite connection with $V_f = 2\%$ and circular tension key.

Chapter 7

7 Finite Element Analysis of Composite Connections

7.1 Introduction

In this chapter, the finite element method (FEM) is used to study the response of the composite connections subjected to pull-out and push-out loading. To this aim, a FEM model capable of matching the experimental load-slip response of the composite connection system subjected to pull-out load, which was reported in the chapter 6 was developed. The validated finite element model was then used to further study the influence of other parametric variations that influence the response of the proposed composite connection system subjected to pull-out and push-out loading.

7.2 Description of Model in ABAQUS

In order to model the behaviour of the proposed composite connections subjected to pull-out loading, a sophisticated FEM model is required to include: complete model configuration, detailed description of the mechanical properties of the materials in tension and compression, loading and boundary conditions, contact and friction model between surfaces, and analysis type. The FEM model of the composite connection system and its components in a 3-D view are given in Figure 7-1. The model consisted of embedded steel plate, concrete beam, double headed stud (DHS), and reinforcement cage that can simulate the whole composite connection.

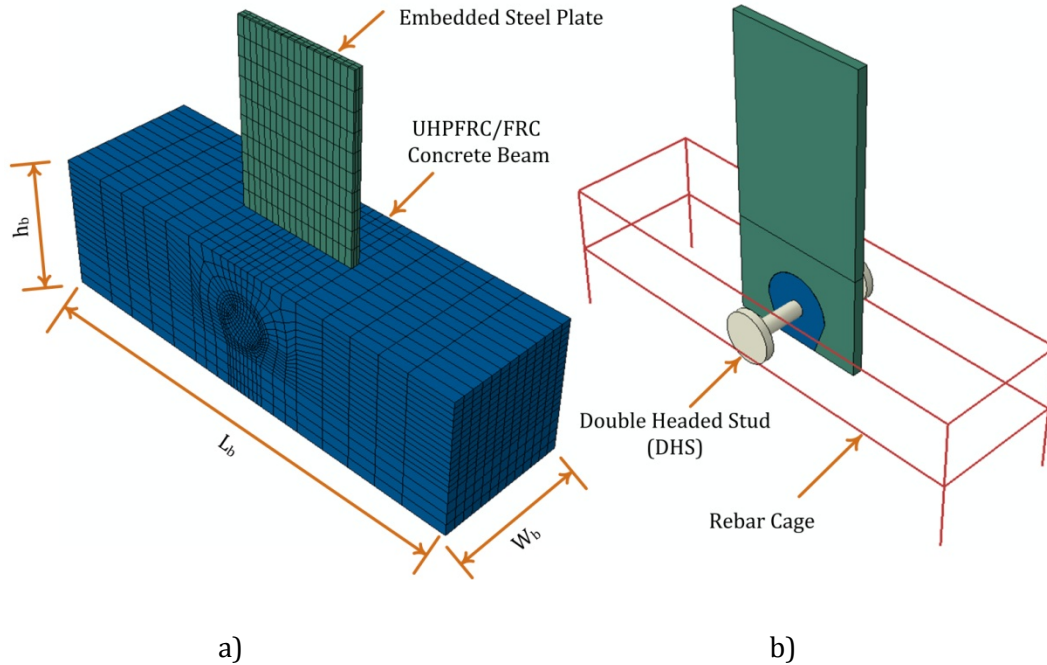


Figure 7-1: Geometry of the composite connection system, a) embedded steel plate in concrete beam, b) Components of connection.

7.2.1 Specimen Configuration

7.2.1.1 Composite Connection under Pull-out and Push-out Loading

Figure 7-2 shows the geometry of the FEM model of composite connection under pull-out and push-out loading. Only one quarter of the composite connection was modeled in ABAQUS/Explicit, as there are two planes of symmetry: one at the centre of the specimen in the longitudinal direction (xy -plane) and the other one in the transverse direction at mid-length (yz -plane), as shown in Figure 7-3. Concrete beam with length \times width of 500 \times 150 mm and two different heights, i.e. 150 and 200 mm were used for the connection subjected to pull-out loading. Similar concrete beam with length \times width of 500 \times 200 mm and different heights were used for the connection subjected to push-out loading. The width and lengths of the embedded steel plate were 140 \times 300 mm respectively for both pull-out and push-out models. Different plate thicknesses, i.e. 8, 10, 12, 16, 20 mm were used. The DHS shank and reinforcement diameter were 15.9 and 10 mm, respectively.

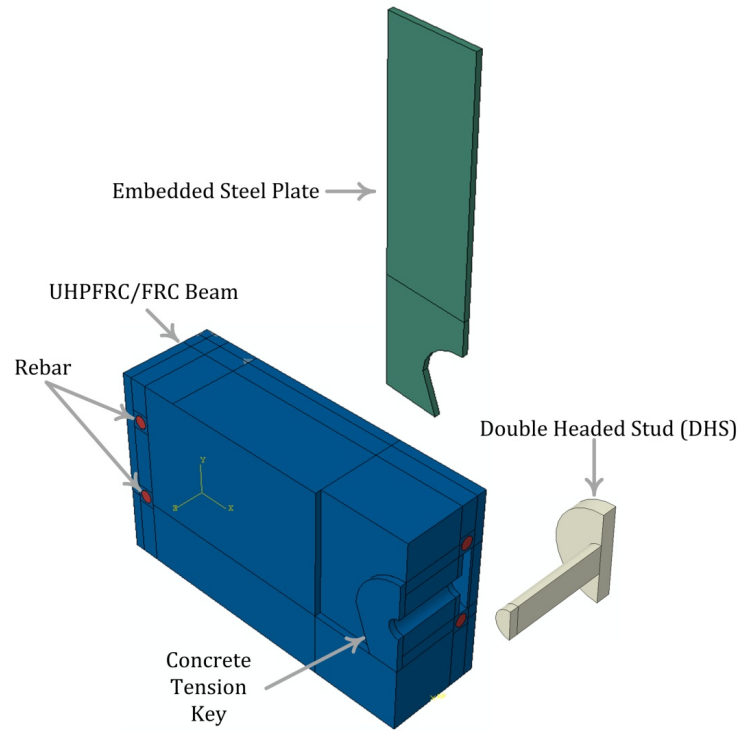


Figure 7-2: Geometry of a quarter of the composite connection.

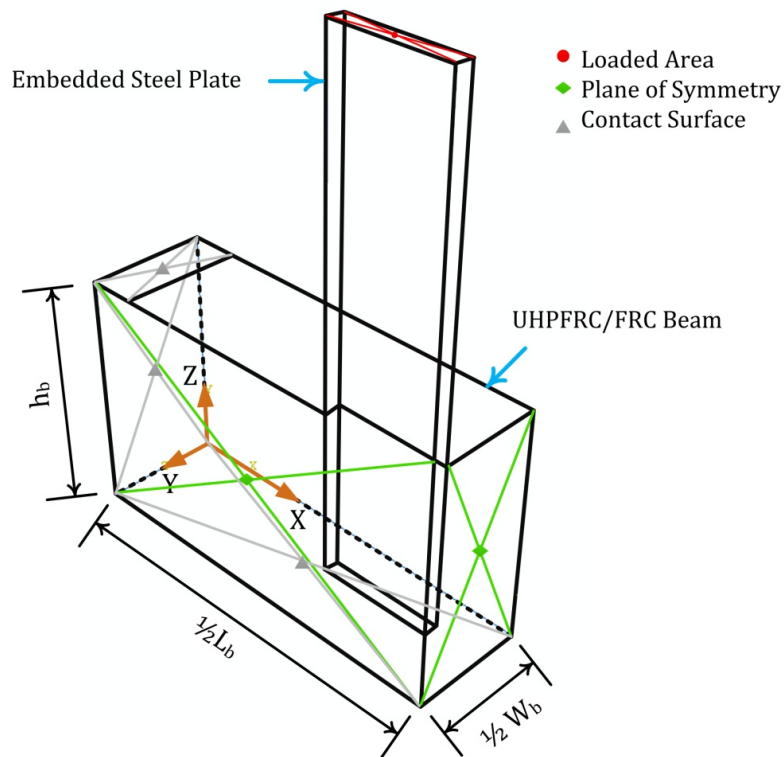


Figure 7-3: Planes of symmetry and loading in pullout test.

7.3 Analysis Type

Two main solution strategies were proposed in the past research for solving the nonlinear quasi-static problems in ABAQUS: ABAQUS/Standard and ABAQUS/Explicit. Each of them uses a different solution strategy for solving nonlinear quasi-static and dynamic problems (DS Simulia 2010).

7.3.1 ABAQUS/Standard

ABAQUS/Standard uses an implicit strategy with an iterative method to establish the equilibrium in nonlinear problem (DS Simulia 2010). This method requires a considerable computational effort, as a large system of linear equation needs to be solved in each iteration. Convergence may not be feasible in the complex problem with severely nonlinear behaviour and contact. The convergence is more critical after some limit points, where the concrete material's degradation starts. ABAQUS/Standard was first adopted in this research, but severe convergence difficulties were observed for most of the models after the maximum principal stresses in concrete beam exceeded the peak tensile strength of concrete. This issue was confirmed by several other researchers (Cofer et al., 2002).

7.3.2 ABAQUS/Explicit

7.3.2.1 Solution Strategy

The explicit solution method (ESM) in ABAQUS program was initially developed for dynamic problems where the inertia plays an important role in the solution process (DS Simulia 2010). However, the ESM with some considerations in the applied loading history was used to solve the quasi-static problems. The use of the ESM was reported to be efficient for extracting the highly non-linear quasi-static response of the composite members made of concrete material (DS Simulia 2010).

Unlike ABAQUS/Standard module, which uses an implicit strategy and require an iteration process, the solution in ABAQUS/Explicit can be determined by explicitly advancing the kinematic state over a small time increment (DS Simulia 2010). The term Explicit refers to the fact that the state at the end of each increment is based solely on the initial values such as displacement at the beginning of the increment

(DS Simulia 2010). The central difference rule is used in ABAQUS/Explicit to integrate the equation of motion explicitly through time. No iteration is required in The ABAQUS/Explicit, thus the convergence problem associated with the implicit strategies (material degradation) do not apply. In addition, the ABAQUS/Explicit features extensive capabilities for modeling contact and surface integration that are not available in ABAQUS/Standard.

7.3.2.2 *Mass scaling Technique*

The small or poorly shaped elements in the FEM model was observed to significantly control the stable time increment and drastically limits the length of the time step in each increment (DS Simulia 2010). To prevent these elements from controlling the stable time increment, a so-called mass scaling technique (MST) is often used in ABAQUS/Explicit. This is a numerical technique that is established to speed up the computations process. To this aim two different methods can be used: 1) reducing the time period of the analysis based on which the ABAQUS/Explicit technique determines the mass scaling factor, 2) artificially increase the mass of the model to keep its kinematic energy small (DS Simulia 2010). In the current research the first method was adopted by prescribing a specific time increment. In MST, all the elements in the model were automatically checked by the program at the beginning of the step. If any element in the model has a stable time increments less than the designated time increments, their masses are independently scaled to ensure that the element-by-element stable time increment equals to designated number. This scaling remains in effect throughout the step (DS Simulia 2010).

In order to gain a quasi-static structural response while minimizing the computational time of the analysis, fixed mass scaling for all elements with three different time increments (TI) were used: $TI = 1 \times 10^{-3}s$, $1 \times 10^{-4}s$, and $1 \times 10^{-5}s$. The influence of three different stable time increments on the load-slip behaviour of a composite connection were studied and the results are given in Figure 7-4. A considerable fluctuation in the load-slip response of the model with a time increment of $1.0 \times 10^{-3}s$ was noted. This fluctuation is mainly attributed to the dynamic effects involved in the analysis (DS Simulia 2010). The fluctuation in the FEM load-slip response was significantly reduced by deploying a lower TI factor. A stable response was observed for $TI = 1.0 \times 10^{-4}s$ and thus was adopted for the rest

of this study. The ABAQUS built-in smooth function, which is derived by moving average of data, was used to remove the small fluctuations in load-slip response which is caused by the numerical errors.

According to past research, an examination of the energy content of the FEM model can provide a measure to ensure that the ABAQUS/Explicit simulation reflects a quasi-static solution (DS Simulia 2010). The internal energy of the system should be nearly equal to work completed by external forces to ensure that a quasi-static response was achieved from the ABAQUS/Explicit analysis. In addition, the kinetic energy of the deformed material should not exceed a small fraction (1–5%) of its internal energy throughout the majority of a quasi-static analysis (DS Simulia 2010).

To evaluate the quasi-static response of the FEM model, the variation of internal and external energy against time was compared. The works completed by the internal forces was found to be nearly equal to that of external forces. In addition, the FEM model's kinetic energy was observed to be insignificant as compared to both internal energy and external work, which indicate that the quasi-static loading condition requirements were met. These relationships were checked for each FEM model.

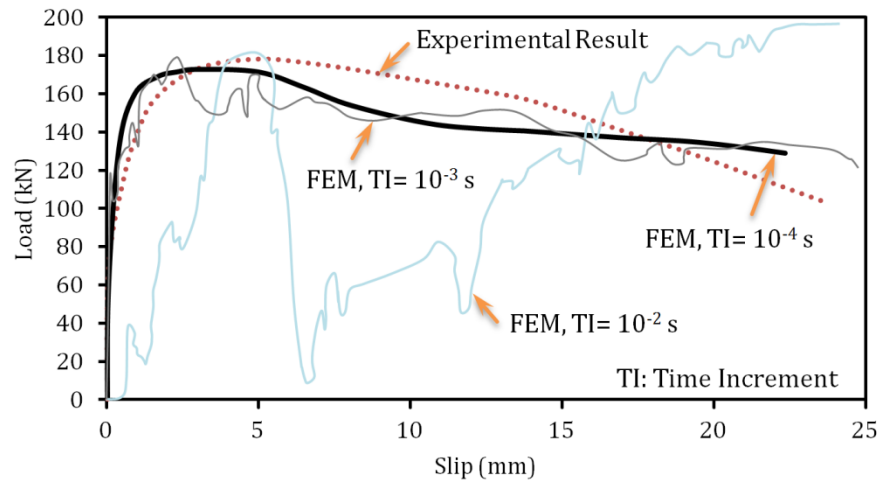


Figure 7-4: Influence of time increment on the load-slip behaviour of composite connection.

7.4 Material Property

The mechanical properties of the material in both compression and tension are necessary to best predict the FEM load-slip response of composite connection subjected to applied loading. ABAQUS/Explicit offers several material models for the concrete and steel materials. Each model defined with various parameters that significantly influence the accuracy of the FEM model (DS Simulia 2010). All the parameters need to be carefully calibrated using the experimental companion test results.

7.4.1 Steel Material

The material of the double headed stud, reinforced cage, and steel plate were modeled in the ABAQUS with an elasto-plastic model. This model is defined as a multi-linear isotropic hardening material in the ABAQUS, which requires a true stress-strain curve of materials. Thus, the engineering stress-strain curves obtained from the experimental coupon test provided in the chapter 5 of this document should be converted to true stress-strain curve. Two following equations can be used to convert the engineering stress-strain data from a uniaxial test to true stress-strain data (DS Simulia 2010).

$$\sigma_{true} = \sigma_{nom}(1 + \varepsilon_{nom}) \quad (7-1)$$

$$\varepsilon_{lm}^{pl} = \ln(1 + \varepsilon_{nom}) - \frac{\sigma_{true}}{E_s} \quad (7-2)$$

where, σ_{nom} and ε_{nom} are respectively the nominal (engineering) stress and strain derived from the material coupon test. The average values of module of elasticity and poisson's ratio for the steel material in the FEM model were assumed to be 210 GPa and 0.3, respectively.

The mechanical properties of steel material in both compression and tension were assumed to be similar and modeled by a three-linear stress strain curve, as shown in Figure 7-5. As depicted in this figure, the behaviour is initially elastic up to a yielding point I, where the Hook's law applies. This point was followed by a plateau until the onset of the strain hardening. See curve I-II. Point III refers the ultimate

stress (F_u). The mechanical properties of the steel material, from the coupon tests, are given in the chapter 5 of this document.

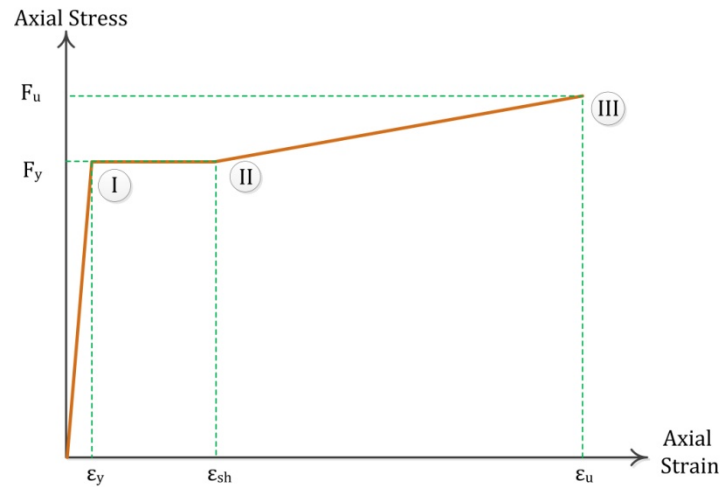


Figure 7-5: Stress-strain relationship for steel material.

7.4.2 Concrete Constitutive Model

The concrete constitutive model (CCM) is a mathematical description of the concrete material response under different loadings, which describes the relationship between the force (or stress) and deformation (or strain) tensor in a concrete material. Among the three available CCM for quasi-brittle material in ABAQUS, i.e. cracking model for concrete (CMC), concrete smeared cracking (CSC), and concrete damaged plasticity (CDP), the last two models were adopted in the current research for both FRC and UHPFRC material. Both models are continuum, and plasticity-based damage model for concrete and are able to model the inelastic behaviour of the concrete material (DS Simulia 2010). The proposed models for the concrete material in both CDP and CSC are almost similar. However the CDP is more comprehensive and versatile compared to CSC and was proved to lead to the less convergence problems than the concrete smeared cracking. Each of them is briefly explained in subsequent sections.

7.4.2.1 Concrete Damaged Plasticity

CDP model was initially developed by Lublinear et al. (1989) and later implemented in ABAQUS by Hibbitt et al. (1997). This model uses the concept of the isotropic

damaged elasticity in combination with the isotropic tensile and compressive plasticity to model the inelastic response of the concrete material in both compression and tension. The CDP uses a modified hyperbolic Drucker-Prager yield surface with a non-associated flow and multi-hardening in compression. It uses linear crack surface with damage elasticity after the cracking in tension (DS Simulia 2010). The CDP is suitable for problems with higher confining pressure.

The uniaxial compressive and tensile behaviour of the concrete material in CDP model is characterized by damage plasticity and illustrated in the Figure 7-6 and Figure 7-7. The CDP model is formulated by adopting the limit states of concrete cracking in tension and crushing in compression. The evolution of the failure surface in CDP is controlled by the tensile and compressive equivalent plastic strains (DS Simulia 2010).

According to stress-strain curve, given in Figure 7-6, the concrete material exhibits a linear elastic stress-strain response in compression up to a cracking stress, which is followed by a compression hardening behaviour. The strain softening behaviour in compression starts after the maximum compressive strength was reached. An almost similar response was noted for the concrete material under the tension loading, where a linear elastic response in tension was assumed for the concrete material until the peak tensile strength was reached. Beyond this point, the concrete material exhibits a softening stress-strain response until the failure was reached.

The CDP model requires definition of parameters related to compressive, tensile, and plasticity behaviours of concrete. These parameters include the dilation angle that identify the plastic strain direction in concrete relative to gradient of yield surface, flow potential eccentricity, which indicate the rate at which the plastic flow function approaches the asymptote, f-factor, K-factor, and a viscosity parameter that defines visco-plastic regularization. These default values are respectively set to 15° , 0.1, 1.16, $2/3$ and 0.0 for both UHPFRC and FRC concrete (Graybeal 2012), as summarized in Table 7-1.

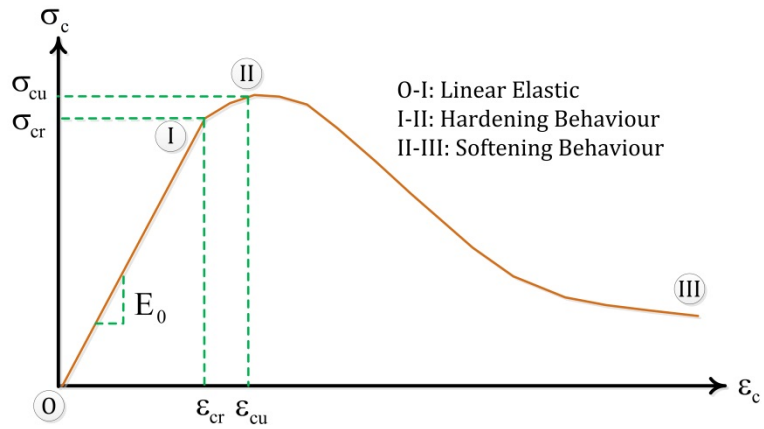


Figure 7-6: Stress-strain relationship of concrete in uniaxial compression.

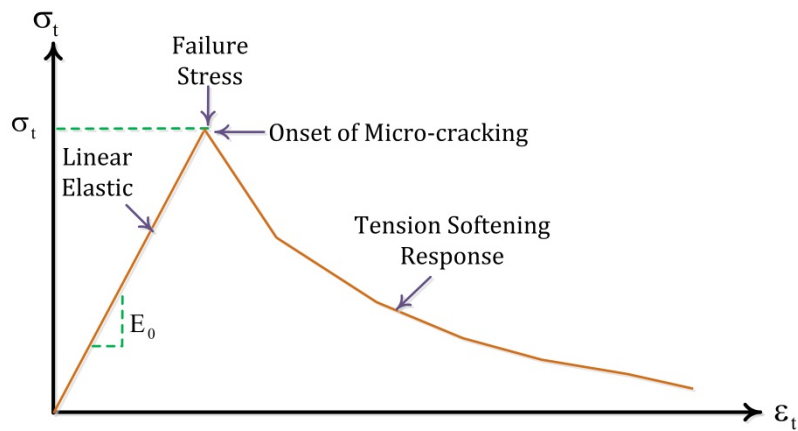


Figure 7-7: Stress-strain relationship of concrete in uniaxial tension.

Table 7-1: The parameters of concrete damage plasticity model

The parameters of concrete damage plasticity model	Dilation angle (Degree)	15
	Eccentricity	0.1
	$f = f_{b0}/f_{c0}$	1.16
	K	2/3
	Viscosity parameter	0

$$f = \frac{\text{initial equibiaxial compressive yield stress}}{\text{initial uniaxial compressive yield stress}}$$

$$K = \frac{\text{the second stress invariant on the tensile meridian}}{\text{the second stress invariant on the compressive meridian}}$$

7.4.2.2 Concrete Smearred Cracking

The concepts of oriented damaged elasticity or smeared cracking were used in the concrete smeared cracking (CSC) model to consider the reversible part of the material's response after cracking failure (DS Simulia 2010). In concrete smeared cracking (CSC) model, associated flow is assumed and cracks are considered to be remained after the formation (irrecoverable). However the crack might open and close during a cyclic loading, if any. The CSC model in ABAQUS can be used for the modeling of many applications in which the concrete is mainly subjected to monotonic straining and exhibits low confining pressure which is the case for the pull-out test in the current research. Cracking in concrete is the main feature of the CSC behaviour and dominates the modeling. The individual macrocracks are not being tracked in this model. Instead, the stress and material stiffness associated with each integration point are modified once the stress level reaches a failure surface that is called the crack detection surface (DS Simulia 2010). The four ratios are used to define the failure surface in the CSCS model as shown in Table 7-2.

Table 7-2: The parameters of concrete smeared cracking (CSC) model

Shear Retention	Rho_Close	1
	Eps_max	0.1
Failure Ratio	R ₁	1.16
	R ₂	0.0509
	R ₃	1.28
	R ₄	1/3

$$R_1 = \frac{\text{Ultimate biaxial compressive stress}}{\text{Ultimate uniaxial compressive stress}}$$

$$R_2 = \frac{\text{Uniaxial tensile stress at failure}}{\text{Ultimate uniaxial compressive stress}}$$

$$R_3 = \frac{\text{Magnitude of a principal component of plastic strain at ultimate stress in biaxial compression}}{\text{Plastic strain at ultimate stress in uniaxial compression}}$$

$$R_4 = \frac{\text{Tensile principal stress at cracking}}{\text{Tensile cracking stress under uniaxial tension}}$$

7.4.2.3 Yield surface

The failure surface of concrete under multi-axial stress is different than those observed under sole uniaxial tension or compression loading. A typical biaxial strength curve for concrete subjected to biaxial plane stress is illustrated in Figure 7-8. This curve was formulated by the relationship between the uniaxial stress-strain response of concrete in tension and compression and the states of multi-axial stress. The response of concrete inside the biaxial compression zone is modeled by an elastic-plastic theory with an isotropic hardening rule and an associated flow (DS Simulia 2010). Cracking in concrete is expected to initiate once the principal stress components in concrete material lies in either biaxial tension zone or in biaxial tension-compression zone. Upon the formation of a crack, the crack orientation is stored and the response of the material in cracked zone is modeled by the damaged elasticity modeled (DS Simulia 2010).

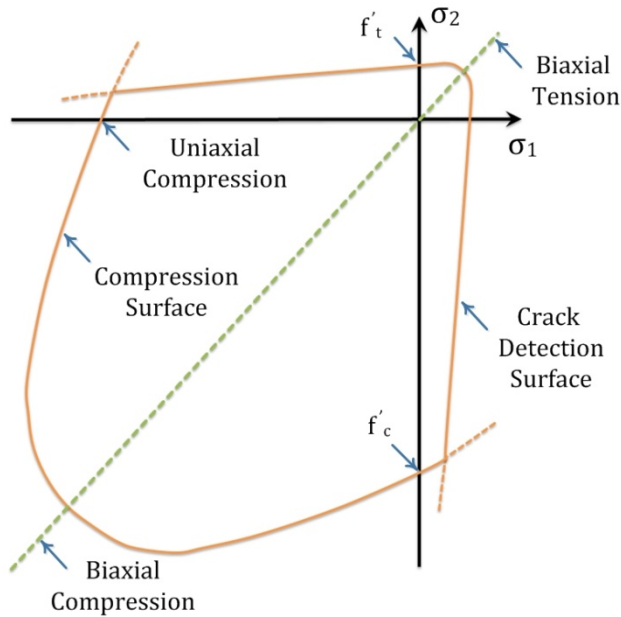


Figure 7-8: Concrete failure in plane stress (DS Simulia 2010).

7.4.3 Mechanical Properties of UHPFRC and FRC Material

Linear Elastic Response—The typical stress-strain response of UHPFRC and FRC material in tension and compression is provided in Figure 7-9 and 7-10. In the first part of the curve, the concrete material is assumed to have a quasi linear-elastic behaviour in both tension and compression until the cracking strength is reached. Two parameters are required to characterize the linear-elastic response of FRC and UHPFRC material in ABAQUS which includes Poisson’s ratio (ν) and Young’s modulus (E). The elasticity modulus and Poisson’s ratio for both FRC and UHPFRC material can be obtained from a uni-axial compression test. Each of these two parameters along with the density for both FRC and UHPFRC material are listed in Table 7-3.

Table 7-3: The elastic parameters for the UHPFRC and FRC material

Parameters	UHPFRF	FRC
Density ($\frac{kg}{m^3}$)	2550	2500
Elastic Modulus (MPa)	40000	22500
Poisson Ratio	0.18	0.22

Nonlinear Response—The inelastic stress-strain response of UHPFRC and FRC material in compression was extracted from the companion uni-axial compression test program which are explained in more detail in chapter 4 and 5 of this document. In order to define the nonlinear response of concrete in tension, there are three different techniques in ABAQUS/Explicit which includes: post-cracking tensile stress-strain response by defining the tension stiffening response of concrete, fracture energy curve by introducing the fracture energy required for crack formation, and stress-crack width curve.

The tension model for CDP or CSC, proposed by ABAQUS, can best represent the response of FRC in tension, as this material experience a linear-elastic response, followed by a softening behaviour. The small hardening behaviour of FRC in tension is not as significant as the UHPFRC material and could be simply ignored. However the UHPFRC behaviour in tension is significantly different than the tension model proposed for either CDP or CSC, as it features a strain hardening response in tension which is not directly considered in the CDP or CSC model. To address this issue, two different methods were used to model the nonlinear behaviour of UHPFRC in tension: 1) hardening-softening model, 2) elasto-plastic response. See Figure 7-9. Similar response was considered by Pichler et al (2010).

The influence of each model on the overall load-slip response of the connections under pull-out loading was studied. No significant difference in the load-slip response of the connection was found before the PPL point for both models. However the use of elasto-plastic model was found to enhance the convergence of the solution. A good agreement between the FEM results and experimental was observed. In order to facilitate the model convergence, a slightly higher CMOD was used in the FEM model.

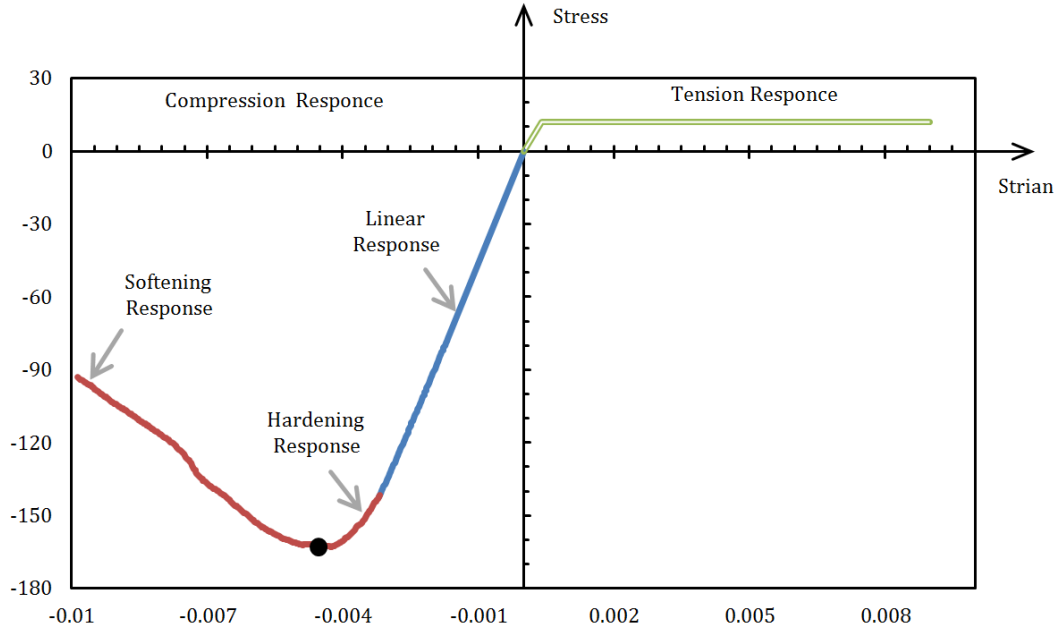


Figure 7-9: Material behaviour of UHPFRC material in compression and tension.

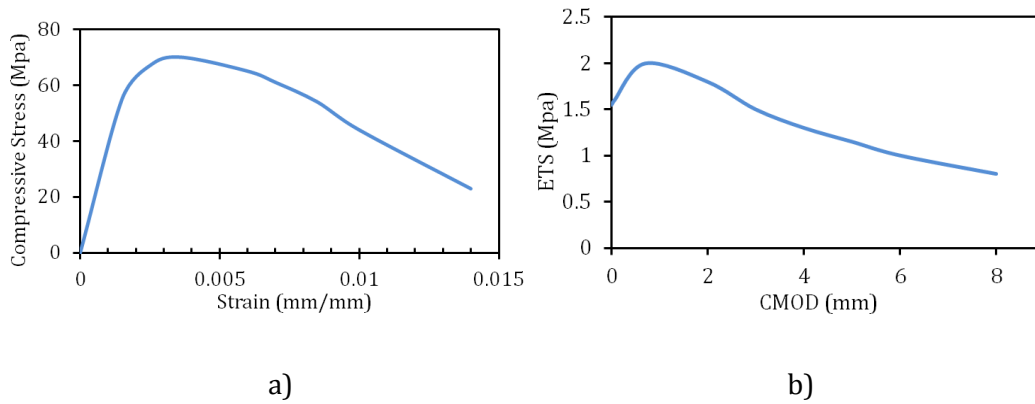


Figure 7-10: Material behaviour of FRC material, a) compressive behaviour, b) tensile behaviour.

7.4.3.1 Dilation Angle Sensitivity

Dilation angle (ψ) is a measure of the change in the volume of concrete during plastic deformation (DS Simulia 2010). In ABAQUS, the dilation angle was used to establish the flow rule and account for the increase of volume—associated with shear distortion of an element—relative to initial state caused by deformation. (Lubliner 1989, Nielsen 1999, and Park et al. 2001, DS Simulia 2010). An increase

in the dilation angle leads to a more confinement strength and eventually a stiffer stress-strain relation (DS Simulia 2010).

$$\sin\psi = \frac{d\varepsilon_v^p}{d\gamma^p} \quad (7-3)$$

where $d\varepsilon_v^p$ is the volumetric strain rate, $d\gamma^p$ is the shear strain rate, and the subscript p is the state of material at plastic. The state of the dilation angle at some limit state point was studied by several past researches (Park et al. 2001, DS Simulia 2010). According to Park et al. (2001), if $\psi < 0$, then the flow rule is non-associative and there will be less volumetric expansion than in associated rule. Associative is a state in which the plastic straining occur normal to the yield surface of concrete. A volumetric expansion of the material with increasing plastic strain was observed in associative state. There would be absolutely no volumetric expansion at $\psi = 0$ and associative flow rate occur (Park et al. 2001, DS Simulia 2010).

To investigate the sensitivity of the load carrying capacity of the composite connections to the dilation angle, a series of finite element analyses were performed in the current research for three different dilation angles, i.e., $\psi = 10^\circ, 15^\circ, 20^\circ$. As expected, the dilation angle has almost no impact on the response of composite connection in the elastic stage. However, the increase in dilation angles was found to result in a more stiff response, i.e., higher slope of the portion of the post cracking load deflection response prior to peak pull-out load. The FEM results of peak pull-out test for three different ψ angles are compared in Figure 7-11. Among the different ψ factors, the model with a dilation angle of 15° was found to best replicate the experimental load-slip response in pre-peak and post-peak part. Similar trends were found for the rest of the samples. Thus a $\psi = 15^\circ$ was adopted for the rest of study.

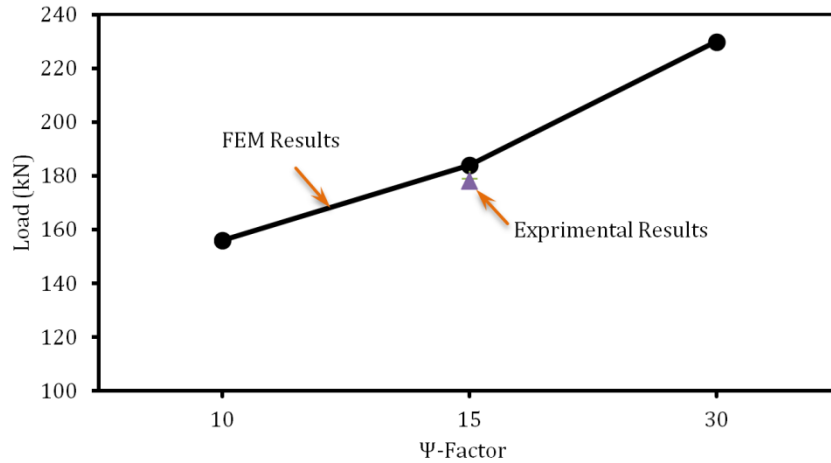


Figure 7-11: Variation of peak pull-out load against the dilation angle of the UHPFRC material (Ψ factor).

7.5 Loading

The experimental pull-out tests were conducted by pulling the embedded steel plate out of the concrete beam with a slow rate which are discussed in chapter 5. The pull-out load in FEM model was applied to the nodes located at the top side of the embedded steel plate through a displacement control loading algorithm. This loading technique allows capturing the post-peak response of the composite connection. The variation of applied displacement against the time can be simulated by several built-in methods in ABAQUS/Explicit including the arbitrary variation of load (tabular), mathematical function, and predefined fields. The first method, tabular technique, can be applied to the FEM model through the use of a linear function (dashed line) or a smooth step function (solid line), as shown in Figure 7-12. Load-slip response with spurious oscillations was found for FEM models with linear amplitude-time function. However the use of smooth step function was found to generate a smoother load-slip response with less oscillation.

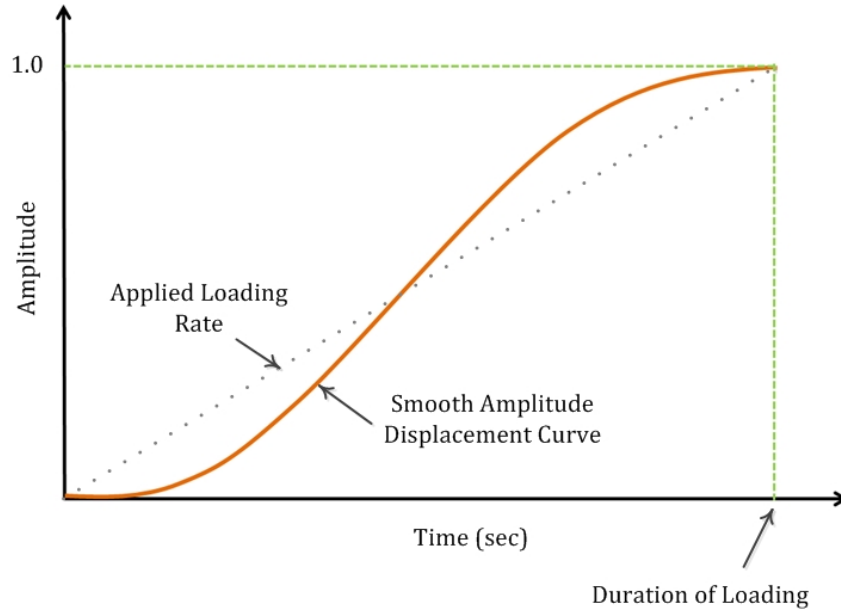


Figure 7-12: Smooth step amplitude definition in ABAQUS.

7.6 Element

Three dimensional eight-node solid elements (C3D8R) with reduced integration, enhanced hourglass control, and distortion control, as shown in Figure 7-13, were chosen to model all the solid parts in the composite connection. Each component of the pull-out test was modeled as a separate part.

The C3D8R element introduce shear locking for bending of thin members and results in a very stiff response (DS Simulia 2010). Thus, the reduced integration formulation was employed in ABAQUS to combine the low computational cost with the capacity to prevent shear locking and maintain a reasonable stiffness. The low computational cost was achieved through the use of integration formula with an order less than that used for exact integration (Pugh et al. 1978). This would significantly reduce the computational effort, which is required to gain convergence (DS Simulia 2010).

The hourglass control was also used to prevent the element instabilities which may caused by the stress-free element deformed shapes. In order to prevent the extremely distorted deformed-shapes that would result in the negative volumes and stiffness matrix, the distortion control is employed. In addition, the average strain

kinematic formulation of accuracy of first order was considered for all the elements (DS Simulia 2010).

The longitudinal rebars were initially modeled with the embedded element and the results were compared with those modeled with C3D8R element. The use of C3D8R element for longitudinal rebars allows the FEM model to captures bending in addition to axial stiffness. This capability is critical in the current model, as the dowel action of the rebars significantly participates in the load transfer mechanism. Best agreement between the FEM and experiment results was found for the model with C3D8R element and was adopted for the rest of the study.

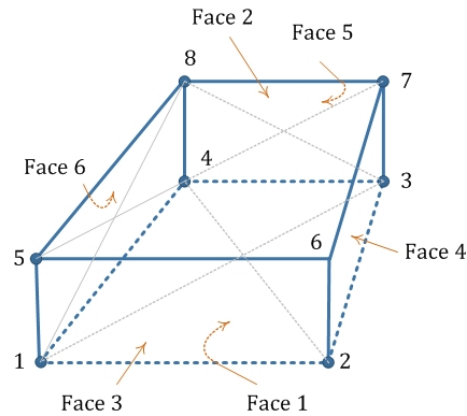


Figure 7-13: Geometry of 8-node element.

7.6.1 Mesh Sensitivity

Generally the use of more elements in the FEM model would result in a higher accuracy solution. This is due to the improved resolution of the stress distribution across the structure. However the use of very refined mesh configuration in FEM model will significantly increase the computational time. Thus, different meshing techniques were used to employ the right elements size in the right locations. In the other words, the element size should be small enough to yield reliable results and yet large enough to reduce the computational time and eliminates the need for expensive high-end computers (DS Simulia 2010).

The sensitivity of the pull-out test response to various mesh configurations was investigated. The mesh size used for the FEM model of composite connection varied

based on the location of the elements. The results of the FEM analyses show that the mesh refinement in the region away from the embedded steel plate has negligible effect on the load-slip response of the composite connection. Thus coarser mesh, in the order of 10-20 mm, was used for parts of the concrete beam which was away from the embedded steel plate and subjected to lower strain gradients.

A finer mesh, in a order of 5-10 mm, was used in parts of the concrete beam in the vicinity of the double headed stud and embedded steel plate. Element size larger than 5-10 mm should be avoided near the embedded steel plate, as some discrepancy between the FEM and experimental results was observed for models with larger mesh size. This is more pronounced for the elements in concrete pin where the stress gradient is significantly high. Therefore the finest mesh size, in the order of 1.5-3 mm, was used for the concrete tension key and the double headed steel (DHS). The final configuration of the FEM model is shown in Figure 7-14. This mesh configuration was found to significantly cut down the computational time required to get the reliable FEM results.

The higher order elements with more complex approximation were implemented to further increase the accuracy of the results. While the computational time was increased by 70% for the model with higher order elements, no significant change in the results was observed over those with lower order elements. All the elements were initially checked for geometric distortions and it was found that they all meet the prescribed criteria set by ABAQUS.

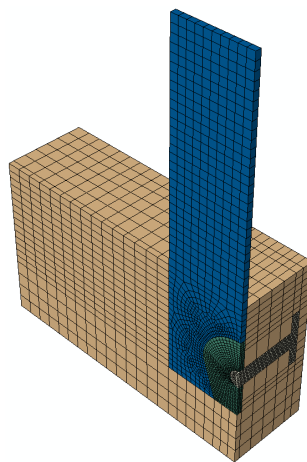


Figure 7-14: Meshing pattern for the FEM composite connection model.

7.7 Contact Interaction

In FEM model, the interactions between the surfaces of different composite components including the concrete beam, embedded steel plate, and rebar cage were modeled by a general contact algorithm (GCA). The GCA utilizes a sophisticated tracking algorithm to identify the contact interaction between the selected surfaces (DS Simulia 2010). In order to enforce the contact interaction, a penalty algorithm was used in the model. In this algorithm, the degree of violation of the contact such as the degree of penetration of one surface into the other was used to generate the contact pressure. A reasonably fine mesh is required in the vicinity of the contact surfaces to best distribute the penalty contact pressure to the element nodes. This would significantly influence the results and prevent any convergence issues (DS Simulia 2010).

A Hard contact pressure-overclosure was used for the normal interaction between each pair of surfaces. Hard contact allows the transmission of the contact pressure at the interface between two different components before they are separated. The contact stiffness is adjusted automatically to minimize penetration (overclosure) without adversely affecting the analysis time (Baltay and Gjelsvik 1990, Rabbat and Russell 1985).

The tangential interaction of contact surfaces were specified with Coulomb friction model. In this friction model, the maximum allowable friction (shear) stress across an interface was related to the contact pressure between the adjacent bodies (DS Simulia 2010). Five different coefficients of friction, i.e., $\mu = 0-0.6$ with an increment of 0.15 were used in the current research. The influence of the coefficient of friction on the peak pull-out load (PPL) of the composite connection with Ω -shaped tension key is given in Figure 7-15. All the results were normalized to the PPL of the specimens with $\mu = 0$. An increase in the friction factor from 0 to 0.15, 0.3, 0.5, and 0.6 resulted in 23%, 47%, 76% and 91%. This improvement in the PPL of composite connection is mainly associated to the fact that a significant portion of the pull-out load was sustained by the friction force between the embedded steel plate and concrete pin. A friction factor of 0.35 was adopted in this research, as it best

matches the experimental results. Similar friction factor between concrete and steel was used by other researchers.

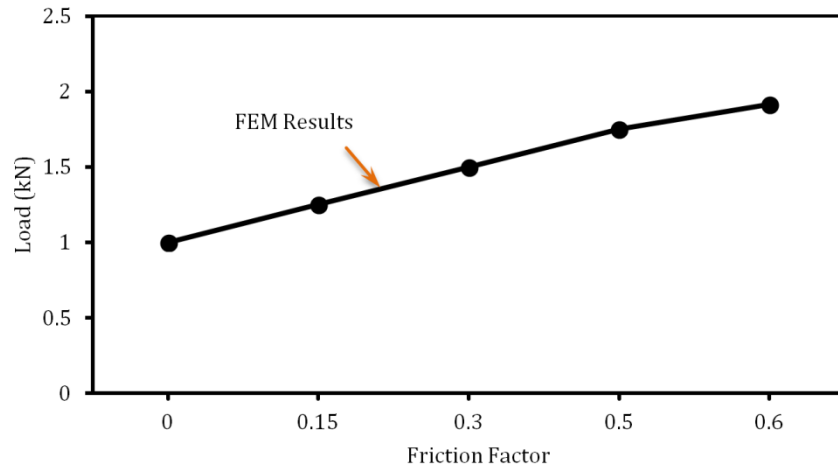


Figure 7-15: Influence of friction factor on the PPL of composite connections with Ω -shaped tension key and UHPFRC material ($V_f = 2\%$).

7.8 Boundary Conditions

Boundary conditions (BC) are the particular values of the field variables on the boundaries of a FEM model and represent structural supports. A U-shaped rigid support block was used to represent the support system used in the experimental program, as shown in Figure 7-16. A contact was defined between the surfaces of the concrete beam and the rigid block to allow the separation of the surfaces when there is not any contact force. The bottom side of the rigid block was fixed through restraining all the six degrees of freedom (translational and rotational) of the reference point located on the rigid support block. The symmetry condition was applied to both longitudinal and transverse planes of symmetry by restraining the degree of freedom in X and Y direction respectively (see Figure 7-3).

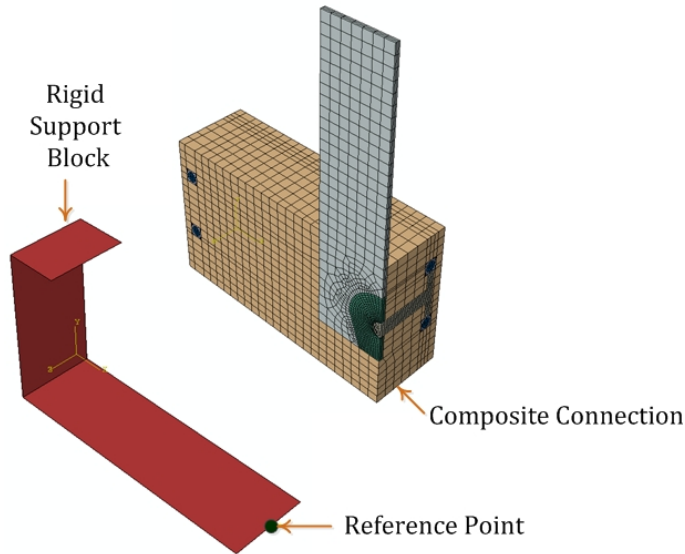


Figure 7-16: Rigid support block.

7.9 Verification of Results

The comparison between the FEM and experimental results allows investigating the suitability of the developed FEM model in predicting the response of the composite connection subjected to pull-out loading. In this section, the results of the FEM analysis of the composite connections are compared against the experimental tests from chapter 6. Description of the geometry and material properties of each experimental test are listed in the Tables 6-1, 6-2, and 6-3. The load-slip response, peak pull-out load (PPL), and failure modes from the FEM analysis were compared against those measured from the experimental results in chapter 6.

7.9.1 General Observation

A comparison of a typical FEM pull-out load-slip response against the experimentally measured curve is presented in Figure 7-17. The slip was measured as the relative displacement between the embedded steel plate and bottom side of the concrete beam. The FEM model was found to be capable of capturing the pre-peak and post peak-peak response of the composite connections. As shown in Figure 7-17, a linear-elastic behaviour was observed until the extreme tensile fiber at the mid-span and at the top side of the beam (Point MT) reached the tensile cracking strength of the concrete. According to CDP model, the cracks tend to form once the

maximum principal plastic strain in the concrete material exceeds zero (DS Simulia 2010). A good agreement between the ascending portion of the load-slip curve predicted by the FEM model with those of experimentally measured response was found for most of the connection specimens except for specimens constructed with UHPFRC material without fiber, where the initial part of the FEM load displacement curves were much stiffer than the one captured in the experimental program. However, compared to the pre-peak response, more discrepancy between the FEM and experimental results after the PPL were observed for most of the specimens made of O-shaped, Ω -shaped, and puzzle-strip tension key. This is most probably attributed to the propagation of the crack-induced damage which would lead to instability of the results in this stage.

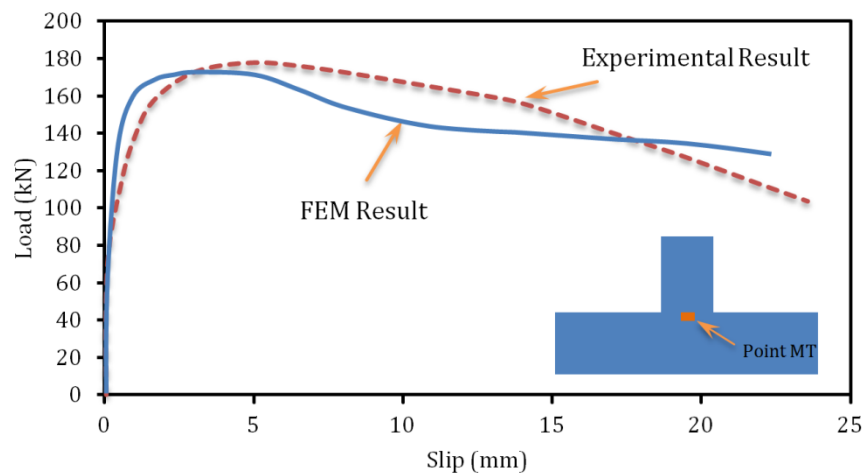


Figure 7-17: comparison of FEM and experimental test result for the composite connection made of UHPFRC material and Ω -shaped tension key.

The FEM failure modes for different connection specimens were checked against those observed in the experimental tests and a good agreement between them was observed for most of the FEM models. The break-out failure mode in the connection system constructed with Ω -shaped plate and UHPFRC material ($V_f = 2\%$) is presented in Figure 7-18, which is similar to the failure mode observed in the experimental program. Unlike few experimental results, no concrete side failure was observed in the FEM models. This is because unlike the experimental test setups, no deviation between the plain of embedded steel plate and that of the concrete beam exists in the FEM model.

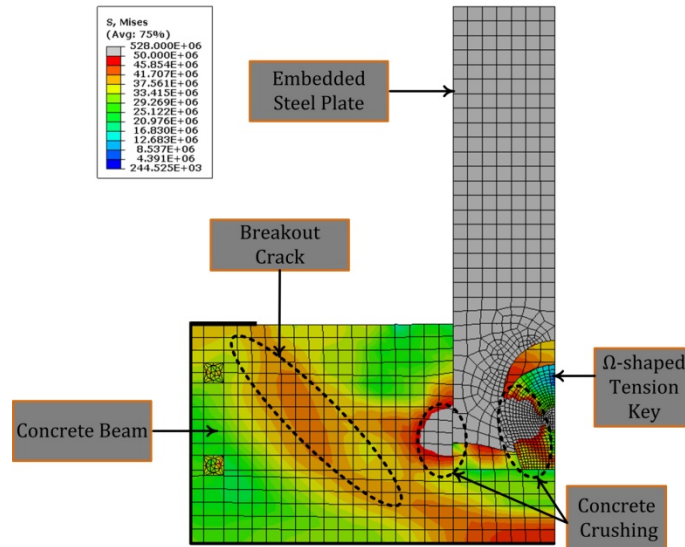


Figure 7-18: Break-out failure mode in the connection system constructed with Ω -shaped plate and UHPFRC material ($V_f = 2\%$).

The results of the PPL extracted from the FEM models were compared with those of the experimental results. It was found that the developed FEM models can precisely predict the PPL of the composite connection systems which are listed in the subsequent sections. However the FEM model was found to underestimate and overestimated the PPL for a few specimens which are listed in the relevant sections.

The mechanical interlock between the embedded steel plate and the concrete pin is the main resisting component against the pull-out load. The overall view of the deformed tension key is provided in Figure 7-18 and 7-19. The inclined sides of the concrete pin were found to experience a combination of compressive crushing and shear failure. Compared to connection systems with FRC beam, a significantly higher PPL was observed for the composite connections made of UHPFRC material. This improvement is more pronounced for the UHPFRC material with higher fiber content, i.e. $V_f = 2\%$ and 4% . This is mainly attributed to the more improved mechanical properties of the UHPFRC material in the tension and shear.

A combination of different failure modes were observed for different specimens including yielding in embedded steel plate, compression crushing at the interface between the tension key and concrete pin, and shear failure in concrete pin.

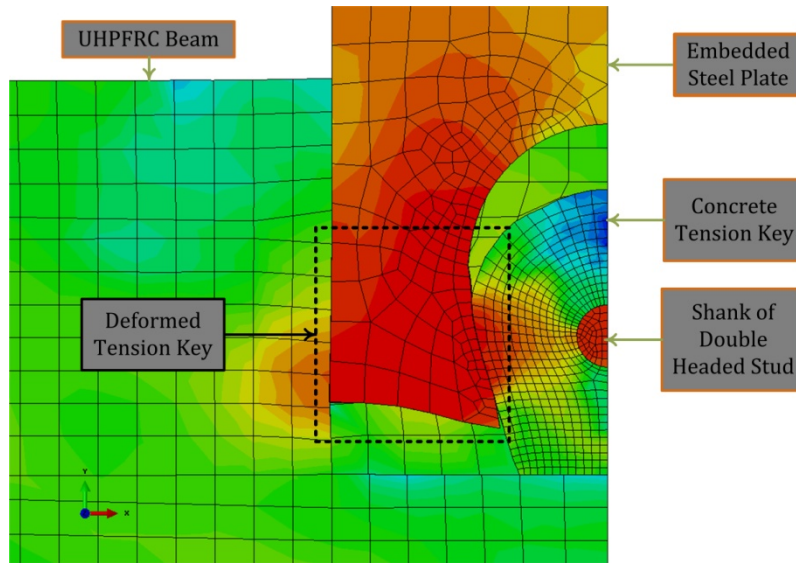


Figure 7-19: Stress distribution in the embedded steel plate and concrete pin.

The discrepancy between the FEM and experimental results can be attributed to a series of factors including:

- The mechanical properties of the companion specimens in both tension and compression may not best represent the material cast in the real specimens.
- The peak compressive strength of the UHPFRC was derived by scaling the compressive strength of 50 mm cube specimen (CU-50) to that of the standard specimen, 100 mm cylinder (CY-100), using the conversion table in chapter 4 of this thesis. Thus, there could be some inaccuracy in the conversion table which influences the results.
- The mechanical properties of the UHPFRC material in tension were derived from the results of an inverse analysis of a PF-50 prism which may not best represent the tensile strength of the beam used in the composite connection.
- Discrepancy between the assumed material model for the concrete material in ABAQUS and the real material model. This is more pronounced in the UHPFRC material, as the CDP and CSC behaviour in tension do not best model the hardening behaviour of UHPFRC material.
- Simplified representation of the cracking in CDP and CSC model may result in some disagreement in the failure pattern.

7.9.2 Comparison of Numerical and Experimental Results

In this section, a series of comparisons between the FEM and experimental peak pull-out load were completed to ensure that the developed FEM model can reproduce the experimental result.

7.9.2.1 Influence of CDP versus CSC

The load-slip response of the Ω -U-70-10-2 composite connection specimen using the CDP and CSC model along with the experimental results are given in the Figure 7-20. According to this graph, similar load-slip responses were found for both models in the early stage of loading. This is mainly because the similar parameters, including the modulus of elasticity and poisson's ratio were used for the linear-elastic part of the CDP and CSC model. However some deviation between the CDP and CSC was observed after the formations of cracks in the concrete beam.

The results of several preliminary FEM analyses on the proposed composite connections indicated that the model with CSC features a stiffer load-slip response in post-cracking stage compared to similar models with CDP. The FEM results from both CSC and CDP were compared against the experimental results, as shown in Figure 7-20. A higher discrepancy between the FEM and experimental load-slip response was found for the models with CSC compared with those with CDP. In addition, for composite connections with plain UHPFRC material ($V_f = 0\%$), the CSC model was found to fail to converge before the PPL reached. Thus, the CDP model was adopted for all the FEM models in the rest of the study.

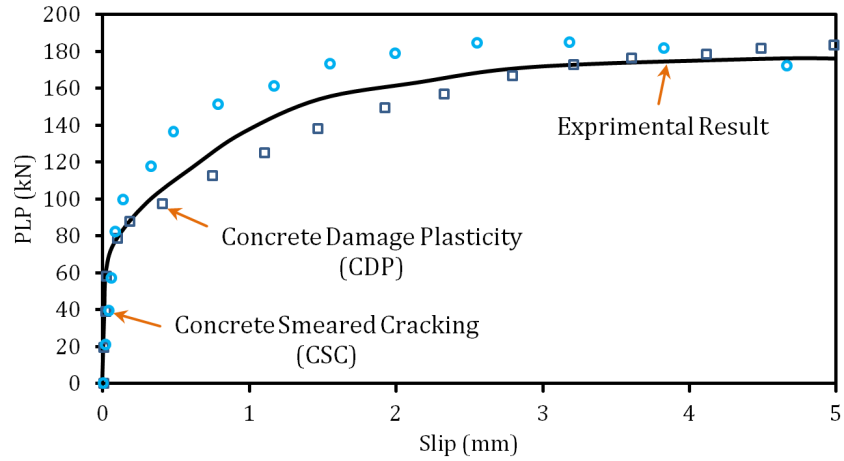


Figure 7-20: Influence of CDP and CSC on the PPL of Ω S-U-70-10-2 composite connection (Ω -shaped tension key, $h_h = 70$ mm, UHPFRC with $V_f = 2\%$, $t_{pl} = 10$ mm).

7.9.2.2 Influence of Ω -shaped Tension Key Size

Figure 7-21 summarizes the numerical and experimental results of the changes in the PPL of composite connection against the size of Ω -shaped tension keys. The UHPFRC beam dimension was 500 x 150 x 150 mm and the embedded length of steel plate was 100 mm. The mechanical properties of the UHPFRC and other steel components (steel plate, rebar, and DHS) along with the experimental results are given in chapter 6. The results of FEM analysis indicate that the increase in the Ω -shaped hole size from 50 mm to 70 mm and 90 mm was resulted in 17% and 20% improvements in the PPL of the composite connection. Comparisons were made between the FEM and experimental results and a good agreement between the results were found which are given in Figure 7-21. As given in this figure, the FEM model tends to slightly overestimate the peak pull-out load of the composite connections, as compared with the average experimental test results.

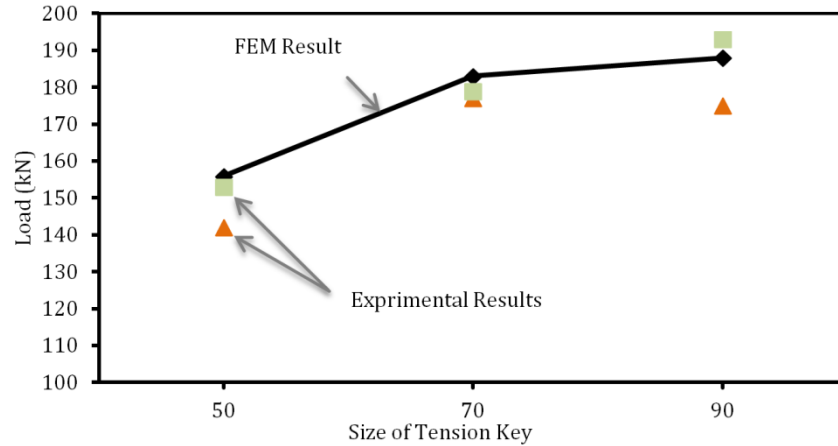


Figure 7-21: Influence of Ω -shaped tension key diameter on the PPL of composite connection with $V_f = 2\%$.

7.9.2.3 Influence of Embedded Plate Thickness

In order to investigate the results of FEM analysis against the experimental results, FEM models of composite connection with plate thickness of 8 to 20 mm was completed and the results were compared against the experimental results. The composite connection model was made of UHPFRC material with $V_f = 2\%$ and embedded steel plate with Ω -shaped tension key ($h_h = 70$ mm). The influence on the PPL of composite connections from different plate thickness is given in Figure 7-22 for both FEM and experimental results. The results of FEM analysis show that compared to composite connection system with a plate thickness of 8 mm, 7%, 24%, 29%, and 24% improvement in the PPL were found for those with a plate thickness of 10, 12, 16, and 20 mm. This is mainly because the thicker plates provide larger bearing surface and thus decrease the bearing stressed at the interface between concrete pin and the embedded steel plate, which eventually leads to a higher PPL.

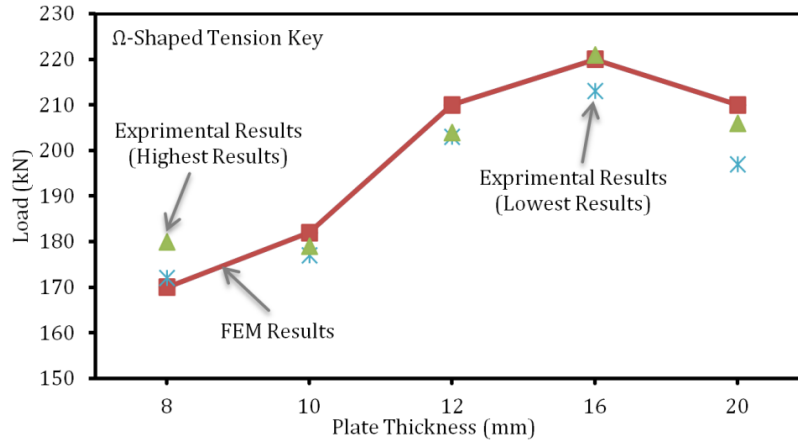


Figure 7-22: Variation of peak pull-out load (PPL) against the embedded plate thickness for composite connection with $V_f = 2\%$.

7.9.2.4 Influence of Embedded Length of Plate

The influences on the load carrying capacity of the composite connection system with Ω -shaped tension key and two different embedded steel plate lengths of 100 and 150 mm are summarized in Figure 7-23. The height of the concrete beam in the composite connections with embedded steel plate length of 100 mm and 150 mm were respectively 150 mm and 200 mm, see Figure 7-24. According to FEM analyses results, 42% improvement in the PPL was found as the embedded length was increased from 100 mm to 150 mm. Similar results were found for those of experimental specimens.

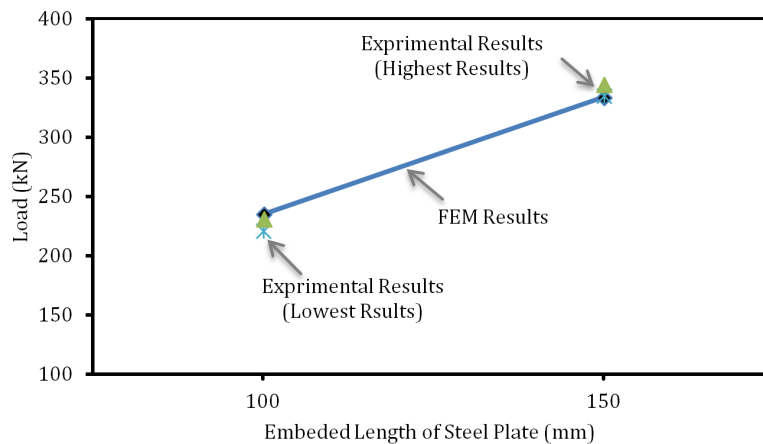


Figure 7-23: Influence of plate embedment length on the PPL of composite connection with $V_f = 2\%$.

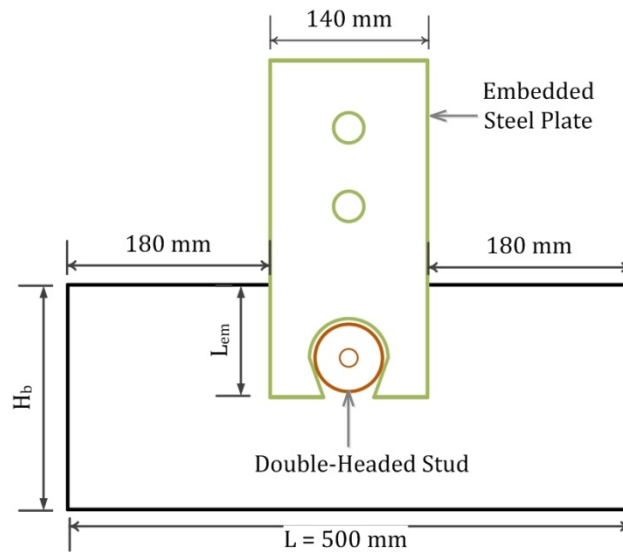


Figure 7-24: Influence of plate thickness on load bearing capacity of composite connection with $V_f = 2\%$.

7.9.2.5 Influence of Fiber Volume Fraction (V_f)

The influences of the UHPFRC material with three different fiber volume fractions, i.e., $V_f = 0\%$, 2% , and 4% , on the FEM load carrying capacity of the composite connections with Ω -shaped tension key are summarized in the Figure 7-25. The FEM results indicated that compared to connections system with the plain UHPFRC mix, $V_f=0\%$, the use of mixes with 2% and 4% steel fibers increased the PPL by 156% and 219% . This significant enhancement in the load carrying capacity of the composite connection is mainly associated to the improved mechanical properties of the UHPFRC material in tension, compression and shear, which prevent the early failure at the concrete pin through a fiber bridging effect.

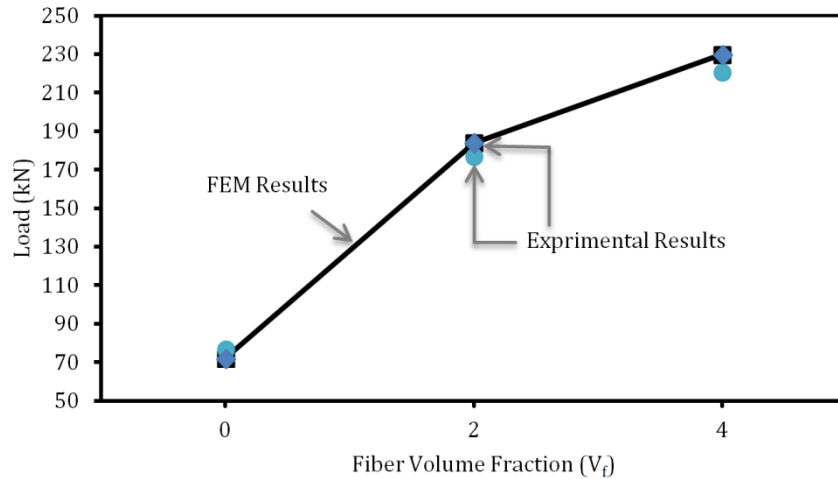


Figure 7-25: Influence of fiber volume-fraction on the PPL of composite connection with embedded length of 100 mm, plate thickness of 10 mm.

7.9.2.6 Influence of Concrete Generation

The influences on the PPL of the composite connections with Ω -shaped tension key from two different embedded plate thickness, i.e. $t_{ep} = 10$ mm and 16 mm, and two different concrete generations, i.e., UHPFRC and FRC material are summarized in Figures 7-26 and 7-27.

The FEM results indicated that compared to connection specimens constructed with the FRC material, the use of UHPFRC material resulted in 70% and 90% enhancement in the PPL of connection specimens with $t_{ep} = 10$ mm and 16 mm respectively. This is because the mechanical properties of the UHPFRC material in tension, compression, and shear are considerably higher than the FRC material, which prevent the premature failure in the concrete pin. The higher rate of improvements in the connection specimens with thicker plate is attributed to a more improved mechanical interlock between the concrete pin and the embedded steel plate, as the bearing stress level at the interface between them was decreased by 35%.

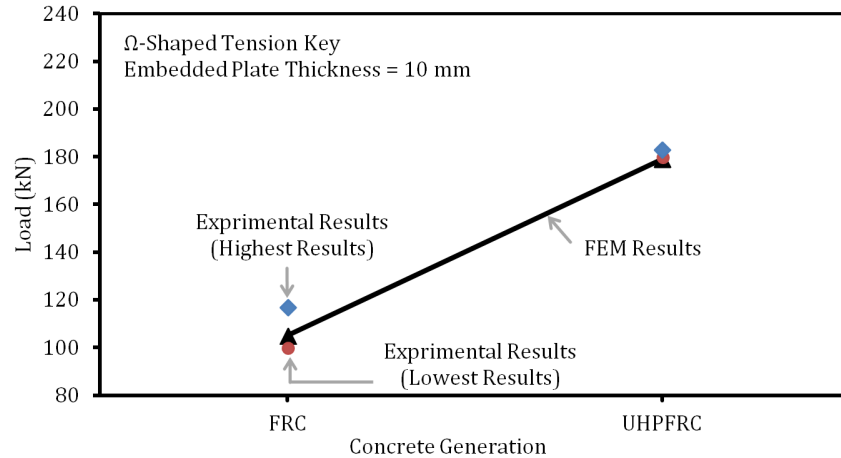


Figure 7-26: Influence of concrete generation on the PPL of composite connection with Ω-shaped tension key, plate thickness = 10 mm.

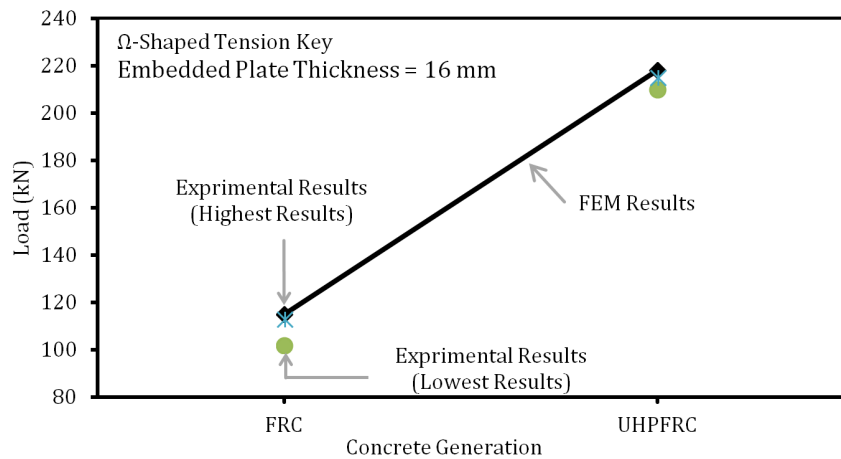


Figure 7-27: Influence of concrete generation on the PPL of composite connection with Ω-Shaped tension key and plate thickness of 16 mm.

7.9.2.7 Influence of Double Headed Stud

The influences of the double headed studs (DHS) on the FEM load carrying capacity of the composite connections with an O-Shaped tension key are summarized in Figure 7-28. Compared to connection system without DHS, an average 16% increase in the maximum load carrying capacity of specimen with DHS was found, which is close to the average improvement obtained from experimental results. The results of the FEM analysis indicates that the use of DHS in a connection system

significantly improve the post-cracking and softening response of the composite connection. Unlike the specimen without the DHS, no sudden or large change of slope in the load-slip relationship was observed for the connection system with DHS. This is most probably because the DHS laterally confined the concrete at both sides of the embedded steel plate and hence retard the formation and propagation of cracks in the concrete pin. Similar improvement was reported by other researchers, where a transverse reinforcement, passed through the holes, was used (Rauscher 2011).

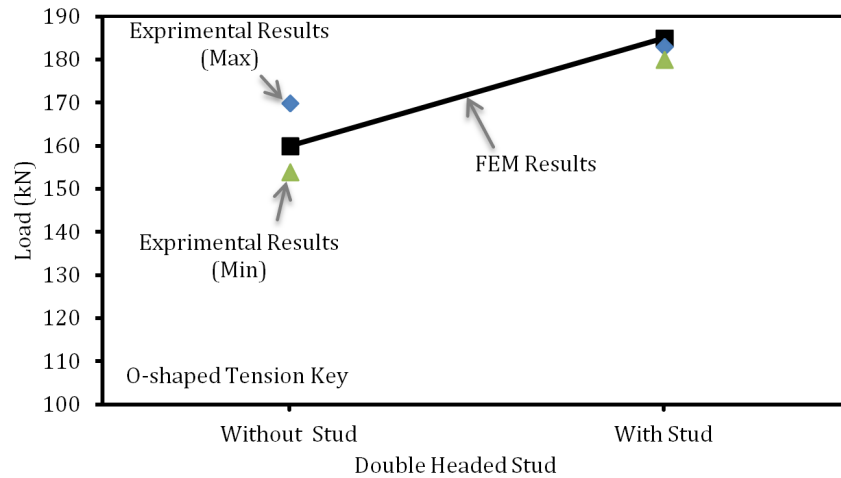


Figure 7-28: Influence of DHS on the PPL of composite connection with O-shaped tension key.

7.10 Parametric Analysis

In this section, the validated FEM model, capable of reproducing the experimental load-slip response of the connection specimens was used to extend the range of applications of the embedded steel plate in the UHPFRC and FRC material. The validated model was used to conduct the parametric analysis to explore further aspect of the composite connection behaviour. The main variables studied in this section includes: 1) geometry of the hole cut through the embedded steel, 2) concrete generations including normal strength concrete (NSC), FRC, and UHPFRC material, 3) tensile strength of UHPFRC material, 4) thickness of embedded plate.

7.10.1 Composite Connection under Pull-out Loading

7.10.1.1 Influence of Ω -shaped tension Key Configuration

The load transfer mechanism from the embedded steel plate to the concrete beam is mainly performed through the inclined sides of the Ω -shaped holes, as shown in Figure 7-29. The angle of inclination, α_{CSK} , was found to directly influence the load carrying response of the composite connections. This is because the increase in the α_{CSK} increases the normal component of the resisting force and therefore enhance the PPL. In order to find the most optimized shape, three different configurations were modeled in the ABAQUS/Explicit which are illustrated in Figure 7-30.

The influence of three different tension key configurations, i.e. 70-60, 70-45, and 70-30 on the PPL of the composite connections with $V_f = 2\%$ is illustrated in Figure 7-31. Compared to connection system with a 70-60 hole configuration, the use of 70-45 and 70-30 configurations were respectively resulted in 87%, 69% improvement in the PPL. This improvement is mainly attributed to the improved mechanical interlock between the concrete pin and the embedded steel plate.

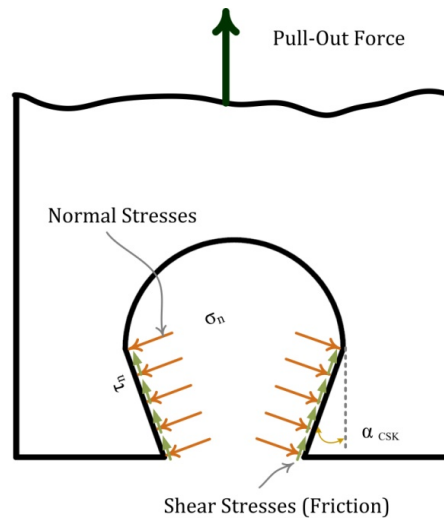


Figure 7-29: Normal and shear stresses on inclined sides of the Ω -shaped holes.

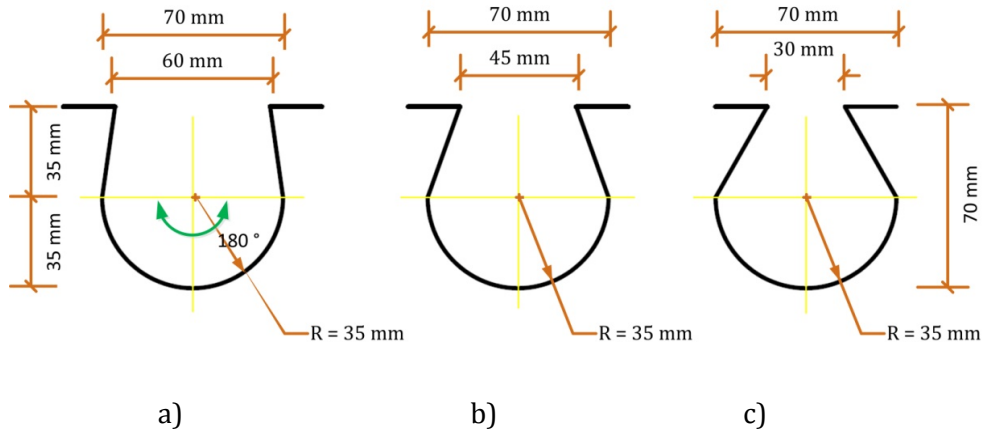


Figure 7-30: Geometry and configuration of Ω -shaped tension key.

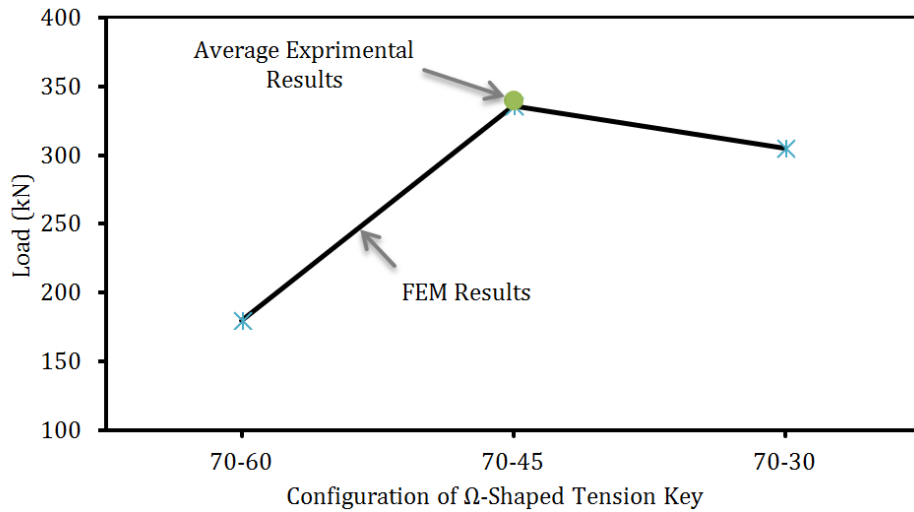


Figure 7-31: Influence of different Ω -Shaped tension key configuration on the PPL of composite connection with embedment length of 150 mm.

7.10.1.2 Influence of Embedded Plate Thickness

Connection system with embedment length of 100 mm: The influence on the PPL of the composite connections with an embedded length of 100 mm and O-shaped tension key from three different plate thicknesses, i.e. $t = 10, 12,$ and 16 mm, and two different concrete generations, i.e., FRC and UHPFRC material, are illustrated in Figure 7-32. No significant improvement in the PPL of the composite connections

with the FRC material was found after the embedded plate thickness increased from 10 mm to 16 mm. In contrast, the increase in plate thickness from 10 mm to 12 and 16 mm was resulted in 11% and 20% increase in the PPL.

Connection system with embedment length of 150 mm: A series of FEM modelling was completed to study the influence of three different plate thicknesses, i.e. 10, 16, and 20 mm on the PPL of the composite connections with an embedded length of 150 mm and a 70 mm Ω -Shaped tension key. The results of the FEM analysis for all the three plate sizes along with the experimental results for the connection specimens with the plate thickness of 16 mm are given in the Figure 7-33. A significant improvement in the PPL with increasing the embedded plate thickness was found for composite connection. Compared to composite connection with a plate thickness of 10 mm, 41% and 50% improvement in the PPL were found for those with a plate thicknesses of 16 mm and 20 mm.

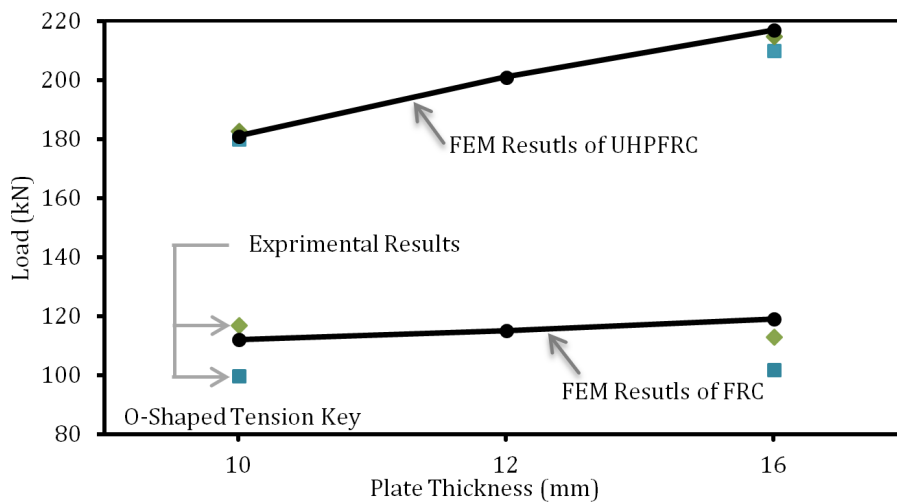


Figure 7-32: Influence of plate thickness on the PPL of composite connection with O-Shaped tension key and UHPFRC material with $V_f = 2\%$.

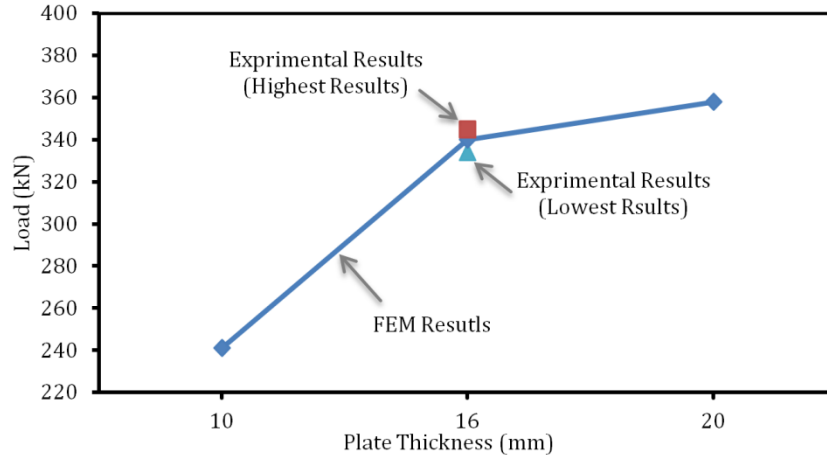


Figure 7-33: Influence of plate thickness on the PPL of composite connections with embedded length of 150 mm and UHPFRC material incorporating $V_f = 2\%$.

7.10.1.3 Influence of Embedded Length of Plate

According to experimental results in chapter 6, the PPL of composite connections constructed with Ω -shaped holes and UHPFRC material are significantly influenced by increasing the embedded length of the steel plate. In order to further investigate the influences on the load carrying capacity of the connection specimens with Ω -shaped holes, FEM models with three different embedded lengths, i.e., $L_{em} = 50, 100,$ and 150 mm were completed and the results are presented in the Figure 7-34. Compared to composite connections with an embedded length of 50 mm, 38% and 96% improvement in PPL was found for those with embedded length of 100 mm and 150 mm.

Similar FEM analyses were completed for the connection system with FRC beam. According the FEM results, the composite connections with the FRC material presents an average 75% lower PPL as compared to the connection system made of the UHPFRC material with 2% volume-fraction of steel fibers.

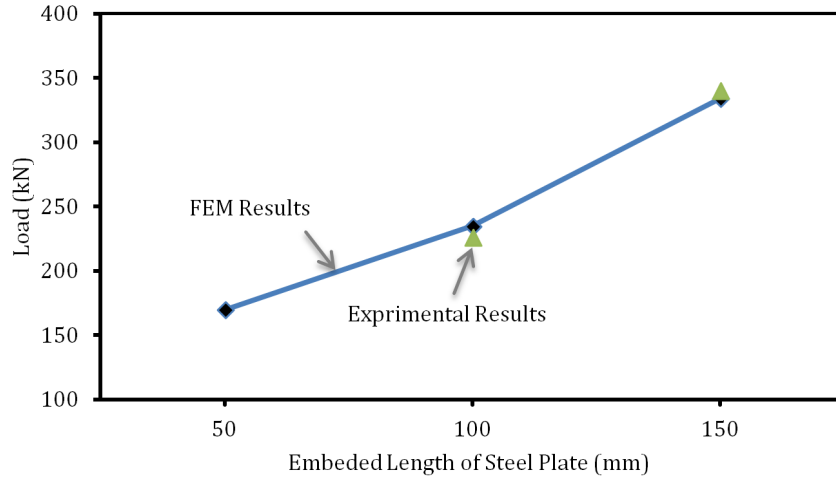


Figure 7-34: Influence of plate embedment length on the PPL of the composite connections with Ω -shaped hole and UHPFRC material incorporating $V_f = 2\%$.

7.10.1.4 Influence of Size of O-shaped tension Key

Figure 7-36 summarizes the FEM results of the change in the PPL of the composite connections against the size of the O-shaped tension key. The size of the circular holes varies from 50 mm to 70 and 90 mm. The results of the FEM analysis are shown with a solid line in this figure. While no significant enhancement in the PPL of composite connections with 70 mm hole was found over that with 50 mm hole, 11% improvement was observed as the tension key size was increased to 90 mm. The results of the experimental program are compared against the FEM results and shown in the Figure 7-35. While a good agreement between the FEM and experimental results was found for the 70 mm tension key, the FEM results presented a 6% lower PPL for 50 mm hole.

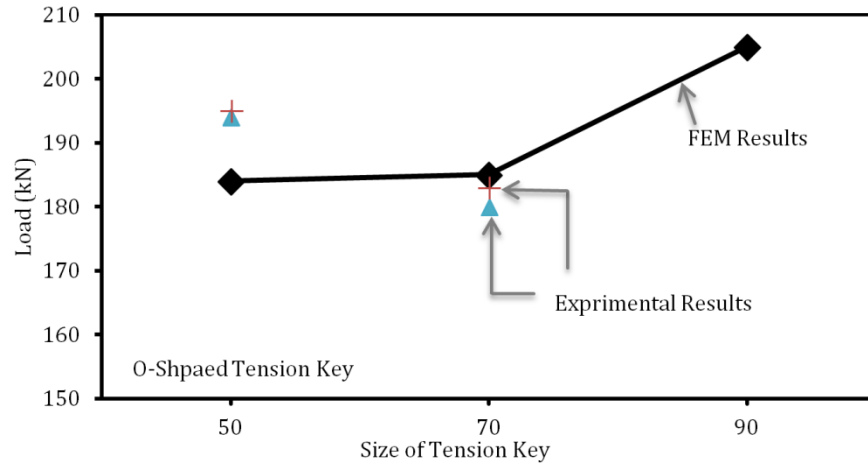


Figure 7-35: Influence of O-shaped tension key size on the PPL of composite connection with UHPFRC material incorporating $V_f = 2\%$.

7.10.1.5 Influence of Fiber Volume-Fraction

In order to study the influence of the UHPFRC tensile strength on the PPL of the composite connections with an embedded length of 150 mm and a 70 mm Ω -Shaped tension key a series of analysis were completed and the results are given in Figure 7-36. A good agreement between the FEM and experimental results was found for the connection system with 2% volume-fractions of short steel fibers, which is illustrated in the Figure 7-36. According to this figure, an almost linear increase in the PPL was found, as the tensile strength of UHPFRC material was increased from 8 MPa to 17 MPa.

The significant improvements in the PPL of the connection systems are attributed to the considerable enhancement in the tensile, compressive and shear strength of UHPFRC which would directly enhance the: 1) capacity of the concrete pin under compression and shear stresses, 2) lateral confinement of the concrete around the embedded steel plate, and 3) flexural capacity of the beam and prevent the formation of the splitting cracking in the mid-span of the concrete beam.

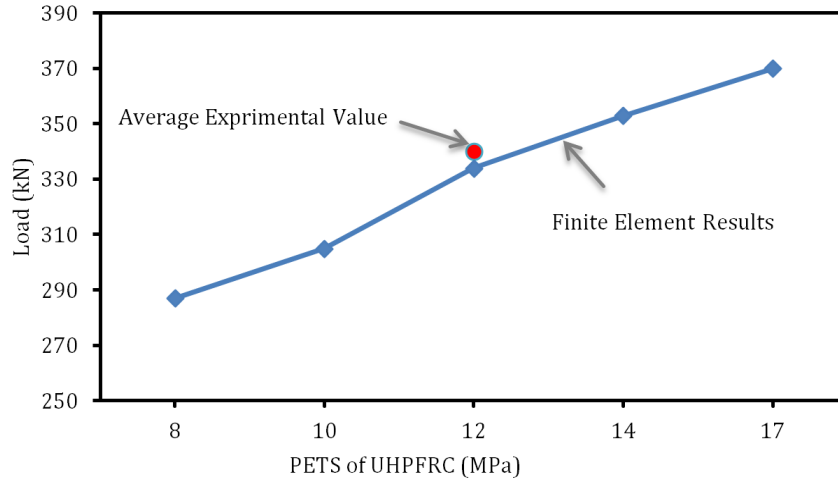


Figure 7-36: Influence of UHPFRC peak equivalent tensile strength on the PPL of composite connections with embedded length of 150 mm, plate thickness of 16 mm, and UHPFRC material incorporating $V_f = 2\%$.

7.10.1.6 Influence of Double Headed Stud

The effect of double headed stud (DHS), passed through the holes, on the pull-out load-slip response of the composite connections made of O-shaped and Puzzle-strip holes were studied. A significant improvement in the post-cracking and softening response of the connections with DHS was found over those without DHS. Unlike the connection system without DHS, a notably more stable load slip response was found for those with DHS.

The influence of the DHS on the PPL of two different hole shapes are given in the Figure 7-37 and Figure 7-38. It was found that the addition of DHS to composite connections respectively resulted in 20% and 23% increase in the PPL of the connection with O-shaped and puzzle-strip tension key. This enhancement in the PPL is most probably because the DHS provides a higher level of confinement to the concrete beam, which prevents the premature failure in the concrete pin.

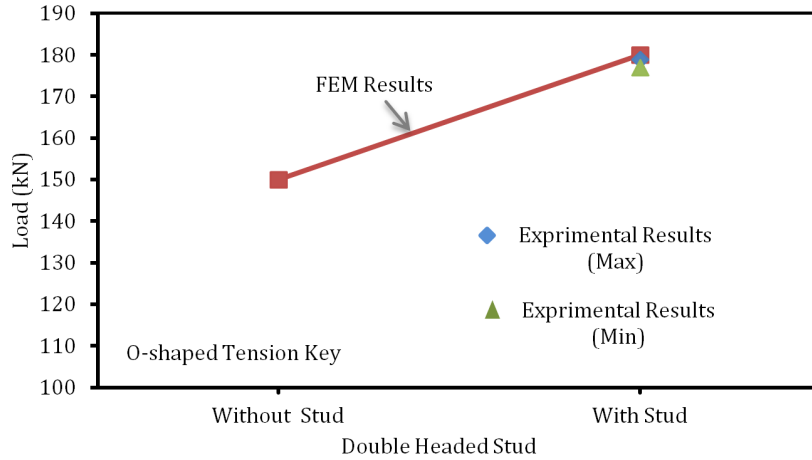


Figure 7-37: Influence of DHS on the PPL of composite connection with O-Shaped tension key.

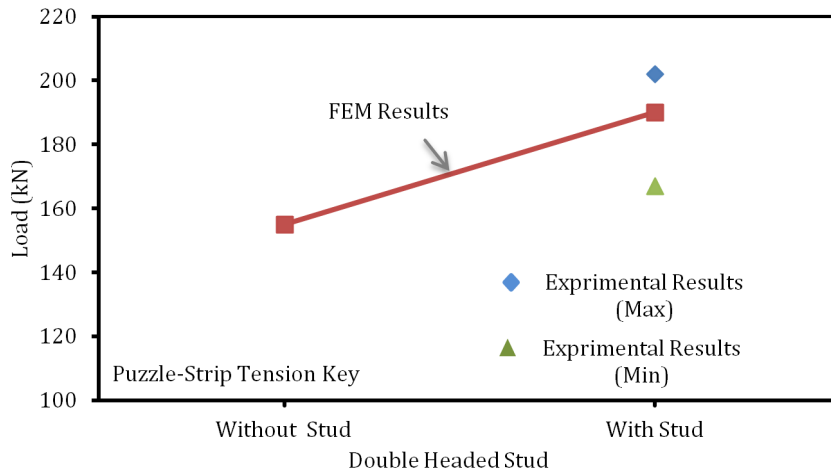


Figure 7-38: Influence of DHS on the PPL of the composite connection with puzzle-strip tension key.

7.10.1.7 Influence of Concrete Generation

The influence on the PPL of the composite connections with Ω -shaped tension key and embedded length of 150 mm, from three different concrete types, i.e., normal strength concrete (NSC), fiber reinforced concrete (FRC), and UHPFRC are summarized in the Figure 7-39. The FEM results indicate that compared to composite connections with NSC, 36% and 155% improvement in the PPL was respectively found for those made of FRC and UHPFRC material. This significant enhancement in the PPL is attributed to the bridging action of the steel fibers across

the adjacent crack surfaces in FRC and UHPFRC material. This phenomenon is more pronounced in the specimens with the UHPFRC material, as the higher bond between the short steel fibers and the matrix leads to higher mechanical properties of the UHPFRC material and eventually results in more enhanced response of the connection subjected to pull-out load.

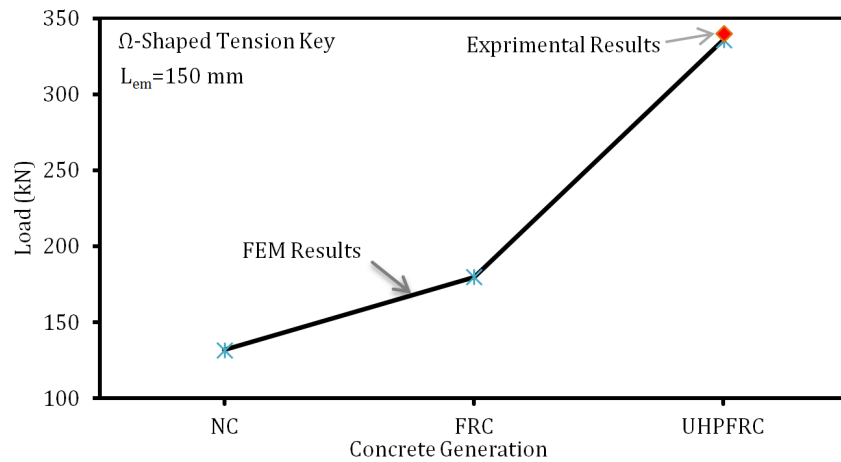


Figure 7-39: Influence of concrete generation on load bearing capacity of composite connection with Ω -shaped tension key.

7.10.1.8 Influence of Multiple Tension Key

In order to extend the range of application of the composite connection under a higher level of pull-out loading, the response of the connection system with multiple holes is investigated through a FEM analysis. A concrete beam size with $L \times W \times H = 880 \times 300 \times 500$ mm was considered for this model. The embedded plate thickness was 25 mm. A combination of Ω -shaped and O-shaped tension key with a hole diameter of 70 mm, as shown in Figure 7-40, was used.

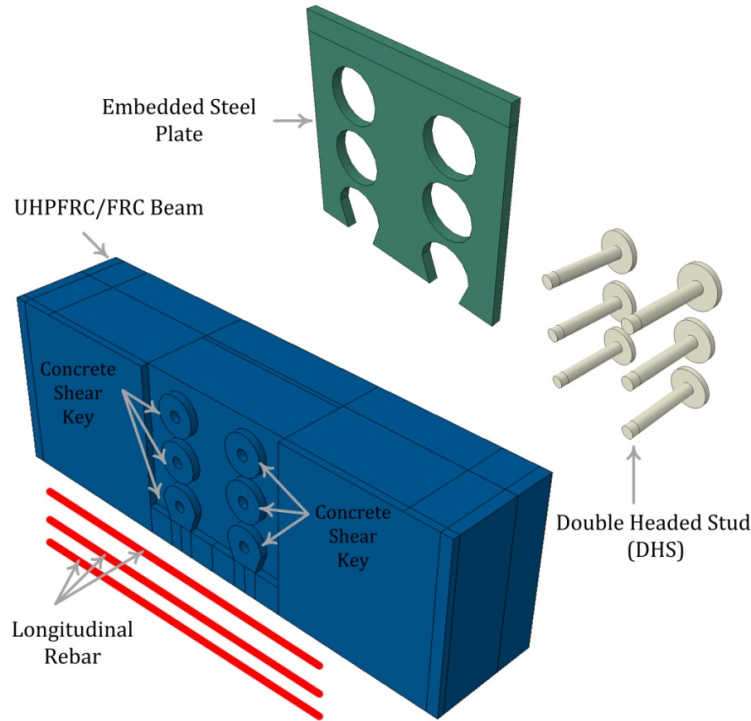


Figure 7-40: Overall geometry of connection with multiple tension keys.

Embedded plate along the beam axis: The configuration of meshed FEM model is given in Figure 7-41 and 7-42. The results of FEM analysis indicated that compared to the composite connection with single tension key, 172% and 284% improvement in the PPL were found for connection system with two and three tension key. Similar analysis was completed for the composite connection made of FRC material. A significantly lower PPL was found for this connection system, as indicated in Figure 7-43. This is mainly because the concrete pin experiences a high shear and bearing stress under the pull-out load and the capacities of the FRC concrete pin (CP) are significantly lower than that made of UHPFRC material and this would directly influence the load carrying capacity of the connection subjected to pull-out loading. According to the FEM results, a higher initial and post-cracking stiffness was found for the connection system made of UHPFRC material over that with FRC material. This is most probably attributed to improved mechanical interlock between the UHPFRC concrete pin and the embedded steel plate which prevent the early concrete crushing in front of the inclined sides of the tension key.

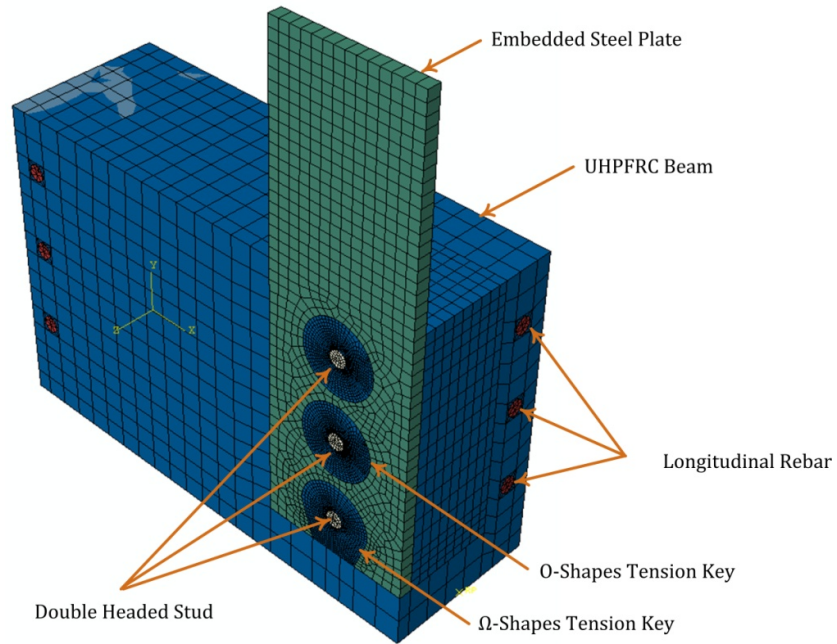


Figure 7-41: Geometry of a quarter of the composite connection with multiple tension key.

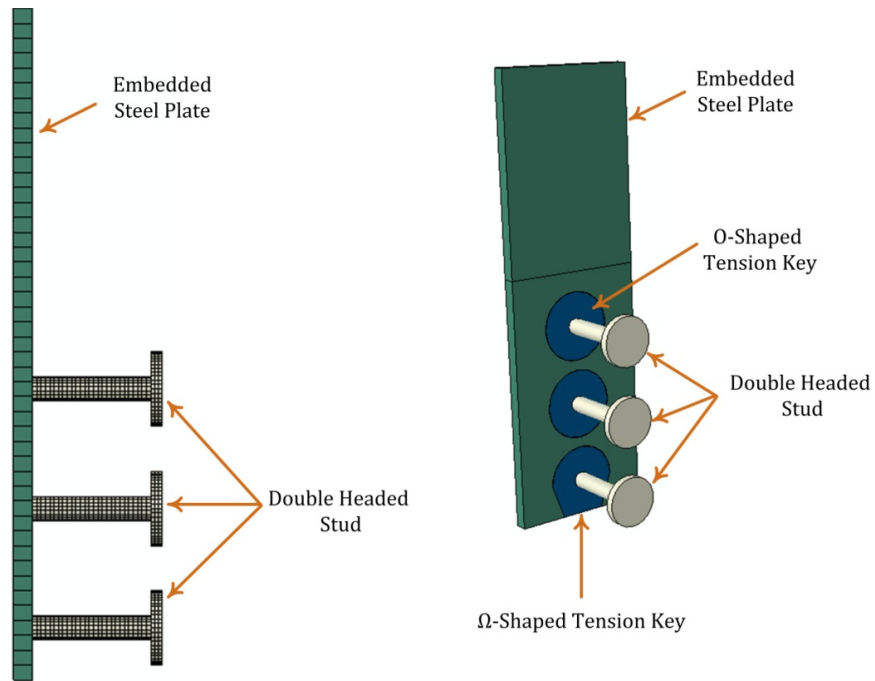


Figure 7-42: Overall configuration of the embedded steel plate, concrete pin, and double headed stud (DHS).

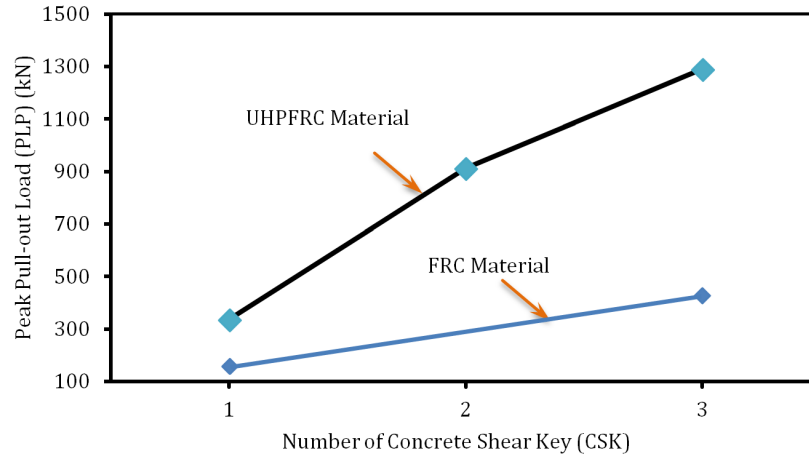


Figure 7-43: Influence of multiple tension keys on the PPL of connection system with of Ω -shaped tension key.

Embedded plate perpendicular to beam axis: In some applications, the use of embedded plate, which is aligned along the perpendicular direction of the beam facilitates the connection detailing between the embedded steel plate and the concrete beam, as shown in Figure 7-44. The influences of the plate direction on the PPL of the composite connections constructed with the UHPFRC material and FRC material are given in the Figure 7-45. Compared to connection system with the embedded plate parallel to the longitudinal axis of the beam, the use of perpendicular configuration resulted in 19% improvement in the PPL. This significant improvement is mainly related to the higher confinement that this configuration provided to the embedded steel plate.

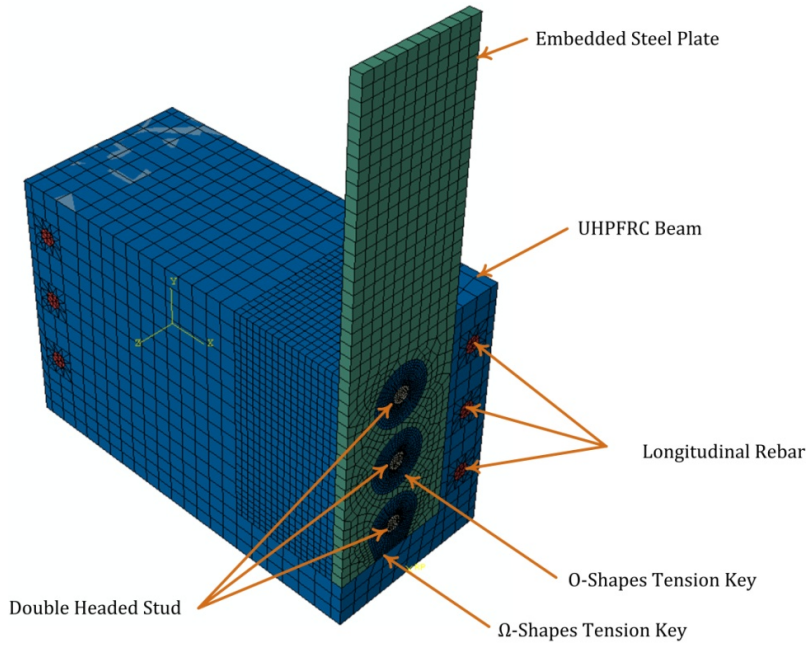


Figure 7-44: Geometry of the FEM model with embedded steel plate oriented perpendicular to the beam axis.

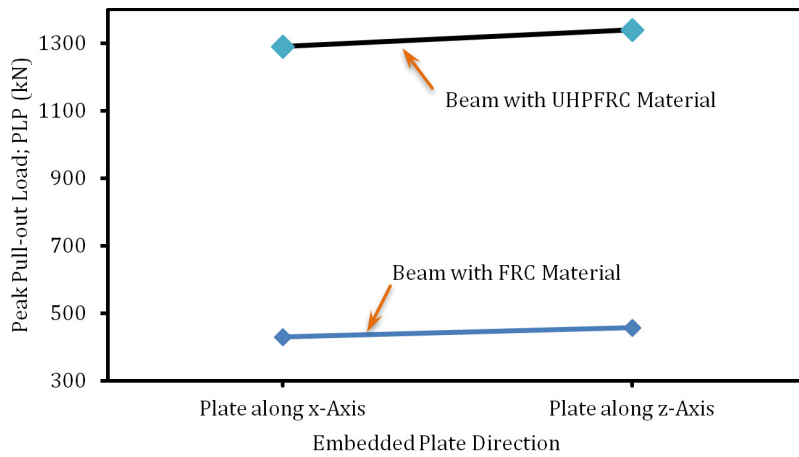


Figure 7-45: Influence of the plate direction on the PPL.

7.10.2 Composite Connection under Push-out Loading

7.10.2.1 Verification of FEM model

A series of FEM analysis were completed to study the influence on the push-out response of the composite connection systems from various parameters. The finite element model was first validated against the experimental results published by Hegger et al. (2009). The schematic of the connection system under the push-out loading is presented in Figure 7-46, which includes a 20 mm thick embedded steel plate in the UHPFRC beam with length x width x height = 500 x 500 x 100 mm.

The results of the FEM analysis along with the experimental results are shown in the Figure 7-47. In general, a good agreement between the experimental and FEM results, including the linear-elastic, post-cracking, and softening stage was observed. The influence of the concrete cover depths on the PPOL of the connection system is presented in the Figure 7-48. According to FEM results, the increase in the cover depth from 20 to 30 mm led to 22% improvement in the PPOL.

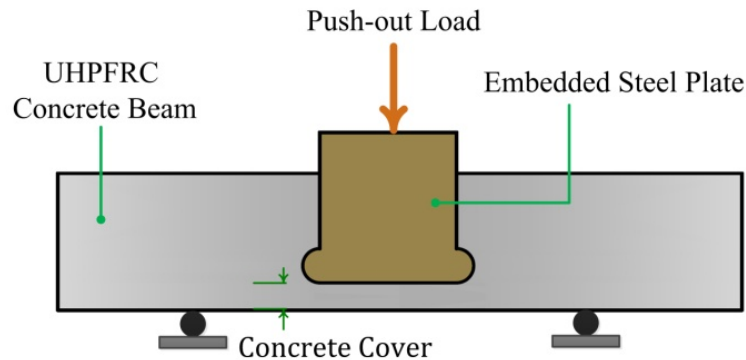


Figure 7-46: Geometry of the push-out test from Hegger et al. (2009).

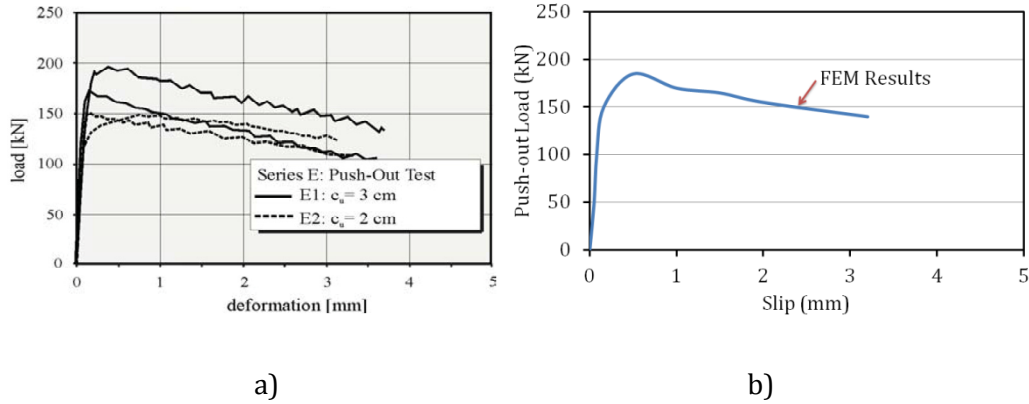


Figure 7-47: Variation of push-out test against the slip between the steel plate and concrete beam, a) Experimental results (Hegger et al. 2009), b) FEM results.

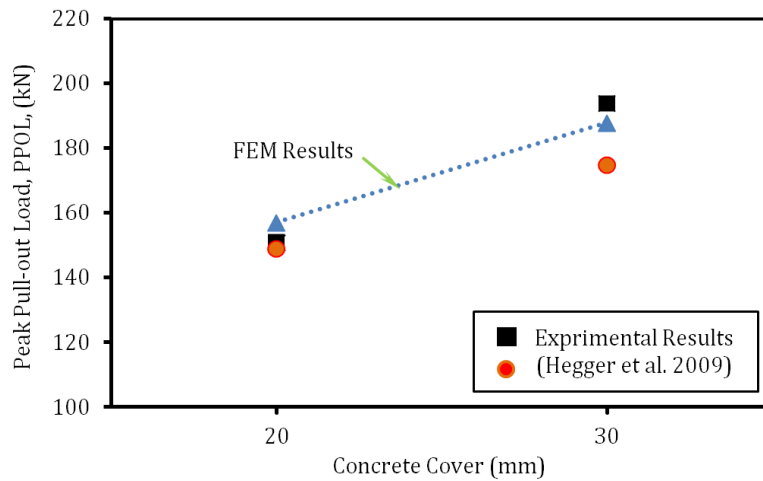


Figure 7-48: Variation of peak push-out load against the concrete cover thicknesses.

7.10.2.2 Influence of Double-Headed Stud

The validated FEM model was used to study the influence of a series of parameters on the push-out response of the composite connections with Ω -shaped hole. The concrete beams with length x width of 550 x 200 mm was used for the FEM modeling. The length and thickness of the embedded steel plate were 100 and 20 mm, respectively. The overall view of the connection system is presented in Figure 7-49.

In order to investigate the effect of DHS on the push-out response of the composite connections constructed with the UHPFRC and FRC material, a FEM model was

developed in the ABAQUS/Explicit and the results are summarized in the Figure 7-50. The addition of DHS to connection system was resulted in an average 22% and 15% increase in the peak push-out load of the connection system with UHPFRC and FRC material respectively. In addition, a significant improvement in the post-cracking and softening stage of the composite connection with DHS was found over those without DHS. This is most probably because the DHS provides a lateral confinement to the expansion of the concrete in transverse direction and prevent the formation of a longitudinal crack parallel to bottom side of embedded steel plate. This would, in turn, lead to higher mechanical interlock between the embedded steel plate and the concrete beam.

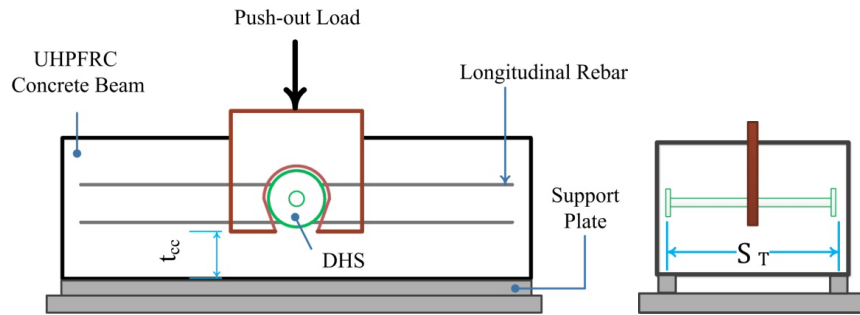


Figure 7-49: Typical layout of the FEM push-out model.

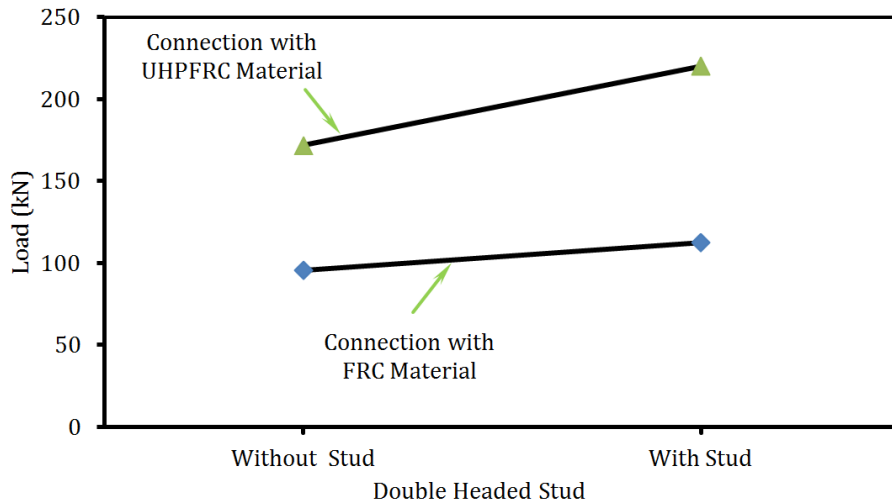


Figure 7-50: Influence of DHS and concrete generation on the peak push-out load of composite connection with Ω -shaped tension key.

7.10.2.3 Influence of Concrete Cover Depth

The mechanical properties of the UHPFRC material allows for more slender and thinner sections to be designed, which the overall strength is maintained or even improved. The influence of the concrete cover depth (t_{cc}) on the peak push-out load (PPOL) of the composite connection systems with Ω -shaped hole are given in Figure 7-51. Five different cover depth, i.e. $t=20, 30, 40,$ and 50 mm were used in the parametric study. In general, connection system showed a ductile response with a stable load-slip response under the push-out load. This is mainly attributed to the fiber bridging effect in the UHPFRC material which retards the formation and propagation of the cracks in the concrete beam. The results of the FEM analysis show that the increase in the cover thickness from 20 mm to 30, 40, and 50 mm results in 24, 38, and 42% improvement in the PPOL of connection system. This improvement is most likely attributed to the higher punching shear strength provided by the thicker concrete cover at the bottom part of the specimens. A less degradation rate after the PPOL was observed for the connection systems with larger concrete cover which leads to higher ductility response.

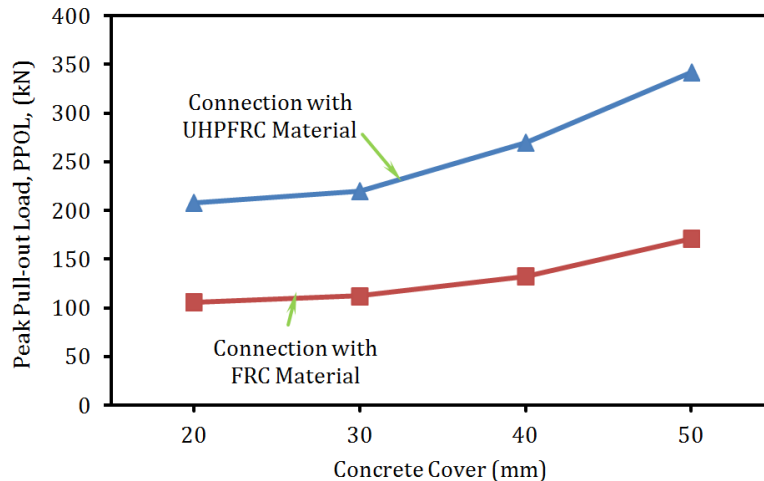


Figure 7-51: Influence of concrete cover depth on the peak push-out load of the composite connections with UHPFRC and FRC material.

7.10.2.4 Influence of Concrete Generation

The influences on the PPOL of the composite connections with Ω -shaped tension key from two different concrete generations, i.e. UHPFRC and FRC, are summarized in Figure 7-51. The FEM results indicate that compared to connection specimens

constructed with the FRC material, the use of UHPFRC with 2% volume-fraction of short steel fibers resulted in 55, 56, 53, and 49% enhancement in the PPOL of connections with cover depth of 20, 30, 40, and 50 mm respectively. The higher load carrying capacity in the connection systems with UHPFRC material is mainly attributed to the higher capacity of the UHPFRC material subjected to high localized punching shear stresses, as compared with those constructed with FRC material.

7.10.2.5 Influence of Fiber Volume Fraction (V_f)

The influences of UHPFRC material with three different fiber volume-fractions, i.e., $V_f = 0\%$, 2%, and 4%, on the peak push-out load of the composite connections with Ω -shaped tension key are summarized in Figure 7-52. The FEM results indicated that compared to composite connections system with plain UHPFRC material, $V_f = 0\%$, the use of 2% and 4% fiber increased the peak push-out load (PPOL) of composite connection by 156% and 219%. In addition, unlike the composite connections constructed with plain UHPFRC material, a significant improvement in the load-slip response was observed for the beam constructed with higher volume-fractions if randomly distributed short steel fibers. This significant enhancement in the load carrying capacity of the composite connection is achieved through the contribution of steel fibers, which restrain the growth of crackes in the concrete.

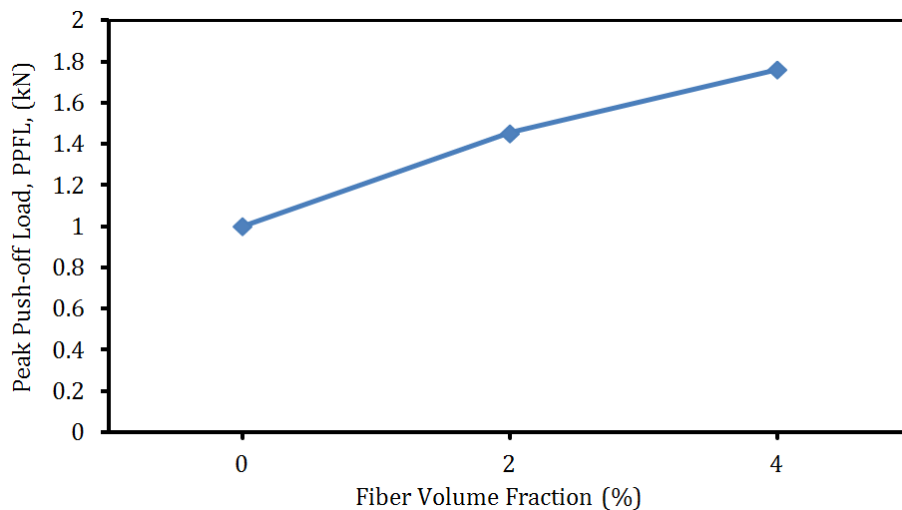


Figure 7-52: Influence of fiber volume-fraction on the PPOL of composite connection with embedded length of 100 mm.

Chapter 8

8 Summary, Conclusion, and Recommendation

8.1 Summary

This research presented herein focused on the: 1) influences of the specimen size and fiber content on the mechanical properties of an ultra-high performance fiber reinforced concrete (UHPFRC) in compression, flexure, flexural-tensile, equivalent tensile strength, and shear; 2) pull-out and push-out response of the composite connections constructed with the embedded steel plate in the UHPFRC and FRC beam. To fulfill the objectives of this research, experimental and numerical works were conducted in both material and structural level.

During the first part of the research, a unique UHPFRC material, suitable for in-situ casting and incorporating 0 to 5% volume-fraction of short steel fibers was developed at the Concrete Research Lab at the University of Alberta using locally available materials. The mechanical properties of the UHPFRC material in compression was developed using cylinder and cube specimens over a size range of 3 and 2 respectively. Un-notched flexural prisms of four different sizes, 50 x 50 x 150 mm, 100 x 100 x 300 mm, 150 x 150 x 450 mm and 200 x 200 x 600 mm, were tested according to the ASTM C1609-10 Standard. A back-analysis technique, originally proposed by the AFGC (2006) standard was used to derive the equivalent tensile mechanical properties relative to the crack mouth opening displacement. Direct shear tests were performed on the prism specimens over a size range of two to establish the influence of specimen size and fiber content on the mechanical properties of UHPFRC material in shear. The measured test results from flexural and shear tests were further analyzed to evaluate the influence of fiber content and

specimen size on the flexural and shear toughness. The digital image correlation (DIC) technique was used during the ASTM C1609-10 flexural tests as a non-contact method to provide continuous data on the prism behaviour and performance without the need for additional instrumentation. The images recorded through the digital image correlation (DIC) system were post-processed to extract the deflections and crack widths. In addition to the mechanical properties outlined above, the influence of UHPFRC mix composition and energy imparted by the mixer on its rheological properties was studied.

The pull-out responses of 42 composite connections constructed with embedded steel plate in the concrete beam were studied in the second phase of the current research. Of these specimens, 32 were constructed with UHPFRC material incorporating 0%, 2%, and 4% volume-fraction of short steel fibers and the rest were constructed with FRC material with 1% of double-hooked fibers to study the influence of the concrete generation and fiber volume-fraction on the pull-out response of the connections. The other variables included the shape of the holes (Ω -shaped, O-shaped, and puzzle strip-shaped), size of the holes cut through the embedded steel plate, embedded plate thickness ($t = 8 - 20 \text{ mm}$), embedment length of plate. The specimens were loaded to failure using displacement control in a MTS 1000 machine. The influence from the connections components on the pull-out load-slip response, failure mode, crack growth pattern, and crack width in concrete beam for each group of pull-out specimens are investigated. The DIC system along with additional physical instrumentation was used to measure the slip and crack width. All the connection specimens were tested in MTS 1000 machine under displacement controlled loading until failure, where failure was defined as a point where the pull-out force on the descending branch of the load-slip relationship is dropped below 85% of the peak pull-out load.

Comparisons between ABAQUS/Explicit and the experimental results were completed for several connection specimens under pull-out loading and it was found that the FEM model is capable of predicting the overall performance of the connection system. Using the validated analytical models, a parametric study was completed to investigate the influence on the composite connections response from a series of parameters including the geometry and shape of the holes cut through

the embedded steel plate, embedded plate thickness, concrete generation (NSC, FRC, and UHPFRC material), and tensile strength of UHPFRC.

8.2 Conclusion

The following conclusions are based on the research presented in this report.

8.2.1 Mechanical Properties of UHPFRC material

8.2.1.1 Compression Response

- A higher silica fume to binder (SF/B) ratio increased the peak compressive strength and the rate of strength gain at early ages. A typical SF/B ratio of 0.26 was adopted in this study.
- The addition of 2 to 5% randomly distributed short steel fibers to the UHPFRC matrix led to 3.7% to 25% improvements in the compressive strength compared to mixes without fibers.
- The experimental results demonstrated that larger cube and cylinder specimens tend to show lower compressive strength by 15%. The cube samples consistently have higher strength than the cylinder samples of the same maximum cross-section dimensions.
- The addition of 3 ml/kg of hydration stabilizer admixture (SA) to UHPFRC mix was found to delay the set time from 8 hours in the mix without SA to 24 hours for mix with SA. Compared to mix without SA, lower rate of strength development was found for mix with SA. Similar compressive strength was found for both mixes after 2 months from casting.
- The Weibull cumulative function was successfully employed to predict the time development of compressive strength of the UHPFRC material with and without fiber.
- The mixer peak energy demand increased linearly with an increase in the steel fiber volume fraction from 0 to 5%.

8.2.1.2 Flexural Response

- Compared to the plain mix, an increase in V_f from 2 to 5% resulted in an almost linear increase in the flexural peak load equivalent strength (PLES) of PF-50 specimens from 40 to 107%.
- While consolidation did not substantially enhance the flexural peak load equivalent strength (PLES) of plain UHPFRC, an average 37% improvement in the PLES of vibrated UHPFRC mix with $V_f = 2-5\%$ was noted compared to the non-vibrated mixes with similar V_f .
- The clear size effect in first crack strength (FCS) and PLES is visible. The FCS was decreased by an average value of 12%, 21%, and 31%, as the specimen size was increased from 50 mm to 100 mm, 150 mm and 200 mm respectively. Similar results were observed for PLES, where an average decrease of 15%, 24%, and 33% in PLES was noted for the PF-100, PF-150, PF-200 compared to PF-50 prism specimens.
- The first crack strength (FCS) at the ages of 135 days was found to be 9%, 7%, and 15% higher than at the 35 days for the mixes with $V_f = 0\%$, 2%, and 4% respectively. Similar results were observed for the PLES, where the 135 days PLES was 11%, 13%, and 9% higher than at the age of 35 days for the mixes with $V_f = 0\%$, 2%, and 4% respectively. Additional flexural testing was completed at the age of two years for plain mix and 21% and 23% improvement in FCS and PLES was found over those at the 35 days.

8.2.1.3 Flexural Toughness Factor (FTF)

- While the plain mix exhibited a very poor FTF, the addition of 2 to 5% fiber was found to increase the FTF of PF-50 up to 80%.
- Compared to UHPFRC mix with $V_f = 2\%$, the use of 4% volume-fraction of randomly distributed short steel fibers was found to increase the FTF by an average of 53%, 57%, 65%, and 63% for PF-50, PF-100, PF-150, PF-200 prism specimens.
- The size effect on FTF is evident. Larger prism samples tend to show lower FTF for both mixes with $V_f = 2\%$ and 4%. For mix with $V_f = 2\%$, the FTF was

decreased by an average value of 16, 27, and 36%, as the specimen size was increased from 50 mm to 100 mm, 150 mm and 200 mm respectively. Similar results were observed for $V_f = 4\%$ mix, where the FTF was decreased by an average value of 14%, 22%, and 33% for PF-100, PF-150, PF-200 samples respectively compared to PF-50 prism specimens.

- The FTF of vibrated mixes was found to be significantly higher than non-vibrated mix. This phenomenon was more pronounced for mixes with higher fiber contents.

8.2.1.4 Direct Shear Responses

- The addition of $V_f = 2\%$, 3%, 4%, and 5% to plain mix was found to increase the SSF by average values of 121%, 174%, 277%, 279% respectively. The non-vibrated mix displayed a similar trend in which the SSF was an average 17% lower than the vibrated one.
- Compared to the plain UHPFRC mix, the use of vibrated mix with $V_f = 2-5\%$, resulted in an 150 to 260% increase in shear strength. The non-vibrated mix displayed a similar trend in which the k_v was an average of 16% lower than the vibrated one.
- Decreases of 25 and 43% in the shear strength were respectively noted for the mixes with $V_f = 2$ and 4% as the specimen sizes doubled. These results indicate that the influence of specimen size on the shear strength increases as the V_f changes from 2 to 4%.

8.2.1.5 Shear Toughness Factor (STF)

- While no significant improvement in the STF was observed for the non-vibrated mix with a change in fiber contents, increases of 59, 79, and 91% in STF were noted for the vibrated mix containing 3, 4, and 5% fiber as compared to the mix with 2% volume-fraction of fiber. The improvement is attributed to the large number of fibers in the fracture zone, which significantly restrains crack propagation in fracture surfaces.
- A 160% improvement in STF was noted for vibrated mix with 2% fiber over the non-vibrated one. Higher improvements were noted for vibrated mix

with 3-5% fiber over the similar non-vibrated mix where an average increase of 235% in STF was obtained.

- The influence of specimen size on the STF was studied and a clear size effect was observed. The test results showed that the STF decreased by 27 and 64% for vibrated mix with $V_f = 2$ and 4% respectively as the specimen size doubled.
- The influence of prism height on the STF increases as the fiber volume-fraction increased from 0 to 4%. Compared to PS-50, the STF of PS-100 increases slightly for change in V_f from 2 to 4%.

8.2.1.6 Equivalent Tensile Strength

- The results of back analysis show that the peak equivalent tensile strength (PETS) was found to be significantly lower than the PLES proposed by ASTM C1018 standard. This phenomenon is mainly attributed to the size effect.
- An almost linear increase of 22%, 64%, 76%, and 116% in PETS of PF-50 was observed after the addition 2%, 3%, 4%, and 5% of steel fibers to UHPFRC matrix. This is because more optimally oriented fibers are present in fracture zone of mixes with higher V_f .
- The results of back analysis on the PF-50 specimens indicated that the PETS of non-vibrated mixes were 27%, 59%, 50%, and 30% lower than the PETS of vibrated mixes with $V_f = 2\%$, 3%, 4%, and 5% respectively.
- The increase in fiber contents from $V_f = 0\%$ to $V_f = 2\%$ and 4% respectively resulted in 11% and 55% improvement in the PETS.
- A size effect was apparent, where an almost linear decrease in the PETS with an increase in specimen height was found. Higher rate of decrease in the PETS was observed for mixes with higher fiber content.
- Compared to mixes with $V_f = 2\%$, the CMOD of mixes with $V_f = 4\%$ at the PETS was found to be 18%, 55%, 62%, and 31% higher for PF-50, PF-100, PF-150, and PF-200, respectively.
- Average values of $\nu = CMOD/\delta$ of 1.24, 1.48, 1.53, and 1.52 were found for PF-50, PF-100, PF-150, and PF-200, respectively.

8.2.2 Composite Connection

Based on the experimental test results and numerical modelings, the following conclusions can be drawn:

- The increase in the Ω -shaped tension key size (hole diameter) from 50 mm to 70 mm and 90 mm was resulted in 25% and 29% improvements in the PPL of the connection systems. This is mainly attributed to the increase in the area of concrete pin, which directly influence the response of concrete pin subjected to pull-out-induced shear. Similar experimental tests were completed for the circular-shaped connection and no improvement in the PPL was found, as the tension key size increased from 50 mm to 70 mm. The specimens with larger hole size tends to show a substantially more stable load-slip response during the post-cracking and softening stage.
- Compared to the composite connection systems constructed with Ω -shaped hole and 8 mm plate thickness, the use of 10, 12, 16, and 20 mm steel plate increased the PPL by 2%, 16%, 24%, and 15% respectively. This is mainly attributed to the lower bearing stress at the interface between the concrete pin and the embedded steel plate, which prevent the concrete crushing. Similar results were found for the connection systems with the puzzle-strip and O-shaped connection, where respectively 14% and 17% improvement in the PPL was found as the plate thickness was increased from 10 to 16 mm.
- An average 55% improvement in the PPL of the composite connection was found, as the embedded length of steel plate was increased from 100 mm to 150 mm. This is mainly attributed to the changes in the tensile stress distribution over the surface of the potential failure path.
- The increase in the volume-fractions of randomly distributed short steel fiber from 0% to 2% and 4% was respectively resulted in 130% and 187% improvements in the peak pull-out load of the connection systems with Ω -shaped hole and embedded length of 100 mm. This significant improvement is mainly attributed to the fiber bridging effect, which shift failure mode from a brittle concrete fracture to a ductile yielding of UHPFRC materials.

This phenomenon retards the uncontrolled propagation of the cracks in the concrete beam and prevents sudden failure in the pull-out response. Higher ductility factor was observed for connection systems with higher fiber contents, make this system suitable for applications where the connection system experience a cyclic loading. A similar trend was observed for the composite connections under pull-out loading, where a linear increase in the peak push-out load was observed, as the fiber volume-fraction increased.

- The scatter of the load displacement curves of specimens with plain UHPFRC ($V_f = 0\%$) is considerably larger than in specimens made of UHPFRC material with higher fiber contents.
- The tests results indicated that compared to composite connection system with Ω -shaped hole and FRC material, the use of UHPFRC significantly increased the maximum peak pull-out load of the connection system by 114% and 54% for 10 mm and 16 mm plate. Similar results were found for the connection systems with O-shaped hole, where the use of UHPFRC material in the connection systems with 10 mm and 16 mm plate resulted in 62% and 123% improvements in the PPL over the similar connection systems with FRC material. This significant improvement is attributed to the unique pseudo-strain hardening response of the UHPFRC material in tension, compression, and shear. Similar results were found for the connection systems with puzzle-strip hole, where the use of UHPFRC material in leads to 120% improvement in the maximum load carrying capacity of the connection system.
- Compared to connection specimens without double headed stud (DHS), a 12% improvement in the peak pull-out load was found for those with DHS. In addition, the use of DHS significantly improved the pre-peak and post peak response of the composite connection, which leads to a significant improvement in the connection ductility factor. This is because the DHS considerably enhances the lateral confinement to the concrete pin and embedded steel plate and prevents any sudden crack growth around the concrete pin. A similar trend was observed for the connection specimens subjected to push-out loading, where a 22% improvement in the connection system with DHS was observed over that without DHS.

- Compared to traditional FRC material, the use of UHPFRC in the composite connection systems leads to an increased stiffness under the service conditions, i.e. the deformations remain smaller for given imposed loads. Moreover, according to DIC test results, the use of UHPFRC material in connection system was found to limit the crack widths and spacing and retard the formation of localized macrocracks.
- The experimental results show that composite connections with UHPFRC material exhibit a higher displacement capacity and ductility factor, which leads to a higher energy absorption capacity compared with connections with FRC material.
- The extremely low crack width at the linear-elastic stage of the connection specimens offers a significant improvement in the permeability of the connection system under the service conditions by preventing the ingress of detrimental substances.
- According to DIC test results, the use of randomly distributed short steel fibers in the connection systems was found to change the cracking mechanism from a macrocrack to several microcracks in the high tensile area in the beam. This phenomenon leads to a considerable enhancement in the permeability of the connection system.
- A wide range of experimental tests were completed on the composite connection under pure tension. The efficiency and accuracy of the FEM model were evaluated through the comparisons between a wide range of FEM and experimental results. The FEM model was found to be well capable of predicting the load-slip behaviour with good agreement between the PPL for different composite connection configuration made of UHPFRC and FRC material. The FEM model was used to expand the pool of experimental results completed in the current research and thus to investigate the effect of several parameters on the response of composite connection.
- In contrast to connection system with plain UHPFRC material, no fluctuation or abrupt change of slope in the pull-out or push-out load-slip response was observed for the connection systems with FRC and UHPFRC material incorporating moderate volume fraction of short steel fibers.

- The influence on the connection system ductility from several parameters was studied. According to test results, compared to connection system with FRC material, the use of UHPFRC with 2% volume-fraction of short steel fibers was resulted in 56% and 43% improvements in the ductility for the connection system with Puzzle-strip and Circular Shape tension key respectively. A more significant improvement was found for the connection system with UHPFRC material and Ω -shaped tension key, where the use of UHPFRC material resulted in an average 232% improvement in the connection ductility. This improvement is mainly associated to the fiber bridging effect, which retard the crack formation and propagation in the concrete beam.
- The test result indicated that the use of DHS leads to 137% improvement in the connection system ductility. This is mainly due to higher confinement provided to the concrete pin by the DHS, which prevent the premature failure at the interface between the steel tension key and the concrete pin. The results of analysis showed that the connection systems with thinner steel plate tends to present a higher ductility factor, which is most likely attributed to the lower degradation rate of the connection system after the peak pull-out load was reached.
- The results of parametric analysis showed that the increase in the cover depth from 20 mm to 50 mm was resulted in a higher peak push-out load.

8.3 Ongoing and Future Research

The current study has helped to further expand the knowledge base regarding the behaviour of UHPFRC material in compression, flexure, flexural-tensile, equivalent tensile, and shear strength. In addition the response of composite connections constructed with UHPFRC and FRC material was studied through experimental and numerical investigations. Based on the findings from this research project, several potential topics for future research are listed below:

- The use of short straight steel fibers is in not the only option available for the UHPFRC material. A hybrid fiber system with a combination of short

steel fibers ($l_f = 6-13$ mm) and long steel fibers ($l_f = 30-60$ mm) can be used to further improve the mechanical properties of the UHPFRC material, particularly in tension.

- This research program mainly focused on the mechanical properties of the UHPFRC material. Additional research into the long term stability behaviours of UHPFRC material, i.e., shrinkage, creep, permeability, freeze and thaw cycles is required.
- Further investigations are essential to investigate the influence of specimen size on the orientation pattern of randomly distributed short steel fiber in the UHPFRC material.
- Develop a full-scale, optimized hybrid bridge superstructure system using the UHPFRC flanges, high-performance corrugated steel web, and axial prestressing. This bridge girder should best utilize the tensile and compressive capacities of the UHPFRC material, while also enhancing the design life of the bridge as a whole by eliminating many of the less durable components of a normal bridge.
- Study the influence of fiber orientation on the capacity and ductility of the connection systems under different loading.
- Investigate the influence of the directly embedded connection system with different hole configurations cut through the plate on an I-shaped composite girder constructed with UHPFRC flanges and corrugated steel web.
- Explore the flexural and shear response of full-scale composite girders with opening in the web.

List of References

- AASHTO T259 (2000). Standard Method of Test for Resistance of Concrete to Chloride Ion Penetration. American Association of State Highway and Transportation Officials, Standard Specifications for Transportation Materials and Methods of Sampling and Testing, Washington, DC.
- Abramski M., Friedrich T., Kurz W., Schnell J. (2008). New prestressed composite slab system for buildings with multiple HVACR installations. Composite Construction in Steel and Concrete Four: Proceedings of the 2008 Conference, July 20-24, Devil's Thumb Ranch, Tabernash, Colorado.
- Abramski, M., Friedrich, T.h., Kurz, W., Schnell, J. (2010). Tragwirkung von Betondübeln für Sandwich-Verbunddecken mit großen Stegöffnungen. Stahlbau 79, 4: 248-258.
- Acker, P., and Behloul M. (2004). Ductal Technology: A Large Spectrum of Properties, A Wide Range of Applications. Proceedings of the International Symposium on Ultra High Performance Concrete, Kassel, Germany, September 13–15, pp. 11–23.
- Acker, P. (2004). Why Does Ultrahigh-Performance Concrete (UHPC) Exhibit Such a Low Shrinkage and Such a Low Creep? Autogenous Deformation of Concrete, ACI SP-220-10, pp. 141–154, American Concrete Institute, Farmington, MI.
- ACI 209R-92 (1994). Prediction of Creep, Shrinkage, and Temperature Effects in Concrete Structures. ACI Manual of Concrete Practice Part 1: Materials and General Properties of Concrete, Detroit, MI, 47 pp.
- ACI 318 (2005). Building Code Requirements for Structural Concrete. Farmington Hills, MI, 430 pp.
- Association Française de Génie Civil (2002). Ultra High Performance Fibre-Reinforced Concretes—Interim Recommendations, Paris, France.
- AFGC/SETRA (2002): Bétons fibrés à ultra-hautes performances. Recommandations provisoires. (Ultra high performance fibre-reinforced concretes). Association Française de Génie Civil, SETRA, Bagneux Cedex. Janvier, pp.1-152.
- Alford N. McN., Birchall J. D. (1985). The properties and potential applications of Macro-Defect-Free Cement. Symposium on very high strength cement-based materials, Ed. by J. F. Young, Materials Research Society symposia proceedings, Pittsburgh, USA, (42) 265-276.

- ASTM C39 (1994). Standard Test Method for Compressive Strength of Cylindrical Concrete Specimens. American Society for Testing and Materials Standard Practice C39, Philadelphia, PA.
- ASTM C39/C39M-09a (2009). Standard test method for compressive strength of cylindrical concrete specimens. West Conshohocken, PA: ASTM International.
- ASTM C78 (1994). Standard Test Method for Flexural Strength of Concrete (Using Simple Beam with Third-Point Loading). American Society for Testing and Materials Standard Practice C78, Philadelphia, PA.
- ASTM C109 (1998). Standard Test Method for Compressive Strength of Hydraulic Cement Mortars (Using 2-inch or [50-mm] Cube Specimens). American Society for Testing and Materials Standard Practice C109, Philadelphia, PA.
- ASTM C230. (1998). Standard Specification for Flow Table for Use in Tests of Hydraulic Cement. American Society for Testing and Materials Standard Practice C230, Philadelphia, PA.
- ASTM C469. (1994). Standard Test Method for Static Modulus of Elasticity and Poisson's Ratio of Concrete in Compression. American Society for Testing and Materials Standard Practice C469, Philadelphia, PA.
- ASTM C512. (1987). Standard Test Method for Creep of Concrete in Compression. American Society for Testing and Materials Standard Practice C512, Philadelphia, PA.
- ASTM C666. (1997). Standard Test Method for Resistance of Concrete to Rapid Freezing and Thawing. American Society for Testing and Materials Standard Practice C666, Philadelphia, PA.
- ASTM C1018. (1997). Standard Test Method for Flexural Toughness and First-Crack Strength of Fiber-Reinforced Concrete (Using Beam With Third-Point Loading), American Society for Testing and Materials Standard Practice C1018, Philadelphia, PA.
- ASTM C1437 (2001). Standard Test Method for Flow of Hydraulic Cement Mortar. American Society for Testing and Materials Standard Practice C1437, Philadelphia, PA.
- ASTM C1609/C1609M (2010). Standard Test Method for Flexural Performance of Fiber-Reinforced Concrete (Using Beam With Third-Point Loading), ASTM International, West Conshohocken, PA, USA ,9pp.
- An, L. & Cederwall, K. (1996). Push-out tests on studs in high strength and normal strength concrete, *Journal of Constructional Steel Research*, (36)15-29

- Bache H. H. (1987). Introduction to Compact Reinforced Composite, Nordic concrete research, (6) 19-33.
- Behloul, M., K.C. Lee, and D. Etienne (2004). Seonyu Ductal® Footbridge. In Concrete Structures: The Challenge of Creativity, FIB Symposium 2004 Proceedings, April 26–28, Avignon, France: Association Française de Génie Civil, 6 pp.
- Bierwagen, D., and McDonald, N. (2005). Ultra-High Performance Concrete Highway Bridge. In: Proceedings of Precast/Prestressed Concrete Institute's National Bridge Conference. Palm Springs, CA.
- Billington, S. L., and Yoon, J. K. (2004). Cyclic Response of Precast Bridge Columns with Ductile Fiber-Reinforced Concrete, Journal of Bridge Engineering, ASCE, 9(4), 353-363.
- Boulekbache, B., Hamrat M., Chemrouk M., Amziane S. (2010). Flowability of fibre-reinforced concrete and its effect on the mechanical properties of the material. Construction and Building Materials. 24 (9), 1664-1671.
- Burger S. (2009). Untersuchungen zum Ermüdungsverhalten von Betondübeln im Verbundbau. PhD dissertation, Germany.
- Carpinteri, A., and Chiaia B. (2002). Embrittlement and Decrease of Apparent Strength in Large-Sized Concrete Structures, Sadhana, India Academy of Sciences, Bangalore, India, 27 (4), 425–448.
- Chanvillard, G., and Rigaud S. (2003). Complete Characterization of Tensile Properties of Ductal® UHPFRC According to the French Recommendations, Proceedings of the 4th International RILEM Workshop on High Performance Fiber Reinforced Cement Composites (HPFRCC4), Ann Arbor, MI, June 15–18, 14 pp.
- CEB-FIP (1999). Structural Concrete: text book on behaviour, design and performance, Updated knowledge of the CEB/FIP Model Code 1990 FIB publication.
- Cohen, M.D., Goldman, A., and Chen, W.F. (1994). The role of silica fume in mortar: transition zone versus bulk paste modification, Cement and Concrete Research, 24(1), 95–98.
- De Larrard, F., Belloc, A., Renwez, S. and Boulay, C. (1994). Is the Cube Test Suitable for High Performance Concrete? Materials and Structures, RILEM Publications, Bagnaux, France, 27(174), 580–583.
- De Larrard, F., and Sedran, T. (1994). Optimization of ultra-high performance concrete by the use of a packing model. Cement and Concrete Research, 24, 997–1009.
- Fehling, E., Bunje, K. (2003). Bemessung für Biegung und Querkraft für Bauteile aus UHFB; In: König, G. et al.: Ultrahochfester Beton; Bauwerk Verlag, Berlin.

- Frettlöhr B., Reineck K. H., and Reinhardt H.W. (2012). Size and Shape Effect of UHPFRC Prisms Tested under Axial Tension and Bending, *HPFRCC 6, RILEM*, 365–372.
- Frettlöhr, B., Reineck, K. H. (2009). Tests on the size effect of thin members out of Ultra-High-Performance fibre reinforced concrete subjected to combined bending and axial forces. Abschlussbericht zum Forschungsvorhaben RE 813/6-1 der Deutschen Forschungsgemeinschaft (DFG). Universität Stuttgart, Institut für Leichtbau Entwerfen und Konstruieren (ILEK).
- Goldszal, A., and Bousquet, J. (2001). Wet agglomeration of powders: from physics toward process optimization, *Powder Technology*, 117,221-231.
- Graybeal, B.A. and Davis, M. (2008). Cylinder or Cube: Strength testing of 80 to 200 MPa (11.6 to 29 ksi) Ultra-High-Performance Fiber-Reinforced Concrete. *ACI Material Journal*, 105(6), 603-609.
- Graybeal, B.A. (2006). Material property characterization of ultra-high performance concrete. Report No. FHWA-HRT-06-103, Federal Highway Administration, Washington, D.C., USA, 186pp.
- Graybeal, B. and J. Tanesi (2007). Durability of an Ultrahigh-Performance Concrete, *ASCE Journal of Materials in Civil Engineering*, 19(10), 850-854.
- Habel, K., Viviani, M., Denarie, E., and Bruehwiler, E. (2006). Development of the mechanical properties of an ultra-high performance fiber reinforced concrete (UHPFRC). *Cement and Concrete Research*, 36(7), 1362–1370.
- Habel, K. (2004). Structural Behaviour of Elements combining Ultra-High Performance Fibre-Reinforced concretes (UHPFRC) and Concrete, EPFL, Swiss Federal Institute of Technology. Doctoral Thesis, No. 3036, Lausanne, Switzerland.
- Habel, K., Charron, J.P., Braikey, S., Hooton, R.D., Gauvreau, P., and Massicotte, B. (2008). Ultra-high performance fiber reinforced concrete mix design in central Canada, *Canadian Journal of Civil Engineering*, 35(2), 217–224.
- Hajar, Z., Simon, A., Lecointre, D., and Petitjean, J. (2003). Construction of the First Road Bridges Made of Ultra-High-Performance Concrete, *Proceedings, 2003 International Symposium on High Performance Concrete*, Orlando, FL, 18 pp.
- Hegger J., and Rauscher S. (2008), High performance materials–Advances in composite constructions. *Taylor Made Concrete Structures – Walraven & Stoelhorst (eds) © 2008 Taylor & Francis Group, London, ISBN 978-0-415-47535-8.*

- Hegger, J., Goralski, C., Rauscher, S., Kerkeni, N. (2004). Finite Elemente Berechnungen zum Trag- und Verformungsverhalten von Kopfbolzendübeln. *Stahlbau* 73(1), 20–25.
- Hegger J., Feldmann M., Rauscher S., Hechler O. (2009). High-Performance Materials in Composite Construction. *International Association for Bridge and Structural Engineering, Structural Engineering International*, 19(4), 438-446.
- Hegger, J., Gallwoszus, J., Rauscher, S. (2009). Load-Carrying Behaviour of Connectors under Shear, Tension and Compression in Ultra High Performance Concrete. In: 11th Nordic Steel Construction Conference NSCC, September 2-4, Malmö/Sweden; Proceedings: Swedish Institute of Steel Construction, 486-493. ISBN 91-7127-058-2.
- Hegger J., Claßen M., Schaumann P., Sothmann J. Feldmann M., Döring B. (2013). Entwicklung einer integrierten Verbunddecke für nachhaltige Stahlbauten. *Stahlbau* 82(1), 11–17.
- Higashiyama, H., and Banthia, N. (2008). Correlating Flexural and Shear Toughness of Lightweight Fiber-Reinforced Concrete, *ACI Materials Journal*, 105 (3), 251-257.
- Hillerborg, A., Modeer, M. and Petersson, P. E. (1976). Analysis of Crack Formation and Crack Growth in Concrete by Means of Fracture Mechanics and Finite Elements, *Cement and Concrete Research*, 6, 773–782.
- Horszczaruk, E. (2004). Abrasion Resistance of High Strength Fiber-Reinforced Concrete, in di Prisco, M., R. Felicetti, and G.A. Plizzari, Eds., *Fiber Reinforced Concretes–BEFIB 2004*, Proceedings of the Sixth International RILEM Symposium, Varenna, Italy, pp.257–266.
- Japanese Society of Civil Engineers. (2008). Recommendations for Design and Construction of High Performance Fiber Reinforced Cement Composites with multiple fine Cracks (HPFRCC).
- JSCE-G 552-1999 (2005). Test Method for Bending Strength and Bending Toughness of Steel Fiber Reinforced Concrete, *Standard Specification for Concrete Structures, Test Methods and Specifications*. 362pp.
- JSCE-G 553-1999 (2005). Test Method for Shear Strength of Steel Fiber Reinforced Concrete, *Standard specifications for Concrete Structures, Test Methods and Specifications*. 362pp.
- JCI Standard SF-4 (1984). Method of tests for flexural strength and flexural toughness of fiber–reinforced concrete. *Japan Concrete Institute Standards for Test Methods of Fiber Reinforced Concrete*, Tokyo.
- Kang, S.T., Lee, Y., Park, Y.D. Kim, J.K. (2010). Tensile fracture properties of an Ultra High Performance Fiber. *Composite Structure*, 92, 61–71.

- Kantro, D.L. (1980). Influence of water-reducing admixtures on the properties of cement paste—a miniature slump test, PCA R&D Bulletin RD079.01T, Portland Cement Association, Skokie, IL, pp. 95-102.
- Kendall K, Howard A. J., Birchall J. D. (1983). The relation between porosity, microstructure and strength and the approach to advanced cement-based materials. Philosophical Transactions of the Royal Society of London, A 310, London, England, pp. 139-153.
- Kohlmeyer C. (2007). Beitrag zum Tragverhalten von Verbundträgern im Bereich von großen Stegöffnungen unter besonderer Berücksichtigung der Querkrafttragfähigkeit des Stahlbetongurtes. Kaiserslautern, Germany.
- Kurita, A., Ohyama, O. (2002). Recent development of steel-concrete hybrid bridges in Japan, fib congress, Osaka, pp.217-231.
- Kyriakides, M. A., and Billington, S. L. (2008). Seismic Retrofit of Masonry-Infilled Non-Ductile Reinforced Concrete Frames Using Sprayable ECC, Proceedings of the 14th World Conference on Earthquake Engineering (14WCEE), Beijing, China.
- Lange, J., Rauscher, S., Benning, W., Hegger, J. (2008). Ellipsen- und Kreisdetektion zur Bestimmung der Orientierung von Stahl- und Glasfasern in Beton, Technisches Messen 75, Oldenbourg Verlag.
- Le, T.T., Soutsos M.N., Millard S.G., and Barnett S.J. (2007). UHPFRC Optimisation of Mix Proportions, Proceedings of CONCRETE PLATFORM International Conference, Belfast, Northern Ireland, 19th – 20th April, pp. 339- 348.
- Le T.T., Soutsos M.N., Millard S.G., and Tang K. (1997). Structural Behaviour of a UHPFRC Flag Pavement, Proceedings of The Second International Symposium on Ultra High Performance Concrete, Kassel, Germany, 5th–7th March, pp. 663-670.
- Li, V. (1997). Engineered Cementitious Composites (ECC)–Tailored Composites Through Micromechanical Modeling. Fiber Reinforced Concrete: Present and Future, Ed. N. Banthia, Canadian Society of Civil Engineers, Montréal, QC, 213 pp.
- Li, V.C., Wu, H.C., Maalej, M., and Mishra D.K. (1996). Tensile Behavior of Cement-Based Composites with Random Discontinuous Steel Fibers. Journal of American Ceramic Society. 79(1), American Ceramic Society, Westerville, OH, pp. 74–78.
- Li, Z., Kulkarni, S.M., and Shah, S.P. (1993). New Test Method for Obtaining Softening Response of Unnotched Concrete Specimen Under Uniaxial Tension. Experimental Mechanics, 33, Society for Experimental Mechanics, Inc., Bethel, CT, pp. 181–188.

- Li, Z., Li, F., Chang, T.P. and Mai, Y. (1998). Uniaxial Tensile Behavior of Concrete Reinforced with Randomly Distributed Short Fibers, *ACI Materials Journal*, American Concrete Institute, Farmington Hills, MI, 95(5), pp. 564–574.
- Lim, T., Paramasivam, P. and Lee S. (1987). Analytical Model for Tensile Behavior of Steel Fiber Concrete, *ACI Materials Journal*, July–Aug, American Concrete Institute, Farmington Hills, MI, 84(4), pp. 286–298.
- Lee, J., and Fenves G. L. (1998). Plastic-Damage Model for Cyclic Loading of Concrete Structures. *Journal of Engineering Mechanics*, 124(8), pp. 892–900.
- Lubliner, J., Oliver, J., Oller, S., and Oñate E. (1989). A Plastic-Damage Model for Concrete. *International Journal of Solids and Structures*, 25, pp. 299–329.
- Ma, J., and Schneider H. (2002). Properties of Ultra-High-Performance Concrete. Leipzig, Annual Civil Engineering Report (LACER), 7, 25-32.
- Ma, J., Dehn, F., Tue, N.V., Orgass, M., and Schmidt D. (2004). Comparative Investigations on Ultra-High Performance Concrete with and without Coarse Aggregates, *Proceedings, International Symposium on Ultra-High Performance Concrete*, Kassel, Germany, pp. 205–212.
- Mangerig I., Burger S., Wagner R., Wurzer O., Zapfe C. (2011). Zum Einsatz von Betondübeln im Verbundbau (Teil 1)–Ruhende Beanspruchung. Ernst & Sohn Verlag für Architektur und technische Wissenschaften GmbH & Co. KG, Berlin, *Stahlbau* 80(12).
- Mazanec, O., Lowke, D., and Schießl, P. (2010). Mixing of high performance concrete: effect of concrete composition and mixing intensity on mixing time, *Materials and Structures*, 43, pp.357–365.
- Markovic I. (2006). High-performance hybrid-fibre concrete–development and utilisation. Technische Universität Delft, Ph.D. thesis.
- Martin C., Bernd, D., Feldmann M., Hegger J., Schaumann P., Sothmann J. (2013). Entwicklung einer integrierten Verbunddecke für nachhaltige Stahlbauten, *Stahlbau* 82 (1), 11-17.
- Montesinos, G. J., and Wight, J. K. (2005). Experimental Study on Seismic Behavior of High-Performance Fiber-Reinforced Cement Composite Coupling Beams, *ACI Structural Journal*, 102(1), Jan.-Feb, pp. 159-166.
- Morin V., Cohen Tenoudji F., Feylessoufi A., Richard P. (2001). Superplasticizer effects on setting and structuration mechanisms of Ultra High-Performance Concrete, *Cem. Concr. Res.* 31 (1), 63–71.

- Morin V., Cohen-Tenoudji F., Feylessoufi A., Richard P. (2002). Evolution of the capillary network in a reactive powder concrete during hydration process, *Cem. Concr. Res.* 32 (12) 1907–1914.
- Morris, A.D., and Garrett G.G. (1981). A Comparative Study of the Static and Fatigue Behaviour of Plain and Steel Fibre Reinforced Mortar in Compression and Direct Tension, *International Journal of Cement Composites and Lightweight Concrete*, 3 (2), 73–91, Elsevier Science.
- Naaman A.E., Reinhardt H.W. (2003). High performance fiber reinforced cement composites 4 UHPFRCC-4: international RILEM workshop. *Mater Struct* 36,710–712.
- Naaman A.E., Reinhardt H.W. (2006). Proposed classification of UHPFRC composites based on their tensile response. *Mater Struct*, 39, 547–555. doi:10.1617/s11527-006-9103-2
- Nataraja, M.C., Dhang, N., and Gupta, A.P. (2000). Toughness characterization of steel fiber-reinforced concrete by JSCE approach. *Cement and Concrete Research*, 30, 593- 597.
- NEN-6720 (1995). Voorschriften beton, TGB 1990, Constructieve eisen en rekenmethoden (VBC 1995), 2nd ed., Nederlands Normalisatie-instituut, Delft.
- Naaman A. E. (2002). Toughness, ductility, surface energy and deflection-hardening FRC composites. Proceedings of the JCI international Workshop on Ductile Fiber Reinforced Cementitious Composites (DFRCC) - Application and Evaluation (DFRCC-02), Takayama, Japan, October, pp 33-57.
- Naaman, A.E. (2003). Strain hardening and deflection hardening fiber reinforced cement composites. In: Proceeding of the 4th international symposium on high performance fiber reinforced cement composites, Ann Arbor, MI, USA, pp. 95–113.
- Nanni, A. (1988). Splitting-Tension Test for Fiber Reinforced Concrete, *ACI Materials Journal*, 85(4), Jul–Aug, American Concrete Institute, Farmington Hills, MI, pp. 229–233.
- Neville, A.M. (1996). *Properties of Concrete*, Fourth and Final Edition, John Wiley & Sons, Inc., New York, NY, 844 pp.
- Novák, B., Röhm, M., Weissbach, M. (2007). New methods of connection for composite girders with corrugated steel webs. Proc. 2nd int'l Symposium on Connections between steel and concrete, Sept 4-7, Stuttgart, ISBN: 978-3-89821-807-8, S. 1381-1390.
- Oguejiofor, E.C., Hosain, M.U. (1996). Numerical analysis of Push-Out specimens with perfobond rib connectors. *Composite Structures* 62, S. 617-624.
- Oguejiofor, E.C., Hosain, M.U. (1994). A parametric study of perfobond rib shear connectors, *Can Journal of Civil Engineering* 21, S. 614-625.

- Olsen, E.C. and Billington, S.L. (2011). Cyclic behavior of precast, self-compacting ductile concrete infill panels for seismic retrofit of steel frame buildings, 108(1), 51-60.
- Popovics, S. (1998). Strength and Related Properties of Concrete: A Quantitative Approach, John Wiley & Sons, Inc., New York, NY, 535 pp.
- Phillips, D.C., and Zhang B.S. (1993). Direct Tension Tests on Notched and Unnotched Plain Concrete Specimens. Magazine of Concrete Research, 45(162), 25-35.
- Pfeifer, C., Bernd, M., Weber, C., and Stark, J. (2010). Pozzolanic reaction of silica fume in Ultra-high performance concrete, 3rd fib International Congress, PCI, Washington D.C., USA, 14pp.
- Parra-Montesinos, G. J. Peterfreund, S. W. and Chao, S.-H. (2005). Highly Damage-Tolerant Beam-Column Joints through Use of High- Performance Fiber-Reinforced Cement Composites, ACI Structural Journal, 102(3), May-June, pp. 487-495.
- Rapoport, J., Aldea, C.-M., Shah, S.P., Ankenman, B. and Karr, A. (2002). Permeability of Cracked Steel Fiber-Reinforced Concrete, ASCE Journal of Materials in Civil Engineering, American Society of Civil Engineers, Washington, DC, Jul-Aug, 14(4), pp. 355-358.
- Rauscher, S., Hegger, J. (2009). Shear Connectors in Steel Fiber Reinforced Ultra High Performance Concrete. IABSE Symposium Bangkok 2009: Sustainable Infrastructure – Environment Friendly, Safe and Resource Efficient, 09.-11. Sept., IABSE Reports, 96, pp. 194-195, ISBN 978-85748- 121-5.
- Rauscher S. (2011). Zum Trag- und Verformungsverhalten von Verbundträgern aus ultrahochfestem Beton mit Verbundleisten. PhD Desertaion, Germany.
- Reineck, K.-H. Frettlöhr, B. (2010). Tests on scale effect of UHPFRC under bending and axial forces. 3rd fib International Congress, Washington DC. Paper 54. 14 pp.
- Reineck, K.-H., Frettlöhr, B. (2011). Versuche zum Maßstabseinfluss bei kombinierter Beanspruchung aus Biegung und Längskraft von UHFFB mit einer Druckfestigkeit von 211 MPa (tests on the scale effect under combined bending and axial forces of UHPFRC with 211 MPa). Bauingenieur 86 (1), 42-52.
- Reineck K.H.; and Frettlöhr, B. (2010). Tests on scale effect of UHPFRC under bending and axial forces, 3rd fib International Congress, PCI, Washington, D.C., USA, 14pp.
- Reineck K.H., Greiner, S. (2007). Scale effect and combined loading of thin UHPFRC members. Advances in Construction Materials, Part II, 211-218.
- Richard, P., and Cheyrezy, M. (1995). Composition of Reactive Powder Concretes, Cement and Concrete Research, 25(7), 1501-1511.

- RILEM, TC 162-TDF. (2001). Recommendations of RILEM TC 162-TDF: Test and Design Methods for Steel Fibre Reinforced Concrete Uni-Axial Tension Test for Steel Fibre Reinforced Concrete, *Materials and Structures*, Jan–Feb, 34(235), pp. 3–6, RILEM Publications, Bagnaux, France.
- Röhm, J. (2009). Untersuchungen zum Tragverhalten von strukturintegrierten Verbindungsmitteln bei Stahlverbundträgern mit Trapezblechstegen im Brückenbau. Universität Stuttgart. 168 pp.
- Rossi, P., Arca, A., Parant, E., and Fakhria, P. (2005). Bending and Compressive Behaviours of a New Cement Composite. *Cement and Concrete Research*, 35(1), 27-33.
- Eligehausen, R., Mallee, R., John F. S. (2006). Anchorage in Concrete Construction, March, Volume 10, Hardcover, 391 pages, ISBN: 978-3-433-01143-0.
- Rossi, P. (1997). High Performance Multimodal Fiber Reinforced Cement Composites (HPMFRCC): The LCPC Experience,” *ACI Materials Journal*, American Concrete Institute, Farmington Hills, MI, Nov–Dec, 94(6), pp. 478–483,
- Saito, M., and Imai. S. (1983). Direct Tensile Fatigue of Concrete by the Use of Friction Grips, *ACI Journal*, American Concrete Institute, Farmington Hills, MI, 80(5), pp. 431–438.
- Sarkar, S.L., and Aïtcin, P.C. (1987). Dissolution rate of silica fume in very high strength concrete, *Cement and Concrete Research*, 17(4) , 591–601.
- Skazlic', M., and Bjegovic, D. (2009). Toughness testing of ultra high performance fibre reinforced concrete. *Materials and Structures*, 42, pp.1025–1038.
- Schmidt, V., Seidl, G., Hever, M., Zapfe, C. (2004). Verbundbrücke Pöcking Innovative VFT-Träger mit Betondübeln. *Stahlbau* 73, 6, 387-393.
- Schießl P., Mazanec O., Lowke D., Plank J., Schröfl C., Gruber M., Schmidt M., Stephan D., Glotzbach C. (2010). Rheology of UHPC-Effect of superplasticizer and silica fume on mixing and workability of UHPC, 3rd fib International Congress, PCI, Washington D.C., USA , 20pp.
- Schmidt, V., Seidl, G., Hever, M., Zapfe, C. (2004). Verbundbrücke Pöcking Innovative VFT-Träger mit Betondübeln. *Stahlbau* 73, 6, 387-393.
- Sedran T., de Larrard F., Angot D. (1994). Prévission des mélanges granulaires par le modèle de suspension solide, I - Fondements théoriques et étalonnage du modèle, *Bulletin de liaison des laboratoires des ponts et chaussées*, No. 194, France, November-December, pp 59-70 (in French).

- Seidl, G., Braun, A. (2009). VFT-WIB-Brücke bei Vigaun – Verbundbrücke mit externer Bewehrung, *Stahlbau* 78, 2, 86-93.
- Tue, N.V., Vinh, B.D., Kuchler, M. (2008). Finite Element Modeling of Composite Beams made of Made of Ultra High Performance Concrete with Full and Partial Shear Connection, 3rd acf-International Conference - ACF / VCA 2008, Ho Chi Minh City, Vietnam, November 11-13.
- Semioli, W.J. (2001). The New Concrete Technology, *Concrete International*, November, American Concrete Institute, Farmington Hills, MI, pp. 75–79.
- Simon A., Hajar Z., Lecointre D., Petitjean J. (2002). Realization of two roadbridges with Ultra-High Performance Fibre Reinforced Concrete, 6th Int. Symposium on High Strength / High Performance Concrete, Leipzig, Germany, june, pp. 753-768.
- Shah S.P., Brandt A.M., Ouyang C., Baggott R., Eibl J., Glinicki M.A. (1995). Toughness characterization and toughening mechanisms. In: Naaman AE, Reinhardt HW (eds) *Proceedings of the second international RILEM workshop*. E&FN SPON, Ann Arbor, USA, pp 193–228.
- Stengel T., Lin X., Schießl P., Gehlen C. (2012). Tailor-Made Steel Fiber Reinforced Ultra High Performance Concrete Single Fiber Pull-Out. Bending Capacity and Fracture Toughness, G.J. Parra-Montesinos, © RILEM 2012, HPRCC 6, pp. 127–135.
- Stiel, T., Karihaloo, B. and Fehling, E. (2004). Effects of Casting Direction on the Mechanical Properties of CARDIFRC®, *Proceedings of the International Symposium on Ultra High Performance Concrete*, Kassel, Germany, September 13–15, pp. 481–493.
- Timoshenko, S., and Goodier, J.N. (1951). *Theory of Elasticity*, 2nd Edition, McGraw-Hill Book Company, New York, NY.
- Petroski, H.J., and Ojdovic, R.P. (1987). The Concrete Cylinder: Stress Analysis and Failure Modes, *International Journal of Fracture*, Springer Netherlands, 34(4), pp. 263–279.
- USBR 4914, (1992). Procedure for Direct Tensile Strength, Static Modulus of Elasticity, and Poisson's Ratio of Cylindrical Concrete Specimens in Tension, United States Department of Interior, Bureau of Reclamation, Washington, DC.
- Völkel, G., Harre, W. (1988). Versuche zum Verbundtragverhalten von Lochleisten, Prüfungsbericht, Forschungs- und Materialprüfungsanstalt Baden Württemberg –Otto-Graf-Institut-, Stuttgart.

- Weil, T., Schnell, J., and Kurz, W. (2011). Design Model for Continuous Composite Beams with Web Openings. *Composite Construction in Steel and Concrete VI*, 173-184. doi: 10.1061/41142(396)15
- Wille K., Kim, D.J., and Naaman, A.E. (2010). Strain-hardening UHP-FRC with low fiber contents. *Materials and Structures*, 44(3), 583,598.
- Wille, K., Naaman, A.E., and Parra-Montesinos, G.J. (2011). Ultra-High Performance Concrete with Compressive Strength Exceeding 150 MPa (22 ksi): A Simpler Way, *ACI Materials Journal*, 108(1), 46-54.
- Wurzer, O. (1997). Zur Tragfähigkeit von Betondübel, Dissertation am Institut für Konstruktiven Ingenieurbau, Universität der Bundeswehr, München.
- Yan H., Sun W., Chen H. (1999). The effect of silica fume and steelfiber on the dynamic mechanical performance of high-strength concrete, *Cem. Concr. Res*, 29 (3), 423–426.